Metal Organic Vapour Phase Epitaxy of Strained InP-$Ga_xIn_{1-x}As_yP_{1-y}$ Quantum Well Lasers

thesis by

Arthur David Smith

submitted for the degree of Doctor of Philosophy in the Electrical and Electronics Engineering Department of Glasgow University.

August 1998

Acknowledgements

Firstly I must thank the management of what was STC Technology, which then became BNR Europe and finally Nortel Technology Europe in Harlow, Essex for their support, encouragement and facilities, without which this endeavour would have been impossible. This translates into Joe Mun, Peter Selway and Alastair Hyndman, with special thanks to Joe for the original support.

Then there is the entire 'laser group' at Harlow. Special thanks go to George Antell, Ted Thrush, Rick Glew, David Greene, Cliff Cureton and Joe Trigg for teaching me the art of InP-based MOCVD. The majority of the technical guidance in this period of research was provided by none other than Alan Briggs, whose constant questioning of the results ('wwwwwweellllll..... I don't really think you can say that', or, 'if I were you, I'd try this') provided a continuous stimulus, thank you Alan! The characteristaion efforts of Keith Scarrot, Alan Briggs and David Boyle, the device design efforts of Andrew Wright, Igor Czajkowski, Bindi Bhumbra, Mark Gibbon and Martin Fice, the processing efforts of Dave Moule, Julie Champolovier, Sue Wheeler and Darren Goodchild. Not forgetting the advice of Steve Clements, Andy Collar, Gordon Henshall, James Whiteaway and Dick Goodwin.

Invaluable technical interactions were had with many outside Harlow. The Physics and Material Science groups at the University of Surrey provided excellent collaboration during a DTI sponsored LINK program. Alf Adams, Eoin O'Reilly, Mark Silver, Vicki Wilkinson, Dave Dunstan, Xiao Zhou and Uschi Bangert (later UMIST) - many thanks for detailed and timely assessment results and technical guidance. The award for the best TEM of the thesis, however, goes to Bob Mallard of Oxford University and now Nortel, Ottawa. He also deserves an award for teaching me and the missus to canoe, a memorable event by any stretch of the imagination.

I think the normal number of PhD supervisors is one or two, I've had four. The first two were Steve Beaumont and Joe Mun, who I had to let go after only one year as I was technically re-vectored, thanks guys - you sewed the seeds of what was to become an 8 year epic! The mantle was then thrust upon the unsuspecting John Marsh and David Greene. Thank you both for your continual reminders and especially John for the 'writing up' guilt trips, I'll miss them! Yes John, it never quite reached the 'my dog ate it' stage but it was getting very close.

Lastly thanks must go to my dear wife, Susan, who succeeded in surpassing the John Marsh guilt trips with comments like, 'how will you be able to live with yourself if you don't finish this' and 'at this rate I'm going to get my PhD before you', thank you darling - I'd never have done it without you.

Table Of Contents

List of Figures

Chapter 2

Chapter 3

Chapter 4

Chapter 5

Chapter 6

Chapter 7

Chapter 8

Chapter 9

List of Tables

Chapter 10

Journal and Conference Publications Related to This Thesis

Chapter 2

A.D Smith, D.A.H. Spear, C.G. Cureton, A.T.R. Briggs and E.J. Thrush, *'MOCVD growth and fabrication of InP-based detector and receiver array OEICs on 2" diameter wafers'*, Published in the Proceedings of the Symposium on Large Area/Scale Epitaxy for III-V Device Fabrication, The Electrochemical Society, volume 91-13, p35-45, 1991.

Chapter 7

A.D. Smith and A.T.R. Briggs, *'The Growth and Assessment of Strain-compensated MQW Lasers'*, published in the Proceedings of the Rank Prize Fund Symposium, July 1992.

U. Bangert, A.J. Harvey, V.A. Wilkinson, C. Dieker, J.M. Jowett, **A.D. Smith**, S.D. Perrin and C.J. Gibbings, *'Evidence for strain relaxation via compositional fluctuations in strained quaternary/quaternary and quaternary/ternary multiple quantum well structures'*, Journal of Crystal Growth, 132(1993), p231-240.

A.P. Wright, A.T.R. Briggs, **A.D. Smith**, R.S. Baulcomb and K.J. Warbrick, *'22GHz-bandwidth 1.5 μm compressively strained InGaAsP MQW ridge-waveguide DFB lasers'*, IEE Electronics Letters, 29(21), October 1993, p1848-1849.

Chapter 8

A.D. Smith, A.T.R. Briggs, K. Scarrott, X. Zhou, U. Bangert, *'Optimisation of Growth Conditions for strain compensated $Ga_{0.32}In_{0.68}As/Ga_{0.61}In_{0.39}As$ multiple quantum wells'*, Applied Physics Letters, 65(18), 31 October 1994, p2311-2313.

X. Zhou, P. Charsley, **A.D. Smith** and A.T.R. Briggs, *' The Characteristics of the Lateral Thickness Modulation in Strained Layer $Ga_xIn_{1-x}As$ Multiple Quantum Well Structures grown by MOVPE'*, Materials Research Society Symposium, Proceedings Volume 340, p337-342, 1994.

I.K. Czajkowski, M.A. Gibbon, G.H.B. Thompson, P.D. Greene, **A.D. Smith** and M. Silver, *'Strain-compensated MQW electro-absorption modulator for increased optical power handling'*, IEE Electronics Letters, 30(11), May 1994, p900-901.

R.W. Glew, K. Scarrott, A.T.R. Briggs, **A.D. Smith**, V.A. Wilkinson, X. Zhou and M. Silver, *' Elimination of wavy layer growth phenomena in strain-compensated GaInAsP/GaInAsP multiple quantum well stacks'*, Journal of Crystal Growth, 145(1994), p764-770.

F. Royo, J. Camassel, R. Schwedler, B. Fraisse and **A.D. Smith**, *'Optical Properties of High-Quality Strain Compensated InGaAs/InGaAs Superlattices grown on InP'*, published in Semiconductor Heteroepitaxy - growth, characterisation and devices applications, 1995, World Scientific Publishing, p502-505.

R.W. Martin, S.L. Wong, R.J. Nicholas, **A.D. Smith**, M.A. Gibbon, E.J. Thrush and J.P. Stagg, *'Band Offsets in strained InGaAsP/InGaAsP quantum well optical modulator structures'*, Journal de Physique IV, Colloque C5, supplement au Journal de Physique II, Volume 3 octobre 1993, p327-330.

E.J. Thrush, R.W. Glew, P.D. Greene, M.A. Gibbon, C.J. Armistead, **A.D. Smith**, A.T.R. Briggs, K. Scarrott, I.K. Czajkowski, C.J. Jones and B.L. Patel, *'The growth of 1550nm integrated laser/modulator structures by MOCVD'*, Proc. International Conference on InP and Related Materials, Santa Barbara, 1994.

Chapter 9

A.D. Smith, A.T.R. Briggs, A. Vranic and K. Scarrott, *'MOVPE Growth and Assessment of InP-based Tensile strained MQW Laser Structures'*, Proceedings of the European Workshop on MOVPE, Malmo 1993, paper E8(University of Lund, 1993)

R.W. Martin, S.L. Wong, R.J. Warburton, R.J. Nicholas, **A.D. Smith**, M.A. Gibbon and E.J. Thrush, *'Variations of hole effective masses induced by tensile strain in $In_{1-x}Ga_xAs(P)/InGaAsP$ heterostructures'*, Physical Review B, 50(11), September 1994, p7660-7667.

G. Jones, **A.D. Smith**, E.P. O'Reilly, M. Silver, A.T.R. Briggs, M.J. Fice, A.R. Adams, P.D. Greene, K. Scarrott and A. Vranic, *' The Influence of Tensile Strain on differential gain and Auger recombination in 1.5μm multiple-quantum-well lasers'*, IEEE J. Quantum Electronics, 34(5), 1998, pp822-834..

Abstract

This thesis describes experimental investigations into the application of strain to the wells and barriers of InP-$Ga_xIn_{1-x}As_yP_{1-y}$ based, multiple-quantum well (MQW) lasers. Material characterisation and device performance results are used to evaluate, both qualitatively and quantitatively, the effects of strain incorporation into structures grown by low-pressure metal organic vapour phase epitaxy. Multiple-quantum well laser structures, operating at wavelengths around 1.5μm, are grown with either strain compensated (zero-net strain) or non-compensated active regions.

Strain compensated $Ga_xIn_{1-x}As_yP_{1-y}$-$Ga_xIn_{1-x}As_yP_{1-y}$ multiple-quantum well structures are shown to suffer from thickness modulations after a given number of wells and barriers are deposited. The thickness modulations in the compressively strained wells are in anti-phase to those observed in the tensile strained barriers. Experimental evidence is presented which relates the severity of this effect to the composition of the alloys used and the conditions under which they are grown. The source of the thickness modulations is attributed to two effects: compositional clustering (spinodal decomposition) of $Ga_xIn_{1-x}As_yP_{1-y}$ alloys and strain relaxation via the expansion and contraction of lattice planes. Further experimental data is presented that describes the optimisation in growth conditions to suppress thickness modulations, enabling larger numbers of planar wells and barriers to be grown. The effects of compositional clustering can be minimised by using higher growth temperatures and selecting alloy compositions outside the miscibility gap. In contrast, strain relief via the expansion and contraction of lattice planes is eliminated by using lower growth temperatures and higher group V pre-cursor gas flows. The growth conditions which best overcome these two effects in ±1% $Ga_xIn_{1-x}As$ and ±1% $Ga_xIn_{1-x}As_yP_{1-y}$ strain-compensated, multiple-quantum well, laser structures are described.

The strain relief behaviour of non-compensated InP-$Ga_xIn_{1-x}As_yP_{1-y}$ based, multiple-quantum well structures is presented. Dislocation generation is identified as the primary strain relief mechanism in $Ga_xIn_{1-x}As_yP_{1-y}$/$Ga_xIn_{1-x}As$ MQW structures with tensile strain in the wells. Thickness modulations are identified as a secondary strain relief mechanism in such structures, occurring at higher values of tensile strain. The growth optimisation techniques developed for strain compensated structures are also shown to suppress thickness modulations in non-compensated structures. Strain relief in non-compensated structures is influenced by the type of barrier material used: a $Ga_xIn_{1-x}As_yP_{1-y}$ well with a $Ga_xIn_{1-x}As_yP_{1-y}$ barrier suffers from thickness modulated growth, whereas the same $Ga_xIn_{1-x}As_yP_{1-y}$ well with an InP barrier is shown to relax via the introduction of strain relieving dislocations.

Broad-area 50μm stripe, ridge waveguide Fabry-Perot, ridge waveguide DFB lasers and electro-absorption modulators are used to study the effects of strain on device performance. Consistent with theoretical predictions, improvements in the threshold current and gain are observed in strain compensated $Ga_xIn_{1-x}As_yP_{1-y}$-$Ga_xIn_{1-x}As_yP_{1-y}$ MQW lasers with compressively strained wells, when compared to similar structures containing lattice matched or compressively strained ternary wells. Further performance improvements are observed in high speed, directly modulated lasers when similar MQW active regions are used. A fourfold improvement in differential gain is observed over a similar lattice matched structure, this contributed to a 3dB frequency response of 22GHz measured on a DFB laser.

MQW lasers containing tensile strained wells demonstrated the highest gain performance of all of the strained laser structures examined. This was achieved when sufficient tensile strain, greater than 1%, was introduced to the wells. An improvement in gain of up to 100% was observed over similar structures containing 1.1% compressively strained, ternary wells.

In addition to improving the material performance of InP-based alloys, strain is used to engineer the valence band of an MQW, electro-absorption modulator structure. By introducing compressive strain in the wells and tensile strain in the barriers, the hole confinement in the wells is reduced. This alleviates the hole trapping effects observed in similar lattice matched structures and results in improved power handling characteristics and high speed (10 Gbits/sec) performance.

Chapter 1

Introduction

As modern telecommunication systems continue to evolve into the fibre-optic domain, the need for high performance and low cost optoelectronic devices operating at the 1.3 μm and 1.55 μm wavelengths becomes obvious. Their application in the high bit-rate (≥ 2.5 Gbits/second), digital transmission backbone of large capacity telecommunication networks, be it in either a sub-marine or a land based system, is now commonplace. With the appetite for telecommunication bandwidth continuing to grow (as a result of the increase in data communication, enterprise network and internet traffic), the implementation of high-bit rate optical transmission has permeated further into telecommunications, moving into metropolitan and local area networks. The proliferation of optical transmission has driven, and been driven by, the progress made in the design and production of the critical components used: directly modulated high-speed laser sources, electro-absorption modulated high speed laser sources, high power pump lasers for optical amplifiers and large bandwidth receivers. Improvements in the performance of these devices have a direct impact on the capability of the optical transmission system.

Indium Phoshide (InP), and the alloys that can be grown lattice matched to it, e.g. Gallium Indium Arsenide Phosphide ($Ga_xIn_{1-x}As_yP_{1-y}$), is the material system most commonly used to fabricate these devices. Material properties such as lattice matching, selective etching and band-gap engineering, have made device structures comprising different compositions of $Ga_xIn_{1-x}As_yP_{1-y}$ possible to fabricate. These material properties, together with demonstrated long term (> 25 years) reliability, has made InP-$Ga_xIn_{1-x}As_yP_{1-y}$ devices the most commonly used in optical transmission systems. The crystal growth of InP-$Ga_xIn_{1-x}As_yP_{1-y}$ devices is usually achieved by metal organic vapour phase epitaxy (MOVPE). Initial device structures were grown with liquid phase epitaxy (LPE), but the large area and uniformity demanded by modern, high capacity production has resulted in MOVPE being the preferred method of epitaxial deposition.

The first InP-based laser devices were fabricated with bulk active regions, but improvements in the performance were achieved by incorporating multiple quantum wells (MQW's). The alloys used in the fabrication of these laser structures were limited to those that could be grown lattice matched to an InP substrate. The use of non-lattice matched alloys was initially avoided due to concerns over the limited thickness of strained material that could be grown without strain relieving dislocations being introduced into the structure. Even if structures were grown without dislocations, concerns

were still present over the latent reliability hazard posed by the presence of a strained layer. Such concerns were very reasonable at that time, as many of the laser applications were in high capacity sub-marine systems where long term reliability is of paramount importance.

It became apparent, however, that the performance of InP-based lasers was limited by certain parasitic effects, which give rise to a less efficient electrical to optical conversion process. Auger recombination and inter-valence band absorption occur more readily in InP-based laser devices than in similar devices fabricated in other material systems, e.g. GaAs/$Ga_xIn_{1-x}As$. The valence band structure of lattice matched InP-$Ga_xIn_{1-x}As_yP_{1-y}$ alloys yields a relatively large hole effective mass. Such a large hole effective mass is known to compromise a number of key laser characteristics. Methods of suppressing such parasitic effects were proposed which rely on the incorporation of coherent strain in the active layer region. By selecting the appropriate magnitude and/or sign of strain, the valence band structure has its in-plane effective mass reduced.

At the time of the commencement of this research (October 1991), a number of reports had appeared in the literature describing the beneficial effects of coherent strain in the wells of MQW laser structures. However, the challenge of further optimisation in the performance of strained layer InP-$Ga_xIn_{1-x}As_yP_{1-y}$ MQW based lasers remained. In this thesis, an experimental evaluation is performed on the effects of introducing coherent strain in the wells and barriers of MQW laser structures, grown by low-pressure MOVPE. Many different types of strained MQW structures are examined and a variety of material assessment techniques are used to determine the quality of the strained layer epitaxy. Broad area (50μm stripe) lasers, ridge waveguide Fabry-Perot lasers, ridge waveguide distributed feedback (DFB) lasers and electro-absorption modulators are fabricated from the strained layer MQW structures grown. Detailed analyses on the effects of well strain on device performance of broad-area devices is presented. The results, together with those measured on the ridge waveguide lasers and electro-absorption modulators, are used in conjunction with the material assessment observations to explain improvements in device performance. The following gives an overview of the contents in each section of this thesis.

Chapter 2 The Metal Organic Vapour Phase Epitaxy of InP-$Ga_xIn_{1-x}As_yP_{1-y}$ Structures

An introduction to InP-based MOVPE is presented. The growth apparatus is discussed in relation to the reactor design and the standard operating procedures used to grow all the samples in this thesis. MOVPE grown, InP electrical purity is reviewed, in addition to intentional n and p-type doping methods. The steps taken to evaluate and optimise the uniformity of the grown layer in a low-pressure MOVPE reactor are described. The results of the uniformity in the composition of Ga_xIn_{1-}

$_x$As and $Ga_xIn_{1-x}As_yP_{1-y}$ alloys are presented, in addition to observations made on the uniformity in layer thickness and electrical characteristics.

Chapter 3 Assessment of InP-$Ga_xIn_{1-x}As_yP_{1-y}$ Alloys

An overview of material assessment techniques commonly used in this thesis is presented. Room temperature photoluminescence (PL) and high resolution X-ray diffraction (HRXRD) are discussed as methods of measuring band-gap energy and lattice mismatch respectively. The methodology of translating these assessment results into a solid phase $Ga_xIn_{1-x}As$ or $Ga_xIn_{1-x}As_yP_{1-y}$ alloy compositions is described. A high level description of the modelling program used to perform these calculations on a routine basis is given. The same modelling program is capable of predicting the quantum well confined energy levels, with the compositions and thicknesses of the wells and barriers taken as input parameters. Other assessment techniques that are used throughout the thesis are also briefly discussed, they include: transmission electron microscopy, capacitance -voltage and Hall techniques for measuring electrical characteristics and methods of determining bulk layer thicknesses.

Chapter 4 The Growth Limitations Imposed by the Critical Thickness-Mismatch Product

This chapter introduces the concepts of mismatch, strain, relaxation and the Matthews-Blakeslee critical layer thickness. Methods of determining the critical layer thickness are reviewed and discussed in relation to the controversy that surrounded reported critical layer thicknesses for the strained layer GaAs/$Ga_xIn_{1-x}As$ material system. Matthews-Blakeslee curves for single layers of InP based strained $Ga_xIn_{1-x}As$ are calculated for grown layers terminated with, and without, an InP capping layer. Experimental results are presented for single layers of InP based material that had exceeded the critical thickness. Photoluminescence imaging is shown to be more sensitive than X-ray diffraction, as a means of discerning when the critical thickness has been exceeded. The crystallographic direction in which strain relieving dislocations form has been shown to depend on the sign of strain in the grown layer, i.e. tensile or compressive.

The concepts of MQW net strain and strain compensation are introduced. The growth of strained layer MQW stacks is discussed in relation to the potential critical thickness limitations: those imposed by the individual strained quantum well and those imposed by the net strain of the stack. In most material systems, strain compensation has been studied via the growth of a thick strained (usually graded) buffer layer, around whose composition tensile and compressive layers can be grown. The study of strain compensation in InP/$Ga_xIn_{1-x}As_yP_{1-y}$ materials is much more elegant, as both compressive and tensile strained alloys can be grown directly on to an InP substrate.

Chapter 5 InP-Based Quantum Well Lasers

Applications of InP-based lasers within an optical transmission system are briefly discussed. An introduction is given to laser action in semiconductor diodes with an emphasis on threshold current, efficiency and temperature sensitivity. The advantages of using quantum wells in the active regions of semiconductor lasers is briefly discussed, followed by a description of the relationship between the threshold current density of a laser and the quantum well gain. This relationship forms the theoretical basis for much of the later analysis presented on lasers fabricated from strained multiple quantum well structures. An overview of the laser fabrication processes is also given.

Chapter 6 The Benefits to be Achieved by Incorporating Coherent Strain in InP-Based MQW Laser Structures

The problems caused by the large hole effective mass, non-radiative Auger recombination and inter-valence band absorption are described. Theoretical predictions have suggested that the incorporation of coherent strain within the wells of MQW laser structures suppresses these parasitic effects, by altering the valence band structure. The theoretically predicted improvements are stated and the effects of coherent strain on the valence band structure are reviewed. The expected improvements in laser performance are also discussed.

Chapter 7 Strain Compensated $Ga_xIn_{1-x}As_yP_{1-y}/Ga_xIn_{1-x}As_yP_{1-y}$ Multiple Quantum Well Structures For High Power and High Speed Laser Applications

The growth of a variety of strain compensated $Ga_xIn_{1-x}As_yP_{1-y}$ MQW structures is performed with varying amounts of compressive strain in the wells and tensile strain in the barriers. A series of structures is grown, with a particular combination of well and barrier compositions, to study the effects of increasing the number of wells. A variety of material assessment techniques is used to examine a deleterious growth effect that is observed after a given number of well-barrier cycles is deposited. The deterioration in structural quality is shown to be caused by periodic undulations in the well and barrier thicknesses. Possible sources of the observed effects are proposed and discussed.

Broad-area and ridge waveguide laser structures are fabricated from the grown laser structures known not to suffer from the thickness modulated growth effect. A detailed analysis of the threshold current density is performed as a function of cavity length and number of wells. Parameters such as material loss, α, the gain per well, $\Gamma_W G_0$, and the infinite cavity length threshold current density, J_∞ , are determined. Comparisons are made between these results and those reported regarding other

MQW lasers. Improvements in the threshold current and output power of a ridge waveguide laser device are obtained, when compared to similar geometry devices comprising either strained or latticed matched $Ga_xIn_{1-x}As$ wells. A six-well, 2μm wide x 750μm long, ridge waveguide device is shown to be capable of delivering 129mW ex-facet power at a drive current of 700mA, making the device a suitable candidate as a high-power 1480nm pumping source for Er doped fibre amplifiers.

Similarly grown MQW structures are used in the active region of a ridge-waveguide device designed for high speed, direct modulation. A DFB, ridge waveguide device with a 3dB bandwidth of 22GHz at a drive current of 125mA is reported. High speed measurements performed on the same structure made into Fabry-Perot laser devices, show a fourfold improvement in the differential gain when compared to similar structures made using lattice matched quantum wells. In a subsequent attempt to increase the available 3dB bandwidth beyond 22GHz, an error was made in the processing, resulting in a lateral strain variation being defined in the direction of the grating. The results from an MQW overgrown on this lateral strain variation assist further in the understanding of the mechanisms responsible for the thickness modulated growth effect.

Chapter 8 Growth and Assessment of Strain Compensated Structures with ±1% $Ga_xIn_{1-x}As_yP_{1-y}$ and ±1% $Ga_xIn_{1-x}As$ MQW Regions

Strain compensation is used to engineer the valence band, in an attempt to improve the power handling characteristics of an electro-absorption modulator. The thickness modulated growth effect is again shown to limit the number of planar well-barrier cycles which can be grown. A 3-well electro-absorption modulator is fabricated and is shown to have eliminated the saturation effects observed in the photocurrent-input power characteristics of lattice matched devices. The thickness modulated growth effect is shown to significantly impair the structural quality of strain compensated MQW structures when a given number of well-barrier cycles are exceeded. A series of experiments are performed on ±1% $Ga_xIn_{1-x}As_yP_{1-y}$ and ±1% $Ga_xIn_{1-x}As$ MQW stacks, in an attempt to understand further the mechanisms of this deleterious growth effect.

Identical strain compensated ±1% $Ga_xIn_{1-x}As_yP_{1-y}$ MQW structures are grown at three different temperatures: 600°C, 650°C and 700°C. Improvements in the structural quality with increasing growth temperature suggest that the miscibility gap for $Ga_xIn_{1-x}As_yP_{1-y}$ alloys plays an important role in how these structures behave, validating one of the mechanisms proposed in chapter 7. To remove the effects of immiscibility, a similar series of structures are grown with ±1% $Ga_xIn_{1-x}As$ MQW regions. Improvements in structural quality are observed by increasing the partial pressure of the group V pre-cursor during growth and, contrary to the $Ga_xIn_{1-x}As_yP_{1-y}$ case, by decreasing the growth temperature. This observation validates the second mechanism proposed in chapter 7.

Under these optimised conditions the ability to grow potentially limitless, i.e. 50, numbers of strain compensated ±1% $Ga_xIn_{1-x}As$ multiple quantum wells is presented. The beneficial effects of strain compensation are demonstrated by the growth and assessment of an identical non-compensated structure with lattice matched, as opposed to tensile strained, barriers. The non-compensated structure contained strain relieving dislocations at the base of the MQW stack and also demonstrated signs of relaxation.

Further evidence is presented of the role of the miscibility gap on the ability to grow strain compensated $Ga_xIn_{1-x}As_yP_{1-y}$ MQW structures. The growth details of a practical electro-absorption modulator structure are described, which are successful in partially overcoming the two temperature-dependent mechanisms. Although it does not permit the growth of a limitless number of strain compensated MQW's, it enables sufficient numbers of wells and barriers to be grown for practical device applications.

Chapter 9 Growth and Assessment of Non-Compensated Strained $Ga_xIn_{1-x}As_y(P_{1-y})/Ga_xIn_{1-x}As_yP_{1-y}$ MQW Structures

A series of MQW structures without strain compensation, i.e. lattice matched barriers, are grown to understand further the structural limitations in strained layer InP-$Ga_xIn_{1-x}As_yP_{1-y}$ MOVPE growth. Increasing magnitudes of tensile strain is incorporated into the $Ga_xIn_{1-x}As$ wells of these samples. Direct evidence of the cross-over from E1-HH1 transitions to E1-LH1 transitions is observed by room temperature PL as the tensile strain is increased. At tensile strain levels greater than 1%, strain relieving dislocations are observed in the PL image. At higher levels of strain, thickness modulations are also observed in these, non-compensated, structures. The occurrence of thickness modulations is also shown to be suppressed by an increase in partial pressure of the group V pre-cursor.

A detailed analysis of the dependence of the threshold current density on the cavity length is performed for structures with tensile strain ranging from 0% (lattice match) to 1.6%. It is shown that, once the heavy-hole to light-hole cross-over has been passed, J_∞ decreases and $\Gamma_W G_0$ increases with increasing tensile strain in the well. The beneficial effects of tensile strain are also demonstrated in the improved performance of 2μm wide x 400μm long, ridge waveguide devices.

A similar growth study is performed on a series of non-compensated $Ga_xIn_{1-x}As/Ga_xIn_{1-x}As_yP_{1-y}$ MQW structures with increasing compressive strain in the $Ga_xIn_{1-x}As$ wells. Data is also presented that highlights the role of the barrier material in defining which strain relaxation mechanism will occur. The two structures, one with lattice matched $Ga_xIn_{1-x}As_yP_{1-y}$ barriers, the other with InP

barriers, are otherwise identical but exhibit very different strain relief properties. The first exhibits thickness modulated growth, whereas the second exhibits planar growth with the introduction of dislocations as the prevalent strain relief mechanism.

Chapter 10 Thesis Conclusions

The key observations and findings relating to the growth of strained layer InP-$Ga_xIn_{1-x}As_yP_{1-y}$, are summarised and discussed. These include the mechanisms responsible for thickness modulated MQW growth and their suppression via the optimisation of the growth 'parameter space'. The improvements in the performance of MQW-based laser and modulator devices are reviewed and discussed in relation to the expectations outlined earlier in the thesis.

Chapter 2

The Metal Organic Vapour Phase Epitaxy of InP-$Ga_xIn_{1-x}As_yP_{1-y}$ Structures

2.1 MOVPE of InP based alloys

2.1.1. Origins and Principles

The term epitaxy is derived from the Greek *epi taxis*, meaning 'on axis' or 'on orientation'. Today it is used to describe the process of growth of thin layers of single crystal material with a similar lattice constant to the host substrate. The epitaxial growth of III-V materials from the vapour phase using metalorganic precursors was first demonstrated in the late 1960's by Manesevit et al[1] with the growth of GaAs on a sapphire substrate. Since then, the technology has progressed from the growth of single layers of binary compounds on small pieces of substrate to a large scale, multi-wafer process capable of growing very complex, multi-layered heterostructures with a high degree of uniformity and repeatability.

The MOVPE process is based around the simple reaction:

$$XH_3 + Me(CH_3)_3 \xrightarrow[H_2]{500\text{-}900C} MeX + 3CH_4 \qquad (2.1.1)$$

where X represents a group V element and Me a group III metal. The group V hydride is gaseous but the group III metalorganic compound is liquid or solid in form. The latter is delivered to the reaction zone by saturating a carrier gas, usually H_2, with the vapour from the metalorganic using a bubbler. The growth process is non-equilibrium, i.e. the reactants are supplied by irreversible pyrolysis of the starting materials on the left hand side of the above equation. Typical growth temperatures tend to be in the range 600-700°C for InP based growth and 700-800°C for GaAs based growth.

MOVPE reaction mechanisms (the intermediate steps in the above equation) are, in general, less well understood than molecular beam epitaxial techniques, the main reason being that the latter is more compatible with in-situ analytical techniques such as RHEED (reflected high energy electron diffraction). The exact reaction mechanism (the order in which the hydrocarbon groups are removed

from the metal alkyl), the role of the hydrides and the effect of other growth conditions are not exactly known. The probable reaction route, as discussed by Butler[2] involves:

- hydride and metalorganic molecules delivered to the hot reaction zone, which normally comprises a radiantly heated graphite susceptor;
- some of the hydrocarbon groups may be removed from the metal alkyl, leaving a highly reactive methyl-metal radicle on the surface of the growing semiconductor;
- the radicle then reacts with the hydride on the surface of the semiconductor, giving solid III-V material and gaseous alkanes and hydrogen. The group III and V atoms are accommodated on appropriate locations of the lattice forming an epitaxial layer.

For the growth of InP from tri-methyl indium and phosphine, the following equations can be used to describe the above process:

$$
\begin{aligned}
&(CH_3)_3In(g) \xrightarrow{\text{gas phase}} (CH_3)In(g) + 2(CH_3)(g) \\
&\text{adsorption of } (CH_3)In(g) \text{ onto the growing surface} \\
&PH_3(g) + (CH_3)In(s) \xrightarrow{surface} InP(s) + CH_4(g) + 2H \\
&2(CH_3) + 2H \xrightarrow{surface?} 2CH_4(g) \\
&2H \xrightarrow{\text{excess } H_2 \text{ liberated from } PH_3} H_2(g)
\end{aligned}
\qquad (2.1.2)
$$

Evidence for the above reaction mechanisms has been compiled from a variety of sources[3-5].

The first developments in MOVPE were demonstrated on reactors that were usually built by the researcher. As the technique progressed, there was a convergence in the reactor design philosophy in the early to mid 1980's, when specialised companies were formed to manufacture initially customised, but more frequently 'off the shelf', MOVPE reactors. One such company, Thomas Swan Ltd. of Cambridge, England, was used by BNR Europe to manufacture MOVPE reactors capable of growing on 2" diameter InP wafers. Figure 2.1 pictures the author operating one such reactor, known as the 'E' reactor, which was used for the majority of the work presented in this thesis. The next section will describe the details and operating principles of this reactor.

2.1.2 Reactor Design and Growth Practice

A schematic diagram of the reactor design philosophy used at BNR Europe is shown in figure 2.2. This is a schematic of the 'C' reactor which is similar in design to the 'E' reactor; the two differ only in the number of source lines that are available to the grower. The 'C' reactor has 4 bubbled source lines and 4 gas source lines whereas the 'E' reactor has 7 bubbled source lines and 7 gas source lines.

The details of the reactor will be described in four sections: the reactor cell, the gas delivery system, in-situ reagent monitoring and general reactor control.

2.1.2.1 The Reactor Cell

Thrush et al[6] developed the reactor cell used throughout this work for optimum uniformity in composition and thickness of the grown layer. In order to optimise uniformity, he found operating the reactor at a reduced pressure of 150 Torr beneficial. This reduced pressure placed constraints on the cell design; figure 2.3 shows a schematic diagram of the reactor cell used. The precursor gas mixture, together with the H_2 carrier gas, is injected into the rectangular cross-section reaction tube. A gas baffle at the tube inlet provides the necessary turbulence that enables the various injected gas flows to mix together. One of the drawbacks of using a rectangular cross section tube is its susceptibility to mechanical weakness when operated at reduced pressure. To prevent this happening, the tube is contained within a circular cross-section 'pressure housing' which is more mechanically robust. When the reactor is in operation at reduced pressure, both the inner reaction tube and the outer pressure housing are operated at 150 Torr giving a zero pressure differential between the interior and exterior of the reaction cell. At the end of each growth the inner cell is coated with deposits from the MOVPE reaction. To help assist in the elimination of memory effects and to improve run-to-run repeatability, the inner cell is removed after each growth and cleaned in aqua regia. Generally speaking, no MOVPE associated deposit is observed on the outer cell.

Another notable feature in the design of the reactor cell, is the use of a removable, in-line scrubbing system for the by-products of the MOVPE reaction. Activated charcoal contained within a stainless steel cylindrical cartridge is used to absorb the by-products that would otherwise lead to the deposition of pyrophoric substances, that are characteristic of phosphine based epitaxy, on the sidewalls of the exhaust system. The cartridge is removed after each growth run and has been shown to be very effective in keeping the downstream exhaust system relatively free of deposit. Upon removal in a nitrogen ambient, the contents are rendered safe by a controlled burn-off procedure effected by passing an oxygen/hydrogen mixture through the cartridge in an extracted enclosure.

Two 2" InP substrates can be located on the silicon carbide-coated graphite susceptor. Heat is transferred to the substrates via the susceptor using radio-frequency (RF) induction. The susceptor temperature is kept under closed loop control by measuring it with a thermocouple located almost half-way along its length. The heated susceptor has a catalytic effect on the decomposition of the gaseous reactants causing crystal growth to occur primarily on the hot surface.

2.1.2.2 The Gas Delivery System

Hydrogen is the most popular ambient gas used in MOVPE. As well as providing the main flow through the reactor, it is also used for bubbling through metalorganic sources and providing controlled dilution for various gaseous reagents. In the reactor configuration shown in figure 2.2, hydrogen is purified from a 'house' supply using Palladium diffusers operated at 300°C, giving very low moisture levels (a dew point of -110°C is routinely measured by an in-line hygrometer). Stainless steel (¼") pipework is installed throughout the system to deliver the various gases to the manifold with "VCR" fittings being used, as required, to make connections with sources, mass flow controllers, baratrons etc. Whenever such a connection is broken (for example to change a metalorganic source), the appropriate section of pipework would be helium leak checked when the connection was re-established. This involves evacuating the line down to a pressure of $5x10^{-5}$ Torr using a combined rotary/diffusion pump vacuum system and then connecting the line to a helium mass spectrometer. Gaseous helium is then 'sprayed' around the connector of interest and the signal on the mass spectrometer is monitored. The helium checking was performed down to $3x10^{-9}$mbarl/s air equivalent. Any signal observed above this level was treated as a leak and corrective action taken.

Isolation of the sources from the rest of the reactor is provided by normally closed pneumatic valves for situations such as the periods between growth runs, or when a source is not used in a growth run. The normally closed valves are pneumatically hard-wired to neighbouring normally open valves as shown in figure 2.2, thus allowing hydrogen to flow through the pipework when the source is not used. Two distinct types of sources are used in the MOVPE system: bubbled metalorganic and gaseous. The gas handling issues for each are quite different. Five metal-organic lines are available on the 'E' reactor: three Trimethyl Gallium (TMGa) and two Trimethyl Indium (TMIn). They are all contained in precisely controlled (±0.1°C) temperature baths, with TMGa kept at -13°C and the TMIn at 33°C. The difference is due to the much lower vapour pressure of TMIn compared to TMGa. The low vapour pressure of TMIn and the subsequent need to run the source at relatively high temperatures creates a significant hardware issue. To prevent condensation of the TMIn saturated H_2 on relatively cold surfaces, the TMIn carrying pipework, pneumatic valves and the appropriate section of the switching manifold, must also be heated to 33°C. The TMIn bubblers were kept at a constant pressure of 760 Torr, whereas the TMGa was kept constant at a higher pressure of 1100 Torr. Constant line pressure was achieved using a '2-4-8' pressure control valve which could be set either manually or via the computer control. The line pressure was measured using an absolute pressure baratron. The vapour pressures of TMIn and TMGa at the bubbler temperatures mentioned above are 4.68 Torr and 34.4 Torr respectively.

The group V hydride sources used are 100% AsH_3 and PH_3. The gases are supplied in regular, commercial gas cylinders and delivered to the reactor via a pressure regulator. The hydride sources can be isolated from the rest of the reactor using hard-wired normally open/normally closed pneumatic switching valves. Again, the main part of the gas line leading into the reaction zone can be purged with hydrogen when the particular line is not required as part of a growth run or between runs. Prior to the delivery of the hydride to the main part of the gas handling system, the gas is passed through a molecular sieve (© BDH) to remove any moisture that may be present in the source which may compromise the quality of growth.

Arguably the most important aspect of MOVPE growth control is the ability to supply accurately metered quantities of gas reproducibly to the reaction zone. This is achieved using mass flow controllers (MFC's) purchased exclusively from MKS. In order to optimise reproducibility, the MFC's are 'zeroed' prior to each MOVPE growth run, i.e. the H_2 gas supply to the MFC is turned off and the flow controls of the MFC are automatically adjusted to give zero output. One of the main limitations of MFC technology is the dynamic range of the metered flow which they can deliver. The manufacturer recommend that they be operated in the 5%-100% range of total permissible flow. In many circumstances however, it is necessary to provide a higher, sometimes more accurate, range of flows. A particularly common problem, in the use of low flow capacity MFC's with bubbled sources, is the concern that it will take significantly longer for the concentration of the metalorganic in H_2 to stabilise with low flows than it would with high flows. Such a stabilisation period could seriously impact the length of time required to perform a growth run. Fortunately this issue can be overcome with the use of a dilution line, where a metered amount of H_2 is mixed with the output of the 'main' MFC and in turn piped into a third MFC. Table 2.1 below lists all the MFC values used in the 'E' reactor along with the minimum and maximum flows that each line can deliver.

If we take the example of AsH_3, we have, with the use of dilution, the ability to deliver accurately metered flows over approximately 3½ orders of magnitude. This flexibility was invaluable in growing many of the complex, multi-layered, multi-composition structures that are described in this thesis.

Table 2.1 Gas handling capabilities of all the sources on E reactor.

Gas Line	Output Capacity	Input Capacity	Dilution Capacity	Minimum metered flow	Maximum metered flow
Carrier flow	50slm			2.5slm	50slm
Vent flow	5slm			0.25slm	5slm
$(CH_3)_2Zn$	500sccm	500sccm	3000sccm	0.2sccm	385sccm
SiH_4	400sccm	400sccm	400sccm	0.95sccm	382sccm
AsH_3-1	300sccm			15sccm	300sccm
AsH_3-2	50sccm	50sccm	50sccm	0.12sccm	47.6sccm
AsH_3-3	600sccm	600sccm	600sccm	1.42sccm	571sccm
PH_3-1	3000sccm			150sccm	3000sccm
PH_3-2	3000sccm			150sccm	3000sccm
Ferrocene	50sccm	50sccm	50sccm	0.12sccm	47.6sccm
$(CH_3)_3Al$	100sccm			5sccm	100sccm
$(CH_3)_3Ga$-1	60sccm	60sccm	50sccm	0.12sccm	47.6sccm
$(CH_3)_3Ga$-2	30sccm	30sccm	50sccm	0.12sccm	47.6sccm
$(CH_3)_3Ga$-3	50sccm	50sccm	50sccm	0.12sccm	47.6sccm
$(CH_3)_3In$-1	500sccm			25sccm	500sccm
$(CH_3)_3In$-2	300sccm			15sccm	300sccm
Make-up flow #1	6slm			0.3slm	6slm
Make-up flow #2	6slm			0.3slm	6slm
Cylindrical cell flush	10slm			0.5slm	10slm

Metered quantities of reagents are switched into either the reaction tube or the vent line by using a vent-run switching manifold. The manifold incorporates fast switching solenoid valves and is heated to approximately 33°C to prevent any condensation of the TMIn discussed above. The design allows reactants to be passed through the pipework prior to being directed into the reactor, enabling the adsorption and desorption processes to equilibrate, and allowing stable conditions to be obtained in the metal-organic bubblers. The manifold is situated at the neck of the reaction tube to minimise the chance of gas diffusion occurring at gas switching events, possibly causing diffuse hetero-interfaces .

It has been demonstrated that transients in the reactor pressure, which may occur at switching events, can cause unscheduled composition perturbations at hetero-interfaces[6]. Roberts et al [7] showed that it is important to have precise balancing of the vent and reactor line pressures in order to obtain transient free switching. In the reactor layout shown in figure 2.2, this is obtained dynamically by utilising a closed loop control system which is based on a measurement of the differential pressure between the vent and reactor lines. The differential pressure signal drives a proportional solenoid valve, controlling a flow of ballasting N_2 into the vent line, and so compensating for any difference. The system allows the differential pressure to be controlled to approximately 0.1 Torr.

In a typical MOVPE growth sequence, the aggregate gas flow required to grow one layer will usually be different than that required by another layer. In addition to the above measures used to compensate for differential pressures between the vent and run lines, the 'E' reactor was also designed with a facility to deliver a constant aggregate gas flow to the reactor, achieved by using two 'make-up' hydrogen ballast flow lines. The lines are used alternately with one switched into the reactor line and the other into the vent line where the ballast flow could be altered, if required, to maintain the constant aggregate flow for the gas mixture used in growing the next layer. Using this arrangement, surges of gas into the reactor can be avoided when we switch from one gas mixture to the next. However, as will be discussed in chapter 7, the optimum ballasting arrangements required for the growth of high quality multi-quantum well structures are not necessarily those of constant aggregate flow.

InP-based MOVPE can be performed successfully at both atmospheric and reduced (so-called low) pressure. In order to satisfy the 'large-area' demands of a device processing activity the ability to grow on complete 2" wafers is essential. Indeed the simultaneous growth on multiple 2" wafers is now desirable. It was found by Thrush[11] of BNR Europe, that to achieve uniform single and multiple wafer growth, it was necessary to operate the reactor cell at reduced pressure. A standard pressure of 150 Torr was therefore adopted. The pressure of the reactor cell is controlled by 'throttling' the pumping speed of a 2-stage, oil-sealed rotary vane pump. The 'throttling' action is provided by a butterfly valve and the reactor pressure is monitored by an absolute baratron.

2.1.2.3 In-situ Reagent Monitoring

It is common practice in most MOVPE systems to pre-flush all the required reagents through the gas delivery system prior to growth, in order to 'stabilise' the adsorption/desorption process on the stainless steel pipework and achieve a constant pick-up rate in the metal-organic sources. Generally speaking, this empirical pre-conditioning routine has enabled high-quality structures to be grown.

However, in the author's experience, one of the major problems that periodically occurs is the irreproducibility of both the growth rate and composition. It was widely suspected that this lack of reproducibility was predominantly due to the variability of the pick-up efficiency of the bubbled TMIn source. To assist in the understanding of this effect, colleagues at BNR Europe designed and built a prototype ultrasonic based mass spectrometry system, that provides an in-line measurement of the TMIn concentration in H_2[8]. It was suspected that the TMIn would have a variable pick-up efficiency because:

- it is a solid source and, unlike liquid sources, has a limited exposed surface area hence the carrier gas that is 'bubbled' through the source may not saturate. As the source is used, the distribution of the solid within the bottle can change affecting the surface-area and the pick-up efficiency;

- it has a low vapour pressure and, consequently, a large gas flow is required to deliver a sufficient molar flow to the growth zone. The use of higher gas flows implies that the H_2 carrier gas will spend less time in the bubbler, hence the pick-up rate will be lower. If a different flow rate is required to grow a structure with a different composition, it is therefore probable that a different, usually indeterminate, pick-up rate will be achieved. This makes the determination of the gas flows required to grow a given composition difficult, although in practice, the TMIn flow is generally held constant during a growth run and different compositions are obtained using different TMGa flows.

These suspicions were proved by the work of Stagg[8,9] who, together with Thomas Swan and Co. Ltd., produced a commercial ultrasonic reagent monitoring system for binary gas mixtures, i.e. metalorganics in H_2, known as the "Epison".

Figure 2.4 shows a schematic of the ultrasonic cell that comprises the "Epison". The binary gas mixture, e.g. TMIn and H_2, flows into the cell. An ultrasonic pulse is transmitted between points A and B and the transit time of the pulse between these two points is measured. This is performed continuously and in real-time. By measuring this transit time, τ, and knowing the temperature of the gas mixture (the cell was controlled at a constant temperature of 60°C), the concentration of TMIn in H_2 can be calculated using the following simple gas equations:

$$
\begin{aligned}
c &= \frac{L}{\tau} \\
c^2 &= \frac{\bar{\gamma}}{\bar{M}} RT \\
\bar{M} &= xM_{TMIn} + (1-x)M_{H_2} \\
\bar{\gamma} &= \gamma(x, \gamma_{TMIn}, \gamma_{H_2})
\end{aligned}
\qquad (2.1.3)
$$

L – distance pulse has to travel (known)
τ - transit time (measured)
c - speed of sound in the gas mixture (calculated)
R - gas constant.
x - concentration of TMIn in H_2 – the unknown.
$\bar{\gamma}$ – weighted average of the ratio of the principal specific heats for the two gases in the mixture.
$\bar{M}$ - mean molecular weight of binary gas mixture.
T - temperature in ultrasonic cell.

By using the Epison to measure the concentration of TMIn in-situ, we can:

- determine when the TMIn concentration has stabilised and so identify a suitable pre-flushing time to give 'stable' growth;
- operate the TMIn source in closed loop control so as to maintain a constant flow-concentration product, hence delivering a constant molar flow to the reaction zone. This feature proved invaluable throughout the work of this thesis, enabling growth runs to be performed with improved reproducibility. Evidence for this will be presented in Chapter Seven.

A schematic diagram illustrating the location of the Epison within the metal-organic line is shown in figure 2.5. The stability of TMIn concentrations can be further improved by running two TMIn sources in series acting as a 'single source'. Any shortfall in the pick-up of the first source could therefore be compensated by the second. Episons are also used on the liquid source TMGa lines, even though their pick-up efficiency is known to be much more stable. The main reason for this is that several growth runs would be wasted from time-to-time as a result of source exhaustion. As the cost of an MOVPE growth run is sufficiently high, we also decided to monitor the TMGa lines to identify source exhaustion as soon as it begins to occur. It was found that the concentration of a liquid source did not instantaneously drop to zero at exhaustion, instead there was a gradual decrease over several runs.

2.1.2.4 Reactor Control

The following aspects of the MOVPE reactor are under computer control during the growth process:

- MFC's, their flows can be changed via a step change or a ramp;
- vent/run manifold switching valves, dictating which gas lines are used to grow the individual layers;
- source isolation valves, when a source needs to be turned on or off;
- reactor temperature, for the initial increase in susceptor temperature and any changes in temperature that were required during the growth run;
- epison control, enabling/disabling the closed loop control and defining the concentration value on which to set the control.

The reactor pressure was set manually by the grower and the bubbler pressures were maintained at a fixed level.

The growth sequence is governed by a spreadsheet-like program, which defines all of the items mentioned above, broken down into a series of steps defined in real time. Multiple step loops can be created in the sequence to make repetitive tasks, such as the growth of multiple quantum well stacks, less program line intensive. The software package that controlled the reactor also had the capability of logging the state of all the instrument readings and valve states periodically (every several seconds) during the growth process. This facility was invaluable in troubleshooting growths that had gone wrong for one reason or another.

2.1.2.5 Growth Procedure

The flowchart shown in figure 2.6 details a summary of the procedure involved in executing the growth runs discussed in this thesis. Each of the steps illustrated in this flowchart are now examined in detail.

Substrate Preparation. The substrates are grown using the liquid encapsulated Czochralski technique. All of the substrates used in this thesis were sawn with (100) orientation surfaces and doped with sulphur in the range $3\text{-}5x10^{18}$ cm^{-3} with a dislocation density of $<1000cm^{-2}$. Unlike GaAs or Si, InP substrates are not yet commercially available in an 'epi-ready' form, despite the claims of many substrate manufacturers. To produce featureless epitaxy reproducibly, the substrate surface is etched with a 4:1:1 mixture of H_2SO_4:H_2O:H_2O_2 at a temperature of 40°C, after which it is rinsed in de-ionised water and spun dry. This etch removes the top surface (~0.5μm) of InP and therefore the polishing damage. After etching, the substrate(s) is then transferred rapidly to the reactor.

Reactor Loading. To minimise the risk of an explosion, the entire reactor gas supply is switched from H_2 to N_2 whenever the reactor is opened for loading or unloading. In fact the system is interlocked so that whenever the reactor exhaust is opened it automatically switches to a N_2 main carrier flow. After the reactor is opened, a clean liner tube is inserted into place, and the wafer (sometimes two) is placed on the susceptor in the same location every time and inserted into the inner tube. Then a fresh charcoal cartridge is inserted at the back end of the inner tube, the reactor is closed and the system automatically switches over to an H_2 purge.

Hydrogen Purge. After the reactor has reverted to H_2 purge, an in-line hygrometer is introduced to the exhaust gas flow circuit to evaluate the moisture levels present after the loading activity. After

loading, the dew point would typically read between -90 and -100°C. The reactor is then left at atmospheric pressure for a sufficiently long time so that the reading falls below -100°C. This would take anywhere between 45 and 60 minutes.

Manual Set-up. Once the above conditions are reached, a series of manual tasks is performed that could either not be accomplished by a computer or are deemed too critical. The manual isolation valves in both the gaseous and metal-organic sources are opened (these are otherwise kept closed for safety purposes). The reactor is then de-pressurised to the operating pressure of 150 Torr. To do this the pumps are turned on and the throttle controller activated to give the required pressure. A visual inspection of the reactor is then performed to check for any possible problems.

Execute Growth Program. Before executing the user defined sequence, the growth program zeros all the MFC's and adjusts all those that are not giving a zero value. The first step in the growth sequence is to open all isolation valves to purge the gas lines with the desired reagents. After approximately 10 minutes (in which time the metalorganic pick-up should have stabilised), the Epison control is activated to give the required flow-concentration product for the metal-organics. The next critical step is the heating of the substrate to the required growth temperature, usually to 650°C, under a flow of PH_3 to prevent dissociation of phosphorus from the substrate surface. Typically a flow of 0.034 mol/min is used. Once at 650°C, the reactor stays in this condition for approximately 5 minutes to stabilise in temperature and hopefully equilibrate the entire susceptor. Epitaxy commences with the growth of InP (be it undoped as part of a test structure or n-doped as part of a laser structure or p-doped as part of a DFB overgrowth). The desired layers are grown as described in the growth program until the last layer is fully grown. At this point the RF source is turned off and the system is allowed to cool under an overpressure of the appropriate group V hydride, i.e. PH_3 if InP is the last layer or AsH_3 if GaInAs is the last layer. GaInAsP is never used as the last layer due to the complexities associated with cooling. The group V hydride is shut off when the substrate temperature falls below 100°C.

N_2 Purge. Once the susceptor reaches room temperature, the system is returned to atmospheric pressure and all the sources manually turned off. The system is then switched to N_2. It is at this point that the MOVPE reactor is in its most dangerous everyday condition. The phosphorus based deposit that coats the reactor walls is pyrophoric in the presence of air, so care has to be taken not to have air, pyrophoric deposit and H_2 present all at one time, hence the N_2 purge.

Unloading. The reactor is opened, with the grower wearing extracted breathing apparatus, and the contaminated charcoal cartridge removed and processed as described in 2.1.2.1. The susceptor is

then removed and the wafer(s) boxed. The inner tube is cleaned in aqua regia to remove the growth deposit. The system is then ready for the next growth run.

2.1.2.6 Safety and Maintenance

Perhaps the main disadvantage of the growth of InP based materials by MOVPE is the need to use highly toxic gaseous hydrides as the group V precursor. Fortunately the number of incidents of human exposure to arsine and phosphine have been few and there have been no reports of a serious gas exposure in an MOVPE laboratory. The main effects of arsine on humans are firstly the inability of blood cells to transport oxygen and secondly as a carcinogen. In order to minimise the risk of exposing workers to a possibly dangerous level, a maximum exposure level is defined. In the UK this is known as the Toxic Limit Value (TLV) which defines the concentration of gas to which a worker can safely and continuously be exposed during a normal working week. The TLV's for AsH_3 and PH_3 are 0.05ppm and 0.3ppm respectively. In his MSc thesis, Butler[2] estimated the concentration of hydrides in the exhaust of an MOVPE system, prior to scrubbing, to be 20000 ppm and 5000 ppm for low and atmospheric pressure systems respectively (assuming *no* consumption of the hydride gases, namely a worst case situation). To meet the TLV requirements it is therefore necessary to treat the exhaust to reduce the hazardous gas content and ensure that sufficient safety features are in place to minimise the risk of a hydride leak into the working area.

The situations which pose the most significant safety risk in MOVPE is that of the hydride cylinder change and maintenance of the hydride gas lines. Many precautions were followed when either of these tasks were performed, sometimes by the author, at BNR Europe. A well documented procedure is followed with each item in the list being checked upon completion. Self-contained breathing apparatus is worn by at least two engineers whenever the hydride lines are opened, a third engineer would be waiting outside the laboratory to help in case of an emergency. A comprehensive hydride detection system is used within the MOVPE laboratory to provide sub-TLV monitoring of possible gas leaks. The system is connected to an audible alarm system which would be activated if a given concentration of hydride is detected. Hydride detectors are located throughout the MOVPE facility but predominantly in those areas in which an operator would be most likely to be exposed to a leak or where a leak may be most likely to occur, e.g. adjacent to the unloading area and within the gas cabinet. Further safety precautions included the air extraction of the entire MOVPE apparatus so that any leaks within the reactor are extracted away via ducting to the outside (hydride detection is also located in the ducting). Also, in common with many modern clean room facilities, it is desirable to operate the room under 'positive pressure', i.e. slightly above atmospheric pressure, so there is no net flow of dirty, untreated air into the room. If, however, a gas leak is to occur this situation would lead to the flow of toxic gas into adjacent rooms. To overcome this, the air

conditioning was hard-wired to the detection system so that the room was switched from positive to negative pressure upon the detection of toxic gas. This would help confine the gas to the MOVPE laboratory which would be under increased extraction to the outside.

The MOVPE exhaust is treated so that when it leaves the ducting into the open air it has a hydride concentration less than the TLV level. This is achieved by using the same principle, only on a grander scale, as the in-line scrubbing system described in section 2.1.2.1. The exhaust is passed through a large, oil drum-like 'barrel' filled with activated charcoal and a flow of N_2 and O_2 passing through it. The passivation of the exhaust would generate heat within the 'barrel', which could be controlled by modulating the O_2 supply.

Unfortunately the metal-organic sources also pose a significant and different safety risk. All of the group III metal-organic sources are spontaneously combustible in air and react violently with water. To make their handling as safe as possible, the sources are packaged by the supplier with 'ready-to-install' input and output connections. Care has to be taken to make sure that pipework connections are leak tight prior to the opening of the input and output valves of the source otherwise air and moisture could leak into the source possibly causing combustion. Caution also has to be exercised when removing metal organic sources, especially ensuring that all traces of the metal-organic are removed from the walls of the pipework downstream of the source. This can be achieved by purging, evacuating and back-filling the appropriate section of pipework prior to removal of the source.

2.2 The Control of Layer Purity, Growth Rate, Alloy Composition, Doping and Uniformity in InP-based MOVPE.

2.2.1 Layer Purity

Unintentionally doped InP-$Ga_xIn_{1-x}As_yP_{1-y}$ alloys grown by MOVPE have an n-type background carrier. There is a strong link between the bulk material quality and performance of InP-based devices. The background purity controls the frequency response, quantum efficiency and leakage current of PIN diodes. Although it is probably less important in a semiconductor laser, a low carrier concentration is important when designing structures with precise changes in doping levels. The main background impurity in InP-based MOVPE is Si and there are two schools of thought on its source. Briggs and Butler[10] suggest that in atmospheric pressure MOVPE, the incorporation of Si into the growing layer is a result of the reduction of the reactor quartzware in hydrogen at growth temperature:

$$\begin{aligned} SiO_2(vitreous) + H_2(g) &\rightarrow SiO(g) + H_2O(g) \\ SiO(g) + H_2(g) &\rightarrow Si(adsorbed) + H_2O(g) \end{aligned} \qquad (2.2.1)$$

Thrush[11] preferred to ascribe the source of contamination to the tri-methyl indium source.

The incorporation of Si in InP can be described by the relation:

$$[Si]_{InP} \propto \frac{[Si]_g \exp(-E_a / kT)}{GR} \qquad (2.2.2)$$

$[Si]_{InP}$ – impurity level in InP
$[Si]_g$ – impurity level in the gas phase
E_a – Arrenhius activation energy of process
T – growth temperature
GR - growth rate

Hence by decreasing the growth temperature, the background carrier concentration can be reduced. A combination of a reduced growth temperature of 570°C and a purified TMIn source, led Thrush to demonstrate undoped InP with a carrier concentration of $3x10^{13}$ cm^{-3} and low temperature mobilities of μ_{50K}=400,000 cm^2/Vs and μ_{77K}=300,000 cm^2/Vs. Such a low growth temperature, however, requires a very high flow of PH_3 gas to maintain stoichiometry as the cracking efficiency of PH_3 at this temperature is poor. As a result, the growth of InP-based materials at this temperature

is impractical. At 650°C, the 'standard' temperature throughout this work, background carrier concentrations in the mid 10^{14} cm^{-3} range are routinely obtained for both InP and $In_{0.53}Ga_{0.47}As$. This level is sufficiently low for most practical device applications.

2.2.2 The Effect of the Group III and V Flux

In MOVPE there are three possible mechanisms of solid state growth from the gas phase. This has been extensively studied in GaAs based MOVPE[12]. At lower growth temperatures (<600°C), the growth of the layer seems to be kinetically controlled with the growth rate of the layer increasing with growth temperature. At higher temperatures (600°C<T_g<900°C), the growth is controlled by the mass transport of species from the gas phase. In this regime, the growth rate is constant with temperature. If the growth temperature is increased further, effects such as desorption from the growing surface can arise and the growth rate decreases with increasing temperature.

InP-based MOVPE is normally performed in the mass transport limited regime. As there is an excess of group V species in the gas phase, the growth rate limiting step is the supply of group III species to the growing layer. It has been demonstrated by Razeghi[13] and others that the variation in growth rate of InP is linear with TMIn flow and insensitive to PH_3 flow. Hence by controlling the flow of metal-organic into the reactor, we can control the growth rate. The molar flow of the metal-organic can be calculated using the following equation:

$$\text{Molar flow (mol / min)} = \frac{\text{Vapour pressure}}{\text{Source pressure}} \bullet \frac{\text{Reagent flow}}{\text{Molar volume}} \qquad (2.2.3)$$

$$\text{Vapour pressure (TMIn): } \log_{10}P(Torr) = 10.52 - \frac{3014}{T(K)}$$

$$\text{Vapour pressure (TMGa): } \log_{10}P(Torr) = 8.087 - \frac{1703}{T(K)}$$

T – temperature of metal - organic source.
Source pressure for TMIn is 760 Torr
Source pressure for TMGa is 1100Torr
Molar volume for TMIn is 22.4 litres
Molar volume for TMGa is 15.5 litres

It is evident that TMGa has a higher vapour pressure than TMIn and will therefore give a greater increase in growth rate for the same increase in flow.

As well as controlling the growth rate, the ratio of TMIn to TMGa also controls the solid phase In:Ga ratio, e.g. in $Ga_xIn_{1-x}As$

$$\frac{x}{1-x} \propto \frac{[TMGa]}{[TMIn]} \qquad (2.2.4)$$

Hence by controlling the ratio of the flows, we can control the band gap and lattice matching of alloys to an InP substrate. This will be discussed further in Chapter Three.

The main role of the group V reactant flow is to provide an excess of the group V species available for growth and to maintain the appropriate stoichiometry during the heat up, growth and cool down stages. In addition, the ratio of AsH_3 to PH_3 in the gas phase controls the solid phase ratio of alloys incorporating these elements, i.e. in $Ga_xIn_{1-x}As_yP_{1-y}$

$$\frac{y}{1-y} \propto \frac{[AsH_3]}{[PH_3]} \qquad (2.2.5)$$

In a similar way to the Ga:In ratio, the As:P ratio also controls the band gap and lattice matching to an InP substrate. The group V reactant flow has also been shown to play an important role in the incorporation of dopant species into the growing layer, e.g. increasing the AsH_3 flow can increase the doping efficiency of Zn in $Ga_xIn_{1-x}As$. The molar flow of group V reactant into the reaction zone is given by the equation:

$$\text{Molar flow (in mol / min)} = \frac{\text{reactant flow}}{\text{Molar volume (22.4 litres at stp)}} \qquad (2.2.6)$$

In addition to using molar flows to describe the gas phase growth conditions, it is common in III-V based MOVPE to define them in terms of the gas phase V:III ratio, i.e. the ratio of the molar flow rates of the total group V flow over the total group III flow. Alternatively, we can express the contribution of each reacting species as a gas phase partial pressure, which is given by:

$$\text{Partial pressure} = \frac{\text{reactant flow rate}}{\text{total flow in reactor}} \bullet \text{reactor pressure} \qquad (2.2.7)$$

The terms molar flow, V/III ratio and partial pressure are used widely in the literature to relate growth conditions to the quality of the grown layer. They are also used frequently throughout this thesis.

2.2.3 Doping

The intentional doping of semiconductors to form n-type or p-type regions is one of the basic requirements of semiconductor device technology. Doping may be achieved by intentional diffusion of an impurity from the semiconductor surface, ion implantation or as part of the growth process where a dopant impurity precursor is present in the gas phase. The incorporation of dopants from the gas phase in MOVPE can be described by the empirical relation[15]:

$$N \propto \phi_{dop}^{\alpha}\phi_{III}^{\beta}\phi_{V}^{\gamma}\exp\left(\frac{-E_a}{kT}\right)$$

or

$$N \propto \frac{\phi_{dop}^{\alpha}\phi_{V}^{\gamma}\exp\left(\frac{-E_a}{kT}\right)}{[GR]^{\beta}} \qquad (2.2.8)$$

N – dopant level in grown layer (cm^{-3})
ϕ_{dop}^{α} – dopant flow to some power α
ϕ_{III}^{β} – group III flow to some power β
ϕ_{V}^{γ} – group V flow to some power γ
E_a – thermal activation energy
$[GR]^{\beta}$ – growth rate to some power β

2.2.3.1 n-type Doping

Elements from both group VI and group IV of the periodic table are suitable as donors in the InP-$Ga_xIn_{1-x}As_yP_{1-y}$ based materials system. Group VI elements such as Sulphur and Tellerium are incorporated into the group V sub-lattice with one valence electron. Group IV elements such as Silicon and Tin are incorporated into the group III sublattice site where they also supply one valence electron. Silicon was used as the n-type dopant throughout the work presented, the main advantages being that InP can be doped well into the 10^{18} cm^{-3} range without any signs of saturation, i.e. α=1, and there is no ampotheric compensation, i.e. incorporation of a group IV element onto a group V site giving rise to a compensating hole[14]. Another advantage of Si is a low diffusion co-efficient which enables the growth of structures with abrupt dopant profiles.

Silane (SiH_4) was used as the dopant precursor in the form of a dilute mixture (approx. 400 vpm) in hydrogen. Prior to using a cylinder of silane for the growth of n-doped regions in device structures,

the source would be calibrated by evaluating the effect of dopant gas flow on the dopant incorporation. Both electrical and chemical impurity concentrations could be determined by electrochemical capacitance-voltage (CV) and secondary ion mass spectroscopy (SIMS) techniques respectively. It was generally found that the dopant incorporation varied linearly with flow rate, i.e. α=1 in equation 2.2.8, and the incorporation varied linearly with growth rate, i.e. β=-1, for both InP and $Ga_{0.47}In_{0.53}As$. Within BNR Europe it was generally found that γ=0, but Woelk et al [15] showed that γ=0.6 for disilane doping of $Ga_{0.47}In_{0.53}As$. One significant difference observed between the incorporation of Si into InP and $Ga_{0.47}In_{0.53}As$, was in their doping efficiencies. InP would incorporate dopant at (least) an order of magnitude greater than $Ga_{0.47}In_{0.53}As$. For an identical range of gas flows, InP could be doped into the mid 10^{18} cm^{-3} range whereas $Ga_{0.47}In_{0.53}As$ could only be doped into the mid 10^{17} cm^{-3} range for similar growth rates. This limitation in the doping range of the latter alloy did not cause any problems in growing the structures discussed in this thesis. The effect of growth temperature on the incorporation of Si was generally described by a positive activation energy, E_a in the above equation. Although it was never thoroughly evaluated, it was noticed that when the growth temperature was reduced the dopant incorporation also reduced. This was most probably caused by reduced cracking efficiency of silane at the reduced temperature.

2.2.3.2 p-type Doping

Zinc, and sometimes Cadmium, both group IIb elements, is the most commonly used p-type dopants in InP-based MOVPE. Zinc was used throughout the work described here with dilute mixtures of 750vpm dimethyl zinc in hydrogen as the dopant precursor. In contrast with Si, Zn is a less 'ideal' dopant. The variation in the incorporation with dopant flow in InP can be described by an α value of approximately 0.5[2]. Butler[2] noted that the Zn incorporation in InP was insensitive to growth rate, suggesting β=0, and in the author's experience the incorporation varied little with γ. A major problem with Zn is its notably high diffusion co-efficient which can lead to significant problems in growing certain device structures. This will be touched upon in later chapters. The incorporation of Zn in InP was also noted to saturate at the $2\text{-}3\times10^{18}cm^{-3}$ range and any subsequently incorporated Zn is interstitial rather than substitutional in nature.

Zn doped $Ga_{0.47}In_{0.53}As$ is less well studied than InP. The main use for Zn doped $Ga_{0.47}In_{0.53}As$ is as a highly doped, low resistance ohmic contact layer to InP. Fortunately its dopant incorporation characteristics give a doping efficiency of at least one order of magnitude greater than InP. It has also been found by the author that γ>0 for Zn doped $Ga_{0.47}In_{0.53}As$, hence the Zn level can be increased by increasing the AsH_3 flow. It was also noted for both InP and $Ga_{0.47}In_{0.53}As$ that, in the growth temperature range 600-700°C, the thermal activation energy

was negative. This suggests that at these temperatures the dimethyl zinc precursor is completely cracked and the incorporation variation with temperature is probably governed by a temperature dependent sticking co-efficient of the gas phase dopant species to the semiconductor surface. These observations were exploited in growing highly doped p-$Ga_{0.47}In_{0.53}As$ (10^{19}-10^{20} cm^{-3}) by increasing the AsH_3 flow and decreasing the growth temperature.

As mentioned above, it is common to grow a highly doped p-$Ga_{0.47}In_{0.53}As$ layer on top of p-InP to reduce the contact resistance of Ti-Pt-Au alloyed metal contacts. Such structures were routinely examined by electrochemical CV and SIMS profiling and no evidence of diffusion of Zn from the highly doped $Ga_{0.47}In_{0.53}As$ into the less doped InP was found. One puzzling observation made by Antell and Butler at BNR Europe[16] was a discrepancy between the electrically active Zn in the p-InP region of p-$Ga_{0.47}In_{0.53}As$/p-InP structures and the electrically active Zn evaluated in p-InP calibration structures. The discrepancy could be removed by either alloying the p-$Ga_{0.47}In_{0.53}As$/p-InP structure in a rapid thermal annealing furnace or by terminating the growth of the p-$Ga_{0.47}In_{0.53}As$/p-InP structure with InP, cooling the structure in PH_3 rather than AsH_3. It was later found that atomic hydrogen, generated by the cooling AsH_3, diffused through the structure thereby passivating the acceptors in the p-InP. This was not observed in any calibration growths as these structures, comprising single p-InP layers, were always cooled in PH_3. As a result all p-$Ga_{0.47}In_{0.53}As$/p-InP structures are capped with InP to avoid cooling in AsH_3.

2.2.4 Uniformity of the grown layer

In order to minimise the variation in device performance across a processed wafer, it is necessary to grow the device structure as uniformly as possible across the wafer area. Variations in composition, thickness and doping must therefore be investigated and minimised.

2.2.4.1 Compositional uniformity

Compositional uniformity is assessed over the entire 2" wafer by employing high density room temperature photoluminescence (PL) and double crystal X-ray diffraction (XRD) mapping[7]. Using these techniques, which will be described in the next chapter, the parametric influence on alloy compositional uniformity has been studied[11,17,18,19].

The compositional uniformity of the ternary alloy (the Ga/In ratio), is a function of the total carrier gas flow through the reactor. This effect is illustrated in figure 2.7 which compares the mismatch uniformity of $Ga_{0.47}In_{0.53}As$ grown with total hydrogen carrier flows of 9.6 slm and 15 slm. Uniformity measurements performed on the quaternary alloy $Ga_xIn_{1-x}As_yP_{1-y}$ grown prior to any

optimisation, displayed a decrease in both PL wavelength and lattice constant in the direction of gas flow. Extraction of the variation in elemental composition from these data indicates that the effect is wholly due to a reduction in As/P ratio with flow direction. Fortunately, the uniformity established with the group III elements in the ternary alloy is maintained when growing quaternary alloys, allowing us to address the uniformity of the As/P ratio independently. Since the thermal activation energy of pyrolysis of AsH_3 is less than that of PH_3, it was perceived that the group V non-uniformity could be improved by adjusting the susceptor temperature profile, making the downstream end of the wafer cooler and hindering the cracking of PH_3 over that area of the wafer. Figure 2.8 illustrates the improvement in PL wavelength uniformity of a quaternary alloy after this modification. Standard deviations in PL wavelength of 4 to 5 nm over an entire 2" wafer can now be routinely obtained in both the ternary and quaternary alloys.

2.2.4.2 Thickness uniformity

Thickness uniformity has been assessed by measuring the variation in the periodicity of InP/GaInAs MQW's by XRD. Figure 2.9 shows the MQW period variation over a 2" wafer, giving a standard deviation of only 2.9%. These measurements agree well with "Dektak" stylus thickness profiles made on partially processed devices. The reduction in thickness observed at the edges parallel to the gas flow is thought to be due to a reduction in gas velocity occurring at the sidewalls of the reactor.[11]

2.2.4.3 Electrical uniformity

Electrical uniformity information has been obtained on layers of p-InP and n-$Ga_{0.47}In_{0.53}As$ by using a matrix of van der Pauw structures patterned over test wafers. Fully automatic wafer mapping was used to measure the variation in sheet resistance. The p-InP layer exhibits excellent uniformity with a standard deviation in sheet resistance of only 5%. The sheet resistance of the n GaInAs, on the other hand, is less uniform , with a standard deviation of 19%.

The sheet resistance decreases, hence the doping level increases, along the flow direction. The model for dopant incorporation described in section 2.2.3.1 would suggest that the downstream area of the wafer is hottest. This is consistent with the observations made in optimising the As/P ratio uniformity in quaternary alloys described above. Similar measurements made on a sulphur doped $Ga_{0.47}In_{0.53}As$ layer using hydrogen sulphide (H_2S) as a source, showed an improvement in electrical uniformity by a factor of about $^1/_3$. We can deduce from these measurements that the incorporation of both Si and S as dopants is more sensitive to temperature variations than the incorporation of Zn. This would suggest that good dopant uniformity requires a more stringent

control of susceptor temperature profile than good alloy compositional uniformity. The doping uniformity evaluation was performed after the quaternary alloy optimisation.

All of the above uniformity studies were evaluated whilst the author was operating on the 'C' reactor at BNR Europe. One notable difference between this reactor and the 'E' reactor used to perform most of the work of this thesis, is the width of the reactor cell. The 'C' reactor had approximately 10mm clearance between the edge of the wafer and the sidewall of the reactor cell. As mentioned in section 2.2.4.2, it is thought that this introduced 'velocity drag' and compromised the Ga/In and thickness uniformity at the wafer edges adjacent to the sidewalls. In the 'E' reactor, however, the width of the reactor cell was increased to avoid this problem so that there was a space of approximately 25mm between the wafer edge and the reactor sidewall.

2.3 Concluding Remarks

InP-based MOVPE is now a mature technology for the production of 1.3-1.5μm optoelectronic devices. The development of the technique from the research laboratory to the production line was relatively rapid after the demonstration of device quality material in the mid 70's. The key milestones in the technology are listed in table 2.2 below, with reference to the main instigator.

Table 2.2 Key milestones in the development of III-V based MOVPE.

Milestone	**Worker**	**Date**
Basic MOVPE growth	Manasevit	1968
High quality $Al_xGa_{1-x}As$	Seki	1975
GaAs FET's	Bass	1975
GaAs/$Al_xGa_{1-x}As$ photocathodes	Bass	1978
GaAs/$Al_xGa_{1-x}As$ CW Lasers	Dupuis	1978
Reliable GaAs/$Al_xGa_{1-x}As$ lasers	Thrush	1979
GaAs/$Al_xGa_{1-x}As$ quantum well lasers	Dupuis	1979
InP/$In_xGa_{1-x}As_yP_{1-y}$ double heterostructure lasers	Hirtz	1980
GaAs/$Al_xGa_{1-x}As$ HEMT's	Andre	1984
InP/$In_xGa_{1-x}As_yP_{1-y}$ buried heterostructure lasers	Nelson	1986
Production of GaAs/$Al_xGa_{1-x}As$ MQW Lasers	STC Paignton	1987
InP/$In_xGa_{1-x}As_yP_{1-y}$ MQW Lasers	Dutta	1987
Strained layer InP/$In_xGa_{1-x}As_yP_{1-y}$ lasers	Thijs	1990

Although the technique has matured into a production line process it does not mean that no more research is required, as this thesis will demonstrate.

References

1. HM Manasevit and WI Simpson, J. Electrochem Soc., 116, p1725, 1969.

2. BR Butler. MSc Thesis, University of Durham, 1989.

3. GB Stringfellow, Third Biennial OMVPE Workshop, Brewster, Mass., USA, 21-23 Sept. 1987.

4. R. Bhat, J. Elec. Materials, 14(4), 1985, pp443-448.

5. M. Naitoh and M Umeno, Jap. J. App. Phys, 26(9), Sept 1987, ppL1538-1539.

6. E.J. Thrush, J.E.A. Whiteaway, G. Wale-Evans, D.R. Wright and A.G. Cullis, J. Cryst Growth, 1984, 68, p412.

7. J. S. Roberts, N.J. Mason and M.J. Robinson, J. Cryst. Growth, 1984, 68, p422.

8. J.P. Stagg, Chemtronics, 3(1988), p44.

9. J.P. Stagg, J Christer, E.J Thrush, J Crawley, J Cryst Growth, 120(1992), pp98-102.

10. A.T.R. Briggs and B.R. Butler, J Cryst Growth, 85(1987), pp535-542.

11. E.J. Thrush, C.G. Cureton and A.T.R. Briggs, J Cryst Growth, 93(1988), pp870-876.

12. S.K. Ghandi and I.B. Bhat, MRS Bulletin, Nov. 1988, pp37-43.

13. M. Razeghi, 'The MOCVD Challenge', Adam Hilger, 1989.

14. A.R. Clawson, T.T. Vu and D.I. Elder, J. Cryst Growth, 83(1986), p211

15. E. Woelk and H. Beneking, GaAs and related compounds, IOP Conf. Series No. 91, Heraklion, Greece, 1987, pp497-500.

16. G.R. Antell, B.R. Butler, A.T.R. Briggs, J.P. Stagg, S.A. Kitching, A.Chew, App. Phys. Lett., 53(9), 1988, pp758-780.

17. C.G. Cureton, E.J. Thrush and A.T.R. Briggs, J. Crystal Growth, **107** (1991), pp 549-554.

18. A.T.R. Briggs et al, published in proceedings of 5th Biennial Workshop On OMVPE, Panama City Beach, Florida, 1992.

19. A.D. Smith, D.A.H. Spear, C.G. Cureton, A.T.R. Briggs and E.J. Thrush, Proceedings of the Symposium on Large Area/Scale Epitaxy for III-V Device Fabrication, The Electrochemical Society, Proc. volume 91-13, 1991, pp35-45.

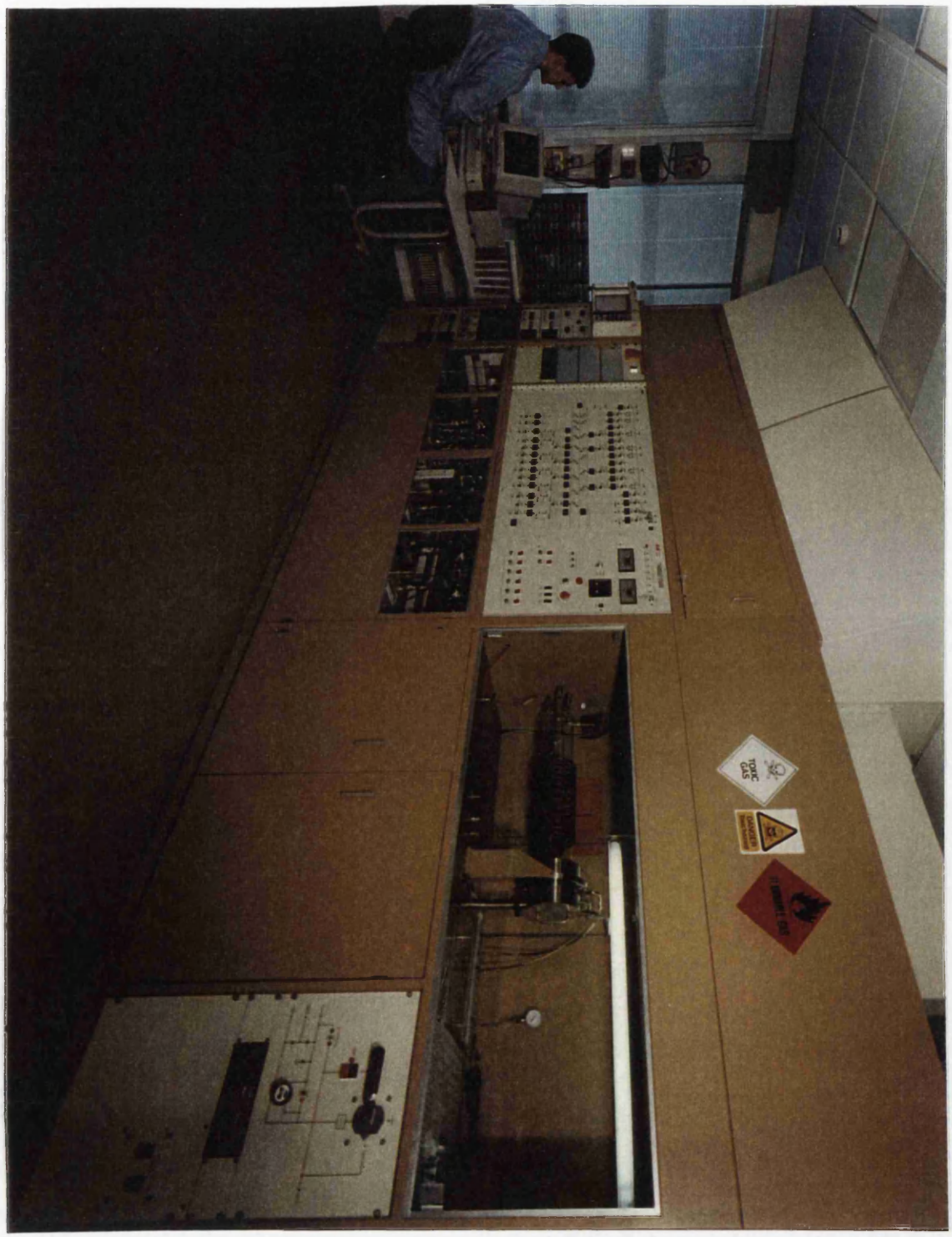

Figure 2.1 Photograph of author operating MOVPE 'E' Reactor, BNR Europe, Harlow, 1994.

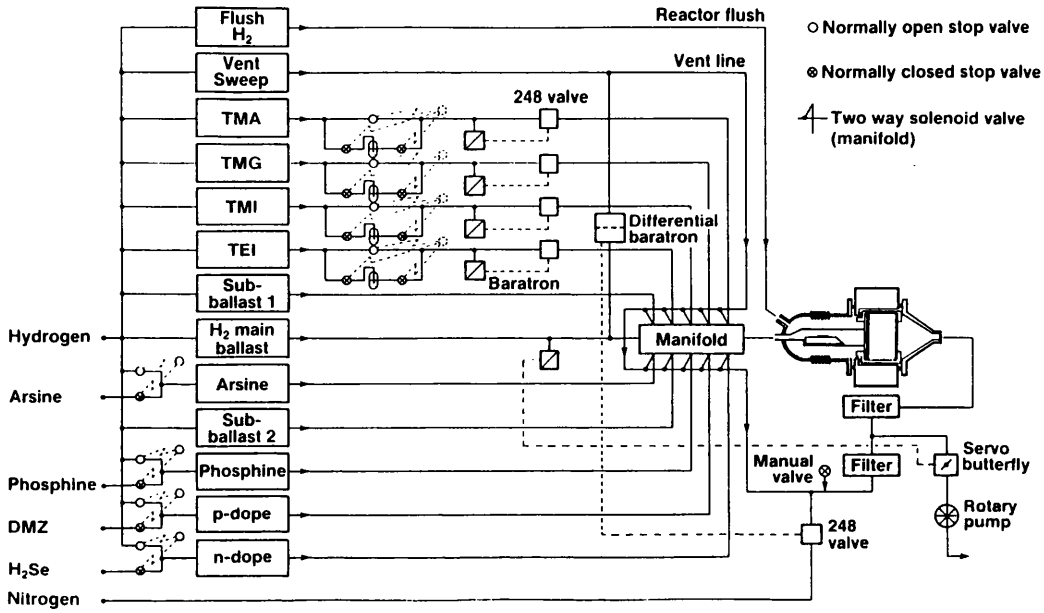

Figure 2.2 Schematic diagram of a vent-run MOVPE 'C' reactor. The actual 'E' reactor configuration is identical to this except for the number of source lines, which is greater than shown here.

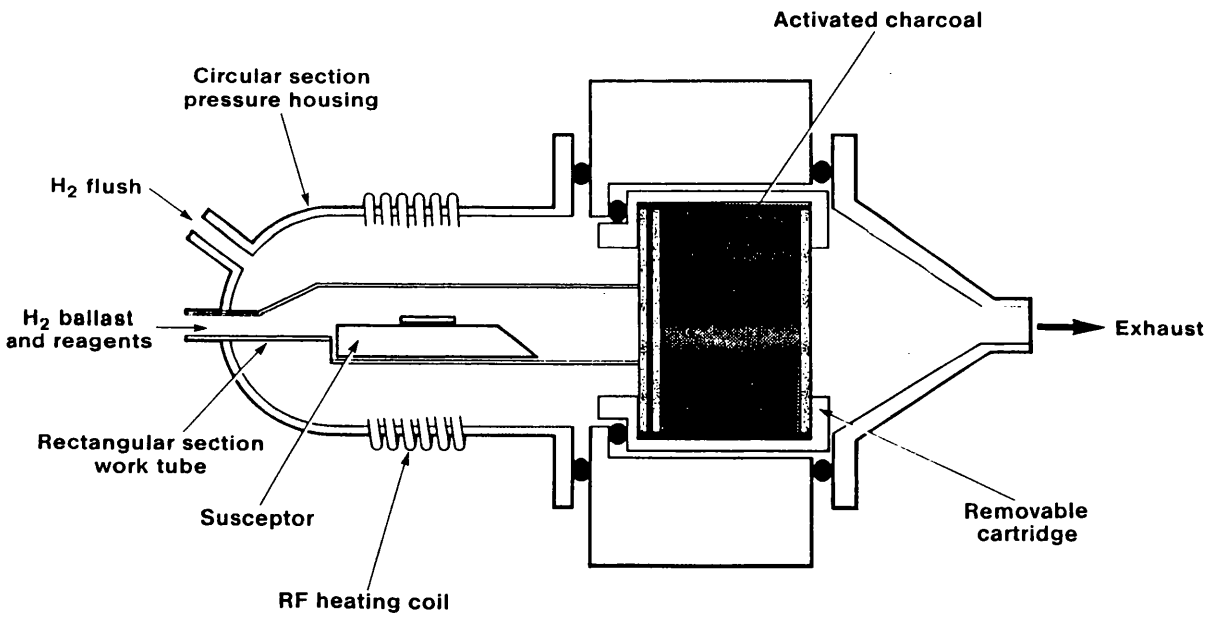

Figure 2.3 Schematic diagram of the reactor cell, detailing the inner rectangular liner (containing the susceptor), the cylindrical pressure housing and the exhaust charcoal canister.

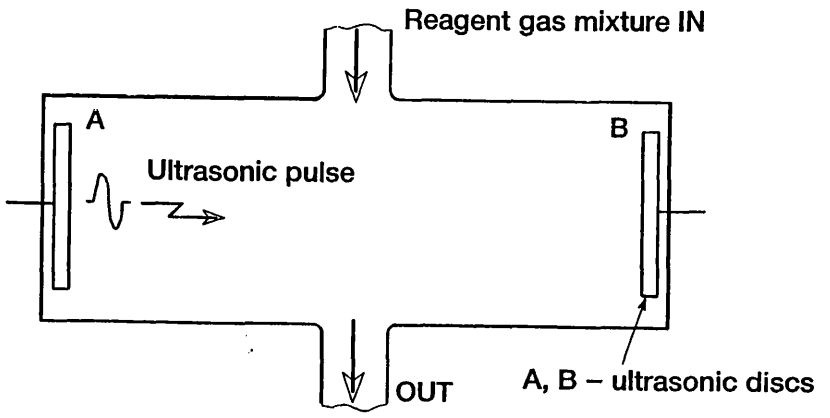

Figure 2.4 Schematic diagram of the ultrasonic cell that is used to determine the relative-concentration of gases as part of a binary gas mixture.

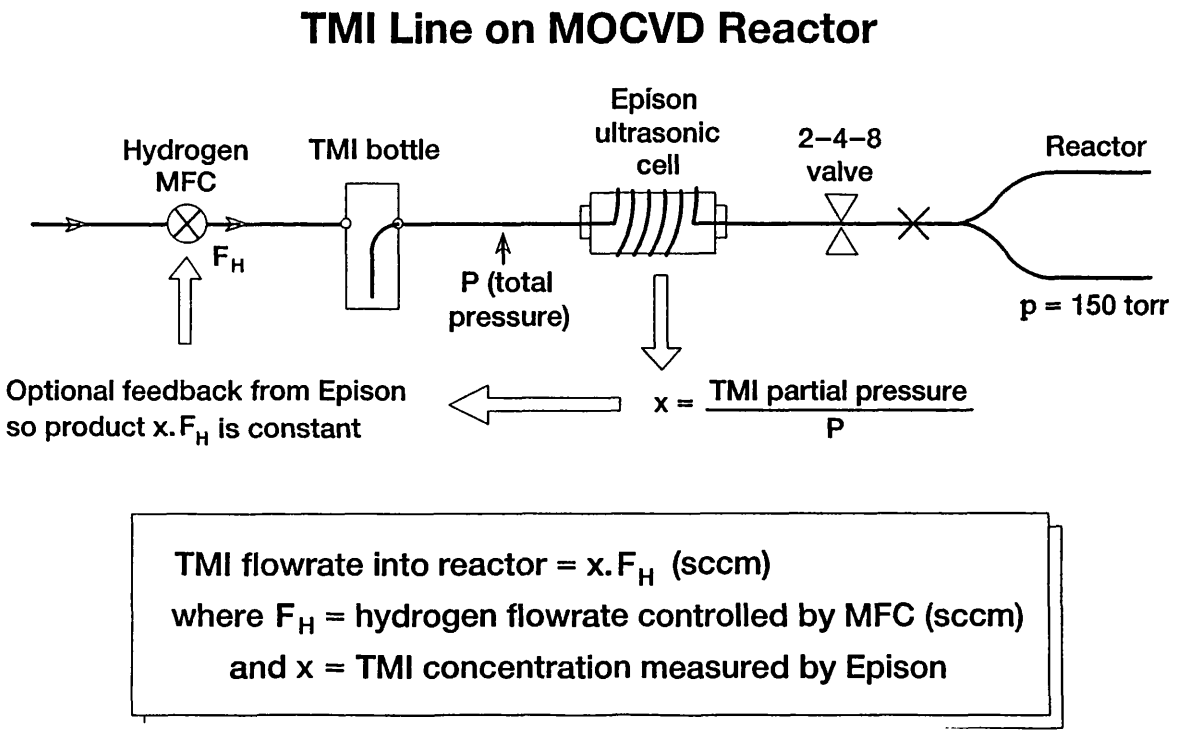

Figure 2.5 Schematic diagram showing the location of the ultrasonic cell in a TMIn gas line. Feedback to the MFC can be provided, as shown, to maintain a constant flow-concentration product.

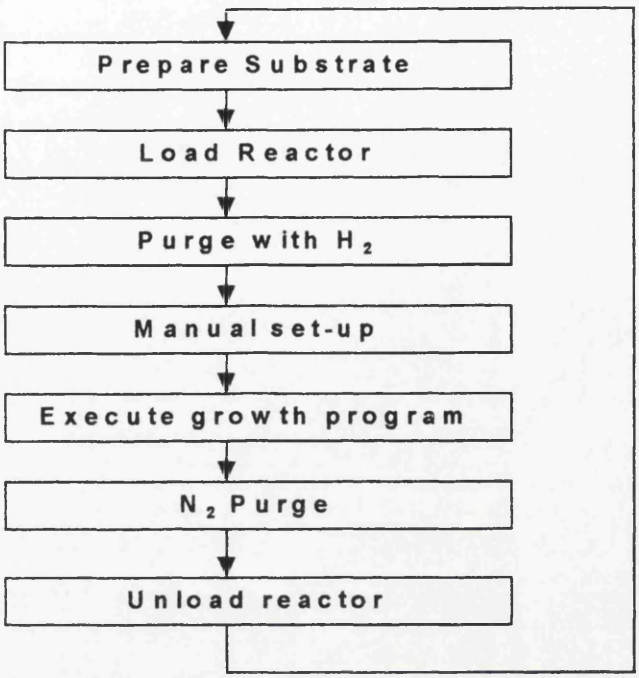

Figure 2.6 - Flowchart describing the sequence of events in a typical MOVPE growth run.

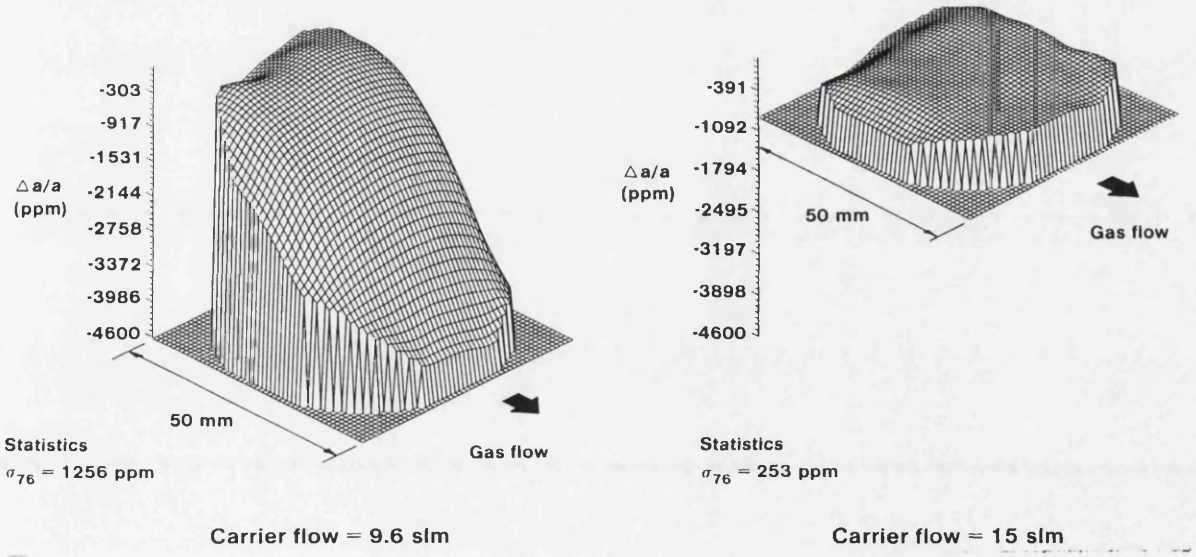

Figure 2.7 Three-dimensional representations of the uniformity in mismatch (composition) of $Ga_xIn_{1-x}As$ over a 2" wafer. The beneficial effects of the increase in total H_2 carrier flow are shown. The standard deviation in mismatch in the optimised case is shown to be 253 ppm.

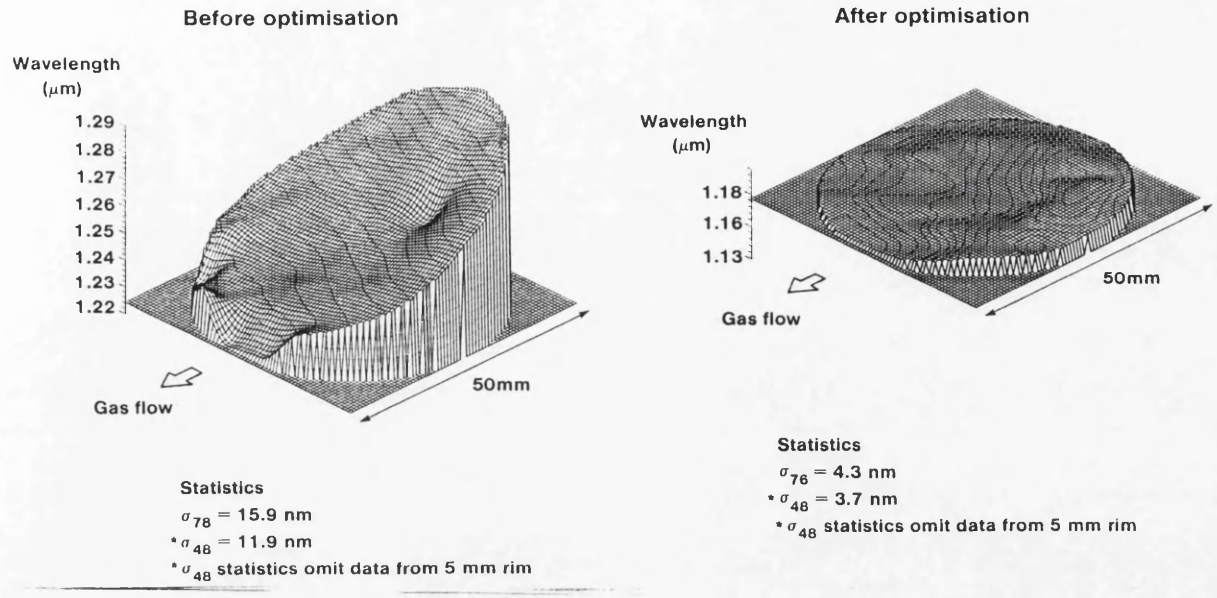

Figure 2.8 Three dimensional representation of the uniformity in PL wavelength over a 2" wafer. The beneficial effects of the optimisation of reactor cell temperature profile are shown. The standard deviation in PL wavelength in the optimised case is shown to be 4.5 nm.

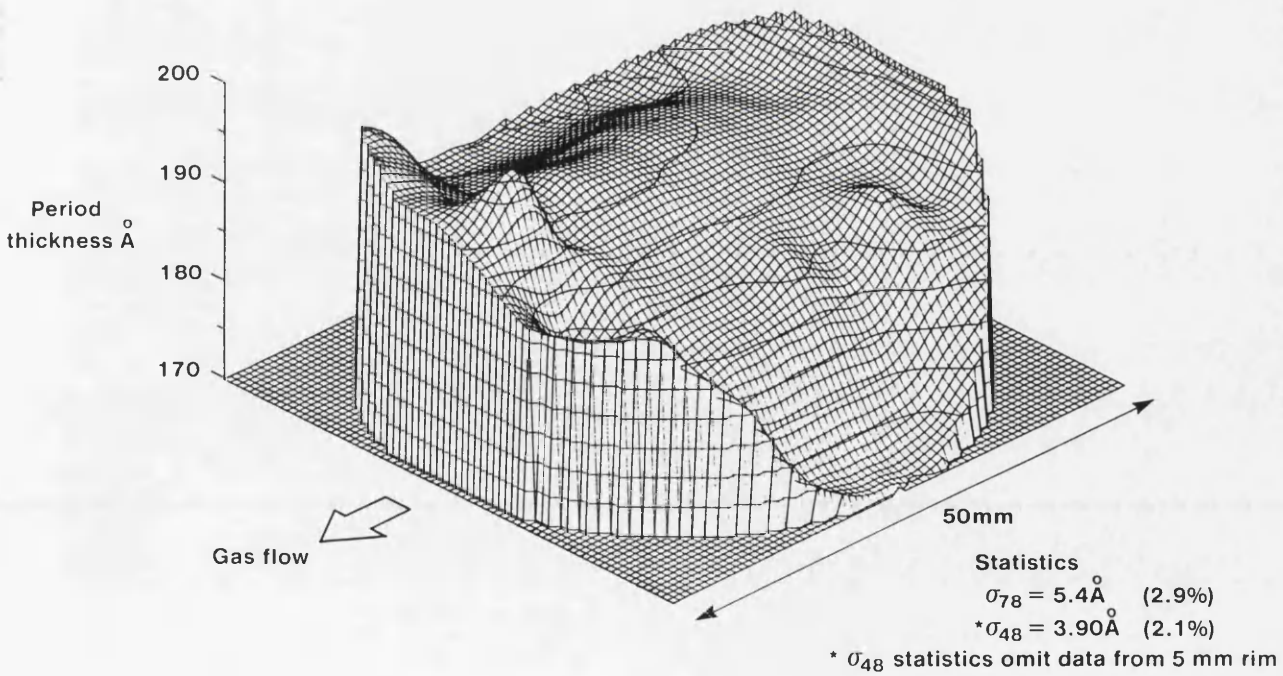

Figure 2.9 Three dimensional representation in the uniformity of thickness over a 2" wafer. The standard deviation in thickness is shown to be less than 3%.

Chapter 3

Assessment of InP-$Ga_xIn_{1-x}As_yP_{1-y}$ Alloys

3.1 InP-$Ga_xIn_{1-x}As_yP_{1-y}$ Material System

In the 1950's and 1960's it was realised that the main limitation to using III-V materials in semiconductor optoelectronic devices was the one-to-one relationship between the lattice constant and the band gap energy of the available binary alloys. Figure 3.1 shows a plot of lattice constant versus band gap for binary III-V alloys[1]. The need for semiconductor material with band gap energies of 0.8 and 0.95 eV was driven by the requirement for optoelectronic sources and detectors for silica fibre based optical communications (this will be discussed in detail in Chapter 5). It can be seen from figure 3.1 that a range of ternary and quaternary alloys of the elements Ga, In, As, P and Al, grown with the correct composition, would have the same lattice constant as InP. The alloy system Ga-In-As-P is most suitable for optical communications, as alloys with band gaps in the range 0.75 eV to 1.35 eV can be grown lattice matched to an InP substrate.

The first preparation of $Ga_xIn_{1-x}As_yP_{1-y}$ alloys lattice matched to InP was achieved in 1972[2] by liquid phase epitaxy (LPE). This, together with the demonstration of room temperature operation of $Ga_xIn_{1-x}As_yP_{1-y}$ lasers[3,4] in the mid-70's, provided the impetus for many telecommunication companies to invest heavily in InP based optoelectronic research and development.

In order to grow $Ga_xIn_{1-x}As_yP_{1-y}$ alloys, it is necessary to have a method of calculating x and y from some assessment technique. The values of x and y can be estimated chemically using techniques such as secondary ion mass spectroscopy and Auger electron spectroscopy but these are generally not used due to poor accuracy. The preferred method of calculation is through an interpretation of the band gap energy of the layer and the mismatch in the lattice constants between the layer and the substrate. Once x and y have been determined, the grower will know if he has to make any alterations to the [TMGa]:[TMIn] ratio or the $[AsH_3]$:$[PH_3]$ ratio in order to achieve the desired composition, i.e. x and y provide the interface between what the grower can control and what properties are desired in the layer. The band gap of the layer is normally assessed using photoluminescence and the layer mismatch using X-ray diffraction. The next sections will describe the elements of these assessment techniques (as well as some others commonly used) and the algorithms used to infer the values of x and y from the information generated by them.

3.2 Photoluminescence

Photoluminescence, sometimes known as luminescence spectroscopy, describes the luminescence observed from a semiconductor that has been excited by photons with energy $h\nu > E_g$, the band gap. The photoluminescence (PL) spectrum can be used to identify electronic transitions that occur intrinsically or as a result of extrinsic impurities or defects. If we want to evaluate band-to band transitions, i.e. estimate E_g, then room temperature PL can supply this information. If, however, we wish to perform a more fundamental study of the material and investigate impurity or defect related transitions then we must perform the measurement at low temperatures (usually liquid helium temperatures, 4.2K). Such a low temperature is required to prevent thermal ionisation of the optically active centres and to minimise the broadening of any sharp spectral features by lattice vibrations. The majority of PL data presented in this thesis will be at room temperature but some low temperature data, courtesy of the University of Surrey, is used to describe material quality.

The photoluminescence was measured in a home made system equipped with both Nd:YAG (1064 nm) and Ar ion (514.5nm) lasers. The latter was rarely used and then only for measuring $Ga_xIn_{1-x}As_yP_{1-y}$ alloys with wavelengths ≤ 1.05 μm. The PL was excited by focusing the laser beam into a $1mm^2$ spot, giving a typical excitation power density of 100 W/cm^2. The photoluminescence was detected using a compositionally graded $InP/Ga_xIn_{1-x}As$ photodiode, i.e. its composition would be graded (with compressive strain) enabling detection of signals up to the 1.7-1.8 μm range. A PbSe detector was available if any longer wavelengths needed to be measured. A commercially available (Biorad) Fourier transform spectrometer was used to acquire the PL spectrum. A schematic of the PL apparatus is shown in figure 3.2.

At room temperature, the photoluminescence is dominated by band-to-band transitions. There have been several reports[5,6] that the peak room temperature PL wavelength, λ_p, is prone to shifting due to the severity of the pumping intensity. Little noticeable variation in the peak PL wavelength was found at, or below, the nominally used intensity of 100 W/cm^2. The pumping intensity was similar to those used by Kuphal[5], who noticed small changes in λ_p (3-4nm), and about three orders of magnitude less than Bassignana[6], who noticed large changes in λ_p (16nm). The room temperature band gap of the alloy under investigation is calculated from λ_p using the expression:

$$E_g = \frac{hc}{\lambda_p}. \qquad (3.2.1)$$

h – Planck's constant
c - speed of light
λ_p – peak PL wavelength

For each samples' PL measurement, the peak wavelength, peak intensity and full width at half maximum (FWHM) would be recorded.

In addition to resolving the PL spectrum, the apparatus shown in figure 3.2 was also capable of spatially imaging the PL using an infra-red vidicon tube, a video camera and a monitor. The image that is generated corresponded, spatially, to about 1mm x 1mm of the wafer surface which, combined with a movable x-y stage, enabled the operator to examine the whole wafer surface. Non-radiative recombination centres present in the grown wafer, e.g. dislocation lines, can be resolved using this technique as demonstrated by Gourley et al[7] to evaluate the critical thickness of GaAs/$Ga_xIn_{1-x}As$ layers. Photographs of such images are used throughout this thesis in the discussion of growth quality. The vidicon used in this apparatus is an Hamamatsu N2606-06 that has a spectral response to over 2μm wavelength.

Perhaps the main advantage of room temperature PL is the non-destructiveness of the technique and the ability to perform measurements on complete grown wafers. In order to improve compositional uniformity (and subsequently verify that grown wafers meet the required composition variation specification), spatial mapping of the room temperature PL is required. The apparatus shown in figure 3.2 was equipped with a 4x2" wafer x-y stage, whose positioning and spectral data acquisition was completely computer controlled. Although the mapping density could be altered, a mapping 'pitch' of 2.5mm was generally used resulting in approximately 660 data points per wafer. As well as providing uniformity data, such maps are often used by device designers to select areas of the wafer (in terms of wavelength) most suitable for their device applications, or also by the grower to notice any growth related variations across the wafer.

3.3 High Resolution X-ray Diffraction

When an alloy of $Ga_xIn_{1-x}As_yP_{1-y}$ is grown on an InP substrate it will have a different lattice constant from the substrate, unless it is grown with a composition that lies exactly on the line of lattice matching shown in figure 3.1. The mismatch in lattice constant between the layer and the substrate is accommodated by a change in crystal symmetry of the layer from cubic to tetragonal. This model assumes that the layer is coherently strained and that all the mismatch can be accommodated in this way. If the layer is coherently strained, the in-plane lattice constant will equal that of the substrate, whereas the lattice constant in the growth direction will be a greater or less value depending on the magnitude of the relaxed lattice constant of the epitaxial layer. This is illustrated in figure 3.3, which shows the tetragonal distortion for an epitaxial layer with a relaxed lattice constant greater than the substrate lattice constant. The relaxed lattice constant is related to the in-plane and growth direction lattice constants by the relation[8]:

$$a_L = c_t\left(1+\left(\frac{2\nu}{1+\nu}\right)\left(\frac{a_s-c_t}{c_t}\right)\right)$$

a_L - relaxed lattice constant
a_s - in-plane lattice constant
c_t - growth direction lattice constant
ν - Poissons ratio (3.3.1)

Using the values of a_L and a_s, we define mismatch as:

$$m = \frac{a_L - a_S}{a_S} \quad (3.3.2)$$

Hence a positive mismatch implies $a_L > a_S$ and a negative mismatch implies $a_L < a_S$. Therefore to measure mismatch we need a technique for assessing both the lattice constants of the substrate and the tetragonally distorted epilayer, or the difference between the two lattice constants.

The Bragg condition for the diffraction of X-rays in crystalline materials is given by:

$$\lambda = 2d\sin\theta$$

λ - X-ray wavelength
d - lattice constant of material
θ - Bragg angle (3.3.3)

This relation can also be expressed in its differential form to describe a mismatched layer grown on a substrate:

$$\frac{\Delta d}{d} = -\cot\theta\Delta\theta$$

Δd - difference in lattice constants
$\Delta\theta$ - difference in Bragg angles (3.3.4)

This equation describes the mismatch in perpendicular (growth direction) lattice constants between the layer and the substrate. The term $\Delta\theta$ represents the difference in Bragg angles between the layer and the substrate. It is sometimes referred as the 'splitting' and is usually expressed in arc-seconds. The mismatch, i.e. the difference in relaxed lattice constants, is related to the perpendicular (growth direction) lattice constant difference $\Delta d/d$ through Poisson's ratio:

$$m = \left(\frac{1-\nu}{1+\nu}\right)\frac{\Delta d}{d} = -\left(\frac{1-\nu}{1+\nu}\right)\cot\theta\Delta\theta \quad (3.3.5)$$

The value of θ, i.e. the Bragg angle of InP, is generally assumed to be constant at 31.7° (for 004 reflection) and the Poisson's ratio is assumed to be 0.33 for all $Ga_xIn_{1-x}As_yP_{1-y}$ alloys.

A schematic diagram of the apparatus used to measure $\Delta\theta$ (the Philips HR1 X-ray diffractometer), is shown in figure 3.4 . It comprises a Cu X-ray radiation source, a four crystal Ge monochromator, the sample stage and an X-ray detector. The semiconductor wafer is mounted on the sample stage and the Bragg angle of the substrate is then determined by 'rocking' the sample until the maximum

diffracted intensity is detected. Once this is determined, the sample is rotated stepwise through the desired angular scan to assess the lattice constant difference of the epi-layer(s) and the substrate. An example of the variation in detected X-ray intensity with the rocking angle for a single layer of near lattice matched $Ga_xIn_{1-x}As_yP_{1-y}$ (λ=1.33μm) is shown in figure 3.5. The most intense peak is that of the substrate and the less intense that of the epilayer. The separation of the two peaks is measured to be approximately -39.6 arc seconds, hence using the above relations, m = 150 ppm (0.015%). The plot shown in figure 3.5 is often referred to as a rocking curve.

One of the major advantages of the X-ray diffractometer used, is the inclusion of a 4 crystal monochromator. First proposed by Bartels[9], it reduces the background intensity noise by almost two orders of magnitude when compared to the more commonly used double crystal X-ray diffraction technique. Consequently, the use of this instrument has been invaluable for interpreting the mismatch data on thin (i.e. low intensity) layers and periodic structures of the type discussed throughout this thesis.

If we replot the rocking curve of figure 3.5 on a logarithmic scale as shown in figure 3.6, we notice that there are other peaks present. These are due to an X-ray interference effect caused by thin layers (<1μm) and are termed thickness fringes. The spacing of these fringes in figure 3.6 is approximately 90 arc seconds. This value can be related to the layer thickness through the formula:

$$t = \frac{\lambda}{2\cos\theta_0 \Delta\theta} \tag{3.3.6}$$

for InP based materials this becomes

$$t(\mu m) = \frac{18.9}{\Delta\theta(\text{arc secs})} \tag{3.3.7}$$

Hence for a fringe spacing of 90 arc secs, we have an estimated layer thickness of 0.21μm, which is close to the expected layer thickness of 0.2μm. In the event of several thin layers being grown, each layer will give rise to its own set of thickness fringes which will almost always interfere with each other and make interpretation nearly impossible. A notable exception is the superlattice structure which consists of alternate layers of material A, with thickness t_A and mismatch m_A, and material B, with thickness t_B and mismatch m_B. The rocking curve of such a structure will consist of a series of satellite peaks similar in appearance to thickness fringes. The intensity of these peaks generally reach a maximum at a value of mismatch that is representative of the weighted mean of m_A and m_B, i.e.

$$m_0 = \frac{m_A t_A + m_B t_B}{t_A + t_B} \tag{3.3.8}$$

This value of mean mismatch is often termed the "zero order peak" or the "net mismatch". Higher order peaks are separated by $\Delta\theta$. In a similar way to thickness fringes, the period of the structure ($p=t_A+t_B$) can be calculated from the equation:

$$p = t_A + t_B = \frac{\lambda}{2\cos\theta_0 \Delta\theta} \tag{3.3.9}$$

Many examples of this type of rocking curve will be presented during this thesis and the 'quality' of the satellite peaks used to assess the quality of growth.

3.4 Determination of the Solid Phase Composition from the alloy band-gap energy and alloy mismatch.

The ability to determine the solid phase composition of a grown alloy is fundamental in the practice of III-V crystal growth. It is essential to the prediction of the gas flows required to grow an alloy of interest. This was highlighted in the previous chapter when the linear relationship between gas phase ratio and the solid phase was discussed. If we know the gas phase 'recipe' for alloy composition A, then in order to develop a gas flow 'recipe' for composition B we must have an indication of the value of the solid phase compositions of A and B, i.e. in the case of $Ga_xIn_{1-x}As_yP_{1-y}$ the values of x and y.

The values of x and y can be determined by direct techniques such as SIMS (secondary ion mass spectroscopy) and Auger electron spectroscopy. These techniques will give ratios of the constituent elements of an alloy. Inaccuracies in such direct detection techniques have prompted most InP-$Ga_xIn_{1-x}As_yP_{1-y}$ crystal growers to use the relationships that exist between the solid composition (x and y), and the values of the band gap energy(via photoluminescence) and the lattice constant (via a mismatch measurement from X-ray diffraction). These relationships will be discussed for both ternary ($Ga_xIn_{1-x}As$) and quaternary ($Ga_xIn_{1-x}As_yP_{1-y}$) alloys.

3.4.1 $Ga_xIn_{1-x}As$

In the case of ternary compounds there is one unknown, x. We therefore only need one piece of information to determine it. We can use either the lattice constant (mismatch) with Vegard's law, or the band gap energy (PL wavelength) and the dependence of E_g on x. Vegard's law for $Ga_xIn_{1-x}As$;

$$a_{Ga_xIn_{1-x}As} = x.a_{GaAs} + (1-x).a_{InAs} \quad (3.4.1)$$

$a_{Ga_xIn_{1-x}As}$ - lattice constant of $Ga_xIn_{1-x}As$
a_{GaAs} - lattice constant of GaAs
a_{InAs} - lattice constant of InAs.

The lattice matching condition to InP is given when

$$a_{Ga_xIn_{1-x}As} = a_{InP} \quad (3.4.2)$$

Using the values of lattice constants in the table 3.1 below, we can show that this is reached when x is approximately 0.47.

Table 3.1 Lattice Constants and Band Gap Energies for Ga-In-As-P Binary alloys[16].

Binary Compound	Lattice constant (Å)	Band Gap (eV)
InP	5.869	1.35
GaAs	5.653	1.42
GaP	5.451	2.74
InAs	6.058	0.36

The relationship between the band gap energy E_g and the composition x is given by:

$$E_g(Ga_xIn_{1-x}As) = x.E_g(GaAs) + (1-x).E_g(InAs) - b.x.(1-x) \quad (3.4.3)$$

$E_g(Ga_xIn_{1-x}As)$ - band gap of alloy
$E_g(GaAs)$ - band gap of GaAs
$E_g(InAs)$ - band gap of InAs
b - bowing parameter for $Ga_xIn_{1-x}As$ (eV)

The third term of this equation takes care of the non-linearity that has been shown to exist in the extrapolation of the ternary band gap from the two binary alloys. This non-linearity is characterised by the bowing parameter for $Ga_xIn_{1-x}As$, the published values of which vary between 0.434 and 0.6eV[10-16].

Unpublished studies by Briggs comparing the values of x determined from X-ray measurements with those determined from PL measurements, have shown that in some instances the accuracy of

equation 3.4.3 is questionable. The inaccuracies may be explained by the magnitude of strain in the grown layer and its effects on the band gap energy. This observation was also made, and corrected for, by Kuphal[5]. As a result of this uncertainty in the relation between E_g and x, the determination of x at BNR Europe was performed almost always by X-ray diffraction.

3.4.2 $Ga_xIn_{1-x}As_yP_{1-y}$

Quaternary compounds have two unknowns, x and y. We therefore need both the lattice constant and the band gap information to determine these values. Vegard's law for $Ga_xIn_{1-x}As_yP_{1-y}$ states:

$$a_{Ga_xIn_{1-x}As_yP_{1-y}} = x.y.a_{GaAs} + x.(1-y).a_{GaP} + (1-x).y.a_{InAs} + (1-x).(1-y).a_{InP} \tag{3.4.4}$$

The lattice matching condition to InP occurs when:

$$a_{Ga_xIn_{1-x}As_yP_{1-y}} = a_{InP} \tag{3.4.5}$$

it can be shown that this is achieved when $x = 0.47y$[17].

The relationship between the band gap and the composition can be expressed by:

$$E_g(Ga_xIn_{1-x}As_yP_{1-y}) = \frac{x.(1-x).\left[y.E_g(Ga_xIn_{1-x}As) + (1-y).E_g(Ga_xIn_{1-x}P)\right]}{x.(1-x)+y.(1-y)} + \frac{y.(1-y).\left[x.E_g(Ga_xAs_yP) + (1-x).E_g(InAs_yP_{1-y})\right]}{x.(1-x)+y.(1-y)} \tag{3.4.6}$$

Each of the ternary band gaps in the numerators of the above expression take the form of equation 3.4.3. Table 3.2 lists the different values of ternary bowing parameters that were available in the literature[10-16].

Table 3.2 - Values of ternary bowing parameters (in eV) found in the literature[10-16].

Ternary	Moon[10]	Nakajima[11]	Nahory[12]	Kuphal[13]	Glisson[14]	Adachi[15]	Krijn[16]
GaInP	0.758	0.758	0.758	0.758	0.758	0.786	0.790
GaInAs	0.478	0.460	0.436	0.436	0.600	0.555	0.434
GaAsP	0.210	0.210	0.210	0.108	0.210	0.146	0.210
InAsP	0.101	0.101	0.18	0.078	0.270	0.091	0.280

From personal experience, it was noted that there were some shortcomings in this model. One particular example is when two alloys were grown, in the same run, with the same group III gas

flows and different group V gas flows. In this example, we had a lattice matched layer and a coherent, compressively strained layer. By virtue of the constant group III gas flows, the x values in the two alloys should have been the same when in fact, using the above model with Kuphal's bowing parameters, they were not. It could be argued that there may be a side reaction in which the gas phase concentration of the group V species affects the cracking of the group III species, but this seems unlikely as a constant composition $Ga_xIn_{1-x}As$ layer can be grown with varying AsH_3 flows. Again there seems to be some shortcomings of this model when strained layers are used.

Fortunately, prior to the commencement of most of the work discussed in this thesis, we became aware of a model developed by Silver at the University of Surrey. His relation between the band-gap and x and y was similar to equation 3.4.6 above, but with an additional term he calls the 'quaternary bowing parameter'. His modified band-gap equation is:

$$E_g(Ga_xIn_{1-x}As_yP_{1-y}) = \frac{x.(1-x).\left[y.E_g(Ga_xIn_{1-x}As)+(1-y).E_g(Ga_xIn_{1-x}P)\right]}{x.(1-x)+y.(1-y)} + \frac{y.(1-y).\left[x.E_g(Ga_xAs_yP)+(1-x).E_g(InAs_yP_{1-y})\right]}{x.(1-x)+y.(1-y)} - x.y.(1-x).(1-y).b_{Ga_xIn_{1-x}As_yP_{1-y}} \quad (3.4.7)$$

The value of quaternary bowing parameter, $b(Ga_xIn_{1-x}As_yP_{1-y})$, Silver used was 1.5eV. It was found that when we used his model in conjunction with Krijn's[16] ternary bowing parameters, we obtained excellent agreement in the values of x in samples like those mentioned above. Again it was thought that the previously used model was prone to the effect of strain on the band gap, exemplified by the example discussed above. The introduction of the quaternary bowing parameter seems to have 'de-sensitised' the model to these effects. This model was used throughout this thesis to determine solid phase compositions.

3.4.3 Alloy Composition and Quantum Well State Modelling Program

In addition to calculating the elemental compositions from the band gap and the mismatch information, the program developed by Silver was also capable of calculating the energy of confined states in a quantum well structure. The implementation of the conduction and valence band line-ups between the well and barrier was achieved using the method of Krijn[16]. The program takes the following information as input:

- well and barrier thickness;

- well and barrier compositions defined as
    - band gap and mismatch, or
    - elemental compositions, i.e. x and y.

The program generated the following as output:

- band gap and elemental composition of the well and barrier materials;
- energy levels of confined electron states;
- energy levels of confined hole (light and heavy) states.

The program was particularly useful in comparing the results of MQW structure growths with expectations from constituent alloys and well/barrier thicknesses.

3.5 Transmission Electron Microscopy

Transmission electron microscopy (TEM) is a characterisation technique that enables us to create images of structures with sub-nanometre resolution, i.e. well beyond the limitations of optical microscopy. This section will describe the principles of the technique in relation to the samples discussed in this thesis.

3.5.1 Overview of Technique[18]

TEM is simply the imaging of electrons that have been either transmitted or diffracted by the sample under examination. In order for there to be an image of the sample there must be a variation in the amplitude of the transmitted/diffracted electron waves that reach either the imaging screen or the photographic material.

When a high energy electron beam is incident on a thin crystalline sample, a fraction of the beam will be directly transmitted and a fraction diffracted in a manner described by Bragg's law. An image of the sample can be created from both of these beams. In the case of the transmitted beam, the image contrast is provided by the variation in the energy loss experienced by the electron beam as it passes through the sample, i.e. a variation in electron intensity. Such an image is referred to as a bright field image. In an MQW structure, for example, the electron beam will experience a different energy loss (associated with scattering) in the well material than in the barrier material. The resultant differences in intensities from the well and barrier will provide the necessary contrast to form an image.

Imaging of the diffracted beam, referred to as the dark field image, enables the microscopist to relate imaging with the diffraction pattern. In common with most crystalline structures, III-V semiconductors produce a transmission electron diffraction pattern that comprises a series of spots

in the imaging plane. These spots correspond to diffraction from the interaction with the electron beam and the various crystal planes in the sample. A TEM image can be taken at any one of these diffraction conditions[18]. The diffraction condition is often quoted in terms of its reciprocal lattice space vector **g**. Most of the images discussed in this thesis are taken under the reciprocal lattice space (400), (200) and the (220) conditions (this is usually written as **g**=(400), for example). The appropriate diffraction condition can be selected over other diffractions or the transmitted beam by the use of an aperture at the objective lens of the microscope. In the diffraction mode the image contrast is provided by the variation in diffraction intensity. Different types of information can be interpreted from the TEM images of $Ga_xIn_{1-x}As_yP_{1-y}$ samples examined under different diffraction conditions. This will be discussed further as appropriate.

3.5.2 Sample Preparation[19-21]

One of the fundamental requirements of the sample under investigation is that it must be thin enough to allow electron transmission. This is commonly realised in one of two ways:

- by examining the corner cleaved edge of the structure, for example in InP based materials, we would cleave the sample along the $(0\bar{1}1)$ and $(0\bar{1}\bar{1})$ cleavage planes;
- by thinning the sample. This can be done either chemically (Br_2CH_3OH to thin InP) or by ion beam milling (usually Ar^+).

Both of the above techniques have their relative merits. The corner cleave method is quick and straightforward to implement but limits the area of the sample that can be viewed. Samples that require 'plan view' examination or detailed viewing of the cross-section need to be thinned. Chemical thinning is often used for plan view analysis but it is not controllable enough to make the thin foils required for cross-sectional examination, so ion-beam thinning is almost always used. There are some sample preparation artifacts associated with ion beam preparation that have to be considered when performing analysis of the TEM images, the main ones are:

- damage to the structure may be introduced during the thinning process, it can be minimised by using optimised conditions such as low beam currents and voltages and low incident angles for the beam. Milling at liquid nitrogen temperatures can also reduce damage.
- coherently strained layers are prone to elastic relaxation at free surfaces
- stresses may be exerted on thinned areas of the sample by unthinned areas.

These facts were borne in mind when interpreting TEM data in this thesis. Images that are presented were prepared by both the corner cleave and the ion-beam thinning technique.

3.6 Other Assessment Techniques

Techniques other than those discussed above, were used to assess the material grown. They can be grouped under thickness measurements and electrical characterisation.

3.6.1 Thickness Measurements

The thickness of the layers comprising an MQW structure were determined using either X-ray diffraction or TEM. The thickness of lattice matched bulk layers were normally determined by either ball lapping or 'Dektak' thickness profiling. These two techniques would be used to determine a first estimate at lattice matched alloy growth rates and to confirm layer thickness in grown device structures.

Ball lapping consists of lapping a small area of the grown wafer with a ball-bearing (of fixed and known diameter) covered in diamond 'lapping compound'. After lapping, a spherical crater would be left in the sample and, further to delineation, the grown layers could be viewed as a series of concentric rings. The viewed ring diameter can be related to the layer thickness if the ball diameter is known.

'Dektak' thickness profiling is a stylus based technique where a thickness profile can be made over mesa features on the wafer. In the case of $Ga_xIn_{1-x}As$ grown on InP for example, we would take a small piece of wafer and place a dot of photoresist on the sample. The sample would then be baked for a short while to harden the resist which would be used to mask the selective etching of $Ga_xIn_{1-x}As$. A mixture of H_2SO_4:H_2O_2:H_2O in the ratio 1:1:25 is known to be effective for this. The resist could then be removed with solvent and the mesa feature profiled by the stylus. This technique was found to be more accurate than the ball lapping as it seemed to give more consistent growth rate results with high resolution techniques such as TEM or X-ray diffraction.

3.6.2 Electrical Characterisation

The techniques of Hall measurements, Hg (mercury) probe capacitance-voltage (CV) profiling and electrochemical CV profiling were available to electrically assess grown wafers.

The van der Pauw based Hall effect was used to determine the resistivity, mobility and carrier type of single layers of material grown on semi-insulating (Fe doped) InP substrates. The theory behind this technique is discussed in detail in original works by van der Pauw.[22,23]

Hg probe CV profiling uses a temporary Schottky barrier in the form of a reservoir of Hg to contact the grown wafer. A standard reverse bias CV profile could be acquired if the relative permittivity of the material was known. This technique only provided an adequate profile if the layer was either undoped or modestly doped, i.e. less than mid 10^{16} cm^{-3}. Carrier concentrations higher than this cause lower breakdown voltages of the Schottky junction resulting in the inability to totally deplete the layer and acquire a full profile. This could be overcome using the electrochemical CV profiling technique where the reverse bias is kept fixed at a value less than the breakdown voltage. The profile is obtained by controllably etching the sample using either anodic or cathodic etching (depending on the type of the sample). The electrolyte provides both the ability to etch and a Schottky barrier. The electrolyte most frequently used at BNR Europe was ammonium tartrate. More detailed descriptions of this technique can be found elsewhere[24].

References

1. G.P. Agrawal and N.K. Dutta, Long Wavelength Semiconductor Lasers, Van Nostrand Reinhold, 1986.

2. G. A. Antypas, R. L. Moon, L. W. James, J. Edgecumbe and R. L. Bell, GaAs and Related Compounds, 1972, Conf. Ser. no. 17, Institute of Physics, London, 1973, p.48.

3. A.P. Bogotov, L.M. Dolginov, L.V. Druzhinina, P.G. Eliseev, B.N. Sverdlov and E.G. Shevchenko, Sov. J. Quantum Electron., 4, 1975, p1281.

4. J.J. Hsieh, Appl. Phys. Lett., 28, 1976, p283.

5. E. Kuphal, A. Pöcker and A. Eisenbach, J. Appl. Phys., 73(9), 1993, p4599.

6. I.C. Bassignana, C.J. Miner and N. Puetz, J. Appl. Phys., 65(11), 1989, p4299.

7. P.L. Gourley, R.M. Biefeld and L.R. Dawson, Mat. Res. Soc. Symp., Proc vol 56, 1986, p229.

8. M.A.G Halliwell, Advances in X-Ray Analysis, 33, pp61-66, Ed. C.S Barrett, Plenum Press, New York, 1990.

9. W.J. Bartels, J. Vac. Sci. Tech. B, 1(2), Apr-Jun 1983, p338.

10. R.L. Moon, G.A. Antypas and L.W. James, Journal of Electronic Materials, 3(3), 1974, pp635-644.

11. K. Nakajima, A. Yamagichi, K. Atika and T. Kotani, Journal of Applied Physics, 49(12), Dec 1978, pp 5944-5950.

12. R.E. Nahory, M.A. Pollack, W.D. Johnston Jr and R.L. Barnes, Applied Physics Letters, 33(7), Oct 1978, pp659-661.

13. E. Kuphal, Journal of Crystal Growth, 67, 1984, pp441-457.

14. T.H. Glisson, J.R. Hauser, M.A. Littlejohn and C.K. Williams, Journal of Electronic Materials, 7(1), 1978, pp1-16.

15. S. Adachi, Journal of Applied Physics, 53(12), Dec 1982, pp 8775-8792.

16. M.P.C.M. Krijn, Semiconductor Sceince Technology, 6, 1991, pp27-31.

17. S. Adachi, Properties of Indium Phosphide, pp387-399, INSPEC(IEE), 1991

18. P. Hirsch, A. Howie, R.B. Nicholson, D.W. Pashley and M.J. Whelan, Electron Microscopy of Thin Crystals, chapters 1 and 13, Robert E. Kreiger Publishing, 1977.

19. G.R. Booker, Inst. Phys. Conf. Ser. No. 76, Oxford 25-27 March 1985, pp 201-210.

20. R.E Mallard, G. Feuillet and P-H Jouneau, Inst. Phys. Conf. Ser. No. 117, Oxford 25-28 March 1991, pp17-20.

21. F Glas, Inst. Phys. Conf. Ser. No. 134, Oxford 5-8 April 1993, pp269-278.

22. L.J. van der Pauw, Philips Research Reports, 13(1), Feb 1958, pp2-9.

23. L.J. van der Pauw, Philips Technical Review, 20(8), 1958/9, pp220-224.

24. M. Razeghi, 'The MOCVD Challenge', Adam Hilger, 1989, Chapter 2.

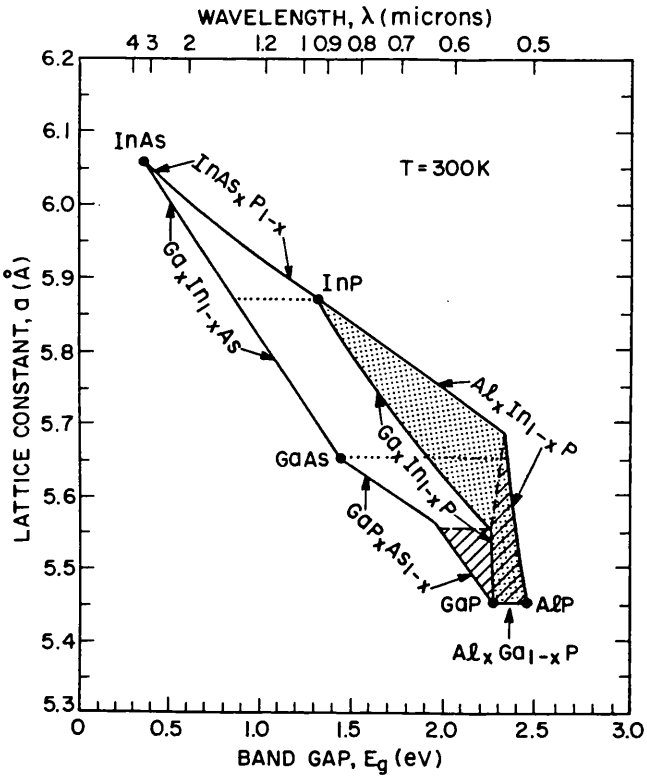

Figure 3.1 Band gap and lattice constant for $Ga_xIn_{1-x}As_yP_{1-y}$ (clear region). Hatched lines indicate areas of indirect band gap. Dotted lines indicate quaternary compositions which are lattice matched to the binary compound.

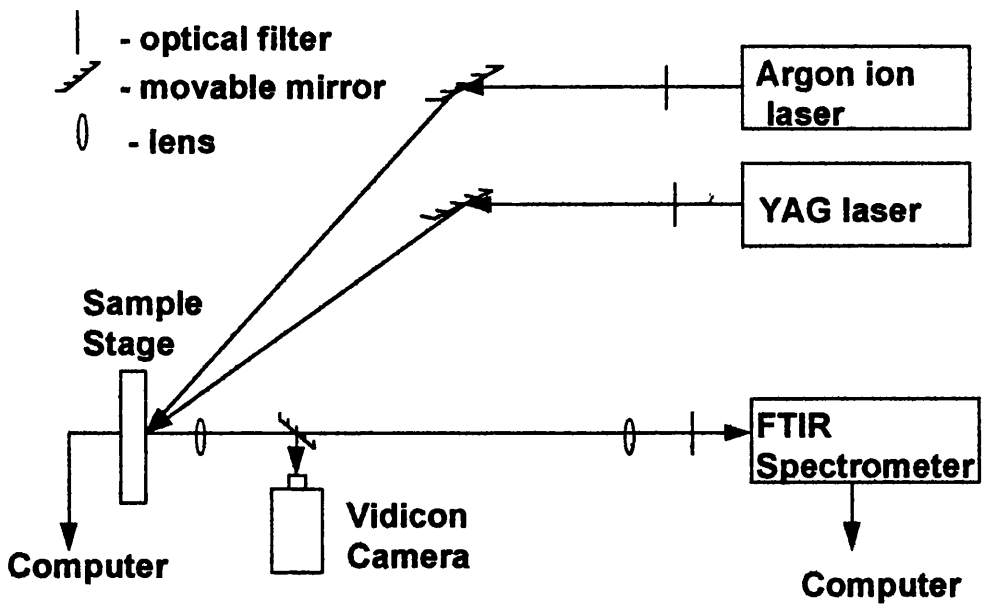

Figure 3.2 - Schematic diagram of room temperature photoluminescence apparatus. The FTIR spectrometer is constantly purged with N_2 to minimise the effects of water absorption lines.

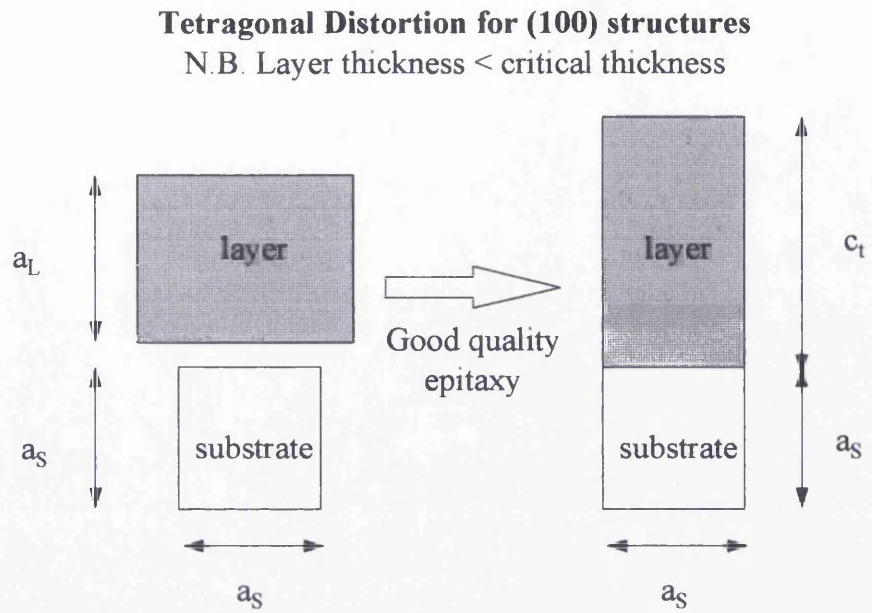

Figure 3.3 Schematic diagram illustrating the concept of tetragonal distortion of a coherently strained layer. Here the relaxed lattice constant of the layer is greater than that of the substrate.

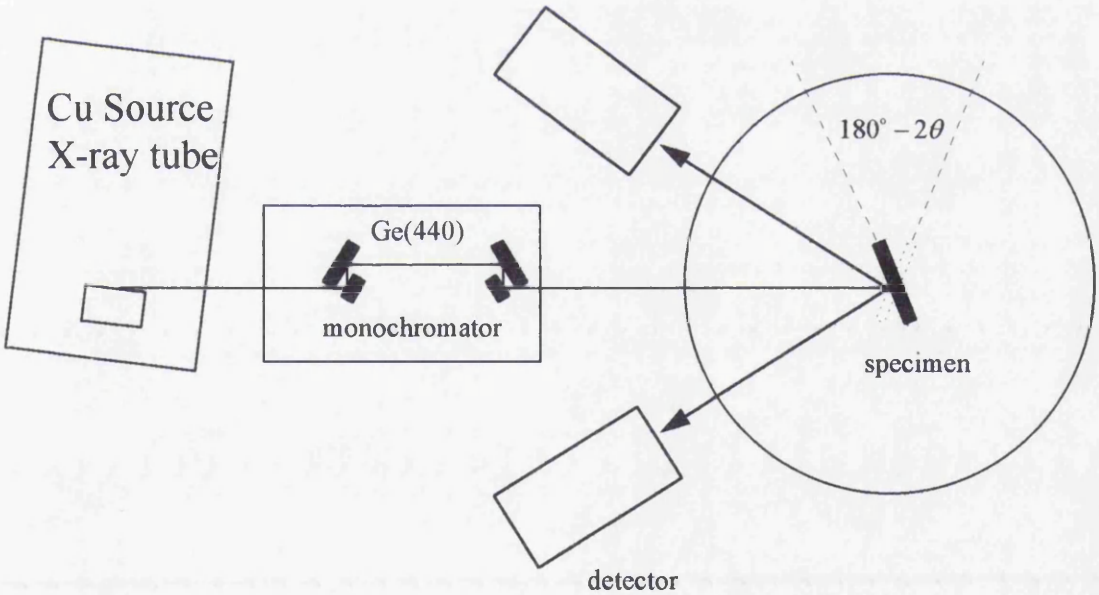

Figure 3.4 - Schematic diagram of high resolution X-ray diffraction apparatus. A four crystal Ge monochromator is employed to minimise the background X-ray count-rate.

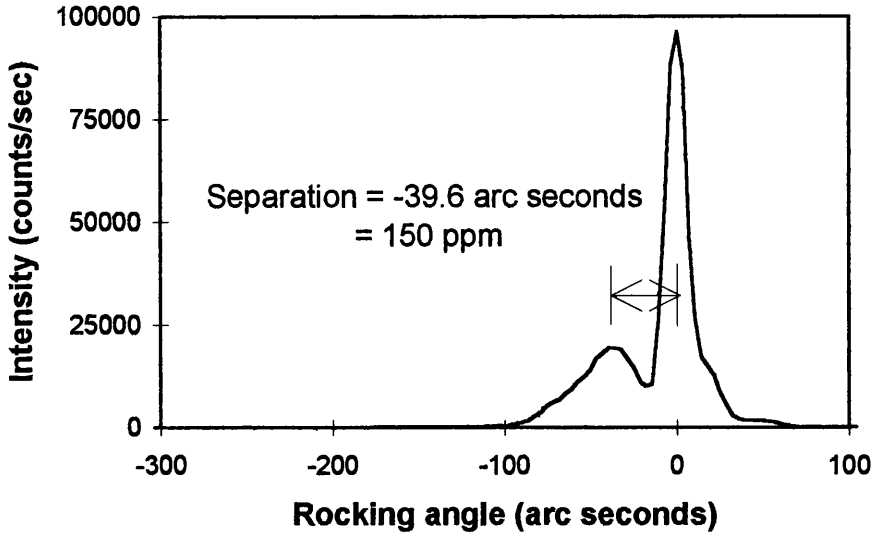

Figure 3.5 - HRXRD Rocking curve of λ=1.33 μm $Ga_xIn_{1-x}As_yP_{1-y}$ layer. The most intense peak is that of the InP substrate and the less intense is that of the grown layer. Since the difference in rocking angles between the layer and the substrate is negative we can deduce that the layer is compressively strained.

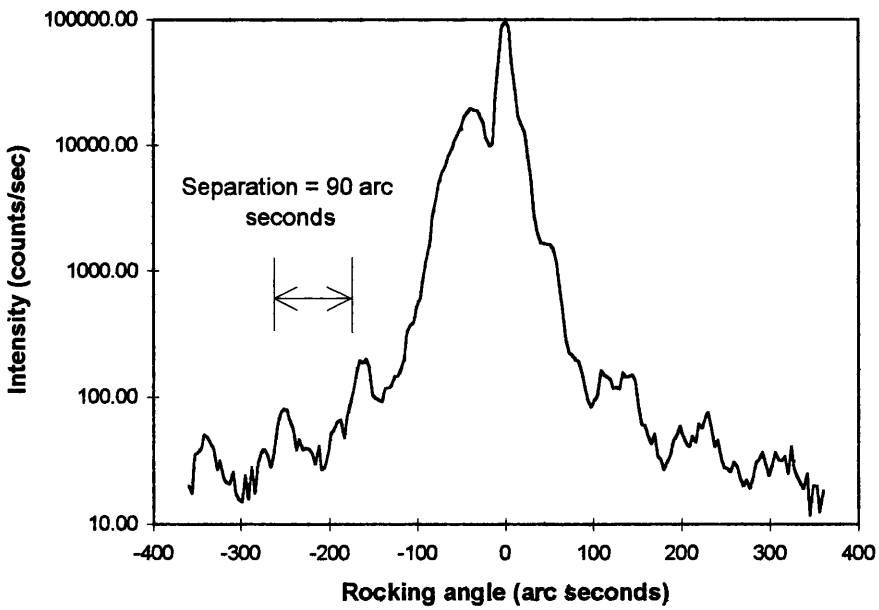

Figure 3.6- HRXRD Rocking curve of the same sample describe in figure 3.5 but with a logarithmic y-axis scale. Such plots are useful for evaluating relatively low intensity periodic fringes which can be observed using HRXRD. These fringes are caused by the layer thickness. The thickness can be estimated from the 90 arc second separation to be 0.21 μm.

Chapter 4

The Growth Limitations Imposed by the Critical Thickness-Mismatch Product

4.1 Introduction

Lattice mismatch arises when an epitaxial layer is grown with a different lattice constant from that of the substrate. In the InP-based $Ga_xIn_{1-x}As_yP_{1-y}$ alloy system the lattice parameter is controlled by the extent to which Gallium and Arsenic atoms are introduced into the group III and group V sub-lattices of InP. The lattice parameter will be increased by the introduction of Arsenic into InP since the size and bond length of Arsenic are greater than those of Phosphorus, whereas the lattice parameter will be decreased by the introduction of Gallium into InP as its size and bond length are less than Indium. By carefully controlling the ratios of the group III and group V species, these two counteracting effects can be balanced, giving rise to a lattice matched epitaxial layer. Figure 4.1 illustrates the range of compositions in the InP-$Ga_xIn_{1-x}As_yP_{1-y}$ material system that have zero mismatch[1]. If the layer is not grown under these conditions then it will have a net mismatch, the sign of which depends on the lattice constant of the epitaxial layer in relation to that of the substrate.

Figure 4.2 illustrates the two possible situations that can occur in InP based epitaxy. When a *thin* epitaxial layer with lattice constant a_L is grown on a relatively thick substrate with lattice constant a_S, so that all the mismatch is accommodated elastically in the grown layer, we define the mismatch, m, as:

$$m = \frac{a_L - a_s}{a_s} = \frac{\Delta a}{a}$$

a_L – relaxed lattice constant of epi-layer

a_s – lattice constant of substrate (4.1.1)

The mismatch is often expressed in parts per million or as a percentage, depending on its magnitude. The term mismatch is often referred to as strain and vice versa, which is a common misnomer. When an epitaxial layer has a positive mismatch, the lattice undergoes compressive strain in the plane of the growth and tensile strain in the growth direction. Conversely a negatively mismatched layer is subject to tensile strain in the plane of growth and compressive strain in growth direction, these scenarios being illustrated graphically in figure 4.2. It is interesting to note from these schematic diagrams that there is a change in the lattice symmetry of the epitaxial layer from

cubic to tetragonal when it is grown on a mismatched substrate. This is known as tetragonal distortion and arises as a result of the in-plane lattice constant assuming the lattice constant of the substrate. The net strain in the growth plane is given by:

$$\varepsilon_{||} = \varepsilon_{xx} = \varepsilon_{yy} = \frac{(a_s - a_L)}{a_s}, \tag{4.1.2}$$

which is often referred as the bi-axial strain. In response to bi-axial strain the lattice constant changes in the growth direction. The strain in the growth direction, $\varepsilon_{\perp}$, is given by:

$$\varepsilon_{\perp} = \frac{-2\nu}{1-\nu}\varepsilon_{||} \tag{4.1.3}$$

where ν is Poisson's ratio. For tetrahedral semiconductors ν is approximately 1/3 so $\varepsilon_{||} \approx -\varepsilon_{\perp}$[2]. The total strain can be resolved into axial and hydrostatic components, these can be related to the strains in the growth plane and in the growth direction. The axial component is given by:

$$\varepsilon_{ax} = \varepsilon_{\perp} - \varepsilon_{||} \approx -2\varepsilon_{||} \tag{4.1.4}$$

and the hydrostatic, or volumetric, component is given by:

$$\varepsilon_{hyd} = \varepsilon_{xx} + \varepsilon_{yy} + \varepsilon_{zz} \approx \varepsilon_{||}. \tag{4.1.5}$$

By resolving the strain into these two components, the effect on the band structure can be calculated[3].

The above equations assume that the epi-layer is grown so that all the strain is accommodated coherently, i.e. a critical thickness-mismatch product has not been exceeded and the entire epi-layer is tetragonally distorted. When this critical product is exceeded the strain must be relieved in an alternative way, which is normally manifest in the generation of crystallographic defects such as misfit dislocations. As the epi-layer continues to grow beyond its critical thickness, the in-plane lattice parameter will gradually change from the value of the substrate to the relaxed value. This process is called relaxation and is defined by:

$$R = \frac{a_t - a_0}{a_L - a_0} \tag{4.1.6}$$

R - level of relaxation (%)
a_L - fully relaxed (bulk) lattice parameter
a_t - partially relaxed lattice parameter
a_0 - coherently strained lattice parameter

The concept of a critical thickness at which a strained epi-layer changes from being coherently strained to being partially relaxed was first proposed by Frank and van der Merwe[4]. It was studied

in depth in the GaAs-$GaAs_{0.5}P_{0.5}$ material system by Matthews and Blakeslee[5]. Some of their key observations were:

- the critical thickness for the onset of misfit dislocations and relaxation is described by the equation

$$\varepsilon = \frac{a}{\sqrt{2}h_c}\frac{\left(1-\frac{\nu}{4}\right)}{2\pi(1+\nu)}\left(\ln\frac{\sqrt{2}h_c}{a}+1\right) \qquad (4.1.7)$$

ε - strain
h_c - critical thickness
ν - Poisson's ratio
a - lattice constant of substrate

- the dislocation lines were parallel to the intersection of the {111} slip planes and the growth interface plane, i.e. (100). This means that the dislocations were parallel to the [011] and $[01\bar{1}]$ directions on the (100) plane.

Figure 4.3 graphically illustrates the above equation for the InP- $Ga_xIn_{1-x}As$ material system. It shows that for a capped layer grown with a strain of 1%, the critical layer thickness is in the region of 240 Å. Although it is unlikely that a strained layer in excess of this thickness will be grown as part of a quantum well structure, it is often necessary to grow relatively thick layers for the purpose of calibrating the layer composition and growth rate against the growth conditions, hence these results have to be borne in mind. The above equation 4.1.7, is the accepted expression for a strained layer that is sandwiched between layers that are nominally lattice matched, i.e. in the case of InP based materials the strained layer would be capped with a layer of InP. Fitzgerald[6] describes, that in the case of uncapped layers, the RHS of the above expression (4.1.7) for critical layer thickness is divided by 2, resulting in a reduction of the critical thickness value. When the critical thickness of a capped structure is exceeded, relaxation occurs via the generation of misfit dislocations at both the bottom and top interfaces of the strained layer. Whereas in the case of an un-capped structure the relaxation occurs via the generation of misfit dislocations at the bottom interface only[8]. The question arises: how does a growing layer know which critical layer thickness to obey, the capped or the un-capped? In other words, if a growing layer exceeds the critical thickness defined by an un-capped structure, why does it not relax at the bottom interface prior to the deposition of the cap? It is conventionally accepted[7] that when a strained layer is grown in excess of its uncapped critical thickness, it becomes metastable with respect to relaxation. Whilst in this metastable condition, relaxation via the generation of misfit dislocations depends on the energy barriers associated with their formation and motion, which are known to be dependent on the temperature of the substrate.

Figure 4.3 illustrates the critical layer thicknesses for both capped and un-capped structures in the InP-$Ga_xIn_{1-x}As$ system.

4.2 Critical layer thicknesses of individual layers

Strained layer GaAs-$Ga_xIn_{1-x}As$ epitaxy has been the most intensely studied III-V strained layer system. The determination of the critical thickness of this material system generated some controversy in the field. Some authors[8] reported agreement with the Matthews-Blakeslee predictions that were outlined in section 4.1. Others[9] reported critical layer thicknesses that were greater by factors ranging from 3 to 10. The controversy was resolved by Gourley et al[10], who demonstrated that some assessment techniques were more sensitive at resolving the critical thickness point than others. They showed that photoluminescence (PL) imaging could resolve dark line defects (misfit dislocations) in capped layers grown slightly over the critical layer thickness i.e. 250 Å of $Ga_{0.8}In_{0.2}As$ (1.4% strain). This was in stark contrast to an assessment by interpretation of the X-ray rocking curve, which only showed signs of relaxation when a layer thickness of 600 Å was grown. The PL image of this layer had shown it to be heavily dislocated. Although Gourley et al resolved the controversy, it was Andersson et al[8] who first used photoluminescence measurements to predict critical thicknesses. This was judged by the reduction in intensity and increase in wavelength of a PL spectrum rather than by the direct imaging of defects. It is generally accepted amongst the PL 'community'[11] that PL imaging is a more sensitive technique.

Fortunately the PL imaging technique was available to the author for assessment of the InP based structures grown as part of this work (for a more detailed description see section 3.2). Its ability to provide a direct indication of whether defect generation has occurred in a non-destructive manner and on a full wafer scale makes it not only a very powerful analytical technique, but also a method of screening out defective wafers when strained layer structures are grown as part of a device production process. Occasionally, when calibration layers are grown to optimise the growth conditions for a particular alloy composition, the critical thickness-mismatch product is exceeded and strain relieving dislocations are introduced. PL imaging is also used in these cases to identify defects. Figure 4.4 shows PL images taken from two wafers, the details of which are given below in table 4.1.

Figure 4.4a is a PL image taken from a 0.8% compressively strained $Ga_xIn_{1-x}As_yP_{1-y}$ layer. It is interesting to note that the defect lines run predominantly in the [011] direction with the occasional defect running in the orthogonal $[01\bar{1}]$ direction. Figure 4.4b is an image taken from a -0.3%

tensile strained $Ga_xIn_{1-x}As_yP_{1-y}$ layer; the preferred direction of the dislocations is opposite to that of the compressively strained sample. Only a few faint defects can be resolved in the [011] direction.

Table 4.1 Description of samples whose PL images are shown in figure 4.4.

	Figure 4.4a	**Figure 4.4b**
Mismatch inferred from rocking curve	0.8035% (compressively strained)	-0.315% (tensile strained)
Mismatch measured on thinner layers	≈0.83%	
Layer thickness	≈550Å	≈3000Å
Predominant direction of dislocations	[011]	$[01\bar{1}]$

It is interesting to note that the X-ray rocking curves of these samples, shown in figure 4.5, are indicative of high quality samples. One of the known effects of layer relaxation is to broaden the FWHM of the layer signal[12], but there are no signs of this in these two samples. In fact the measured mismatch of the 0.8% compressively strained sample was almost identical to the value inferred from an MQW structure grown with wells of the same composition as this layer but with thicknesses well below the critical value (see section 7.2.2). These observations are consistent with those of Gourley et al[10], confirming that PL imaging is more sensitive than X-ray diffraction for detecting when the critical thickness has been exceeded . X-ray diffraction can still be a useful characterisation tool when the layers of interest are thicker. In such 'heavily relaxed' layers, the dislocation density can be so great that it quenches all the photoluminescence making imaging impossible. Figure 4.6 compares the rocking curves of two samples grown with the same composition of 0.95% compressively strained $Ga_xIn_{1-x}As_yP_{1-y}$ material. Figure 4.6a is the rocking curve of the sample shown in figure 4.6b, in which the layer thickness, 350 Å, is approximately a factor of 1.5 greater than the critical value. A sharp, well defined, peak with strong 'thickness fringes' (a sign of good layer quality, see section 8.3) is observed in this sample. Figure 4.6c is the rocking curve of the variable thickness quantum well stack shown in figure 4.6d, the single thickest layer of strained $Ga_xIn_{1-x}As_yP_{1-y}$ in this structure being 1200 Å, approximately 5 times greater than the critical value. It is obvious from the rocking curve that the layer peak is diffuse with no thickness fringes. Again these observations are consistent with those of Gourley et al[10].

There are reported differences between the GaAs-$Ga_xIn_{1-x}As$ and InP-$Ga_xIn_{1-x}As$ material systems in the manner in which individual layers relax. Wagner et al[19] have shown that in the case of

tensile strained, uncapped InP-$Ga_xIn_{1-x}As$ layers, relaxation is via the nucleation of partial dislocations at the upper, un-capped surface. Tsuchiyu et al[20] did not observe this in the same tensile strained structures, but instead observed cracks in the tensile layer. In the case of compressively strained InP-$Ga_xIn_{1-x}As$ un-capped layers, Tsuchiyu et al[20] reported relaxation via the generation of misfit dislocations at the interface between InP and $Ga_xIn_{1-x}As$. The behaviour of compressively strained InP-$Ga_xIn_{1-x}As$ is therefore similar to that of compressively strained GaAs-$Ga_xIn_{1-x}As$.

4.3 Multiple Quantum Well Structures Incorporating Strained Layers

The behaviour of strained MQW stacks whose barrier material is of the same lattice constant as the substrate is, generally speaking, less well studied than that of the single quantum well case. In the GaAs-$Ga_xIn_{1-x}As$ system Fritz et al[13] have studied such structures. In their paper, they seem to suggest that the introduction of misfit dislocations into the structure is governed by the critical thickness of the single quantum well. In addition, it is expected that a second critical thickness, imposed by the net strain of the stack, will also be an overall thickness limitation, i.e. limiting the number of well-barrier cycles which can be grown.[14] The net strain of an MQW structure is given by the expression:

$$\left(\frac{\Delta a}{a}\right)_{n=0} = \frac{L_w\varepsilon_w + L_b\varepsilon_b}{L_w + L_b} = \frac{L_w\varepsilon_w + L_b\varepsilon_b}{\Lambda} \qquad (4.3.1)$$

L_w, L_b – well and barrier thicknesses
$\varepsilon_w, \varepsilon_b$ – well and barrier strains
Λ – MQW period = $L_w + L_b$
$\left(\frac{\Delta a}{a}\right)_{n=0}$ – net strain of MQW structure or mismatch of 'zero-order' peak as observed in X-ray diffraction.

In summary, there are two critical thickness conditions for an MQW structure: one for the individual strained well, the other for the strained stack. Beanland et al[15] have discussed this and proposed that if :

$$N.\Lambda > h_c\left|\left(\frac{\Delta a}{a}\right)_{n=0}\right. \quad \text{and} \quad L_w < h_c$$

N – number of well / barrier cycles
Λ - MQW period = $L_w + L_b$
L_w – well width
$h_c\left|\left(\frac{\Delta a}{a}\right)_{n=0}\right.$ – critical thickness of strained MQW stack
$\left(\frac{\Delta a}{a}\right)_{n=0}$ – net strain of MQW structure or mismatch of (4.3.2)
'zero - order' peak as observed in X - ray diffraction.
h_c – critical thickness of the 'individual well'

then the structure will relax, not through the generation of dislocations within the quantum well stack, as in the case of the individual well exceeding its critical thickness, but at the interface between the entire stack and the GaAs buffer layer. This phenomenon has also been observed experimentally by Gourley et al[16], who demonstrated using PL imaging that dislocations were present in such a structure only at the interface between the stack and the buffer layer. They achieved this by varying the depth to which the incident excitation beam penetrated the structure, enabling the PL emission to be probed in a vertical sense. With shallow probing they could examine the upper quantum wells in isolation from the rest of the structure, whereas with deep probing they could resolve the behaviour of the structure at the buffer/stack interface. No dislocations were observed in the upper wells, but the interface between the stack and the buffer layer was heavily populated with strain relieving defects.

In the GaAs-$Ga_XIn_{1-X}As$ MQW system, the criteria for an individual well, $L_W < h_C$, in equation 4.3.2 has been shown to be governed by that of the capped critical thickness[13,14]. In the InP-$Ga_XIn_{1-X}As$ MQW system, Temkin[17] presented experimental evidence which indicated that the un-capped critical thickness described the misfit dislocation behaviour of the individual well. Similar experimental evidence was presented in the InP-$Ga_XIn_{1-X}As$ MQW system by Le Corre et al[18].

4.4 Multiple Quantum Well Structures with Strain Compensation

The problem of generating misfit dislocations at the interface of the strained quantum well stack and the buffer can be overcome by growing the structure with zero net strain between the stack and the buffer layer. Zero net strain, or strain compensation, can be achieved by growing the wells under compressive strain and the barriers under tensile strain or vice versa, the strain being relative to the buffer layer. Only compressively strained layers can be grown in the GaAs-Ga(In,Al)As(P) based

material system. Hence, to attempt strain compensation, a buffer layer must be grown that is graded in composition from that of the substrate to a value with a strain equal to the net strain of the stack that is to be grown. Matthews and Blakeslee[21] demonstrated this by growing a GaAs/$GaAs_{0.5}P_{0.5}$ MQW stack on a $GaAs_{0.75}P_{0.25}$ buffer layer. The buffer layer was graded in composition over 30 μm in thickness from GaAs to $GaAs_{0.75}P_{0.25}$ and continued at this composition for a further 5 μm. GaAs grown on top of this material will have a relative tensile strain of 0.9% and $GaAs_{0.5}P_{0.5}$ will have a relative compressive strain of 0.9%. Therefore by growing the wells and barriers with the same thickness, a strain compensated structure can be grown. There is now the possibility of growing potentially limitless numbers of well/barrier cycles providing that the net strain is kept as small as possible. One of the problems that plague this approach is that misfit dislocations are generated as part of the graded buffer layer process and their presence at the interface of the buffer layer and the MQW stack is difficult to prevent. However strained layer superlattices have the useful metallurgical property of inhibiting the vertical propagation of threading dislocations that occur as a result of misfit strain. Such strain compensated structures have been grown and studied by many groups, too numerous to mention.

Even though the strain compensated structure acts as a 'dislocation filter', it is thought by many that the presence of misfit dislocations at the base of the stack would be a latent reliability hazard for any electronic or optoelectronic device using such a stack as its active region. In the InP-$Ga_xIn_{1-x}As_yP_{1-y}$ based material system, nature has been kinder to the crystal grower as both compressive and tensile alloy materials can be grown directly onto an InP substrate, so allowing the opportunity of investigating strain compensated MQW growth without the complication of growing graded buffer layers. The following chapters describe the growth and assessment of both compensated and non-compensated MQW structures in InP based materials, with consideration of the results that have been reported in the literature for the GaAs-$Ga_xIn_{1-x}As$ and other strained layer material systems.

References

1. G.P. Agrawal and N.K. Dutta, Long Wavelength Semiconductor Lasers, Van Nostrand Reinhold, 1986.

2. E.P. O'Reilly, Semiconductor Sci. Tech., (1989), 4, p121.

3. G. Jones, PhD. Thesis, University of Surrey, 1994.

4. F. C. Frank and J.H. van der Merwe, Proc. Roy. Soc. (London), A 198, (1949), p216.

5. J.W. Matthews and A.E. Blakeslee, J. Cryst. Growth, 27, (1974), p118.

6. E.A. Fitzgerald, Materials Science Reports, 7(3), 1991, p87.

7. P. Mandeville, Ph.D. Thesis, Cornell University, 1994.

8. T.G. Andersson et al, Appl. Phys. Letts., 51(10), 1987, p752.

9. P.J. Orders et al, Appl. Phys. Letts., 50, 1987, p980.

10. P.L. Gourley et al, Appl. Phys. Letts., 52(5), 1988, p377.

11. Private communication, A.T.R. Briggs.

12. M.A.G. Halliwell and I. Bassignana, MRS Short Course C-23 on X-Ray Diffraction Characterisation of Semiconductors, Fall 1992.

13. I.J. Fritz et al, Appl. Phys. Lett., 46(10), 1985, p967.

14. D. Teng et al, J. Cryst. Growth, 135, 1994, p36.

15. R. Beanland et al, Advances in Physics, unknown publishing date(if published).

16. P.L. Gourley et al, Mat. Res. Soc. Symp. Proc., vol 56, 1986, p229.

17. H. Temkin, Appl. Phys. Lett., 55(16),1989, p1668.

18. A. Le Corre, J. Cryst. Growth, 120, 1992, p353.

19. G. Wagner, Zeitschrift für Kristallographie, 189(1989), p269.

20. T. Tsuchiya, Jpn. J. Appl. Phys., 33(1994), p230.

21. J. W. Matthews and A.E. Blakeslee, J. Cryst. Growth, 32, 1976, p265.

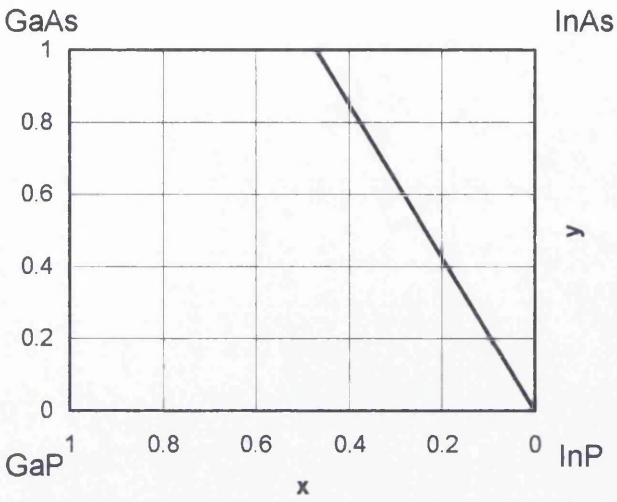

Figure 4.1 Solid line indicates the range of $Ga_xIn_{1-x}As_yP_{1-y}$ compositions that can be grown lattice matched to InP. Compositions to the right (left) of this line have a net compressive (tensile) strain when grown on InP[1].

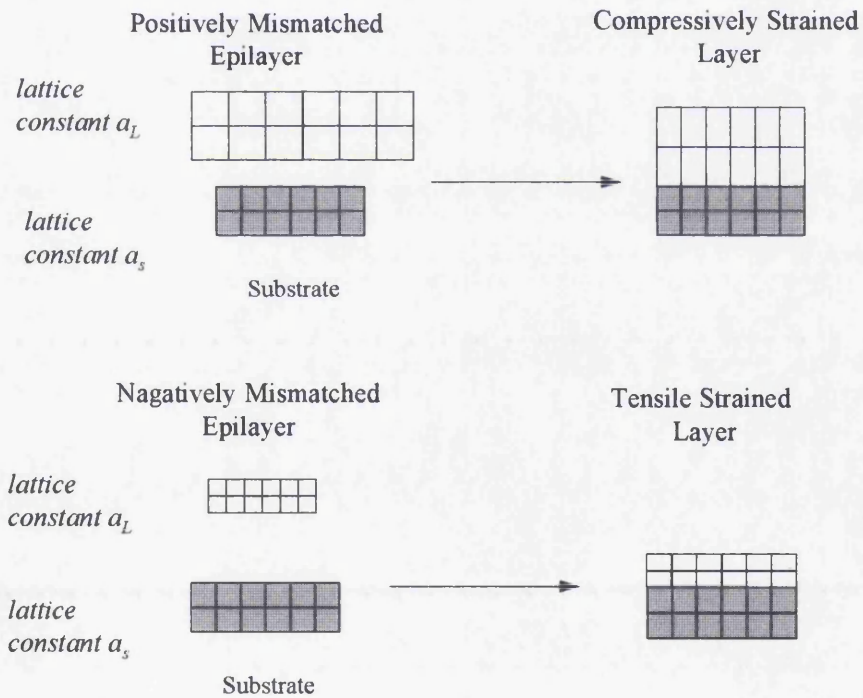

Figure 4.2 Schematic diagram illustrating the change in the lattice symmetry which occurs when either a compressive or tensile layer is grown on a thick substrate. Note how the lattice constant in the growth direction depends on the sign of the mismatch.

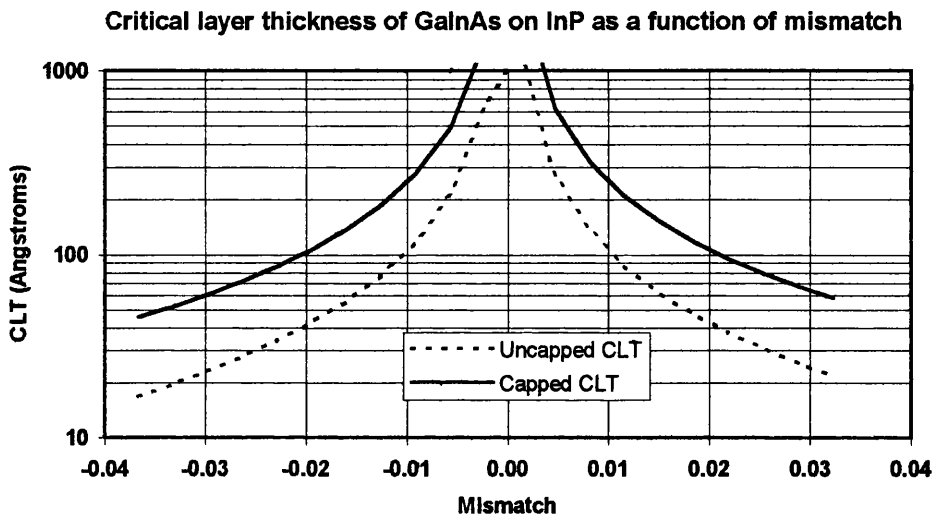

Figure 4.3 Plot of the Matthews-Blakeslee critical layer thickness for strained $Ga_xIn_{1-x}As$ alloys grown on InP substrates. Plot shows the critical thicknesses for both capped and uncapped structures.

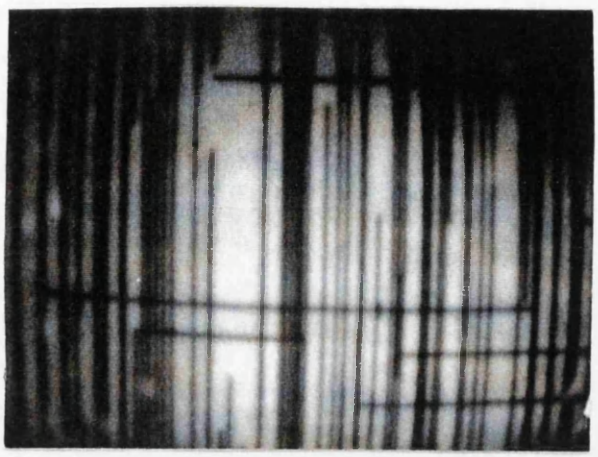

Figure 4.4a Photoluminescence image taken from approx. 550Å thick 0.8% compressively strained $Ga_xIn_{1-x}As_yP_{1-y}$ layer. Note how the dislocations run predominantly in the [011] direction.

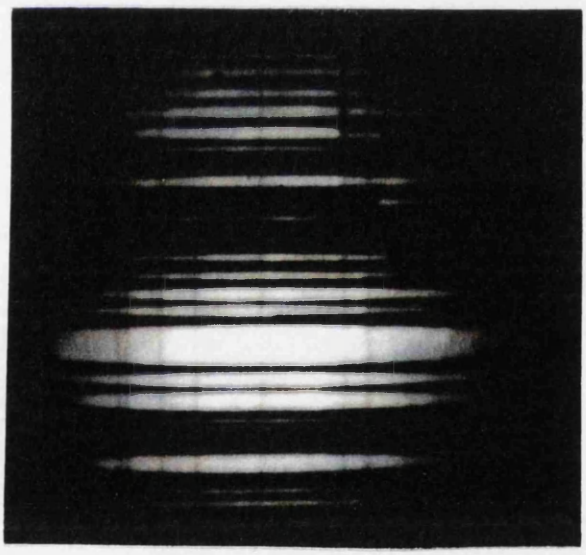

Figure 4.4b Photoluminescence image taken from approx. 3000Å, 0.315% tensile strained $Ga_xIn_{1-x}As_yP_{1-y}$ layer. Note how the dislocations run predominantly in the [01$\bar{1}$] direction.

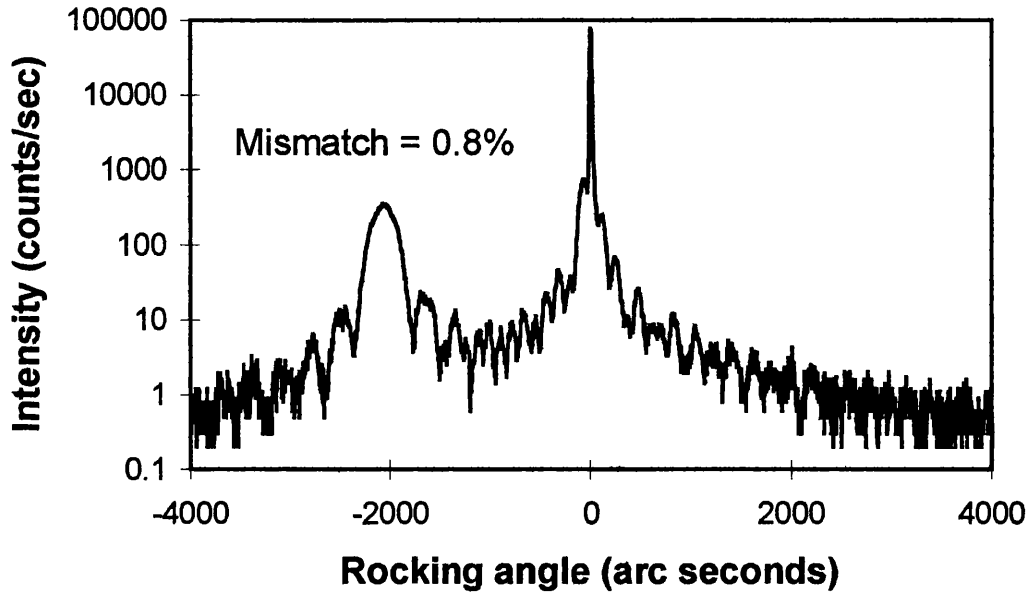

Figure 4.5a Rocking curve of sample whose PL image is shown on figure 4.4a. There is no indication of any deterioration in the quality of the layer.

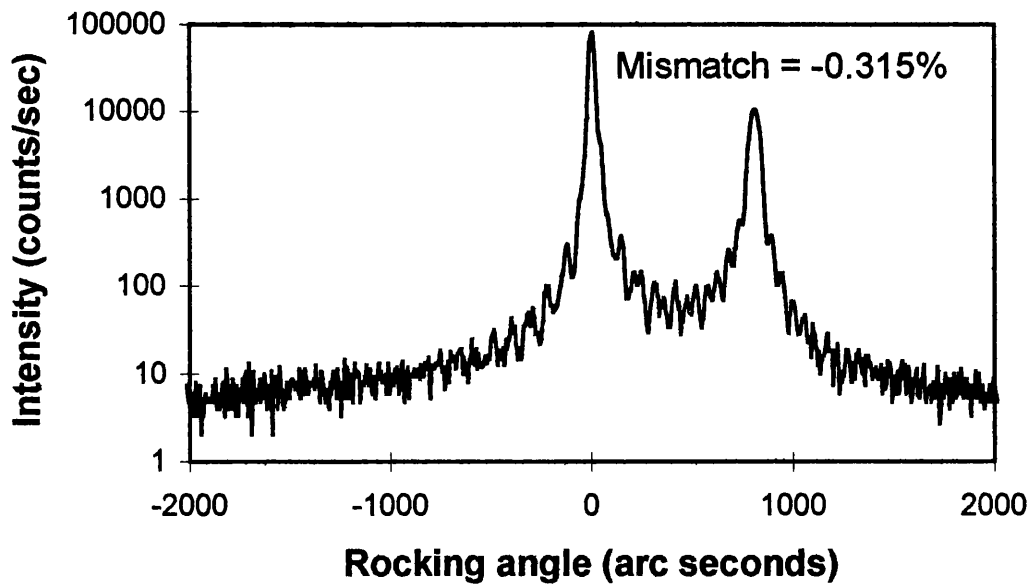

Figure 4.5b Rocking curve of sample whose PL image is shown on figure 4.4b. Again, there is no indication of any deterioration in the quality of the layer.

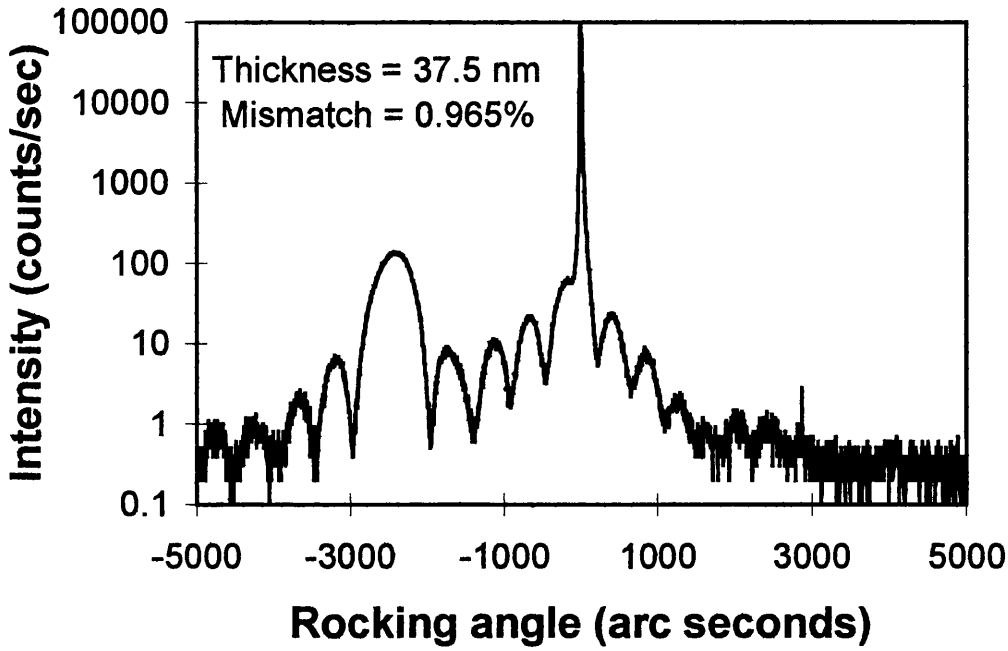

Figure 4.6a Rocking curve of structure shown in figure 6b below. The sample exceeds the critical layer thickness but exhibits a sharp well defined layer peak with strong thickness fringes.

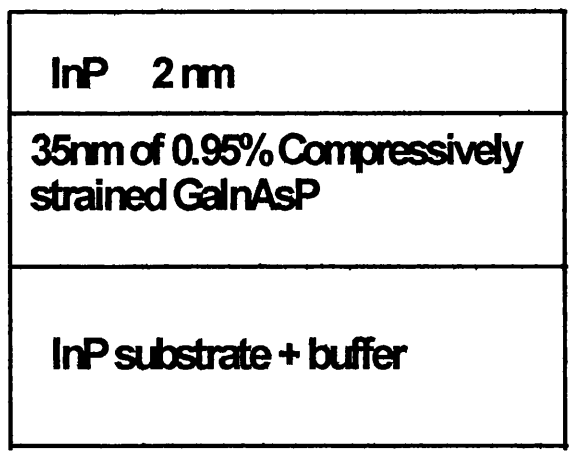

Figure 4.6b Structure of sample whose rocking curve is shown in figure 4.6a above.

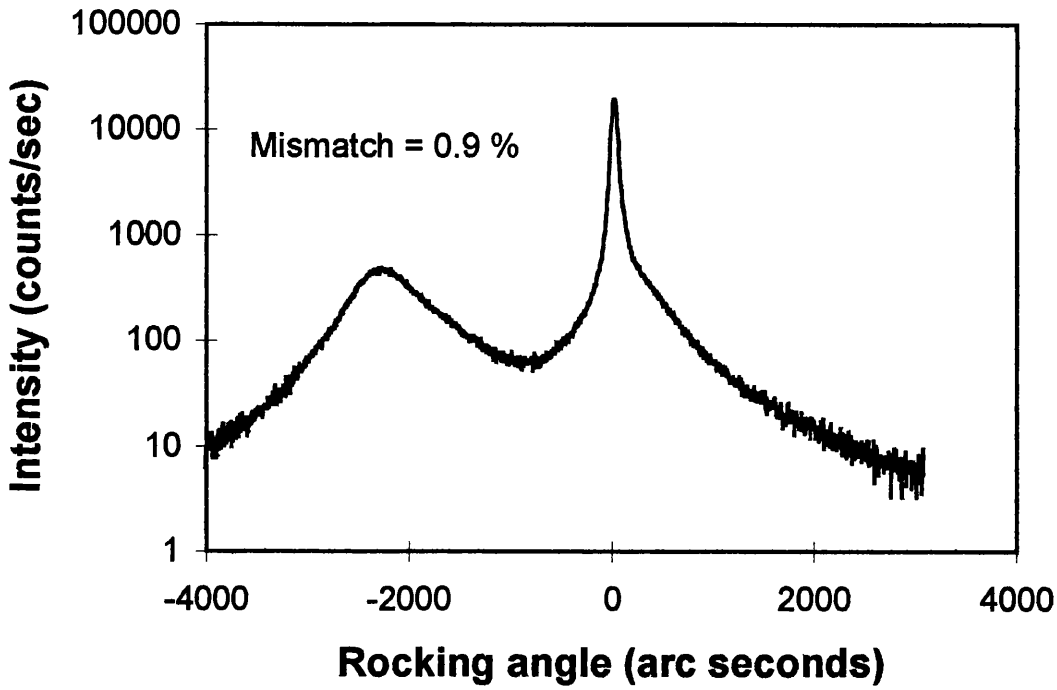

Figure 4.6c Rocking curve of structure shown in figure 6d below. The sample exceeds the critical layer thickness and the deterioration in layer quality is demonstrated by the broadening of the layer peak.

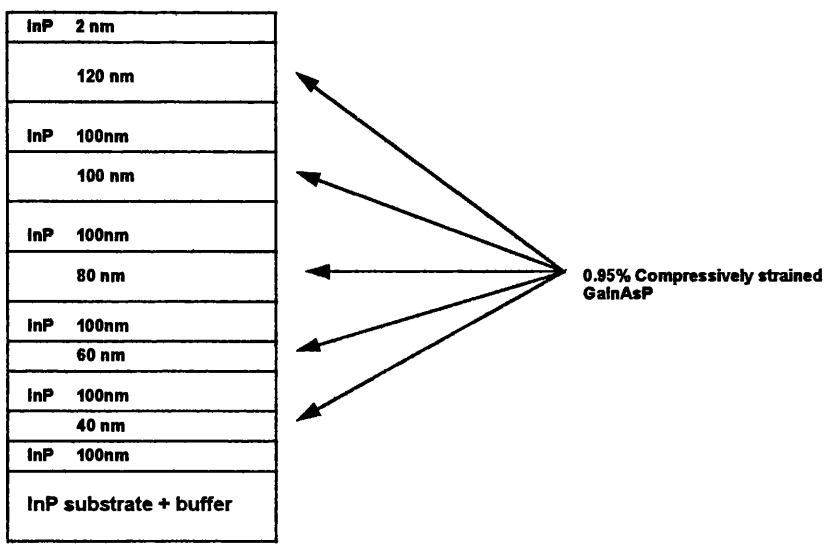

Figure 4.6d Structure of sample whose rocking curve is shown in figure 4.6c above.

Chapter 5

InP-Based Quantum Well Lasers

5.1 The Role of InP Based Lasers in Modern Telecommunication Systems

The development of the InP-based laser has been fueled by the developments in silica optical fibres. The first semiconductor diode lasers, however, were GaAs based and operated in the 0.8-0.9 μm wavelength range. It was by using this material system that the technology of semiconductor laser fabrication was developed. A disadvantage of this material system was that the wavelength of operation was not well matched to the low loss and low dispersion characteristics of optical fibres, as shown in figure 5.1. In comparison however, the InP-$Ga_xIn_{1-x}As_yP_{1-y}$ based material system, by virtue of the band gap energy of the alloys involved, enables laser diode structures to be fabricated with active regions that will operate in the important 1.3μm and 1.55μm wavelength windows that are identified in figure 5.1. One further advantage of InP-$Ga_xIn_{1-x}As_yP_{1-y}$ over GaAs based lasers, is that the former seem to be less susceptible to degradation in performance (predominantly caused by the generation of dark line defects), over long periods of time.

This combination of wavelength compatibility with a low loss/dispersion transmission medium and highly reliable performance, has made the InP based laser one of the key building blocks that has driven the highly successful optical fibre transmission business. One of the most important and profitable areas of this business is trans-continental systems that are deployed under the sea. These so-called sub-marine systems can carry many parallel optical fibre channels and enable telecommunication data to be transmitted to an end receiver with minimal delay. It is this feature of minimum delay together with the economics of capital investment and maintenance that makes optical fibre transmission more attractive than satellite based systems for the major telephone companies that provide long haul trunk telephony.

The first example of a commercial sub-marine optical telecommunication system was the so-called TAT-8 link between Europe and North America. It was laid in 1988 and was based on an operating wavelength of 1.3μm. The information carrying capacity of this system exceeded the total capacity of all previously laid sub-marine copper cables. The next systems, for example TAT-9 and 12, were based at 1.5μm operating wavelength where the loss of the fibre is lower than at 1.3μm. The problem of fibre dispersion at this wavelength can be minimised by using narrower spectral linewidth distributed feedback (DFB) lasers or by employing specially fabricated dispersion shifted

fibre, where the dispersion zero is shifted from 1.3μm to 1.5μm. One common feature of all of the above systems is the need to provide a regeneration of the optical signal at periodic lengths along the optical train to overcome the finite loss of the fibre. In the above systems this was provided by optical repeaters which convert the optical signal into an electrical one, electrically amplify the signal, re-synchronise the signal with the system clock frequency before re-converting back into an optical signal for transmission. These repeater systems consist of many sub-systems and components, all of which provide a finite reliability hazard and contribute to the overall reliability budget of the system as a whole.

The Erbium doped fibre amplifier was developed in the late 1980's and is now an attractive alternative to the repeater as it is much simpler to construct, has fewer associated control electronics and is cheaper. Another main advantage of the fibre amplifier is that it is 'bit-rate transparent', i.e. unlike optical repeaters it does not require a major re-design in the high-speed electronics (that perform signal re-generation) each time the bit-rate is increased. The optical signal passes through, and is amplified by, the fibre amplifier. The gain is provided by the Er ions which have to be optically pumped at either one of two wavelengths: 0.98μm or 1.48μm The former yields an amplifier with better noise characteristics than the latter. Despite this, the first long-haul optical systems using fibre amplifier technology used 1.48μm InP-based high power laser pumping sources, by virtue of the high reliability track record that InP-based devices have when compared to GaAs based devices. Although the systems using InP based pumps are in successful operation, system designers now prefer the low noise characteristics offered by the 980nm pump source which can be fabricated using the strained GaAs-$Ga_xIn_{1-x}As$ material system.

As optical transmission technology has matured, the speed at which data is transmitted, the bit rate, has grown to cope with the increasingly diverse demands of telephony and data communications. Table 5.1 below lists the evolution in the standardised bit-rates as defined by ITUT for SDH (European based Synchronous Digital Hierarchy standards) and ANSI for SONET (North American based Synchronous Optical Network)

Table 5.1 Evolution of standardised bit-rates for SDH and SONET.

SONET	SDH	Line Rate (Mbits/sec)
OC-1	N/A	51.84
OC-3	STM-1	155.52
OC-12	STM-4	622.08
OC-24	N/A	1244.16
OC-48	STM-16	2488.32
OC-192	STM-64	9953.28

The majority of optical transmission systems operate at maximum bit-rates defined by OC-48/STM-16, but most large telecommunication equipment suppliers are developing and deploying 10 Gbits/sec systems. The systems operating up to, and including, 2.5 Gbits/sec, were mostly based on lasers that were directly modulated, e.g. a 2.5 Gbits/sec electrical pulse waveform would directly modulate the biasing of the diode laser. At 10 Gbits/sec and beyond this becomes increasingly difficult due to wavelength chirp (spectral broadening caused by carrier-induced refractive index changes in the laser). This can be overcome by driving the laser in a CW mode and using an external intensity modulator.

5.2 Lasing Action in InP Based Lasers and the Advantages of Quantum Wells

There are several detailed texts that discuss the theory of operation of semiconductor lasers[1] in general and InP based lasers[2] in specific. Only a few important aspects of the principles of operation are outlined here.

5.2.1 Basics of Laser Action in Semiconductor Lasers

There are three possible ways that an electron can interact with a photon in a direct band-gap semiconductor:

- Spontaneous emission of a photon occurs when an electron recombines with a hole to produce a photon;
- Absorption of a photon with an energy greater than the band gap of the semiconductor will result in an electron being excited from the valence to the conduction band;
- The third, and most important interaction as far as lasing is concerned, is that between a sufficiently energetic photon and an electron in the conduction band. This interaction gives rise to two photons, with the emitted photon being in the same frequency and phase as the incident photon. This process is termed stimulated emission and is, in comparison to the other two, the least probable transition to occur under thermal equilibrium conditions.

If we approximate the band structure of a semiconductor to a 2 level electronic system, we can describe the thermal equilibrium of upward (valence to conduction) and downward (conduction to valence) transition rates in the presence of an optical field by

$$A_{21}n_2 + B_{21}n_2\Phi(\nu) = B_{12}n_1\Phi(\nu) \qquad (5.2.1)$$

A_{21} – Einstein A co-efficient describing spontaneous emission (s^{-1})
B_{21}, B_{12} – Einstein B co-efficients describing stimulated emission and absorption respectively (m^3 / Js^2)
n_1, n_2 – populations in the respective energy levels (m^3)
$\Phi(\nu)$ – optical field (Js/m^3)

The LHS of equation 5.2.1 represents spontaneous and stimulated emission rates (which both depend on the population in level 2) and the RHS represents absorption (which depends on the population in level 1). By further assuming a Boltzmann approximation for the distribution in electron energy, i.e.

$$\frac{n_2}{n_1} = \exp\left[\frac{-(E_2 - E_1)}{k_B T}\right] = \exp\left[\frac{-h\nu}{k_B T}\right] \tag{5.2.2}$$

k_B – Boltzmann's constant 1.381×10^{-23} J / K h – Planck's constant 6.626×10^{-34} Js
T – temperature (K) $h\nu$ – Energy of tansition (J)

we can show that:

$$\frac{n_2}{n_1} = \frac{B_{12}\Phi(\nu)}{A_{21} + B_{21}\Phi(\nu)} = \exp\left[\frac{-h\nu}{k_B T}\right] \tag{5.2.3}$$

If $B_{12}=B_{21}$, i.e. the probability that a photon will transfer an electron from level 1 to 2 is the same as from 2 to 1 then we can say:

$$\frac{\text{stimulated}}{\text{absorption}} = \frac{n_2}{n_1} \text{ and } \frac{\text{stimulated}}{\text{spontaneous}} = \frac{B\Phi(\nu)}{A} \tag{5.2.4}$$

Hence in order to achieve laser action, we require an excess population in level 2 (i.e. population inversion) and an intense optical field so that stimulated emission is much more likely to occur than spontaneous emission. The ratio of stimulated to spontaneous emission can be likened to a signal to noise ratio.

The state of population inversion can be achieved in a p-n junction by biasing the device in the forward direction so that there is a higher density of electrons in the conduction band than there would be under thermal equilibrium. A simple schematic of band bending in a homojunction p-n diode under forward bias is shown in figure 5.2. Electrons and holes participate in the stimulated emission process only within the depletion region of the p-n junction.

5.2.2 Threshold Current, Efficiency and Temperature Sensitivity

As the level of population inversion increases, a point will be reached when there will be an equal probability of an incident photon being either absorbed, or participating in stimulated emission. At levels of population inversion greater than this, the device will provide gain. The general condition for net gain is given by Bernard and Duraffourg[3] as:

$$E_{fc} - E_{fv} > h\nu \geq E_g \qquad (5.2.5)$$

E_{fc} – Quasi - Fermi level in conduction band
E_{fv} – Quasi - Fermi level in valence band
$h\nu$ – photon energy

Hence there is a window of photon energies between the band gap, E_g, and $E_{fc} - E_{fv}$ in which net stimulated emission will occur. The injected current density at which this occurs is often termed the transparency current density.

Although the main criterion for lasing action, i.e. net stimulated emission, is met at the so-called transparency current density, there still exist other 'loss' mechanisms that have to be overcome and therefore require an additional amount of excited electrons. The point at which these losses are overcome is termed the threshold condition. Like any other laser, a semiconductor laser requires a reflective cavity to generate the optical feedback that gives rise to laser oscillation. This is achieved in semiconductor lasers by the use of a Fabry-Perot cavity where the cleaved ends (facets) of the laser chip act as partially transparent mirrors and the cavity length defines the longitudinal mode spacing. Alternatively, the feedback can be provided by a grating etched in a layer of the laser structure along the length of the active region, the longitudinal mode properties being defined by the grating characteristics. This is often termed a distributed feedback (DFB) device[2]. A third type of feedback can be provided by a combination of the Fabry-Perot structure and the DFB, this is known as a distributed Bragg reflector (DBR) structure[2]. These three types of feedback mechanisms are illustrated in figure 5.3.

There are two types of losses we have to consider: internal losses and mirror losses. At threshold, the gain of a Fabry-Perot laser cavity must exactly balance these losses. i.e.

$$\Gamma g = \alpha_m + \Gamma\alpha_{\text{int}} = \frac{1}{2L}\ln\left(\frac{1}{R_1R_2}\right) + \Gamma\alpha_{\text{int}} \tag{5.2.6}$$

Γ – optical confinement factor (dimensionless) α_{int} – internal losses (cm^{-1})
g – material (or intensity) gain (cm^{-1}) L – laser cavity length (cm)
α_m – mirror loss (cm^{-1}) R_1, R_2 – facet reflectivities.

One of the main sources of internal loss is non-radiative recombination, where electrons and holes recombine without the generation of a photon. These mechanisms will be discussed further in chapter 6. The injection current density at which threshold occurs can be written as:

$$J_{th} = J_{rad} + J_{nonrad} + J_{se} \tag{5.2.7}$$

J_{th} – threshold current density (Acm^{-2})
J_{rad} – radiative recombination current density(Acm^{-2})
J_{nonrad} – non-radiative recombination current density(Acm^{-2})
J_{se} – current density required for stimulated emission(Acm^{-2})

Radiative recombination is a commonly used term to describe spontaneous emission.

Figure 5.4 illustrates the effect of increasing the injection current on the optical output power of a 'typical' semiconductor laser, such a plot is commonly termed as a light-current (L-I) characteristic. Once the threshold condition has been met, any further increase in injected current results in the optical power increasing by several orders of magnitude. After this, the increase in output power is linear with the injection current, until some saturation point is reached where the relationship becomes sub-linear. An important parameter that is used to describe the performance of such a device in the linear region, is the external (or differential) quantum efficiency, η_d, which relates the efficiency with which the laser can convert injected current into optical output. The external quantum efficiency at an operating current I, is described by:

$$\eta_d = \eta_i\left(\frac{\text{photon escape rate}}{\text{photon generation rate}}\right)$$

$$\eta_d = \eta_i\left(\frac{\frac{1}{2L}\ln\left(\frac{1}{R_1R_2}\right)}{\Gamma\alpha_{\text{int}} + \frac{1}{2L}\ln\left(\frac{1}{R_1R_2}\right)}\right) = \frac{P_{out}}{(I - I_{th})}\frac{e}{h\nu} = \frac{dP}{dI}\frac{e}{h\nu} \tag{5.2.8}$$

η_i – internal quantum efficiency P_{out} - output power of laser
I_{th} – threshold current of laser $h\nu$ - photon energy

The internal quantum efficiency, η_i, is the ratio of radiative to total recombination rates and has an ideal value of unity when stimulated emission is achieved, i.e. above threshold.

Both threshold current and external quantum efficiency are sensitive to changes in the temperature at which the device is operating. The threshold current is commonly (empirically) found to vary with temperature as:

$$I_{th} = I_0 \exp\left(T/T_0\right) \tag{5.2.9}$$

where I_0 is a constant and T_0 is known as the characteristic temperature. Ideally it would be desirable to have a T_0 as high as possible to minimise the effect of temperature on device performance.

5.2.3 The Advantages of Using Multiple Quantum Well Active Regions

A quantum well is a thin layer, for example less than 200Å, of a relatively low band gap semiconductor (e.g. $Ga_{0.47}In_{0.53}As$) sandwiched between two layers of higher band gap semiconductor (e.g. InP or $Ga_xIn_{1-x}As_yP_{1-y}$). The lower and higher band gap materials are referred to respectively as wells and barriers. A multiple quantum well is a sequence of such "sandwiches", usually with a constant well and barrier thickness through the sequence. The different relative energies of the well and barrier materials give rise to a square well potential in the conduction band, due to the conduction band offset, and similarly in the valence band due to the valence band offset. Such a structure is the physical realisation of the quantum mechanical 'particle in a one dimensional box' problem. The well-known solution to this problem is the quantisation of the energy levels, for both electrons in the conduction band and holes in the valence band, into discrete levels[4]. The position of the energy levels in the wells depends on the effective mass of the carrier, the conduction/valence band discontinuity and the well width. The energy levels can be calculated by solving the Schrödinger wave equation. In general the conduction and valence band offsets are relatively constant in the InP-$Ga_xIn_{1-x}As_yP_{1-y}$ based materials system at[5]:

$$\begin{aligned} \Delta E_c/\Delta E &= 0.39 \pm 0.01 \\ \Delta E_v/\Delta E &= 0.61 \pm 0.01 \end{aligned} \tag{5.2.10}$$

where $\Delta E_{c(v)}$ is the difference in the conduction(valence) band edges, and ΔE is the difference in the band gap. The holes are therefore in a much deeper well, and consequently more confined, than the electrons (the confinement also depends on the effective mass, the greater the effective mass, the greater the confinement) .

The presence of discrete energy levels means that carriers will be quantised in motion in the growth direction but free to move in the x-y plane, i.e. the growth plane. If an electron and hole recombine in a quantum well structure, the wavelength of the emitted photon is no longer defined by the band gap, but by the separation in the energies of the n=1 valence band level and the n=1 conduction band level. Thus by controlling the thickness of the well material we can control the wavelength of emission.

A further consequence of the quantisation of the energy levels is that the density of states is no longer continuous and parabolic with the energy of the carrier, but is quantised into a series of discrete steps (each step occurring when the energy of the carrier equals that of the quantised level). In a semiconductor laser, the majority of radiative transitions occurs at the band edge as no change in momentum is required, hence we can relate the efficiency of the laser to the density of states (DOS) close to the conduction band edge. In a device with a bulk active region, the DOS at this point is low, whereas in a quantum well laser the DOS has a step like change to a finite value, which is relatively large compared to the bulk case. Therefore a quantum well laser should be more efficient, i.e. higher gain for a given injection level, than a bulk device. In summary, the effects of the increased DOS at the band edge on laser performance are:

- reduced threshold current density due to higher gain for a given current injection level;
- higher differential gain at low injection levels;
- increased modulation bandwidth and reduced spectral linewidth due to increased differential gain;
- reduced wavelength chirp as a result of increased differential gain.

One major limitation of the quantum well laser is the effect of gain saturation that results from the step-like nature of the DOS. An important parameter to optimise in the design of a quantum well laser is the optical confinement factor, i.e. the fraction of the intensity in the guided region that interacts with the active region. Unlike a bulk active region device, it is often necessary to include a separate confinement heterostructure (SCH) to maximise the optical confinement factor, Γ, in MQW

based devices. A further improvement in MQW based devices is the reported improvement in characteristic temperature, T_0[6].

The InP-based MQW active region laser is, however, not without its problems. These will be discussed in Chapter 6.

5.3 Threshold Current Density Analysis of Quantum Well Lasers

For GaAs-based quantum well lasers, McIlroy et al[7] deduced theoretically that the relationship between the gain co-efficient per unit length, g, and the injection current density, J, could be approximated by the relationship:

$$\Gamma g = N\Gamma_w G_w = N\Gamma_w G_0 \ln\left(\frac{eJ}{NJ_0}\right) \tag{5.3.1}$$

$N\Gamma_w$ – optical confinement factor for structure expressed as number of wells times the confinement factor per well
G_w – gain co-efficient per well
G_0, J_0 – constants
e - Eulers constant, i.e. exp(1) = 2.713

The gain co-efficient required to reach threshold, g_{th}, may be equated to the total losses as defined by the equation in section 5.2.2:

$$g_{th} = N\Gamma_w G_0\left(1+\ln\left(\frac{J_{th}}{NJ_0}\right)\right) = \frac{1}{2L}\ln\left(\frac{1}{R_1R_2}\right)+\Gamma\alpha_{int} \tag{5.3.2}$$

g_{th} – gain of structure at threshold = Γg
$\Gamma\alpha_{int}$ – loss of structure = α

re-arranging this equation for $\ln(J_{th})$

$$\ln(J_{th}) = \left(\frac{1}{2LN\Gamma_w G_0}\right)\ln\left(\frac{1}{R_1R_2}\right)+\frac{\alpha}{N\Gamma_w G_0}+\ln(NJ_0)-1 \tag{5.3.3}$$

This theoretical relationship is supported experimentally in GaAs-based lasers[7] and InP-based MQW lasers[8], by the observation of the empirical relationship:

$$\ln\left(\frac{J_{th}}{J_\infty}\right) = \frac{k}{NL}$$

J_∞ – threshold current density for the infinite cavity length
k – constant

(5.3.4)

By equating the empirical observations with the theoretical predictions, we obtain

$$J_\infty = NJ_0 \exp\left(\frac{\alpha}{N\Gamma_w G_0} - 1\right)$$

and (5.3.5)

$$k = \frac{1}{2\Gamma_w G_0} \ln\left(\frac{1}{R_1 R_2}\right)$$

Hence if we plot the threshold current density of an MQW laser against the reciprocal cavity length, we can evaluate the values J_∞ and k. The latter gives direct information on the well gain through the $\Gamma_W G_0$ product. If the experimental analysis is extended further by plotting the threshold current density against the reciprocal length for a variety of number of wells, we can attempt to evaluate the parameters J_0 and $\Gamma_W G_0$ that appear in the above equations and

$$\Gamma_w G_w = \Gamma_w G_0 \left(1 + \ln\left(J_w / J_o\right)\right) \quad (5.3.6)$$

J_w – threshold current density per well

using the following procedure:

1- assume a value for the loss in the structure, α;

2- evaluate g_{th} for a given value of N, since we know α, R and L;

3- evaluate $\Gamma_W G_W$, i.e. g_{th}/N;

4- for each threshold condition at each device length evaluate J_W, i.e. J_{th}/N;

5- plot $\Gamma_W G_W$ as a function of ln (J_W);

6- go back to step 2 and repeat analysis for a different value of N until analysis complete;

7- if the choice of α is correct then a straight line fit should be observed for all lengths of devices at all number of wells. If no straight line fit is observed then go back to step 1 and revise the estimate of α. Repeat analysis until a good fit is obtained;

Once a satisfactory experimental curve of the above relationship has been obtained, the values of J_0 and $\Gamma_W G_0$ can be inferred from the slope and the intercept of the curve respectively. This analysis technique is used several times in this thesis to evaluate the effect of different magnitudes and signs of well strain. Broad area (50μm wide) stripe lasers are ideal for investigating the effect of changing material properties on device behaviour. Such devices are easy to fabricate, as will be mentioned in the next section, and their simple structure minimises the influence of processing variations on the end result.

5.4 Typical InP-Based MQW Ridge Laser Fabrication Process

All the lasers, whose results are discussed in this thesis, were fabricated in a 'standard' manner by the laser processing team at BNR Europe, Harlow. Any deviations from the norm will be explicitly highlighted in the text. The best way to summarise the fabrication process is through a flow chart as shown in figure 5.5. There are three 'types' of semiconductor lasers that will be mentioned in this thesis: the broad area laser, the DFB ridge waveguide laser and the Fabry-Perot cavity ridge waveguide laser.

As mentioned above, the broad area laser is primarily a vehicle for evaluating the 'quality' of the semiconductor material and the effect of varying the material properties on the device performance. The main points to note, are that the structure does not employ any scheme for lateral current confinement and that the cleaved facets define the reflectivities (approximately 29% for air/InP based material interface). The 'end on' view of a typical broad area device is shown in figure 5.6. The processing of these structures involves steps 1, 4, 5 and 7 as defined in figure 5.5. The full device structure is grown in a single stage of MOVPE and then the p-contact window is defined by etching SiO_2 which has been deposited on the wafer surface. After the thinning of the substrate, the p and n side metallisations are deposited and alloyed as required. The devices are then cleaved to the desired length and tested.

The ridge waveguide laser is an example of a weakly index guided laser. This is achieved by defining a ridge of material into, but not beyond, the p-InP layer of the laser structure; a schematic example of this is shown in figure 5.7. The ridge controls the optical mode in two ways: it inhibits the spreading of the current injected from the p-contact, hence controlling the area over which population inversion will be achieved, and it provides lateral optical guiding via the discontinuity in the refractive index between the semiconductor material in the ridge and the oxide surrounding the ridge. The processing of such structures involves steps 1, 3, 4, 5, 6 and 7 of figure 5.5 (steps 8 and 9 are taken if further testing or packaging are required). Figure 5.7 represents a ridge structure with a MQW active region surrounded with un-doped $Ga_xIn_{1-x}As_yP_{1-y}$ waveguiding layers. The ridge

width is typically 2μm. The most attractive features of this device are the ease of fabrication (only one MOVPE growth step) and the fact that the active region remains buried within the structure, receiving no direct contact with any the processing steps. Hence there is little risk of incorporating re-growth or processing related defects that may compromise the long term reliability of these devices. These features undoubtedly contribute to the well-established reliability track record of ridge lasers.

In a Fabry-Perot ridge waveguide laser, the optical feedback, as mentioned above, is provided by the end facets. Cleaved crystal facets provide 29% reflection. However they are very rarely used in practice, instead facet coatings are deposited on either end of the cavity to precisely define the reflectivity to the requirement of the device designer. One of the disadvantages of the Fabry-Perot cavity is that it supports a number of longitudinal modes defined in frequency by

$$\nu_m = \frac{mc}{2nL} \tag{5.4.1}$$

ν_m – frequency of optical mode, m. n – effective refractive index of the guided mode
m – integer L – cavity length.
c – speed of light

The only longitudinal mode discrimination is provided by the gain spectrum. Generally the gain spectrum is much wider than the frequency separation of the Fabry-Perot modes hence, when viewed on an optical spectrum analyser, one sees a series of modes whose intensity is modulated by the gain curve. These 'side-modes' are problematic when the laser is directly modulated at high frequencies, especially when used in conjunction with non-dispersion shifted fibre, therefore for high speed transmission applications a single frequency source is preferred.

The multi-mode behaviour of a simple Fabry-Perot laser can be overcome by making the feedback frequency dependent so that the mirror losses are different for different longitudinal modes, thus suppressing the modes that are outside the frequency of interest. One of the most successful ways of doing this is to define a grating in the plane of the cavity of the device making the so-called distributed feedback laser (DFB). Unlike in a Fabry-Perot structure, the feedback mechanism in a DFB laser is not provided by the facets but by the grating that is etched continuously along the cavity in one of the layers close to the active region. In most of the structures discussed in this thesis, the grating is defined in the upper layer of the waveguide core. The feedback is provided by a periodic variation in the refractive index, which is generated by the fabrication of a grating in, or near, the waveguide. The refractive index modulation gives rise to both forward and backward travelling

waves as a result of the reflection from the index variations. Coupled wave theory[9] predicts that at wavelengths near the Bragg wavelength of the grating the forward and backward travelling waves are coupled. The Bragg wavelength is defined by

$$\lambda_{Bragg} = \frac{2n\Lambda}{m} \qquad (5.4.2)$$

Λ – period of grating λ_{Bragg} – Bragg wavelength of grating
m – order of grating (m = 1 = first order) n – refractive index of active region

Coupled wave theory also predicts that the grating generates a stop band, i.e. only a fixed range of wavelengths are allowed to propagate. In a uniformly fabricated grating the stop band allows the lasing of the two longitudinal modes whose wavelengths are closest to the Bragg wavelength. Lasing action can be forced to occur in a single mode by either coating only one facet with an anti-reflection coating or by introducing a $\lambda/4$ phase shift into the grating.[10]

One of the main disadvantages of the DFB structure is the added complication that defining a grating has on the fabrication process. For a 1.55μm wavelength device, the required grating pitch is of the order of 100's of nanometres and therefore involves fine line lithographic techniques such as X-ray lithography, holographic photolithography or, more commonly, electron beam lithography. The need for a grating to be defined in the upper layer of the waveguide core implies that two growth steps have to be performed: the sub-structure growth which comprises the n-side buffer layer, the active region and the waveguiding core layers, followed by the overgrowth of the grating etched sub-structure which comprises the p-side layers. This process is summarised schematically in figure 5.8.

5.5 Summary

The InP-based MQW laser is far from optimum in design. There are many aspects of its performance that are inferior to GaAs-based MQW lasers and most of them are attributable to the basic material properties of the InP-$Ga_xIn_{1-x}As_yP_{1-y}$ alloys used. The next chapter highlights these inferiorities, describes the causes and discusses the proposed changes to the conditions under which the quantum wells are grown that can hopefully improve the device performance.

References

1. G.H.B. Thompson, Physics of Semiconductor Laser Devices, John Wiley and Sons, 1980.

2. G.P. Agrawal and N.K. Dutta, Long Wavelength Semiconductor Lasers, Van Nostrand Reinhold, 1986.

3. M.G.A. Bernard and G.Duraffourg, Phys. Status Solidi, (1961), p699.

4. C. Kittel, Introduction to Solid State Physics, John Wiley and Sons Inc., New York, NY, 1986.

5. G.P. Agrawal and N.K. Dutta, Long Wavelength Semiconductor Lasers, Van Nostrand Reinhold, 1986.

6. C. Weisbuch and B. Vinter, Quantum Semiconductor Structures, Chapter 5, Academic Press, 1991.

7. P.W.A. M^{c}Ilroy, A. Kurobe and Y. Uematsu, IEEE J. Quant. Elect., 21(12), 1985, p1958.

8. J.E.A. Whiteaway, G.H.B. Thompson, P.D.Greene and R.W. Glew, IEE Electron Lett., 27, 1991, p340

9. A. Yariv, Optical Electronics, Holt-Saunders International, 1985.

10. A. Collar, Lecture given at Semiconductor Optoelectronic Devices course, University of Surrey, September 1988.

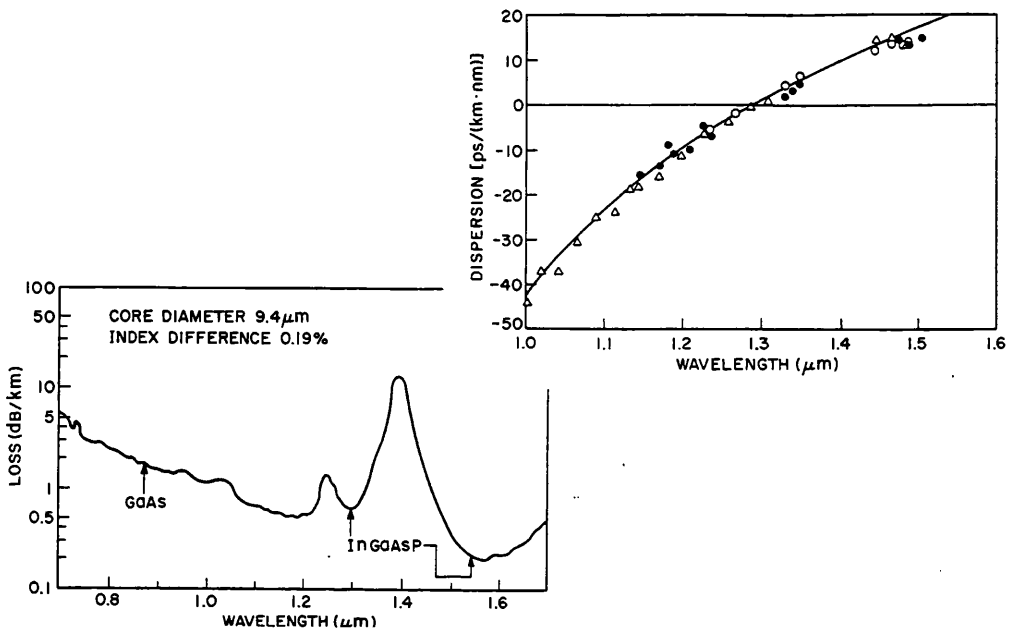

Figure 5.1 Optical loss and dispersion characteristics of silica optical fibre. Low loss windows are evident at 1.3μm and 1.55 μm along with a dispersion minima at 1.3μm.[2]

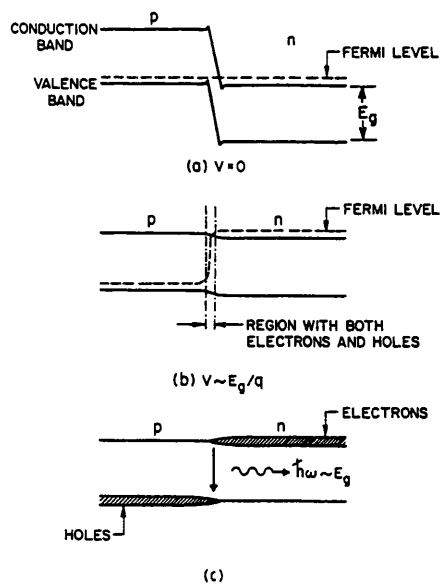

Figure 5.2 Schematic diagram of band bending in a homo-junction p-n diode under (a) zero and (b) forward bias. A schematic representation of the electron/hole densities is displayed in (c) illustrating why radiative recombination occurs in the depletion region.[2]

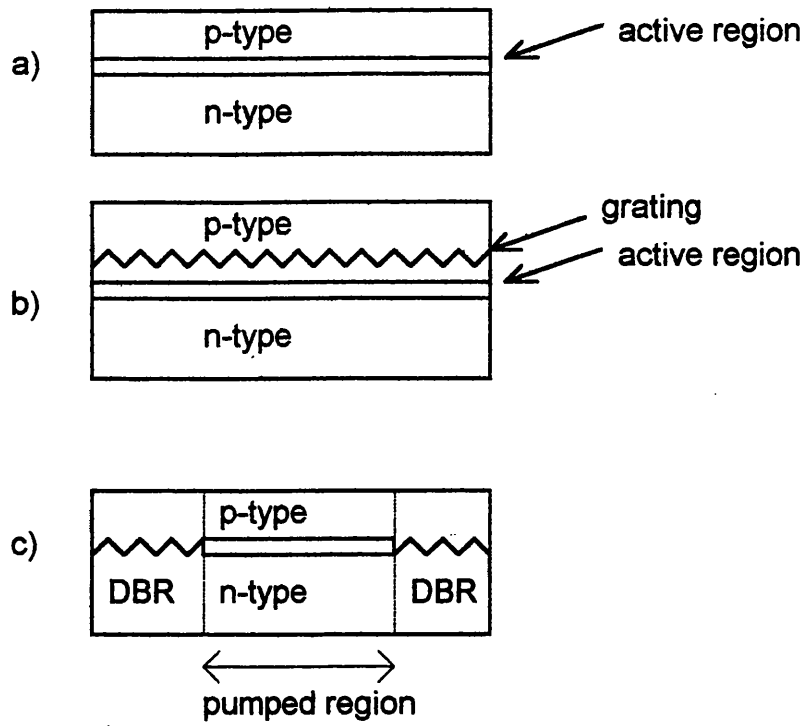

Figure 5.3 Schematic diagram illustrating the three most commonly used methods of obtaining optical feedback in a semiconductor laser: the Fabry-Perot etalon, the distributed feedback laser and the distributed Bragg reflector.

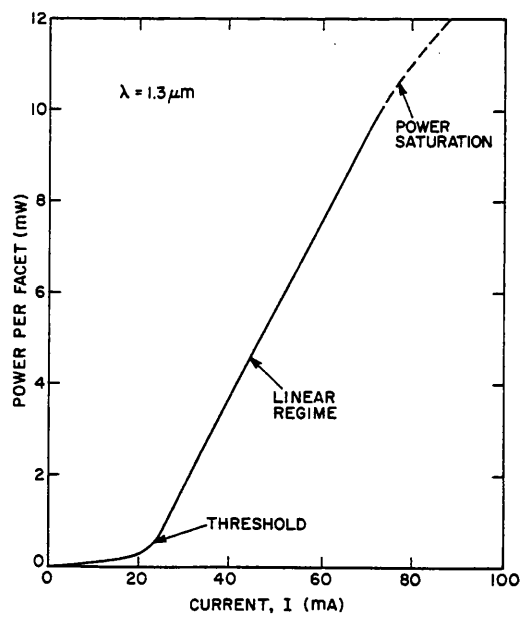

Figure 5.4 Typical light-current (L-I) characteristic of InP-$Ga_xIn_{1-x}As_yP_{1-y}$ laser. The three operating regimes of sub-threshold, linear and sub-linear are illustrated.[2]

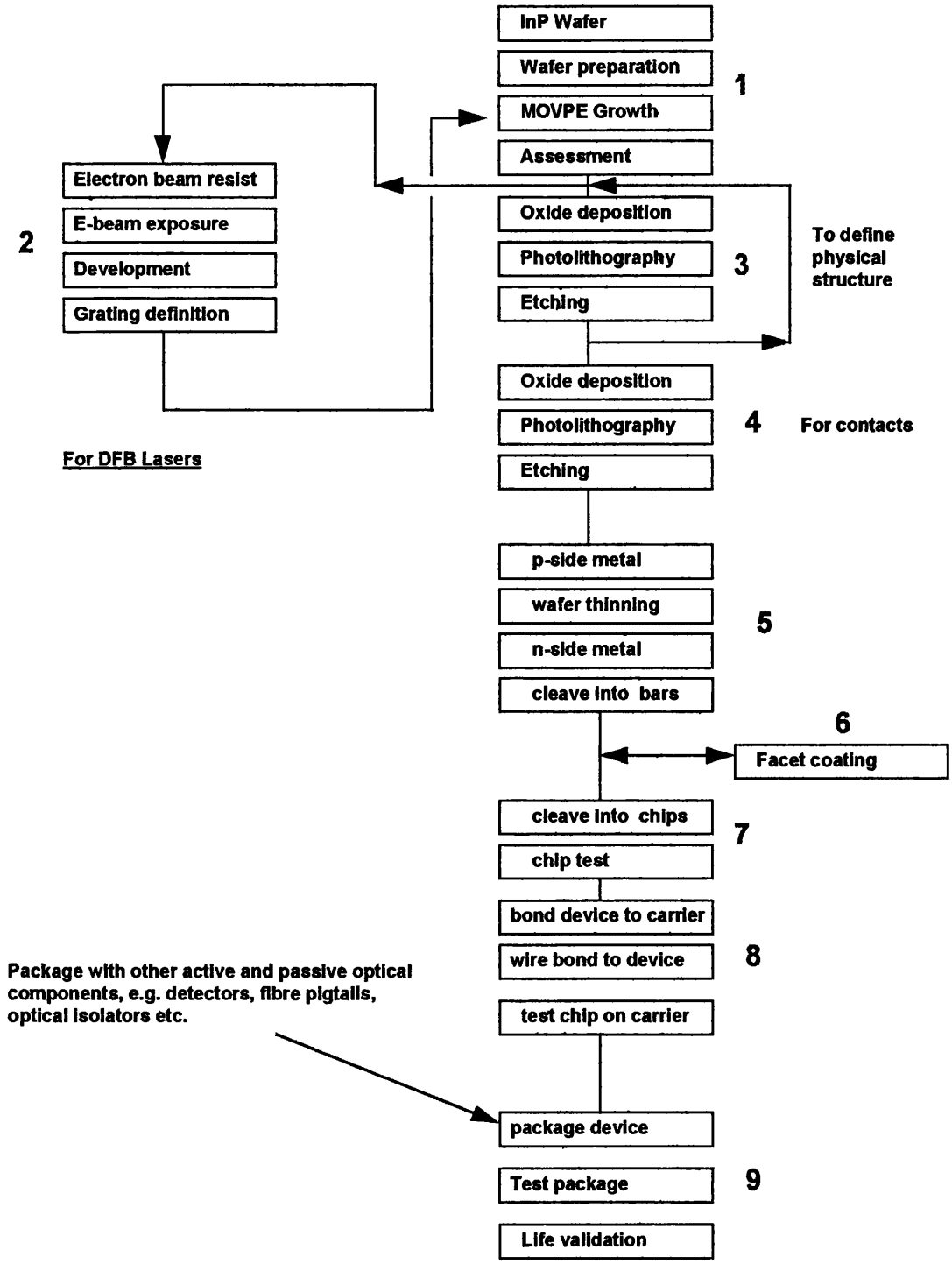

Figure 5.5 Flowchart describing the fabrication process of an InP-$Ga_xIn_{1-x}As_yP_{1-y}$ based laser structures.

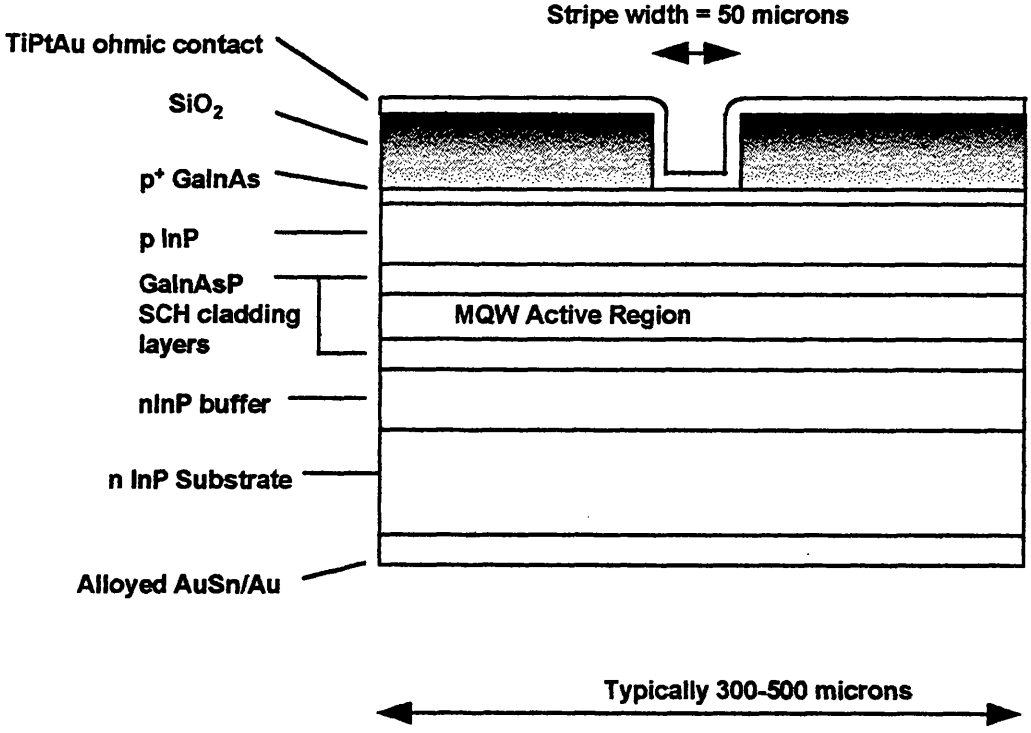

Figure 5.6 End-on view of a broad-area (50μm) stripe laser. The grown laser structure remains completely planar and the current injection area is defined by an oxide stripe.

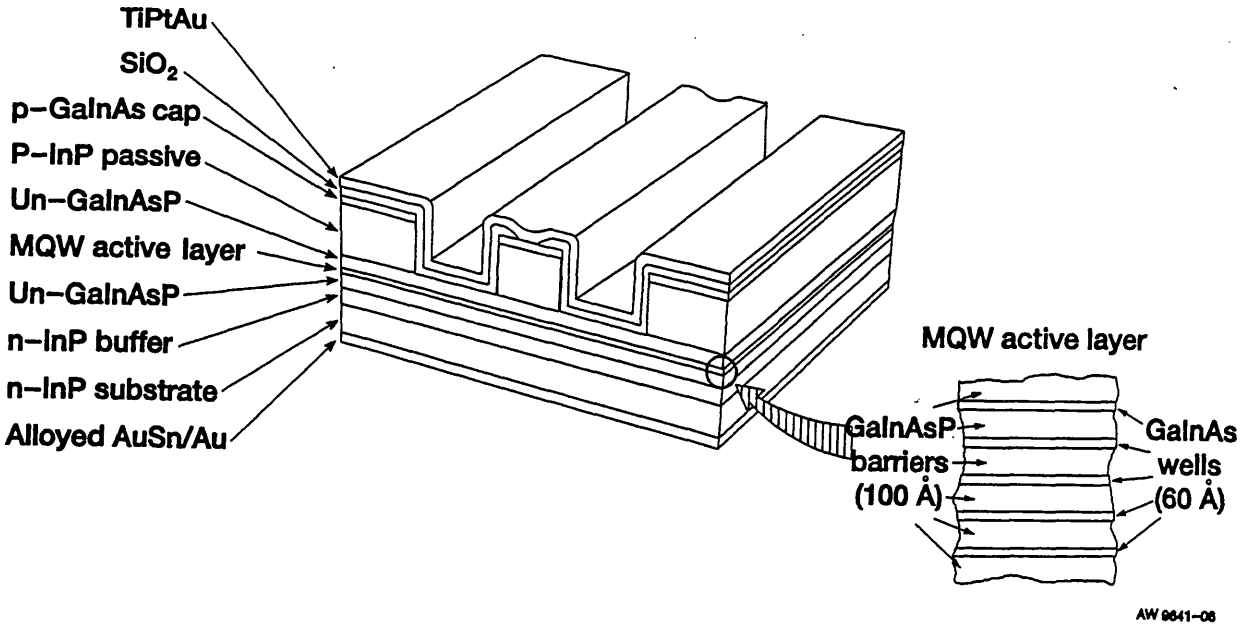

Figure 5.7 Schematic diagram of typical ridge waveguide, Fabry-Perot, MQW laser (lattice matched $Ga_XIn_{1-X}As$ wells) fabricated at BNR Europe.

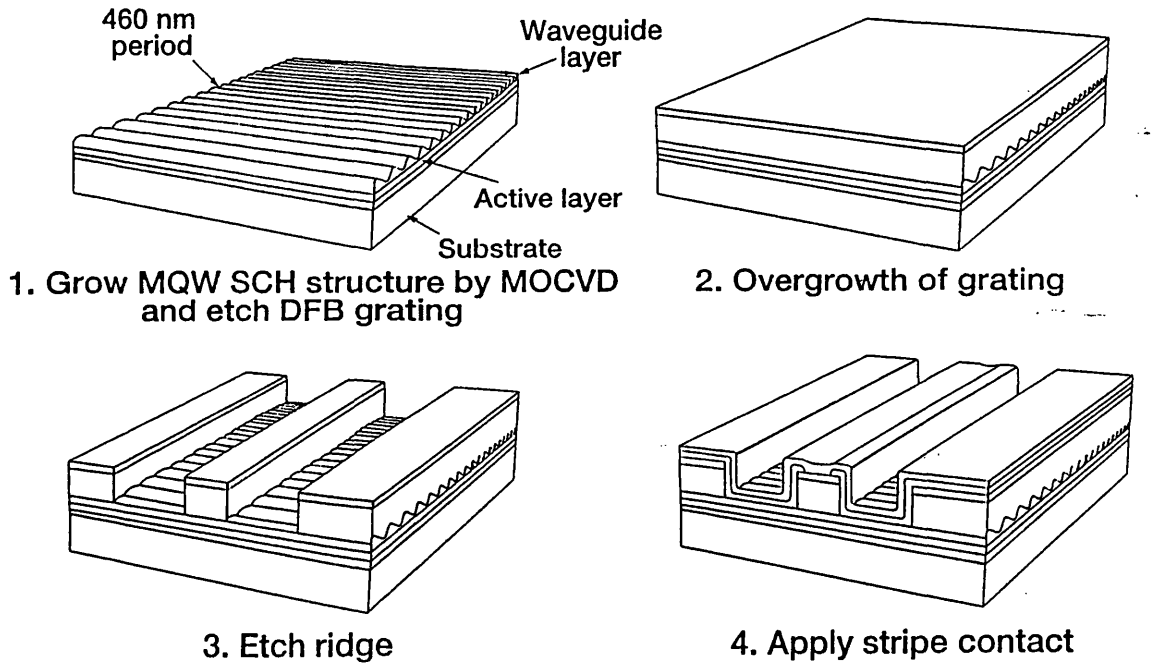

Figure 5.8 Schematic diagram illustrating the key process steps in the fabrication of a ridge waveguide, DFB laser.

Chapter 6

The Benefits to be Achieved by Incorporating Coherent Strain in InP-Based MQW Laser Structures

6.1 The Shortcomings of InP-Based MQW Lasers with Lattice Matched Active Regions

The causes of most of the limitations associated with InP based lasers are directly related to the complex valence band structure. In their keynote paper, Adams et al[1] stated, '*the ideal semiconductor for the production of lasers and light emitting devices should have conduction and valence bands that are mirror reflections of one another about the centre of the band gap. The bands should have low density of states so that the electron and hole distributions become degenerate at low injected carrier densities. Also there should be no other bands within the band gap energy of the band extrema, which can enhance harmful loss mechanisms*'. Figure 6.1 illustrates the band gap dispersion, i.e. energy as a function of momentum, of bulk InP. At the Brillouin zone centre, the Γ point, the conduction band has low effective mass (m_e=0.073m_0), however the valence band is threefold at the same point in k-space. The high curvature, heavy-hole band (m_{hh}= 0.4m_0) and the low curvature, light hole band (m_{lh} = 0.078m_0) are degenerate at the valence band maxima. The spin-split-off band (m_{soh}= 0.15m_0) is separated in energy by 0.11eV from the valence band maxima[2]. The band structure of $Ga_xIn_{1-x}As_yP_{1-y}$ alloys is similar to that of InP, however the values of the effective masses of electrons and holes tend to become smaller as the band gap becomes smaller.

As a result of this valence band structure, the degenerate distribution of electrons in the conduction band and holes in the valence band described in the previous chapter does not, in reality, apply. This is due to the density of states associated with the heavy-hole band, which is large in comparison to the density of states in the conduction band. Hence, for a given current injection condition we can have filled states in the conduction band and only partially filled states in the valence band., i.e. the hole quasi-Fermi level is above the valence band maxima (non-degenerate). Ideally, as highlighted by Adams et al[1], it would be desirable to have conduction bands and valence bands with similar effective masses (density of states) so that both bands would have the same level of filled states for the same level of current injection. This would reduce the current injection required to give

population inversion, i.e. reduce the threshold current density. As well as affecting the threshold current, the relatively heavy hole effective mass has an impact on the differential gain, dg/dN (where N is the carrier density), since

$$dg/dN \propto \frac{\sqrt{m_e m_h}}{m_e + m_h}. \qquad (6.1.1)$$

m_e - effective mass of electron
m_h - effective mass of hole

The differential gain affects the linewidth enhancement factor, $\alpha_H \propto 1/(dg/dN)$, and the relaxation oscillation frequency, $f_r^2 \propto (dg/dN)$.

As discussed in section 5.2.2, the threshold current density of a semiconductor laser consists of a contribution J_{nonrad} that accounts for electrons and holes that re-combine non-radiatively. A variety of non-radiative recombination mechanisms exist: defect associated recombination, surface recombination and Auger recombination. The latter is the most prevalent mechanism in InP-based lasers by virtue of the smaller band gaps involved, when compared to GaAs based devices. There are two main types of Auger recombination: band-to-band and phonon assisted. With band-to-band Auger recombination, an electron and hole recombine and, instead of generating a photon, they excite a third carrier to a high energy. The third carrier, an electron, can be either excited to a higher electronic energy in the conduction band or excited from the spin-split-off band into a empty heavy hole state, these transitions being shown schematically in figure 6.2. The transitions, which conserve momentum, tend to occur off-zone-centre where the energy difference between the spin-split off band and the LH and HH bands is closer to the value of the band gap. With phonon assisted Auger recombination, the final state which the electron reaches is similar to that in the band-to-band process but it requires an interaction with a phonon, i.e. there is a change in momentum. The band-to-band Auger process can be approximated by the equation [3]

$$R_a = C_r n^3 \exp\left(-\Delta E / kT\right) \qquad (6.1.2)$$

R_a – recombination rate
C_r – recombination constant
n – carrier density
ΔE – activation energy for the process
T – temperature of device

Depending on the activation energy, the above process can be strongly temperature dependent. The effect of temperature on the non-radiative contribution of the threshold current density is the main cause of the temperature sensitivity of the threshold current discussed in the previous chapter.

Another problem that plagues InP based lasers is free carrier absorption that occurs after lasing threshold has been achieved. Termed inter-valence band absorption (IVBA), it requires the excitation of an electron from the spin-split-off band to the heavy hole band via the absorption of a photon, this transition is shown schematically in figure 6.3. This process also tends to occur more readily off the zone-centre, where the difference in energy between the heavy hole band and the spin-split off band is closer to the band gap energy. IVBA manifests itself in device performance by increasing the internal losses, α_{int}, and reducing the efficiency of the device, η.

It has been proposed by many authors[1,4,5] that the intentional incorporation of coherent strain in the quantum wells of InP based devices would alter the band structure in such a way as to reduce the magnitude of all of the above problems, improving the performance of the InP based device. The next section describes the effect of coherent strain on the band structure.

6.2 The Effect Of Quantum Confinement and the Application of Coherent Strain on the Band Structure of InP Based Materials.

The discrete energy levels in k-space for a quantum well are given by the equation:

$$E(n,k_x,k_y) = E_n + \frac{\hbar^2}{2m_n^*}(k_x^2 + k_y^2) \qquad (6.2.1)$$

E_n – nth confined particle energy level in the z direction, this value varies inversely with m_n^*

m_n^* – effective mass for this level

A heavy hole will therefore have a lower confined energy level than a light hole and so the most favourable energy transition will be between the first confined electron level in the conduction band and the first confined heavy-hole level in the valence band, as is shown schematically in figure 6.4. Thus by simply providing quantum confinement, the degeneracy at the valence band maxima has been lifted. The magnitude by which the degeneracy has been lifted is still insufficient to overcome the effects mentioned in section 6.1.

The incorporation of coherent strain has two major effects on the band structure:

- a change in the volume of the unit cell gives rise to a change in the band gap, E_g. The magnitude is defined by the volumetric (hydrostatic) component of the strain (see section 4.1, equation 4.1.5)

$$\Delta E_g = a\varepsilon_{vol} \qquad (6.2.2)$$

ΔE_g – change in band gap
a – hydrostatic deformation potential
ε_{vol} – hydrostatic component of strain

- a change in the unit cell from cubic to tetragonal gives rise to a change in the heavy-hole and light-hole energies. The magnitude of this change is controlled by the strain energy, S, which is defined by the axial component of the strain discussed in section 4.1, equation 4.1.4.

$$S = -b\varepsilon_{ax} \qquad (6.2.3)$$

b – axial deformation potential
ε_{ax} – bi-axial component of strain

With the exception of the change in band gap the application of strain has little effect on the characteristics of the conduction band.

Let us now examine, in turn, the effect of strain on the band structure of both bulk materials and structures with quantum wells. Figure 6.5a schematically illustrates the effect of biaxial compression on the band structure of bulk $Ga_xIn_{1-x}As_yP_{1-y}$ [6]. It can be seen that the valence band becomes strongly anisotropic with crystallographic direction. In the growth direction (001), θ=0°, the hole mass is still heavy-hole like, but in the 'in-plane' directions, θ=90°, the hole-mass becomes relatively light. This anisotropy gives rise to a reduced effective density of states at the top of the valence band. The introduction of compressive strain also decreases the band gap of the material, since ε_{vol} is negative, and increases the energy difference between the top of the valence band and the spin-split-off band.

Figure 6.5b illustrates the effect of biaxial tension on the band structure of bulk $Ga_xIn_{1-x}As_yP_{1-y}$ [6]. In this case it can be seen that the anisotropy of the valence band structure is the reverse of the compressive case, with a heavy hole mass in the 'in-plane' direction, θ=90°, and a relatively light mass in the growth direction, θ=0°. The introduction of tensile strain increases the band gap of the

material since ε_{vol} is positive and again the energy difference between the top of the valence band and the spin-split-off band is increased as in the compressive case.

Before we start discussing the effects that these valence band changes may have on laser performance, it is worthwhile to perform a similar analysis of the effect of coherent strain on the band structure of quantum wells. Adams and O'Reilly[7] have performed a very useful theoretical prediction of exactly this on practical laser structures. Figure 6.6 depicts the valence band dispersions of four different $Ga_xIn_{1-x}As$ well structures; the combination of well strain (composition) and well width have been chosen for each case to give a band gap that will emit at the desirable 1.55μm wavelength; the dispersion is plotted as a function of the 'in-plane' wave-vectors. The salient points for each of the three cases of lattice-matched, compressive and tensile strained quantum wells are summarised in table 6.1.

Another point worth noting is the significant depression in the energy of the HH1 and LH1 bands in figures 6.6b and d respectively, away from the zone centre. Yablonivitch and Kane[5] reported that both IVBA and Auger recombination could be suppressed by reducing the density of off-zone-centre holes. They predicted that the effects observed in the above figures could give rise to a reduction in IVBA of a factor of e^{-3} and a reduction in Auger recombination of a factor of e^{-6} (where e in both cases is Euler's constant, 2.7182....).

With these theoretical predictions in mind, the next section discusses the possible advantages that strained MQW laser structures have over similar lattice matched structures.

Table 6.1 Key features of the valence band dispersion schematics shown in figure 6.6

Figure 6.6a lattice matched	• the degeneracy at the valence band maxima is lifted, reducing the DOS
Figure 6.6b compressive strain	• the degeneracy at the valence band maxima is lifted, more so than in the lattice matched case, further reducing the DOS. • the curvature is greater at the top of the valence band when compared to the lattice matched case and hence the hole mass is smaller, further reducing the DOS.

Figures 6.6c and 6.6d tensile strain	• moderate tensile strain eliminates any of the advantages that quantum confinement provided, pushing together the HH and LH bands and increasing the effective DOS. • at higher tensile strains the LH band will become the uppermost band. At sufficiently high strains the separation between the two will be sufficient to reduce the curvature of the light hole band and offer a reduction in hole mass when compared with lattice matched devices.

6.3 The Proposed Effects of Strain on MQW Laser Performance

In summary, the proposed effects of the application of coherent strain on InP MQW laser performance are:

- a reduction in threshold current density through a combination of a reduction in the density of states at the top of the valence band and a reduction in the non-radiative component of the threshold current through the suppression of Auger recombination;
- a reduction in the temperature sensitivity of the threshold current through the suppression of Auger recombination;
- a reduction in material loss, α, associated with the suppression of IVBA, leading to an improved quantum efficiency, η;
- improved high frequency performance through the optimisation of dg/dN caused by the increased similarity in the values of m_e and m_h;
- improved power output at a given injection current due to a combination of reduced threshold current density and increased efficiency.

Another important aspect of quantum confinement and 'valence band engineering' is the effect the modified band structure has on the state of polarisation of the photons emitted. Photons emitted by the spontaneous emission process can be polarised in any direction, whereas photons emitted by stimulated emission will be polarised in either the transverse electric (TE) or the transverse magnetic (TM) mode, i.e. one of two well defined, orthogonal, directions. Theoretical calculations[8] have shown that transitions between the conduction band and the HH1 valence sub-band result in lasing action occurring almost totally in the TE mode of polarisation. This should therefore be the case for unstrained, compressively strained and moderately tensile strained quantum well structures. The

same calculations also showed that for transitions between the conduction band and the LH1 valence sub-band, the lasing mode is polarised predominantly in the TM mode. This should therefore be obtained in quantum well structures with large amounts of tensile strain. The theoretical predictions for the relative transition strength of the TE and TM modes for E1-HH1 and E1-LH1 transitions are shown in figure 6.7.

6.4 Conclusions and General Aims

It is obvious from the above that the intentional incorporation of coherent strain into the grown lattice of quantum wells can offer a possible solution to many of the problems that plague the lattice matched InP quantum well laser structure. At the time this research commenced (October 1991), results on the successful growth and improved performance of InP-based strained MQW lasers were only beginning to appear in the open literature[9]. At that time there were two key thrusts in the device direction at BNR Europe. The first was the demonstration and production of a high power, high reliability, 1480nm optical pumping source for Er doped fibre amplifiers. The second was a transmitter for system applications beyond 2.5 GBit/s, i.e. a directly modulated laser or a cw laser with an external modulator. The following chapters follow the development of InP based strained layer epitaxy at BNR Europe, its application to these devices and the successes, or otherwise, of the results.

References

1 A.R. Adams, Electron Lett, 22, pp249-250, 1986.

2 M. Razeghi, The MOCVD Challenge, Adam Hilger, 1989.

3 G. P. Agrawal and N.K. Dutta, Long Wavelength Semiconductor Lasers, Van Nostrand Rheinhold, 1986.

4 E.P. O'Reilly, Semiconductor Sci. Tech., 4(1989), pp121-137.

5 E. Yablonovitch and E.O. Kane, J. Lightwave Tech., 6(8), 1988, p1292.

6. G. Jones, Ph.D. Thesis, The University of Surrey, 1994.

7 A.R. Adams and E.P. O'Reilly, Strained Quantum Well Lasers, in Semiconductor Lasers 1, Ed. E. Kapon, Academic Press Inc., 1998.

8. S.W. Corzine, Ran-Hong Van and L.A. Coldren, Quantum Well Lasers, Chapter 1, Academic Press Inc., 1993.

9. PJA Thijs, T van Dongen, Electron. Lett., 25, pp1735-1737, Dec. 1989.

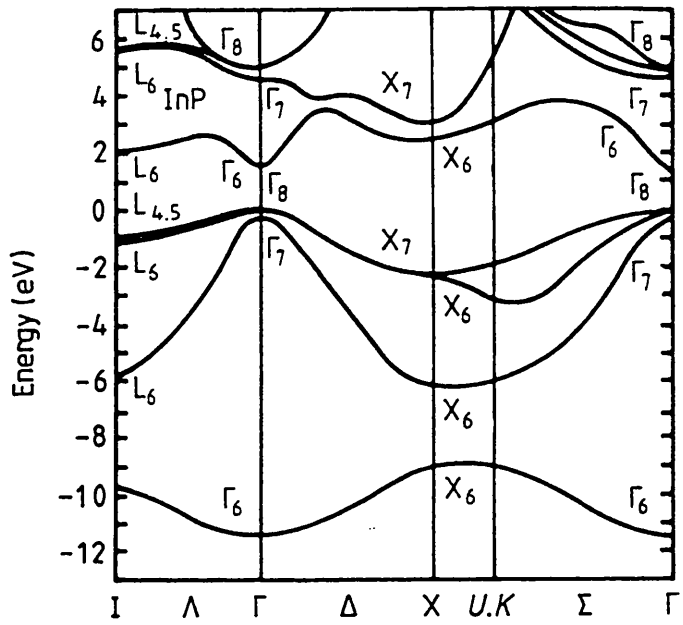

Figure 6.1 Band gap dispersion (energy vs. momentum) of InP. Note how the valence band is threefold at the Brillouin zone centre, the light and heavy hole bands are also degenerate at this point.[2]

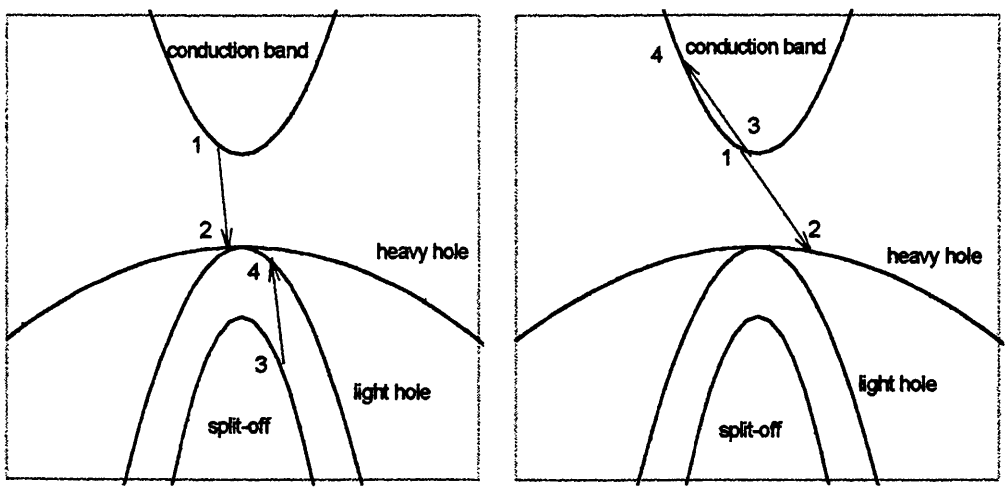

Figure 6.2 Two examples of band-to-band Auger recombination in bulk InP. In the first case an electron recombines with a heavy hole, this then excites an electron from the split-off band into a empty light hole state. The second case is similar but with an electron being excited to a higher conduction band state. Note in these cases momentum is conserved.[3]

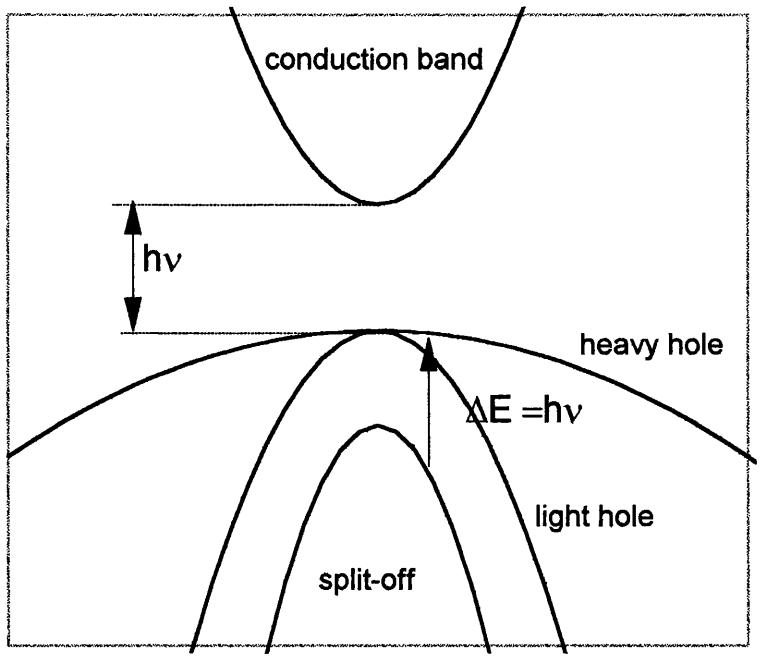

Figure 6.3 Schematic diagram illustrating inter-valence band absorption where an electron in the split off band is excited to a heavy hole state via the absorption of a photon.[3]

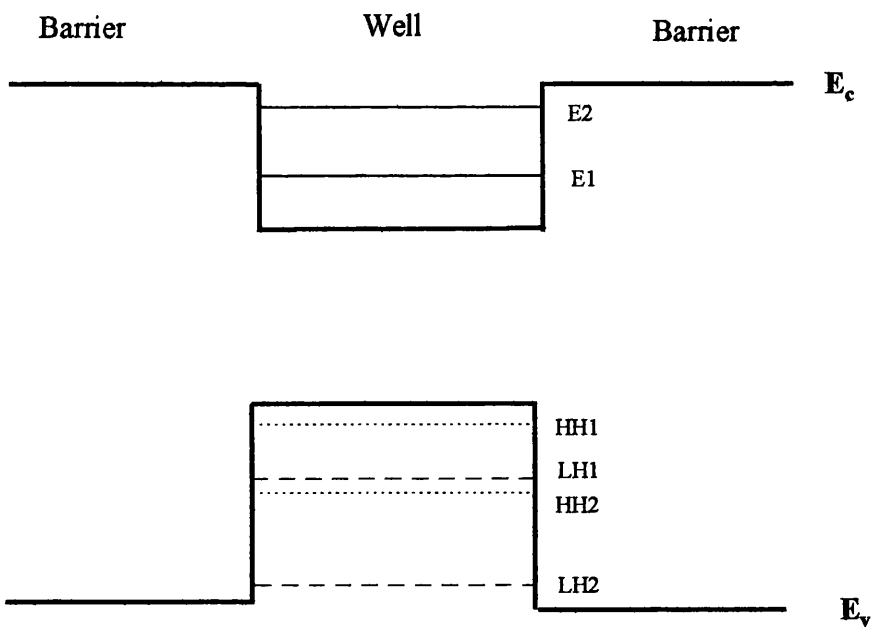

Figure 6.4 Schematic diagram of quantised electron, light and heavy hole levels in an all lattice matched InP-$Ga_xIn_{1-x}As_yP_{1-y}$ based quantum well structure (energy levels and band offsets not to scale).[4]

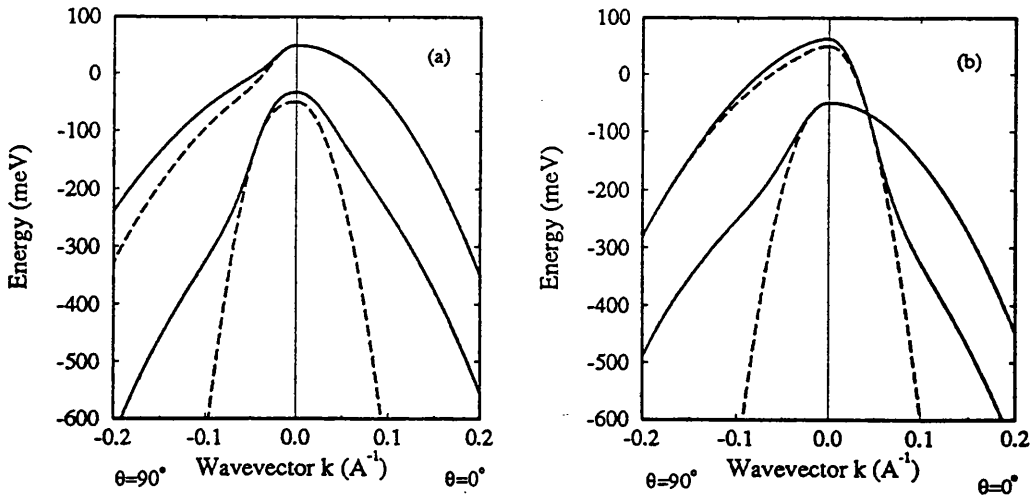

Figure 6.5 The effect of (a) compressive strain and (b) tensile strain on the band gap dispersion of InP based alloys.[6]

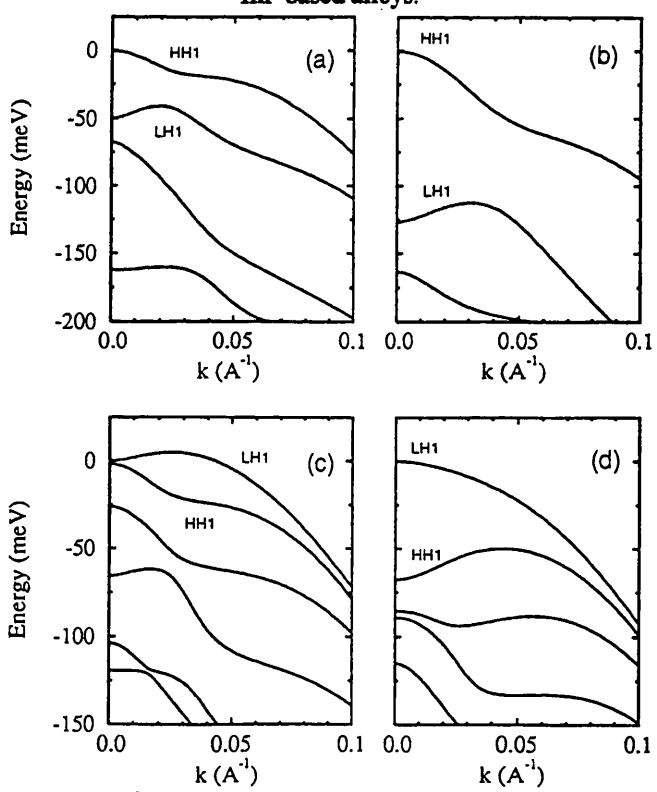

Figure 6.6 Valence band dispersions of $Ga_XIn_{1-X}As$ taken from Adams and O'Reilly[7] for (a) unstrained 50Å well, (b) 1.2% compressively strained, 30Å, (c) 0.4% tensile strained, 90Å and (d) 1.2% tensile strained, 110Å. All combinations of well width and strain are designed for 1.55μm operation.[7]

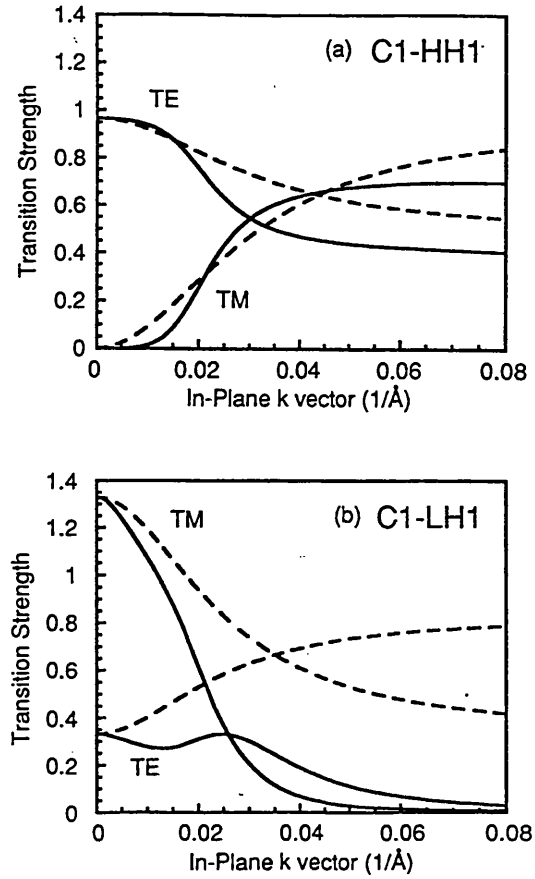

Figure 6.7 Relative transition strengths of the TE and TM modes for E1-HH1(C1-HH1) and E1-LH1(C1-LH1) transitions[8]. The dashed curves represent calculated relative strengths if parabolic bands are assumed.

Chapter 7

Strain Compensated GaInAsP/GaInAsP Multiple Quantum Well Structures For High Power and High Speed Laser Applications

7.1 Introduction

The use of compressive strain in the wells of semiconductor lasers was first applied to GaAs based devices[1] not, initially, to enhance performance, but to access the 0.88μm-1.1μm window that cannot be achieved with either lattice matched GaAs or InP based quantum well structures. As discussed earlier, it was proposed that the application of compressive strain in the wells of InP-based structures would help reduce the parasitic effects observed in long wavelength lasers, viz. Auger recombination, inter valence band absorption and poor temperature sensitivity of the threshold current. Thijs et al[2] first successfully demonstrated the compressively strained InP-based MQW laser at 1.55μm using 4x30Å $Ga_{0.2}In_{0.8}As$ wells (corresponding to 1.8% compressive strain) and lattice matched GaInAsP (λ=1.3μm) barriers. One of the potential shortcomings of such a device structure is that, after the growth of a given number of wells, a cumulative critical thickness-mismatch product may be exceeded and strain relieving crystallographic defects may be introduced into the structure, as discussed in section 4.3 and equation 4.3.2. A method of overcoming this limitation in InP-$Ga_xIn_{1-x}As_yP_{1-y}$ structures was suggested by Miller et al[3]. This involved growing the barrier material under tensile strain in such a way that the tensile barrier/compressive well structure had a net strain of zero, i.e.

$$L_w\varepsilon_w + L_b\varepsilon_b = 0 \qquad (7.1.1)$$

L_w, L_b - well and barrier thickness
$\varepsilon_w, \varepsilon_b$ - well and barrier strains

The technique potentially permits a large number of well/barrier cycles to be grown without incorporating any strain associated defects (assuming that the thickness of the individual wells and barriers is not greater than their critical layer thickness). Briggs et al[4] demonstrated a simple technique for achieving strain compensation that relied on using the same solid phase Ga:In ratio in the wells and barriers. The barrier composition chosen was $Ga_{0.31}In_{0.69}As_{0.62}P_{0.38}$ (λ=1.29μm, Δa/a=-0.17%). $Ga_{0.31}In_{0.69}As$ wells (Δa/a=1.1%) were grown using the same source gas flows as

the barrier material but with the phosphine switched to vent for the duration of the well growth. Strain compensation was achieved by setting the barrier thickness to be 1.1/0.17 (=6.4) times that of the wells. A 20 well strain compensated structure, with a well thickness of 21Å and a barrier thickness of 136Å, was demonstrated using this method. Low threshold current density broad area lasers were also produced.

There are, however, several disadvantages in using compressively strained InGaAs wells:

- there is only one degree of freedom, i.e. for a given wavelength of operation there is a unique combination of well strain (composition) and well thickness that can be used;
- the application of compressive strain to an InP based alloy reduces its bulk band gap, hence, to maintain a given emission wavelength, the structures grown under compressive strain must have their well widths reduced in proportion to the amount of strain incorporated. Such thin layers are generally more difficult to grow;
- thin wells give rise to reduced optical confinement factors, Γ, which in turn reduces the gain co-efficient of the device leading to, amongst other things, higher threshold current densities;
- thin InGaAs wells are very susceptible to the wavelength shift associated with their chemical interdiffusion with the GaInAsP barriers. This phenomenon occurs in post-epitaxy heat treatment e.g. in the growth of contact layers over a DFB grating and/or the growth of current blocking layers in buried heterostructure devices. At any well/barrier interface there usually exists a concentration gradient between the group III and group V elements. The group Vs' have the largest concentration gradient as the well group V sub-lattice is exclusively occupied by As atoms. In the case of MQW structures with GaInAsP barriers and GaInAs wells, phosphorus tends to diffuse from the barrier into the well, changing the composition in the region of interdiffusion and causing a departure from the square well model. This results in a reduction of the emission wavelength of the structure. The magnitude of the reduction has been shown to increase with thinner wells[5]. The extent of the interdiffusion has been shown to depend on the etch pit density of the substrate and, to a lesser extent, on the group V gas phase partial pressure during epitaxy[5].

As a result of the disadvantages caused by using compressively strained InGaAs wells, the use of compressively strained GaInAsP wells was proposed. Figure 7.1 shows the Ga-In-As-P parameter space, plotted with constant band-gap contours and lines of constant mismatch (lattice match and ± 1% strain). The shaded region is where emission at ≥1.55μm can be achieved by bulk layers, and it can be seen that, for a given compressive strain of 1%, there is a line of compositions varying from $Ga_{0.32}In_{0.68}As$ (λ=1.91μm) to $Ga_{0.18}In_{0.82}As_{0.7}P_{0.3}$ (λ=1.55μm) that would enable structures emitting at 1.55μm to be grown. Hence, for a given wavelength of application, the well

composition would depend on the desired well width and vice versa. This extra degree of freedom offers the device designer the ability to tailor the well strain and width, overcoming the inflexibility posed by using GaInAs wells. It is also anticipated that the use of quaternary wells will suppress the extent of the interdiffusion, as there is less of a concentration gradient at the well/barrier interface.

This chapter describes an investigation into the growth and assessment of a variety of strain compensated GaInAsP/GaInAsP MQW structures with different values of well and barrier mismatch. In addition to observations made on the structures grown, measurements on broad-area stripe lasers are also reported, as well as details of devices designed and assessed by colleagues using similarly grown structures. Wherever possible, device characteristics and trends will be discussed in relation to material issues. At the time of commencement of this work (December 1991) there were no reports in the open literature about the use of strain compensated GaInAsP/GaInAsP MQW growth. Most publications were related to GaInAsP/GaInAsP MQW's with compressively strained wells and lattice-matched barriers.[6,7,8]

7.2 The Growth and Assessment of GaInAsP/GaInAsP MQW Structures for High Power Applications

This section constitutes the first serious attempt to grow strain compensated quaternary well structures at BNR Europe and follows the learning procedure of that process. The MQW structures described here comprise barriers with tensile strains of between 0.2% and 0.3% and wells with compressive strains of between 0.6% and 1%. The first series of experiments was an initial 'look-see' to determine if there were any extreme difficulties in growing such structures. The second series built on the successes of the first generation combined with a more thorough investigation into the optimisation and limitations of the growth process, together with a detailed analysis of the performance of devices made from these structures. The third, and final, series addressed the issues of reproducibility of such structures in a production environment. Devices fabricated from these structures are also reported.

7.2.1 First Generation of GaInAsP/GaInAsP Structures

7.2.1.1 Growth and Assessment

The strategy for the growth of the first generation of strain compensated GaInAsP MQW structures was based on the approach used by Briggs et al[4] for strain compensated ternary well structures, i.e. the use of a constant Ga:In ratio in the wells and barriers. This is achieved by using the same TMIn and TMGa gas flows to grow the well and barrier material and, as a result, gives a constant growth

rate in the wells and barriers. The main advantage of this technique is that strain compensation can be easily achieved by setting the ratio of well to barrier growth time equal to the reciprocal of the ratio of the well to barrier mismatch. The disadvantage is that it constrains the choice of well and barrier compositions to a fixed Ga:In ratio. The value of the Ga:In ratio used in the MQW structure must be such that it enables the barrier material to have a given tensile mismatch, for some As:P ratio, and for the compressive well to have a composition that enables the MQW structure to emit at around 1.5μm. The As:P ratio in the well must be chosen so that 1.55μm emission can be achieved using a well width of not less than 50Å. The tensile barrier composition was determined from the growth of a calibration layer using the procedure described in Chapter 3. The growth rate of the well and barrier material was also determined from measurements of the thickness of this calibration layer. A series of MQW structures using this tensile barrier material were grown, in which the well and barrier thicknesses were chosen to be approximately 50Å and 250Å respectively. The AsH_3 and PH_3 flows used to grow the well material were varied until the MQW structure had a net strain close to zero as measured by HRXRD. The full layer structure of the first sample with good strain compensation is shown in figure 7.2. The structure consisted of a 1μm n-type InP buffer layer doped to $5x10^{17}cm^{-3}$ with Si, followed by the lower waveguide layer which consisted of 0.06μm of lattice matched GaInAsP (λ=1.17μm). The first and last barriers of the four well strain compensated active region are half the thickness of the others in order to preserve the strain symmetry of the overall structure. A 0.2μm lattice matched GaInAsP (λ=1.17μm) upper waveguide layer is deposited on the MQW region and the whole structure is capped with 0.1μm of undoped InP.

The HRXRD rocking curve of the 4-well strain compensated structure is shown in figure 7.3 to consist of a series of well-defined and intense satellite peaks. The zeroeth order peak is thought to lie under the substrate peak; its mismatch is determined by taking the average of the ±1 satellite peaks. The periodicity of the MQW structure (i.e. well thickness + barrier thickness) is determined from the separation of the satellite peaks as described in section 3.3. The lattice matched, λ=1.17μm, waveguide layers are thought to account for the peak at -328 ppm. The MQW periodicity gives a more precise value for the growth rate of the wells and barriers. As the growth rate is constant, the well and barrier thicknesses can be derived from the MQW period, as ratio of well to barrier growth times is known. The structure exhibited room temperature PL at 1.423μm. Interference contrast optical microscopy showed that the grown wafer surface had a specular morphology. The structure was also assessed by cleaved edge TEM, and a micrograph (x 800,000 magnification) is shown in figure 7.4. It is clear that all the interfaces are abrupt and the well/barrier thicknesses are consistent with those inferred from HRXRD and predicted by the ratio of growth times. This supports the assumption that a constant gas phase TMGa:TMIn ratio gives constant solid phase Ga:In ratio in the wells and barriers. Details of the growth conditions, assessment results on the barrier calibration

layer and the MQW structure are given in the table 7.1 below, along with the inferred compositions of the well and barrier material.

The simulation of an MQW structure (using the program of Silver discussed in section 3.4) containing the above compositions, with well thickness =51.5Å and barrier thickness = 256Å, gave λ_{PL} = 1.423 μm and $(\Delta a/a)_{n=0}$= -550ppm, a good fit to that measured experimentally .

Table 7.1 - Summary of growth, assessment and composition details of first generation samples.

Growth conditions	Well V/III ratio	122
	Barrier V/III ratio	1745
	Well/barrier growth rate	137 Å/min
	Ratio well:barrier thicknesses	1:4.97
Assessment results	Barrier material	(Δ a/a)= -0.21%, λ =1.2μm
	4 well MQW structure	$(\Delta a/a)_{n=0}$=-460ppm,λ_{PL}=1.423μm
Inferred Compositions	Barrier $Ga_0 \cdot 27In_0 \cdot 73As_0 \cdot 53P_0 \cdot 47$	(Δ a/a)= -0.18%, λ =1.245 μm
	Well $Ga_0 \cdot 27In_0 \cdot 73As_0 \cdot 76P_0 \cdot 24$	(Δ a/a) = 0.57%, λ = 1.535 μm

7.2.1.2 Broad-area Device Performance

To assess the suitability of this structure as a laser, it was overgrown with 1.5μm of p-InP and 0.25 μm of p-GaInAs and processed into lasers with 50μm oxide defined stripes in the manner described in section 5.4. The p doping was increased half way through the growth of the InP from approximately $5x10^{17}cm^{-3}$ to $10^{18}cm^{-3}$. Bars of devices were cleaved into different lengths and the threshold current density assessed, with at least six devices of each length being measured to give a mean value. Figure 7.5 shows a plot of the logarithm of the threshold current density against the reciprocal cavity length, which follows the relationship;

$$\ln\left(\frac{J_{th}}{369}\right) = \frac{1.24}{4L} \qquad (7.2.1)$$

this is of the form

$$\ln\left(\frac{J_{th}}{J_{\infty}}\right) = \frac{k}{NL} \qquad (7.2.2)$$

J_{th} - threshold current density
J_{∞} - infinite cavity length threshold current density
N - number of wells
L - cavity length

The parameter k is known to depend on the optical confinement and the gain per well (see section 5.3). If we compare this result with that reported by Briggs et al[4] for strain compensated compressive ternary wells, we note that the J_{∞} of 369 A/cm^2 is consistent (333 A/cm^2 for 3 wells and 500 A/cm^2 for 6 wells). More important, however, is the decrease in k: 1.28 compared to 1.5, which can either be due to increased gain per well or optical confinement factor. As the use of a quaternary well affords a wider well, it is more probably the latter, because the well width is increased to 51Å compared to 21Å. It should be noted that the reduction in k does not scale exactly with the perceived increase in Γ_W, i.e. k should be decreased by a factor of 2.5.

In spite of the success of these results, many features of this work remain non-optimum. The wavelength of operation at 1.423 μm was not practically useful; operation at either 1480nm for pumping Er doped fibre amplifiers or 1550nm for transmission are the main wavelengths of interest. It was also felt to be desirable to incorporate more compressive strain into the wells (e.g. 1%), as many of the reports of improved performance strained InGaAs MQW lasers used values of compressive strain between 1-2%[4,9,10,11]. Questions relating to the growth also remained unanswered. Does strain compensation provide a means of growing as many well/barrier cycles as one would wish, or is there some limit to this process? These issues were addressed in the second generation of these strain compensated structures.

7.2.2 Second Generation of GaInAsP/GaInAsP MQW Structures

7.2.2.1 Growth and Assessment

The well and barrier material compositions were determined in the same way as the first generation. This time, it was deemed desirable to have more compressive strain in the wells, for the reasons mentioned above, and also more tensile strain in the barriers, so that strain compensation could be achieved with thinner barriers than before. Otherwise the MQW structures were similar to those grown in section 7.2.1. Table 7.2 summarises the growth conditions, the calibration results and the inferred compositions.

Simulation of an MQW structure containing the inferred compositions from table 7.2 with a well width of 48.5Å and barrier width of 170Å gave λ_{PL} = 1.496 μm and $(\Delta a/a)_{n=0}$ = -100ppm, a good fit with the experimentally observed results. These compositions were used to grow all the structures described in this section.

Table 7.2 - Summary of growth, assessment and composition details of second generation samples.

Growth conditions	Well V/III ratio	136
	Barrier V/III ratio	3727
	Well/barrier growth rate	126 Å/min
	Ratio well:barrierthicknesses	1:3.5
Assessment results	Barrier material	$(\Delta a/a) = -0.29\%$, $\lambda = 1.22$ μm
	Typical MQW structure	$(\Delta a/a)_{n=0}$=-72ppm, $\lambda_{PL} = 1.501$ μm
Inferred compositions	Barrier $Ga_{0.27}In_{0.73}As_{0.51}P_{0.49}$	$(\Delta a/a) = -0.25\%$, $\lambda = 1.222$ μm
	Well $Ga_{0.27}In_{0.73}As_{0.84}P_{0.16}$	$(\Delta a/a) = 0.83\%$, $\lambda = 1.659$ μm

The performance of MQW based devices can be affected by any lack of abruptness of the hetero-interfaces. In common with many modern MOVPE reactors, the 'E" reactor at BNR Europe incorporates dynamic pressure balancing between the vent and run lines. In spite of this, rapid fluctuations in the reactor pressure can occur when changing from one gas mixture to the next at the heterojunction. It is thought that these pressure transients can compromise interface quality, however their effect can be minimised by switching a counter-acting pulse of ballast hydrogen simultaneously with the switch between alloy mixtures. To optimise these switching conditions, variable thickness quantum well stacks, with each quantum well grown under different hydrogen ballasting conditions, were grown and assessed by low temperature PL. The FWHM of the emission from each quantum well can give some indication of the interface quality. Such a structure normally requires relatively thick barrier layers to isolate each quantum well, so, in order not to incur any critical thickness problems with the barrier material, a lattice matched alloy with the same Ga:In ratio as the wells and barriers described above was used. The composition of this alloy was $Ga_{0.27}In_{0.73}As_{0.58}P_{0.42}$. Figure 7.6a illustrates the structure that was grown. The 'ideal' condition is that which produced the smallest switching transient as illustrated in the reactor pressure trace shown in figure 7.6b. The low temperature (10K) PL spectrum of this structure is shown in figure 7.7; emission from the first well cannot be seen. The well with the narrowest FWHM of 3.5 meV is the one that was switched with 2 litres/min less hydrogen than the 'ideal' case, i.e. the well material was grown with 2 litres/min less H_2 than the barrier material. This switching condition was used as standard in all further structures.

In order to investigate the effect of increasing the number of wells on the structural quality, a series of samples with 1, 2, 4, 6, 8, 12, 16 and 32 wells was grown. These samples had the added advantage that they could be used for a rigorous analysis of the effect of the number of wells and cavity length on the threshold current density of broad area (50 μm stripes) lasers. The series of

samples was identical except for the thicknesses of the lattice matched, λ=1.17 μm, waveguide layers, which were reduced in proportion to the increasing number of wells.

Deterioration in the surface morphology of structures with more than 8 wells was observed. Figure 7.8 shows x 500 interference contrast micrographs of the 8,12,16 and 32 well samples, the other samples being specular. The surface appears to 'ripple' when the growth of more than 8 wells is attempted, and the density of the 'rippling' increases as more wells are deposited. The 'rippling' seems to occur in a very well defined direction in the 12 and 16 well samples, occurring predominantly in the $[01\bar{1}]$ crystallographic direction. The density of defects in the 32 well sample was too high to identify any particular orientation. The morphologically inferior samples varied in appearance to the naked eye; with the 12 well sample still having a 'shiny' finish whereas the 32 well sample had a matt finish. The HRXRD rocking curves also degraded in quality with higher number of wells, figure 7.9 shows the evolution of the rocking curves for 8,12,16 and 32 well samples. The 8 well sample behaved generally as expected, with well-defined satellite peaks, but the 12 well sample varied in quality across the wafer. At the wafer centre, the satellite peaks were more diffuse than at the wafer edge (opposite the minor flat), indicating that the 12 well sample is at the onset of the mechanism causing the structural degradation. The 16 and 32 well samples both suffered from severe broadening of the satellite peaks.

High density room temperature PL mapping was also used to assess these samples. PL intensity mapping is often used to assess the 'quality' of epitaxial layers e.g. many growth and substrate related defects can be observed by high resolution intensity mapping or by directly imaging the PL[12]. Figure 7.10 shows the variation in PL intensity across the full 2" wafer for the structures with 8, 12, 16 and 32 wells. From previous experience of mapping lattice-matched alloys and quantum well structures, one can say that the intensity distribution for both the 8 and 12 well samples is normal. There is no indication on the intensity map of the 12 well sample that a significant difference in structural quality exists between the wafer centre and the edge opposite the minor flat, i.e. the right hand side of the wafer as viewed in figure 7.10, as observed by HRXRD. This would suggest that HRXRD is more sensitive than room temperature PL at assessing this structural degradation. The 16 well sample, however, shows a marked variation in intensity across the wafer. In fact the intensity distribution corresponded very well with the appearance of the wafer surface to the naked eye. Figure 7.11 shows a macroscopic image of the 16 well sample. The dark crescent extending from the top of the wafer clockwise to the right hand side had the best (most shiny) morphology and corresponding high PL intensity, whereas the rest of the wafer had a dull, matt like appearance with correspondingly low PL intensity. The 32 well sample in figure 7.10 had a uniformly poor intensity.

Examination of the room temperature PL image showed that the sample with 16 wells had many dark spots. An example of one area of the wafer, namely the centre, is shown in figure 7.12. The spots are most probably due to non-radiative recombination, however they are unlike any defect observed hitherto in the assessment of InP-based MQW structures (except for the spots that occur due to poor wafer cleaning prior to epitaxy). The defects could also be perceived in the 32 well structure, but the intensity was so weak that it was difficult to take a copy of the image with a meaningful contrast.

In summary, the following has been observed when growing strain compensated MQW structures with increasing number of 50Å, $Ga_{0.27}In_{0.73}As_{0.84}P_{0.16}$ wells:

- the surface morphology degrades between 8x50Å and 12x50Å wells;
- the HRXRD rocking curve satellite peaks become more diffuse when we grow 12 or more such wells;
- the PL intensity begins to drop at and beyond the growth of 16 wells;
- the PL wavelength does not vary between samples, beyond the normal run-to-run variations;
- dark spots are observed in the image of samples with 16 wells or more.

One of the consequences of diffuse satellite peaks in the HRXRD rocking curve may be the variation of well and barrier thicknesses across the area sampled by the X-ray spot (approximately 3 mm^2). A possible explanation is poor switching of the gas mixtures between wells and barriers, but this does not seem likely as a 10K PL FWHM of 3.5 meV was demonstrated for a structure using identical well material and growth procedures. It also does not account for the deterioration of the growth quality as we increased the number of wells. Relaxation of the lattice through the generation of dislocations, as observed in bulk material that has exceeded a given thickness, was not observed in these samples. However the dark spots observed in the PL image of the 16 well sample could represent an alternative type of defect associated with the structural degradation of these samples. To help clarify some of these issues, the samples were assessed further by TEM.

Figure 7.13 shows a combination of cleaved wedge and cross sectional TEM micrographs of the structures with 8,12 and 32 wells. The 8 well sample, figure 7.13a, is well behaved with planar well and barrier interfaces, confirming the observations made by other assessment methods. In the twelve well sample, figure 7.13b, the well and barriers in the upper third of the quantum well stack are seen to fluctuate in thickness. It would appear that when the well becomes thicker the next deposited barrier layer becomes thinner and vice versa. The deleterious growth effects are even more pronounced in the 32 well sample shown in figure 7.13c. It shows that the growth no longer remains planar but instead the wells and barriers develop a periodic undulation in thickness which

occurs in anti-phase. The amplitude of this undulation increases with each successive layer and, when the amplitude is greater than the thickness of the individual layer, defects, in the form of dislocations, are introduced into the stack. The 32 well sample also shows why a rippled surface morphology is observed; the thickness undulations that arise in the wells and barriers are not planarised by the deposition of the lattice matched layers deposited on top of the quantum well stack. The 32 well sample was also examined by TEM under a diffraction condition (g=220) that is known to delineate variations in strain as variations in the contrast of the image; figure 7.13d shows an image of such a measurement. It is clear that there exists a periodic contrast variation that has a similar periodicity to the thickness modulations. This would therefore suggest the existence of a lateral modulation in the strain directly associated with the modulation in the thickness. These observations also help explain the trends observed in the HRXRD measurements. The X-ray spot samples greater thickness undulations in the structures with larger numbers of wells hence increasing the broadening of the satellite peaks. It is interesting to note that the MQW periodicity remained approximately constant with different numbers of wells, suggesting that the net amount of well and barrier material deposited remained approximately the same.

It was still desirable, in spite of the growth problems observed in structures with more than 8 wells, to evaluate the broad area laser performance and compare them with the first generation of devices, as well as with strained ternary devices and lattice matched devices made previously at BNR Europe.

7.2.2.2 Broad-area and Ridge Structure Device Results

The 2, 4, 6, 8 and 12 well structures were overgrown with p-type InP and p-type GaInAs and processed into broad area (50μm stripes) lasers in a similar way to the first generation of devices. The devices were then cleaved into a variety of lengths, between 200μm and 2mm, and the threshold current density was measured at 20°C. Six devices of each combination of cavity length and well number were measured and the mean threshold current density calculated. Figure 7.14 shows the plot of the logarithm of threshold current density against reciprocal cavity length for each of the 2,4,6,8 and 12 well structures. This logarithmic relationship is of the form described by equation 7.2.2 and table 7.3 below lists the values of J_{∞} and k for each structure.

The value of k measured for the 2, 4, 6 and 8 well structures was similar to the value determined for the 4 well device in the first generation, but there was a significant increase in J_{∞} of the 4 well device in the second generation. The 12 well device had a very high threshold current density and a larger k value. The latter was probably due to the thickness undulations in the upper wells perturbing the optical confinement factor and the well gain. It may also indicate that not all of the

12 wells were participating in the lasing action, since if we replace the number of wells in the denominator of equation 5.3.4 by a smaller number we can achieve a similar value of k.

Table 7.3 - Values of J_∞ and k against well number for the second generation structures.

Number of wells	J_∞(A/cm^2)	k(cm^{-1})
2	429	1.35
4	534	1.28
6	582	1.37
8	670	1.43
12	1009	2.23

As discussed in section 5.3 we can attempt to fit the gain co-efficient per well at threshold to the threshold current density per well for each of the structures by choosing a suitable value of α, the cavity absorption coefficient. Figure 7.15 shows such a plot fitted to α = 22 cm^{-1}, the fit being described by the equation

$$\Gamma_w G_w = \frac{g_{th}}{N} = 9.06\left(1+\ln\left(\frac{J_w}{176}\right)\right) \qquad (7.2.3)$$

Table 7.4 below compares these results of the M^{c}Ilroy analysis with other MQW structures with different well strain conditions

Table 7.4 - Comparison of the second generation M^{c}Ilroy analysis results with other reported MQW structures with different well strain condition

Structure	k (cm^{-1})	$\Gamma_W G_0$ (cm^{-1})	J_0 (Acm^{-2})	α(cm^{-1})
Greene et al[13] (lattice matched InGaAs wells)	1.74	7.1	228	11
Briggs et al[4] (1% compressive InGaAs wells)	1.5	8.1	179	14
First generation	1.24	-	-	-
Second generation	1.28	9.1	176	22

The increased value of $\Gamma_W G_0$ represents an improvement in performance, it being higher in these devices than either the lattice matched or compressively strained ternary cases. The value of J_0 is

not significantly different from that using 1% strained ternary wells. The high value of cavity loss, 22 cm^{-1}, explains why the threshold current densities of these samples are higher than observed in the first generation. The high value of α in these samples may be accounted for by a higher level of Zn in the overgrown p type InP adjacent to the upper waveguide layer. In the second generation samples, the carrier concentration in the p type InP was measured by electrochemical CV profiling to be 2 - 2.3 x 10^{18} cm^{-3}, whereas in the first generation sample the corresponding carrier concentration was 6.9 x 10^{17} cm^{-3}. The higher Zn level overgrowth can lead to diffusion of Zn into the active region. Increased p doping in the active region is known to increase the threshold current density[14], by causing increased non-radiative recombination and increased optical absorption.

The samples were also processed into Fabry Perot ridge lasers. Two cavity configurations were assessed: 400μm length without facet coatings and 750μm length with HR and LR TiO_2/SiO_2 coatings. All devices had 2μm ridge width and measurements were performed under CW operation at 20°C. Figure 7.16 shows the variation in the threshold current with the number of wells for both these device lengths, the trends being consistent with the measurements on the broad area devices. The effect of the number of wells on the output power, with both cavity length and bias as a parameter, is shown in figure 7.17. Six well structures are observed to give the maximum output power.

A comparison of the light-current characteristics (L-I) of lattice matched, compressively strained ternary and compressively strained quaternary well devices, is shown in figure 7.18. These three devices had similar geometry, 400μm long and 2μm ridge widths, no facet coatings and containing 4 quantum wells. The quaternary well device has both the lowest threshold current density and the highest output power at any given bias current. However the onset of saturation of the output power seems to occur at similar bias currents in all three samples. The best result achieved with a facet coated device, using a detection numerical aperture (NA) of 0.5, is shown in figure 7.19. The six well, 750 μm long, 2μm ridge width device with HR/LR coatings, exhibited a maximum output power of 129 mW at a bias current of 700 mA. It is often very difficult to compare such numbers with those presented in the open literature. For example, the measurement conditions are often not discussed in detail and many authors do not list the NA of their detection process. In addition, some measure the output from both facets and report the sum as the output power, while others often quote measurements from devices with very long cavities to achieve the highest output powers and the lowest threshold current densities. Such devices tend to be unrepresentative of what would be used in practice, because the operating current is so high and the device slope efficiency is low.

Table 7.5 below attempts to compare the result reported here with similar devices reported in the literature.

Table 7.5 Comparison of the results reported here with similar devices reported in the literature.

Report	Type of structure	P(mW)	I_{th}(mA)	Length (μm)
Thijs[15]	1.2% compressive InGaAs wells Buried heterostructure	325 @ 1400mA	~33	1000
Coblentz[6]	Compressive InGaAsP Wells Buried heterostructure	206 @ 900 mA	-	890
This work	6x0.85% compressive InGaAsP wells Ridge structure	129 @ 700mA	25	750

It would appear that buried heterostructure devices are more efficient than ridge structures in delivering more power for a given current, suggesting that buried heterostructures provide improved electrical and optical confinement. However, one possible disadvantage with buried heterostructures is the potential reliability hazard when the exposed sidewalls of the strained quantum well active region are overgrown with the current blocking layers. This is one of the main sources of degradation in lattice matched buried heterostructure devices[16] and one could postulate that the situation would only get worse when a mismatched interface was involved. On the other hand, the ridge device, in which the quantum well region remains buried and unexposed to any further growth and processing steps, has a well proven reliability track record.

Overstress life testing was performed on a number of 4-well devices. Details of the percentage change in threshold current with time is shown in figure 7.20. The devices were subject to an initial 'burn-in' at 240 mA to screen out devices prone to rapid degradation. After burn-in, the devices showed a mean change in threshold current density of 9.9%. The devices were then subject to further ageing at a bias of 213 mA and a temperature of 125°C. This process can assist in the prediction of device performance under normal, i.e. less severe, temperature and biasing conditions over a longer period of time. The devices showed a mean change in threshold current density of +3.6% over 3700 hours, these results being indistinguishable from lattice matched quantum well devices. (Note the devices are aged at 125°C, the threshold current density is measured periodically at 50°C).

7.2.2.3 Summary

The structures here have been shown to deteriorate when we grow more than 8x50Å wells. However devices made with less than 12 wells exhibit lower threshold currents and high output powers when compared to similar lattice matched and strained ternary well devices. The occurrence of thickness modulations in the upper wells and barriers of structures with larger numbers of wells may suggest that a latent device reliability hazard exists in structures with fewer wells. Long term, accelerated ageing of the potential degradation processes has, however, shown this not to be the case.

Such characteristics make these devices suitable for application as optical pumping sources for Erbium doped fibre amplifiers. The next section discusses the issues relating to the growth of 4-well structures as part of a 1480 nm pump laser production line.

7.2.3 Production Growth - the Third Generation of GaInAsP/GaInAsP MQW Structures

This section briefly describes the attempts to grow a 4 well strain compensated laser structure, similar to that discussed in the previous section, repeatedly on a pilot production scale, bearing issues like reproducibility and uniformity in mind. All the growths performed so far were with a single 2" wafer in the reactor cell. MOVPE, like many other CVD techniques, tends to suffer from a loading effect, i.e. when you attempt to grow on more or less substrate area, the conditions in which a given alloy composition is obtained change. The 'E' reactor has the capacity to grow 2x2" wafers simultaneously, so another wafer was added to the susceptor upstream of the conventional position which is now referred to as downstream. The well and barrier alloy compositions were now determined with 2x2" wafers and the conditions were also adjusted to give slightly more compressive strain in the wells. Table 7.6 below summarises the growth conditions, assessment results and inferred compositions for these structures.

Table 7.6 Summary of growth, assessment and composition details of third generation samples.

Growth conditions	Well V/III ratio	279
	Barrier V/III ratio	1232
	Well/barrier growth rate	157 Å/min
	Ratio well: barrier thickness	1:4.2
Assessment results	Barrier material	$\Delta a/a$)=-0.27%, λ =1.201μm
	4 well structure	$\Delta a/a)_{n=0}$=-226 ppm, λ_{PL} =1.520μm
Inferred compositions	Barrier $Ga_{0.26}In_{0.74}As_{0.48}P_{0.52}$	$\Delta a/a$) = -0.28%, λ =1.197 μm
	Well $Ga_{0.26}In_{0.74}As_{0.87}P_{0.13}$	$\Delta a/a$) = 1%, λ =1.724 μm

Simulation of an MQW structure, containing the above well and barrier compositions, and with 45 Å wells and 189 Å barriers gave an emission wavelength of 1.522μm and $(\Delta a/a)_{n=0}$=-340 ppm, a good fit with the experimental data. The 4-well structures had similar characterisation results as those grown previously.

Once these alloy compositions had been established, the laser structure was grown over 2x2" wafers simultaneously. Figure 7.21 shows the room temperature PL wavelength and intensity maps of the two wafers, termed upstream and downstream to reflect their position on the susceptor with respect to the direction of gas flow. The detailed wafer statistics are given in table 7.7 below.

Table 7.7 Two wafer PL uniformity statistics from a single MOVPE growth run.

Number of points = 238 per wafer.				
	Upstream wafer		**Downstream wafer**	
	Mean	*Standard deviation*	*Mean*	*Standard deviation*
Peak wavelength (nm)	1481.5	5.4	1480.5	6.4
Intensity (a.u.)	0.096	0.0078	0.076	0.0086
FWHM (meV)	41.5	1.2	41.4	1.5

In this growth run, all of the area over both the 2" wafers was of a suitable wavelength for processing into ridge lasers for use as 1480nm pumps. It is difficult to compare wavelength uniformities with data presented in the literature as no two mapping matrices seem to be the same. For example fewer or more points may be measured (the central limit theorem of data sampling says that the error in the estimation of the population standard deviation is reduced by the number of points sampled) and sometimes the outer periphery, where most non-uniformity occurs, is omitted from the map. However in the author's experience of the growth of other InP-based structures over one or two 2" wafers, the results presented here are state-of-the-art. Another key issue of production growth is the run-to-run reproducibility in assessment results, especially the PL wavelength. Figure 7.22 illustrates the mean variation in peak PL wavelength over 33 wafers which were grown in as near an identical manner as possible. It shows that the standard deviation in wavelength is only 15.8 nm. Such reproducibility helps improve the overall laser fabrication process yield and also helps reduce the end component cost. The excellent reproducibility results are thought to be due to precise control of the metal-organic reagent supply to the gas phase through the use of ultra-sonic reagent monitoring. Well-defined growth procedures, such as the use of clean reactor furniture for every growth run, are also thought to assist in achieving good run-to-run repeatability.

7.3 Growth of GaInAsP/GaInAsP MQW Structures for High Speed Laser Applications

7.3.1 Introduction

The direct modulation of semiconductor lasers is governed by a pair of rate equations which describe the photon and electronic carrier densities inside the laser structure[16]:

$$\frac{dN}{dt} = \frac{J}{qd} - \frac{N}{\tau_s} - vg(N)S \tag{7.3.1}$$

$$\frac{dS}{dt} = \Gamma vg(N)S - \frac{S}{\tau_p} + \beta R_{sp} \tag{7.3.2}$$

N - carrier density
S - photon density
G - optical confinement factor
J - pumping current density
d - active region thickness
τ_s – recombination lifetime of carriers
t_p – photon lifetime
$g(N)$ - optical gain, function of N
v - group velocity
q - electronic charge
β - fraction of spontaneous emission entering lasing mode
R_{sp} – spontaneous emission rate.

When a semiconductor laser is turned on, from a sub-threshold condition to one above, a relatively long time (~ several nanoseconds) elapses before steady state output conditions are reached. In this transient regime, the power distribution in the various longitudinal modes varies periodically as the laser goes through relaxation oscillations. During these relaxation oscillations the energy stored in the laser oscillates between the electron and photon populations. An understanding of the frequency of the relaxation oscillations is particularly important when the laser current is modulated in the GHz frequency range, i.e. optical telecommunication transmission rates, as InP-based lasers are reported to have relaxation oscillations frequencies in the GHz range[16]. It can be shown[16] via a small signal analysis of equations 7.3.1 and 7.3.2, that the frequency of the relaxation oscillations is given by:

$$f_r = \frac{1}{2\pi}\sqrt{GG_N S} \tag{7.3.3}$$

f_r – relaxation oscillation frequency
G - steady state gain
G_N – gain derivative
S - photon density

It is also known that,

$$S = \frac{(I - I_{th})}{qG} \tag{7.3.4}$$

I - laser current in 'on' condition

I_{th} - threshold current

and,

$$G_N = \frac{\Gamma v_g \, dg/dn}{Wt} \tag{7.3.5}$$

dg/dn - differential gain

Wt - active layer area

The difference between the operating current and the threshold, $I-I_{th}$, can be expressed through equation 5.2.8 as

$$(I - I_{th}) = \left(\frac{\alpha_i}{\ln(1/R)} + \frac{1}{L} \right) \frac{Pq}{h\nu} \tag{7.3.6}$$

Therefore equation 7.3.3 can be expressed as

$$f_r = \frac{1}{2\pi} \sqrt{P \frac{dg}{dn} \frac{2 v_g \Gamma}{h \nu W t} \left(\frac{\alpha_i}{\ln(1/R)} + \frac{1}{L} \right)} \tag{7.3.7}$$

The factor of 2 in the numerator of the above expression arises as we consider the output of one facet only during the measurement of f_r.

The relaxation oscillation frequency can be measured experimentally by evaluating the small-signal frequency response of a modulated laser. The frequency response of the laser output is known to peak (resonate) at f_r[16]. Such a measurement can be performed through the use of a commercially available network analyser used in conjunction with a calibrated photodetector which is known to have flat frequency response over the measured frequencies of interest. The network analyser provides a frequency swept modulation current to drive the laser, it also performs the analysis of laser output as a function of modulation frequency.

In common with well established RF measurement practices, it is necessary to match the impedance of the laser chip to that of the modulation source to avoid RF reflections which will deteriorate the measurement. Laser chips are normally evaluated in device packages that have known good RF

performance. This typically involves the use of a microstrip and a matching resistor in series with the laser to bring the total impedance of the device under test equal to that of the RF source, 50Ω.

7.3.2 Compressively Strained GaInAsP/GaInAsP MQW Lasers

It has been proposed[17] and reported[18] that the incorporation of compressive strain in the wells of MQW devices improves the maximum speed at which a laser can be directly modulated. This is, as discussed in section 6.1, a result of improved differential gain caused by decreased hole effective mass. Up to this point, all laser devices produced at BNR Europe for such 'high speed' applications had used lattice-matched InGaAs quantum wells; in order to take advantage of the reported benefits, the structure illustrated in figure 7.23 was proposed. The well and barrier compositions were identical to those grown in section 7.2.3. Exact strain compensation was not possible in this structure as constraints were placed on the barrier width by carrier dynamic considerations (a thicker barrier would compromise the speed of the device), however partial strain compensation was provided.

The HRXRD rocking curve of this sample, as shown in figure 7.24, highlights well defined satellite peaks. This observation, together with a specular surface morphology, indicated that no thickness modulated quantum well growth had occurred. This was an initial concern as a total of 6x75Åx1% (=450Å.%) of well material was grown, which lies between the known limits of acceptable growth of 8x50Åx0.83% (=332Å.%) and 12x50Åx0.83% (=498Å%). The structure also has less strain compensation. In addition to using compressive strain to enhance the differential gain, the waveguide layer thicknesses were reduced and the entire SCH region was p-doped in an attempt to reduce the transit time[18,19]. A DFB grating was defined by direct write electron beam lithography and etched in the upper waveguide of the structure shown in figure 7.23. The structure was then overgrown with p-InP and p-InGaAs. Parasitic capacitance, which reduces the maximum speed at which the device can be directly modulated, was minimised by selectively patterning the p-side metallisation.

Spectral measurements of the resonant frequency as a function of the square root of the output power (which was varied by changing the device bias) were performed on Fabry Perot devices to evaluate the slope D in the relationship:

$$f_r = DP^{0.5} \qquad (7.3.8)$$

f_r - resonant frequency
P - output power

The value of f_r was measured by mounting the laser chips in a 'high speed' package with the laser drive fed from a Wiltron k bulkhead connector along a microstrip and through a 47Ω chip resistor in series with the laser. For measurements at frequencies up to 20GHz an HP8703 network analyser with an internal calibrated detector was used, and for measurements between 20 and 30GHz an HP 8722A 40GHz network analyser was used in conjunction with an HP83440D detector, which is flat to within ±1dB up to 30 GHz.

By evaluating this slope for devices with different cavity lengths (250, 350 and 600 μm), the differential gain dg/dn can be determined through the equation:

$$D^2 = \frac{1}{4\pi^2}\frac{dg}{dn}\frac{2v_g\Gamma}{h\nu Wt}\left(\frac{\alpha_i}{\ln\left(\frac{1}{R}\right)}+\frac{1}{L}\right) \qquad (7.3.9)$$

dg/dn - differential gain
v_g - group velocity in the cavity
Γ - optical confinement factor
R - mirror reflectivity
h - Planks constant
α_i - internal cavity losses
ν - frequency of light
L - device length
Wt - active layer area

The plot of D^2 against reciprocal cavity length is shown in figure 7.25. The differential gain was determined to be 25×10^{-16} cm^2 - a fourfold improvement in the value determined for similar devices for lattice matched InGaAs wells. Further spectral measurements on a fully packaged 300μm DFB indicated a modulation bandwidth of 22 GHz at a bias current of 120 mA. When this result was published it represented the highest reported modulation bandwidth for a 1550 nm DFB although Morton et al[18] reported 25 GHz for a 7 well compressively strained MQW buried heterostructure Fabry Perot device.

One of the limits on the performance of the above device structure was the constraint placed on the p-side waveguide layer thickness by the need to accommodate the grating. This need can be overcome, and the layer thickness reduced, by fabricating the grating on the n-side of the device. The proposed structure comprises a grating defined in lattice matched n-type GaInAsP that has been grown on an n-InP substrate. The grating is then overgrown with n-type InP, n-GaInAsP waveguide layer, the quantum well active region, reduced thickness p-GaInAsP waveguide layer, p-InP and the p-GaInAs contact layer. Such a laser structure was overgrown on a grating defined in a lattice

matched GaInAsP (λ=1.17μm) layer, however the grating was unintentionally overetched into the InP substrate. The HRXRD rocking curve of the overgrown sample is shown in figure 7.26. The satellite intensity and width are both inferior to the sample described above which was grown on a planar substrate and whose rocking curve is shown in figure 7.24. The reduction in intensity may be partially explained by the presence of a thick p-InP layer on top of the SCH region but the broadening of the satellite peaks cannot be explained. To investigate this anomaly further, the structure was assessed by TEM. Figure 7.27 clearly shows the grating defined in the GaInAsP layer with overetching into the substrate. It also illustrates the success of the n-InP at planarising the growth. Planar interfaces are also observed in the lower GaInAsP waveguide layers, however, after the deposition of the first well, it is obvious that thickness undulations are occurring during the growth of the MQW active region. The undulations appear to be localised to regions extending upwards from each grating trough. To the author's knowledge, no reports have been made on this effect, yet similar structures have been grown successfully by chemical beam epitaxy[20]. Thickness modulations have been observed when compressively strained GaInAs/GaAs MQW structures are grown off {133} facets[21]. The facets on the sidewalls of a DFB grating are {111}A, but, by the time the quantum wells are deposited, the growth has planarised to the (100) direction. Hence the effect cannot be explained by a facet dependent growth mechanism. Further examination by TEM showed that a significant amount of material had mass-transported from the n-GaInAsP layer into the trough of the grating, which is located in the InP substrate. This is just discernible in the TEM image of figure 7.27. The mass transport most likely occurred during the heat-up and pre-epitaxy heat-treatment of the sample. This resulted in an alloy of unknown composition, most probably strained, at the bottom of the trough. Hence a periodic, lateral variation in strain exists as we move across the grating. The MQW material between the grating grooves is deposited on a region that is lattice matched. However the MQW material directly above the grating grooves is deposited on a region that has a net strain. It is in these regions of lateral strain variation that thickness modulations occur. This observation supports the suggestion that thickness modulated growth is a strain relief mechanism that occurs in strain compensated MQW structures.

7.4 Discussion

It has been shown that the growth of strain compensated MQW structures suffers from a loss in planarity after the deposition of a given number of strained wells and barriers. The resultant thickness modulations are periodic in nature and are in anti-phase, i.e. when the well becomes thicker the barrier becomes thinner and vice versa. The thickness modulations are accompanied by a contrast modulation in the strain sensitive TEM image, with a similar periodicity to the thickness modulations. As well as being evident in the TEM images, the effect also manifests itself as a rippled surface morphology, a diffuse HRXRD rocking curve and a room temperature PL image with

dark spots. This is different from the strain relief mechanism that occurs in the uncompensated GaAs/InGaAs strained layer system where the InGaAs wells are compressively strained with respect to the GaAs barriers and substrate. The dominant strain relief mechanism in the GaAs/InGaAs strained layer system is through the generation of misfit dislocations lying in the (100) growth plane along orthogonal [011] and [01$\bar{1}$] directions[22]. Dislocations were only observed in the strain compensated MQW structures as an adjunct to thickness modulations. Thickness modulations, however, are not new in strained layer epitaxy; Cullis et al[23] have reported similar, but not identical, behaviour in the Si-Si_xGe_{1-x} system. These structures comprised relatively thick (0.1μm) layers of compressively strained Si_xGe_{1-x} grown on Si, i.e. with no strain compensation. They attributed the thickness modulation effect to a partial relief of the strain via the expansion and contraction of the lattice planes during the growth of the strained layer, leading to a rippled layer profile as illustrated in figure 7.28. For a compressive layer, the local strain decreases in the region of lattice plane expansion, the ripple peak, and increases in the region of lattice plane contraction, the ripple trough. The overall strain energy is reduced as the volume of the stress-reduced regions (the peaks), was greater than the volume of the stress-increased regions (the troughs). This variation in lattice expansion/contraction along the thickness modulated surface, makes it more energetically favourable for larger atoms to reside on the peaks (larger lattice spacing) and small atoms to reside on the troughs (small lattice spacing), further enhancing variations in composition and growth rate.

The TEM micrographs, shown in figure 7.13, demonstrate that a similar effect is occurring in strain compensated MQW structures using GaInAsP alloys. The thickness modulations are periodic in nature with a similar periodicity to the contrast variations observed in the strain sensitive images. It has also been demonstrated in figure 7.27 that the onset of thickness modulated growth can be accelerated by defining a lateral periodic variation in strain prior to the deposition of the strain compensated MQW stack. The periodic strain variation was defined, unintentionally, by the mass transport of lattice matched GaInAsP (λ = 1.17μm) into the grooves of a DFB grating resulting in a composition, i.e. strain, difference between the area immediately in and around the grooves and the areas between the grooves. Thickness modulations occurred in this sample whereas they did not occur in an identical sample grown on a planar substrate. The thickness modulations occurred in columns precisely defined by the grating pitch and planar growth was observed in the regions between the grooves, demonstrating that thickness modulations arise as a result of lateral variations in strain.

Bangert et al[24] proposed an additional mechanism that is particular to GaInAsP alloys. They demonstrated that the propensity for a strain compensated MQW stack to undergo thickness modulated growth is influenced by the proximity of the well and barrier compositions to the centre of

the miscibility gap for GaInAsP alloys. The miscibility gap is an area of the Ga-In-As-P phase diagram in which the alloys are prone to compositional clustering, also known as spinodal decomposition. Here an alloy finds it thermodynamically more stable to 'phase separate' or cluster into regions of different compositions, rather than remain a single uniform composition. The miscibility gap has been calculated by several authors[25,26] for thermal equilibrium conditions, with the region becoming smaller as the growth temperature increases. It should be mentioned that MOVPE growth does not occur under thermal equilibrium, so these theoretical curves may not be totally valid for this growth technique. Figure 7.29 illustrates the miscibility gaps for 600°C, 650°C, and 700°C as calculated by Stringfellow[25] and shows the positions of the well and barrier compositions used so far in this work. Bangert's observations were based on TEM measurements of structures reported in section 7.1.2 and other strained structures grown by colleagues at BNR Europe and elsewhere, her argument being based on a theoretical analysis by Glas[27]. He modelled compositional clustering as a periodic modulation in lattice parameter in a direction parallel to the substrate surface and demonstrated that this modulation eventually led to expansion and contraction of the lattice planes resulting in a thickness modulated layer.

At this time, similar results on the growth of strain compensated GaInAsP MQW structures by gas source molecular beam epitaxy, were reported by Ponchet et al[28]. Their structure comprised $Ga_{0.18}In_{0.82}As_{0.2}P_{0.8}$ barriers ($\Delta a/a$ = -0.5%) and $Ga_{0.18}In_{0.82}As_{0.7}P_{0.3}$ wells ($\Delta a/a$ = 1%). It is interesting to note that they also used the constant Ga:In ratio approach used in this work. The well and barrier thicknesses were 80 Å and 160 Å respectively. They observed that thickness undulations occurred after the deposition of only the second barrier layer, but the deposition of the subsequent well planarised the growth again. This continued to happen until the deposition of the fifth well when undulations were observed in both the well and barrier layers, occurring in anti-phase. A periodic contrast in the strain sensitive TEM image was also observed. Ponchet et al[28] also saw a strong anisotropy in the thickness modulations. Thickness modulations occurred in the [011] direction but no modulations were observed in the $[01\bar{1}]$ direction, a situation best visualised by the schematic diagram of the undulations shown in figure 7.30. This anisotropy in thickness modulation was emphasised by plan view TEM's which showed a rippled surface morphology with the peaks and troughs running in the $[01\bar{1}]$ direction. These observations were consistent with the surface morphology micrographs shown in figure 7.8. The anti-phase nature of the thickness modulation can be explained by assuming that growth is easier on relaxed crystalline zones. Hence a tensile layer (with a relaxed lattice parameter < InP), would find it energetically more favourable to grow on a trough of a compressive layer, as the (011) lattice spacing is smaller due to strain relieving contraction in the compressive layer, leading to an enhanced growth above the compressive layer trough. However a compressive layer (with a relaxed lattice parameter > InP) would find it

energetically more favourable to grow on the trough of a tensile layer, as the (011) lattice spacing is larger due to strain relieving expansion in the tensile layer, leading to an enhanced growth above tensile layer trough, as illustrated in figure 7.31. The alloys are strain enhanced in the thinnest regions and relaxed in the thick regions, giving rise to the lateral variation in strain observed in the strain sensitive TEM image. Thickness modulations were observed by Ponchet et al[28] after the deposition of only the second well, much sooner than in the structures described in this Chapter. It would appear to support the compositional clustering/miscibility gap argument, as the samples were grown at 500C, typical for GSMBE, and the alloy compositions would therefore be more prone to the effects of immiscibility than if they were grown at a higher temperature.

The question arises: what happens first, the expansion and contraction of the lattice planes or compositional clustering? The former promotes the latter as the thickness modulations must be accompanied by a growth rate modulation, i.e. a Ga:In ratio modulation. The latter also promotes the former as shown by Glas[27]. Are they two separate mechanisms and do they always occur together? An attempt to answer these questions is made in the next chapter.

In spite of the growth problems that were observed in the structures grown with more than 8 wells, improved device performance was seen in strain compensated GaInAsP MQW structures when compared to the performance of compressively strained and lattice matched GaInAs MQW structures grown previously at BNR Europe. The reduction in hole effective mass, non-radiative recombination and IVBA that have been extensively reported in compressively strained GaInAs well structures and manifesting itself as a reduced threshold current density, have also been observed here in structures employing strain compensated GaInAsP MQW active regions. However, the effect of strain on the threshold current density can often be masked by other effects in the growth of the laser structure. The higher Zn level in the overgrowth of the second generation of structures undoubtedly contributed to poorer threshold current densities when compared to the first generation.

Improved output powers have also been observed in structures with strained GaInAsP wells when compared to strained and lattice matched GaInAs well structures. The reduced hole effective mass, non-radiative recombination and IVBA, combined with an increase in the optical confinement factor are the causes. Thicker wells are a direct result of the use of GaInAsP as the chosen well material as it affords some flexibility in the choice of both well thickness and strain for a given wavelength of emission. In contrast, the well width for a given wavelength of emission is fixed using GaInAs. Output powers of up to 129 mW ex facet have been measured at a drive current of 700 mA, making these devices suitable candidates as pumps for Er doped fibre amplifiers. Over 3700 hours of accelerated life testing was performed with only a +3.6% change in the threshold current,

indistinguishable from lattice matched devices, i.e. there is no obvious reliability penalty incurred by the use of strain.

A fourfold improvement in the differential gain of compressively strained GaInAsP MQW structures was observed when compared to lattice matched InGaAs well structures. This is a direct result of the reduced hole effective mass that occurs under compressive strain. This improved differential gain, along with other steps such as reduced p waveguide thickness, p doping of the active region and patterning the p-side metallisation, has resulted in a DFB laser with a modulation bandwidth of 22 GHz.

References

1 W.D. Laidig, P.J. Caldwell, Y.F. Lin and C.K. Peng, Appl. Phys. Lett.,44, pp653-655, Apr 1984.

2 P.J.A. Thijs, T. van Dongen, Electron. Lett., 25, pp1735-1737, Dec. 1989.

3 B.I. Miller, U. Koren, M.G. Young and M.D. Chien, Appl. Phys. Lett., 58(18), pp1952-1954, May 1991.

4 A.T.R. Briggs, P.D. Greene and J.M. Jowett, , IEEE Phot. Tech. Lett., 4(5), May 1992.

5 R.W. Glew, Proc. 5th Conf. on InP and Related materials, Paris 1993, p29.

6 D. Coblentz, T. Tanbun-Ek, R.A. Logan, A.M. Sergent, S.N.G. Chu and P.S. Davisson, Appl. Phys. Lett., 59(4), pp405-407, July 1991.

7 J.S. Osinski, Y. Zou, P. Grodzinski, A. Mathur and P.D. Dapkus, IEEE Phot. Tech. Letts., 4(1), Jan 1992, pp10-14.

8 J.D. Evans, T. Makino, N. Puetz, J.G. Simmons and D.A. Thompson, IEEE Phot. Tech. Lett.,4(4), Apr 1992, pp299-301.

9 C.E. Zah, F.J. Favire, R. Bhat, S.G. Menocal, N.C. Andreadakis, D.M. Hwang, M. Koza and T.P. Lee, Proc. 12th Semiconductor Laser conference, Davos, Switzerland, Sept 10-13, 1990. Paper D1, pp42-43.

10 U. Koren, M. Oran, M.G. Young, B.I. Miller, J.L. de Miguel, G. Raybon and M. Chien, Electron. Letts., 26(7), March 1990, pp465-466.

11 P.J.A. Thijs and T. van Dongen, Proc. 22nd Conf. on Solid State Devices and Materials, Sendai, 1990, pp541-544.

12 C.J.L. Moore, C.J. Miner, J. Crystal Growth, 103(1-4), 1990, pp21-7.

13 P.D. Greene, J.E.A. Whiteaway, G.D. Henshall, R.W. Glew, C.M. Lowney, B. Bhumbra and D.J. Moule, Proc. 17th international Symposium on GaAs and related compounds, Inst Phys Conf Series vol 112, pp555-560, 1990.

14 G.P. Agrawal and D.K. Dutta, 'Long wavelength semiconductor lasers', Van Nostrand Rheinhold, 1986, Chapter 5.

15 P.J.A. Thijs, L.F. Tiemeijer, J.J.M. Binsma and T. van Dongen, IEEE J. Quant. Elect., 30(2), Feb 1994, pp477

16 G.P. Agrawal and D.K. Dutta, 'Long wavelength semiconductor lasers', Van Nostrand Rheinhold, 1986.

17 A. Ghiti, E.P. O'Reilly and A.R. Adams, Electron Lett, 25, pp821-825 June 1989.

18 P.A. Morton, R.A. Logan, T. Tanbun-Ek, P.F. Sciortino, A.M. Sergent, R.K. Montgomery and B.T. Lee, Electron Lett, 28, pp2156-2157, 1992.

19 R. Nagarajan, T. Fukushima, S.W. Corzine and J.E. Bowers, Appl. Phys. Letts., 59,pp1835-1837,1992

20 W.T. Tsang, F.S. Choa, M.C. Wu, Y.K. Chen, R.A. Logan, S.N.G. Chu, A.M. Sergent, P. Magill, K.C. Reichmann and C.A. Burns, J. Cryst. Growth, 124, 1992, pp716-722.

21 P. Grodsinski, Y. Zou, J.S. Osinski and P.D. Dapkus, J Cryst. Growth, 107, 1991, pp583-590.

22 P.L. Gourley, I.J. Fritz and L.R. Dawson, Appl. Phys. Lett, 52(5), pp377-379, Feb 1988.

23 A.G. Cullis, D.J. Robbins, A.J. Pidduck and P.W. Smith, J Cryst Growth, 123, pp333-343, 1992.

24 U. Bangert, A.J. Harvey, V.A. Wilkinson, C. Dieker, J.M. Jowett, A.D. Smith, S.D. Perrin and C.J. Gibbings, J Crystal Growth, 132, pp231-240, 1993.

25 G.B. Stringfellow, J Cryst. Growth, 58, pp194-202, 1982.

26 B. de Cremoux, P. Hirtz and J. Ricciardi', 7th International Symposium on GaAs and related compounds, Vienna, Inst Phys Conf Series, p115, 1980.

27 F. Glas, J Appl. Phys., 62(8), Oct 1987, pp3201-3208.

28 A. Ponchet, A. Rocher, JY. Emery, C. Starck and L. Goldstein, J Appl Phys, 74(6), Sept 1993, pp3778-3782.

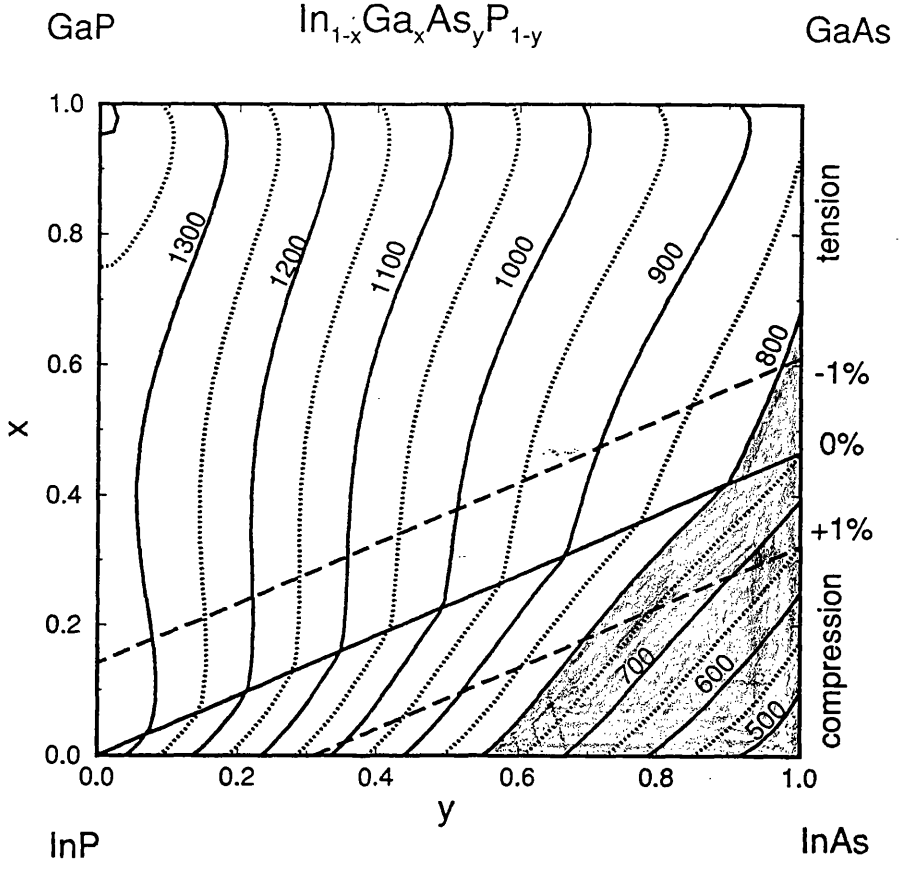

Figure 7.1 Constant band-gap energy contours in the Ga-In-As-P parameter space. The shaded region defines compositions with $\lambda \geq 1.55\mu m$. Lines of lattice match and ±1% mismatch are also defined.

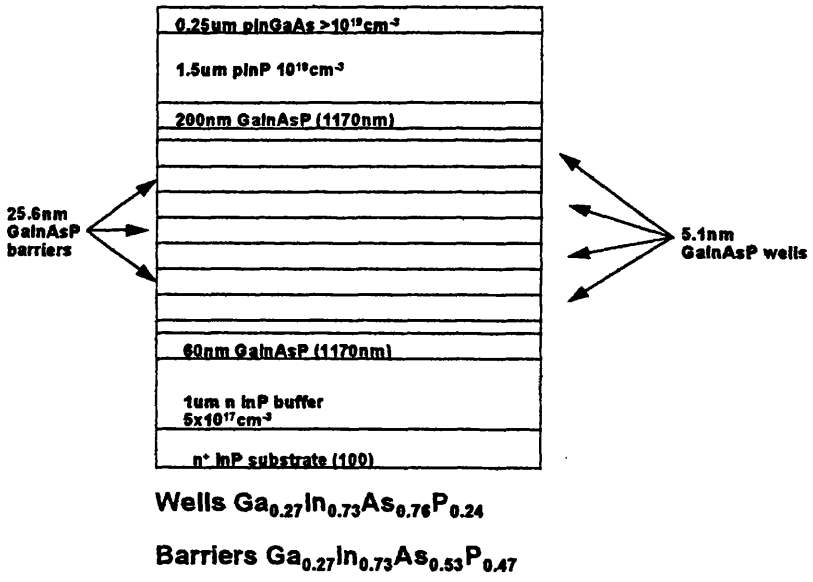

Figure 7.2 Layer structure of first generation, strain compensated GaInAsP/GaInAsP MQW laser. The MQW stack begins and ends with 'half-thickness' barriers to help maintain strain symmetry. The subsequently overgrown p-InP and p-GaInAs layers are also shown for completeness.

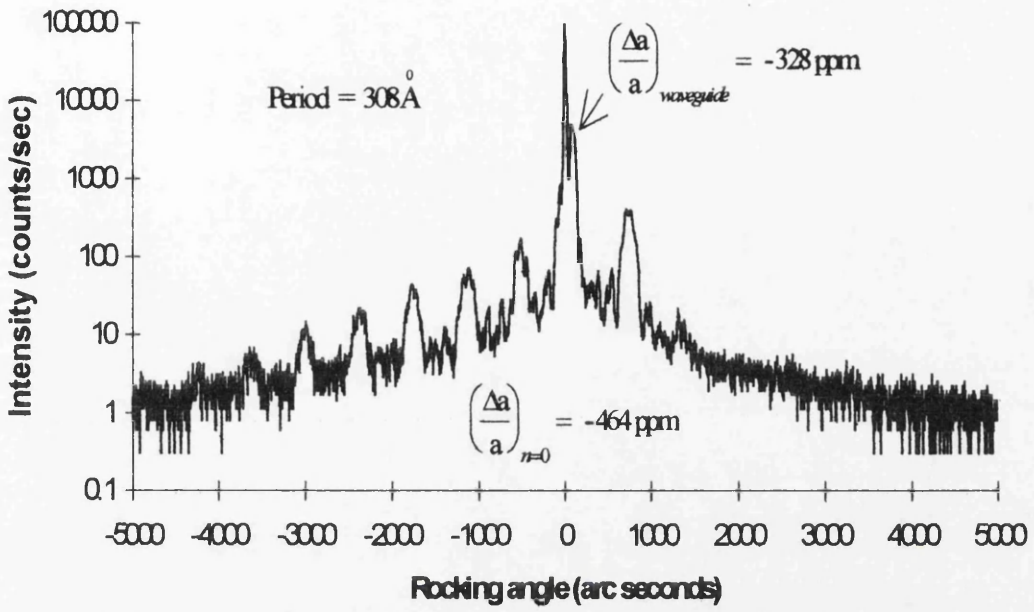

Figure 7.3 HRXRD rocking curve of structure shown in figure 7.2.

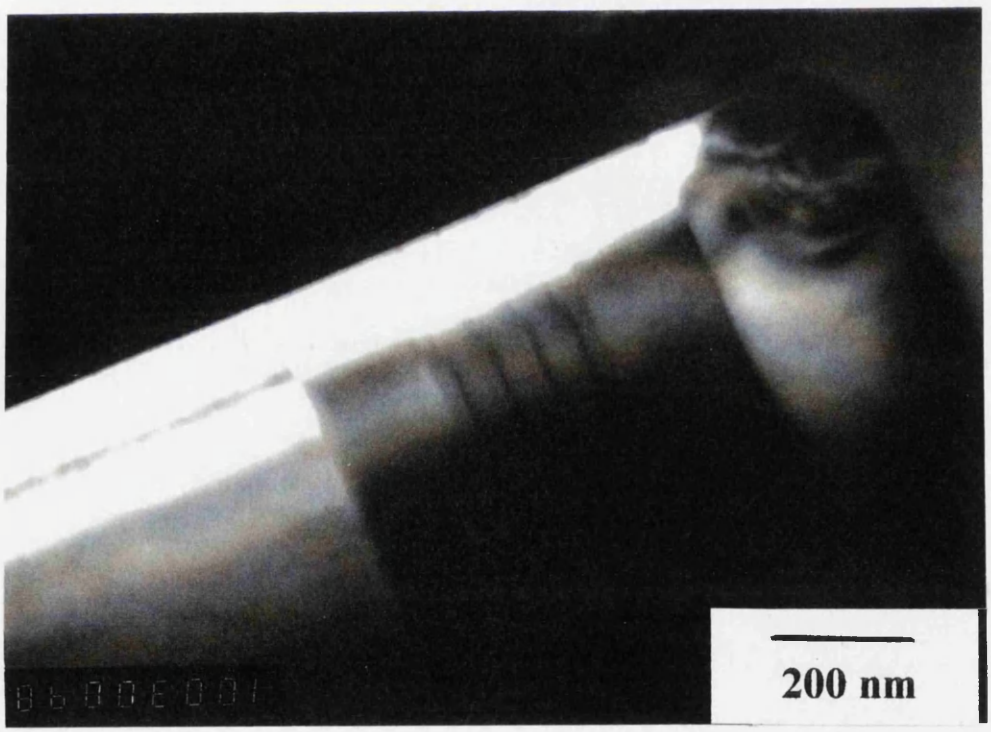

Figure 7.4 Cleaved edge TEM micrograph of structure shown in figure 7.2. The well and barrier interfaces are abrupt and their thicknesses are consistent with those predicted by HRXRD in figure 7.3.

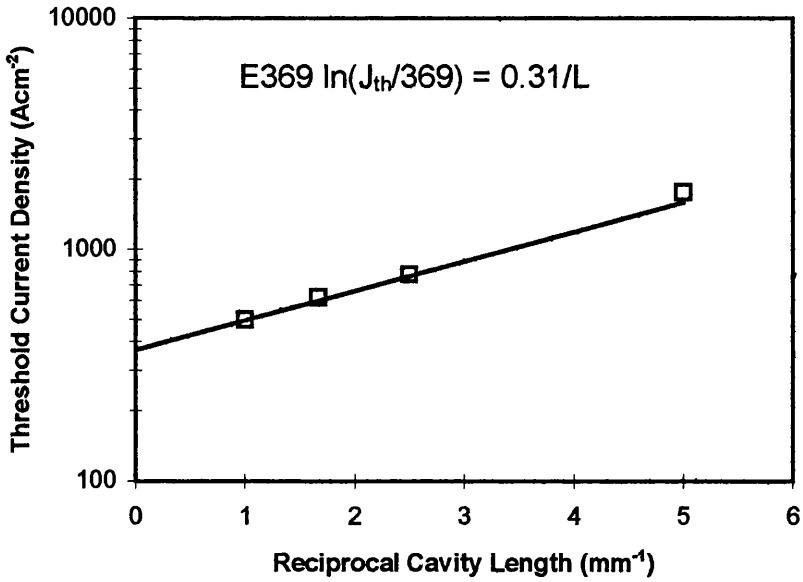

Figure 7.5 Logarithm of threshold current density versus reciprocal cavity length for the laser structure shown in figure 7.2. Measurements were made on 50μm, oxide stripe devices with cavity lengths of 200, 400, 600 and 1000μm.

10 nm InP cap	
50 nm barrier	
12nm well	'Ideal '
50nm barrier	
8.5nm well	'Ideal - 2l litres/min H_2
50nm barrier	
6.5nm well	'Ideal' + 2 litres/min H_2
50nm barrier	
5nm well	'Ideal' - 1 litre/min H_2
50nm barrier	
3.7nm well	'Ideal' + 1 litre/min H_2
50nm barrier	
3 nm well	'Ideal'
25nm barrier	
1um InP buffer	
nInP substrate (100)	

Barrier material : $Ga_{0.27}In_{0.73}As_{0.58}P_{0.42}$

Well material : $Ga_{0.27}In_{0.73}As_{0.84}P_{0.16}$

Figure 7.6a Variable thickness quantum well stack which was grown to evaluate the effect of hydrogen ballasting conditions on interface quality.

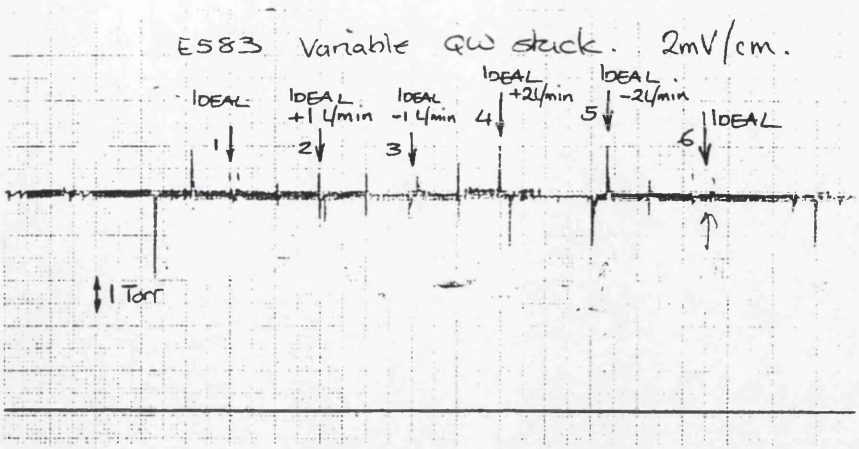

Figure 7.6b Reactor pressure trace obtained during the growth of the structure described in figure 7.6a. The so-called 'ideal' condition is that which yields the smallest pressure excursion during switching from well to barrier and vice versa.

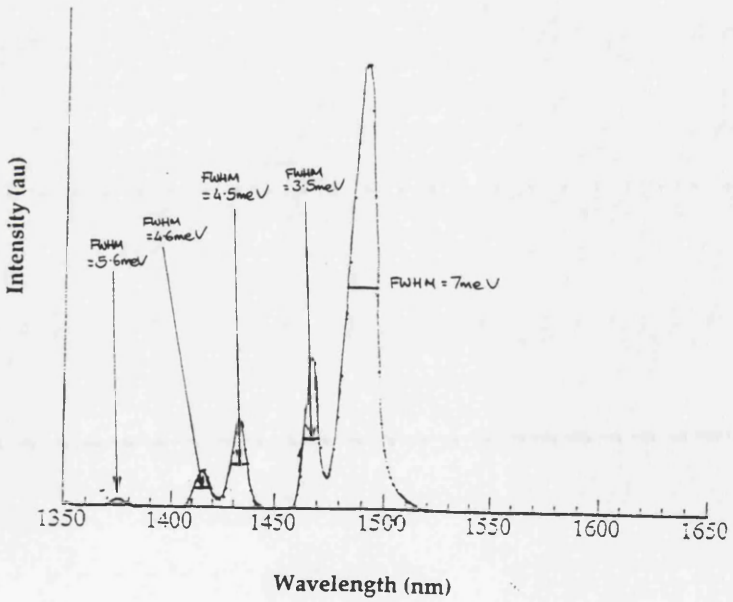

Figure 7.7 Low temperature (10K) PL spectrum of structure described in figure 7.6a. Narrowest FWHM can be seen to occur at the 'ideal'-2 l/min condition. This growth condition was subsequently used in all the structures described in this chapter.

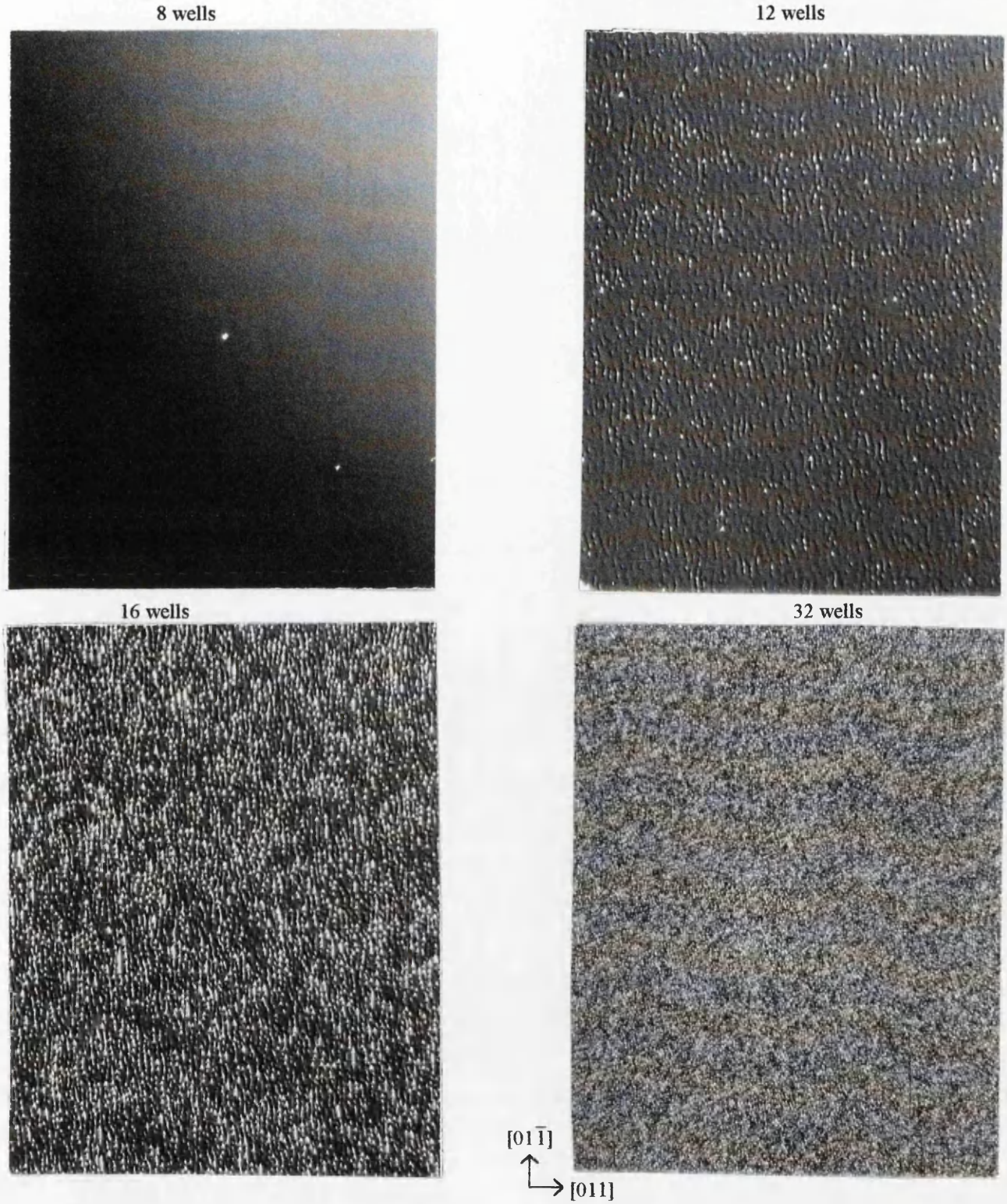

Figure 7.8 Optical microscopy (Normarski) images (x500) of samples grown with 8, 12, 16 and 32 wells. It can be seen that after the deposition of 12 or more wells there is a deterioration in surface morphology. It is discernible from the 12 well image that the rippling seems to run in the [01$\bar{1}$] direction.

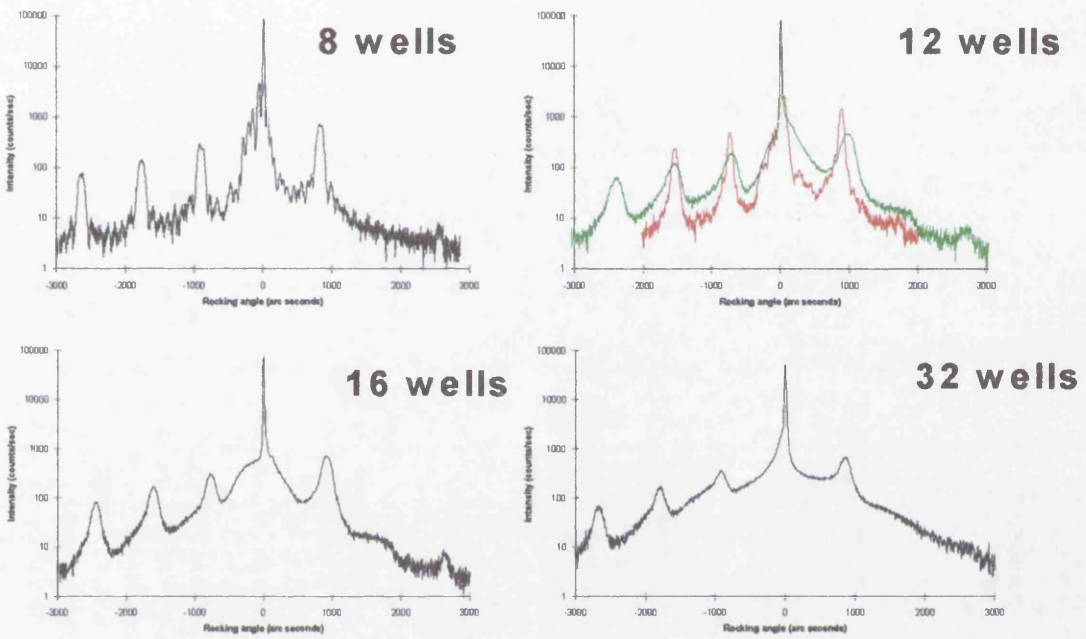

Figure 7.9 HRXRD Rocking curves of samples with 8, 12, 16 and 32 wells. A deterioration in the 'quality' of the rocking curve is observed on/after the growth of 12 wells. Variability in quality is observed across the 12 well wafer. Note that the period (well + barrier thickness) remains approximately constant in all cases.

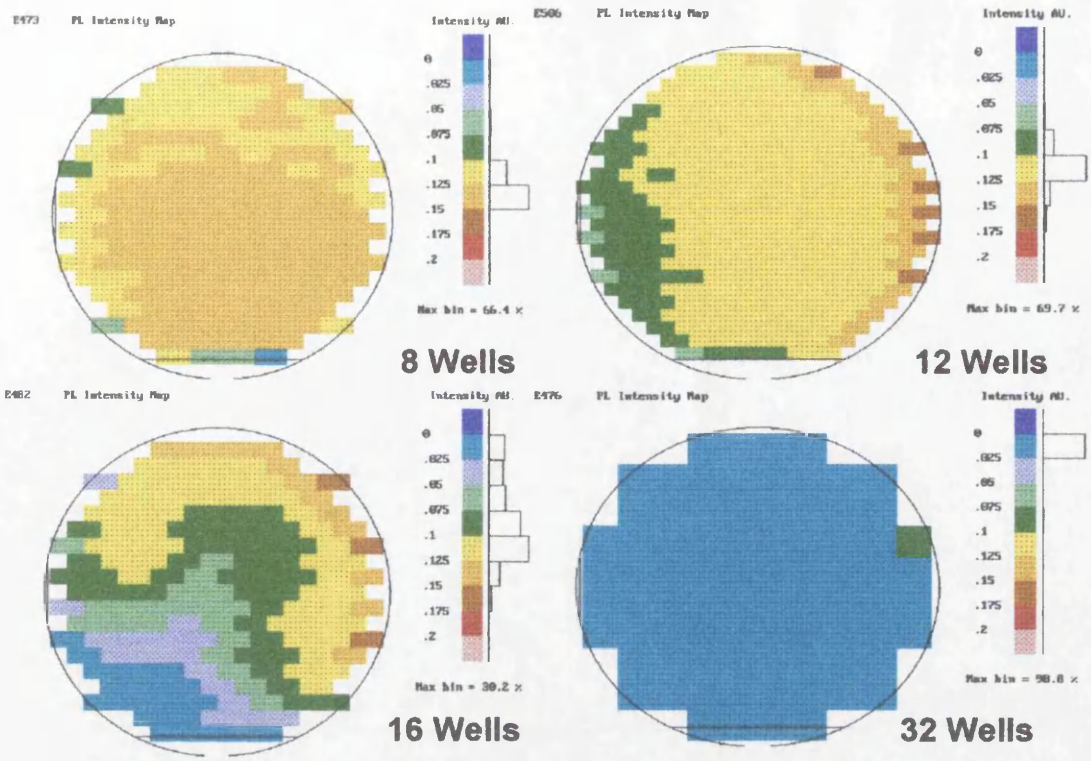

Figure 7.10 Room temperature PL intensity 2" wafer maps of the 8, 12, 16 and 32 well samples. A deterioration in PL intensity is observed in the 16 well sample, indicating that this technique is less sensitive than either optical microscopy or HRXRD in detecting this deterioration in quality.

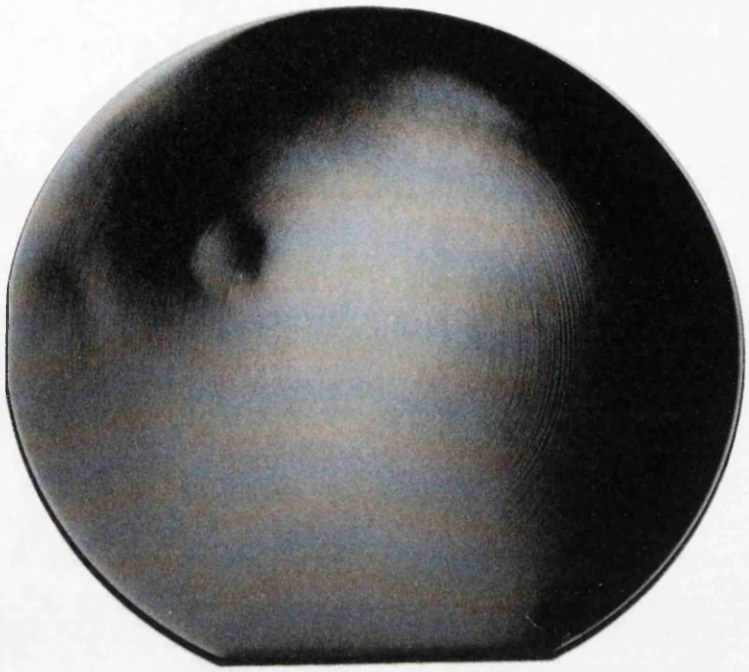

Figure 7.11 Macroscopic image of the 16 well sample: note how the variation in surface finish reflects that of the PL intensity of this wafer shown in figure 7.10.

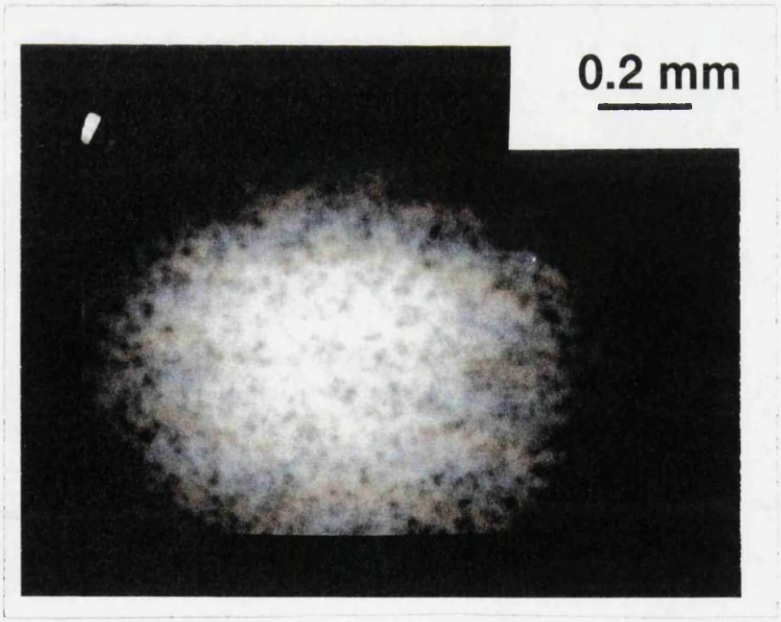

Figure 7.12 Room temperature PL image taken from the centre of the 16 well structure. The dark spots observed here are unlike any other image observed on lattice matched structures.

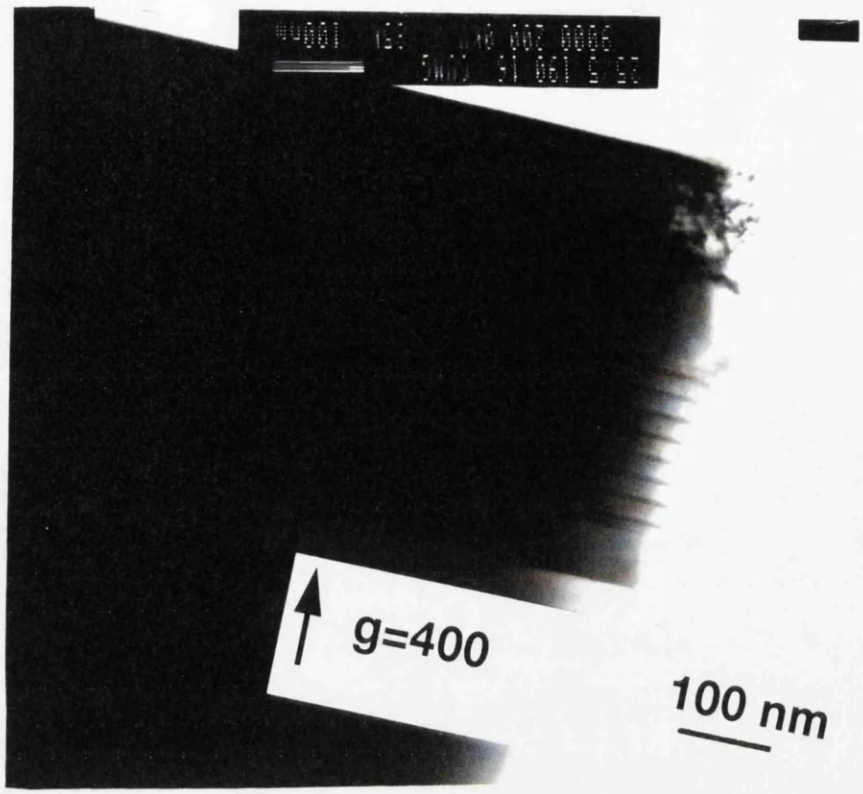

Figure 7.13a Cleaved edge TEM image (g=400) of 8 well sample. The wells and barriers appear planar and thicknesses appear to be as expected. The wells appear as a dark contrast.

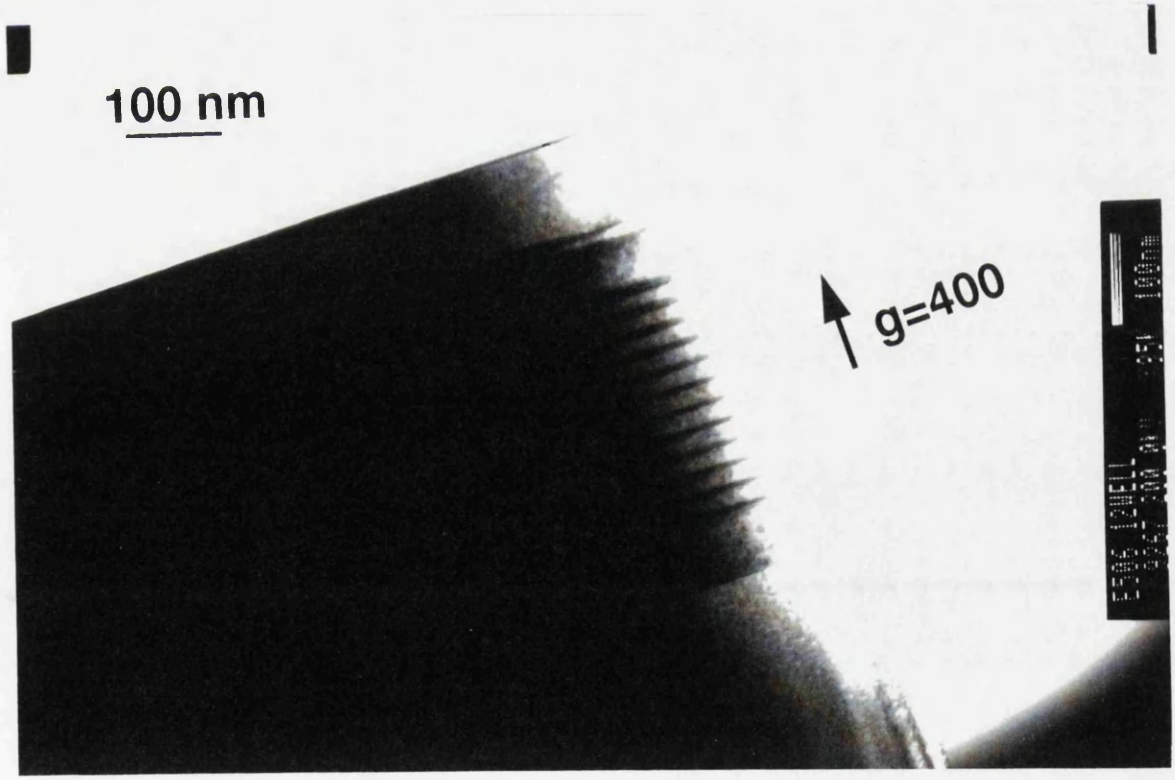

Figure 7.13b Cleaved edge TEM image (g=400) of 16 well sample. There is evidence in the upper third of the stack that the wells are getting thicker and the barriers are getting thinner.

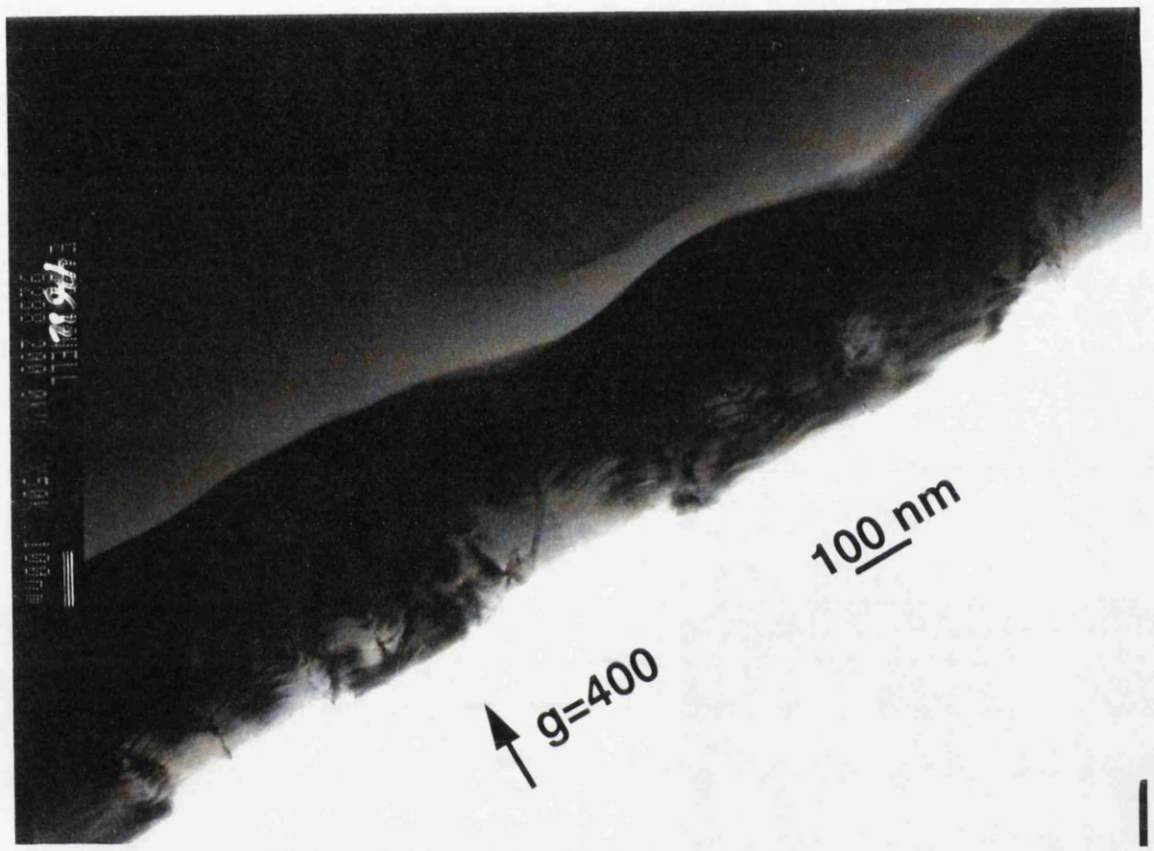

Figure 7.13c Cross sectional TEM image (g=400) of 32 well sample. It is evident that the wells and barriers are no longer planar, in fact the surface of the sample is rippled. Dislocations can also be observed in the MQW stack.

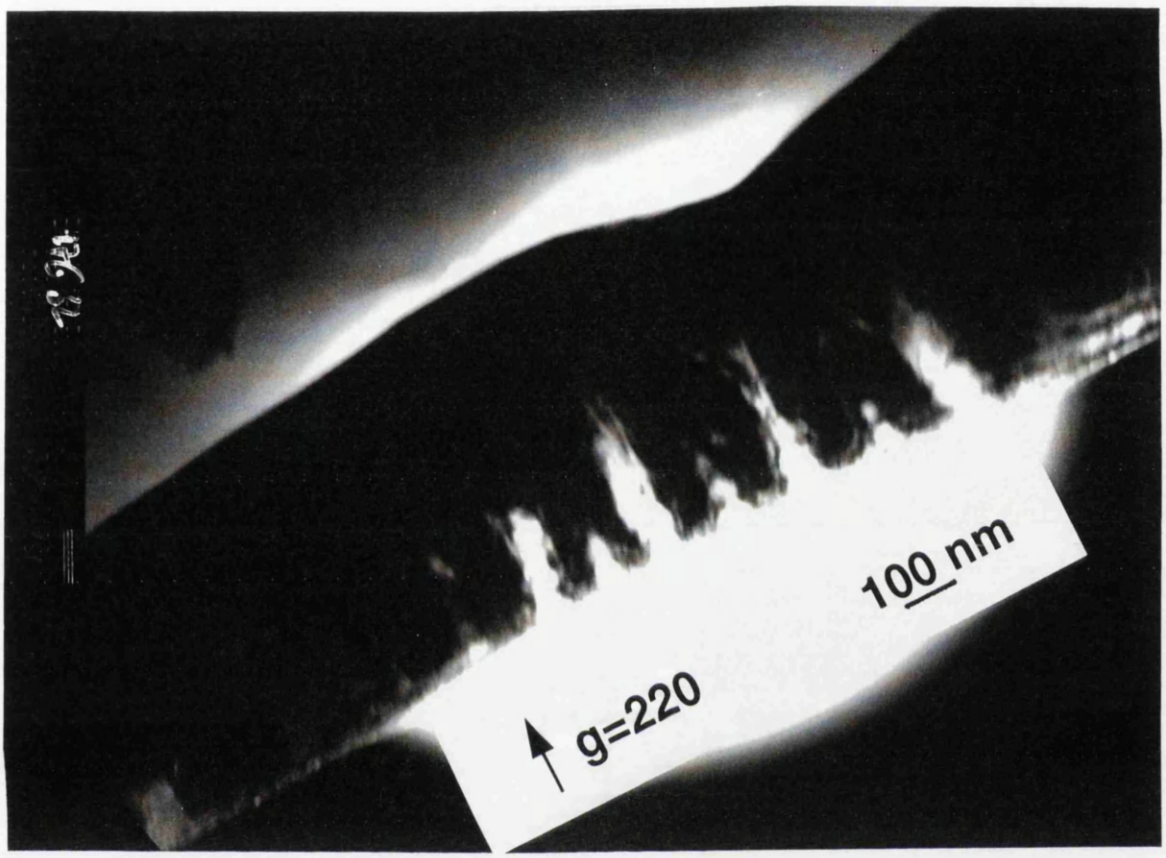

Figure 7.13d Cross sectional TEM image (g=220) of 32 well sample. Image is acquired under a diffraction condition which is sensitive to variation in strain. The observed contrast is indicative of a strain field existing with a similar periodicity to the thickness modulations observed in figure 7.13c.

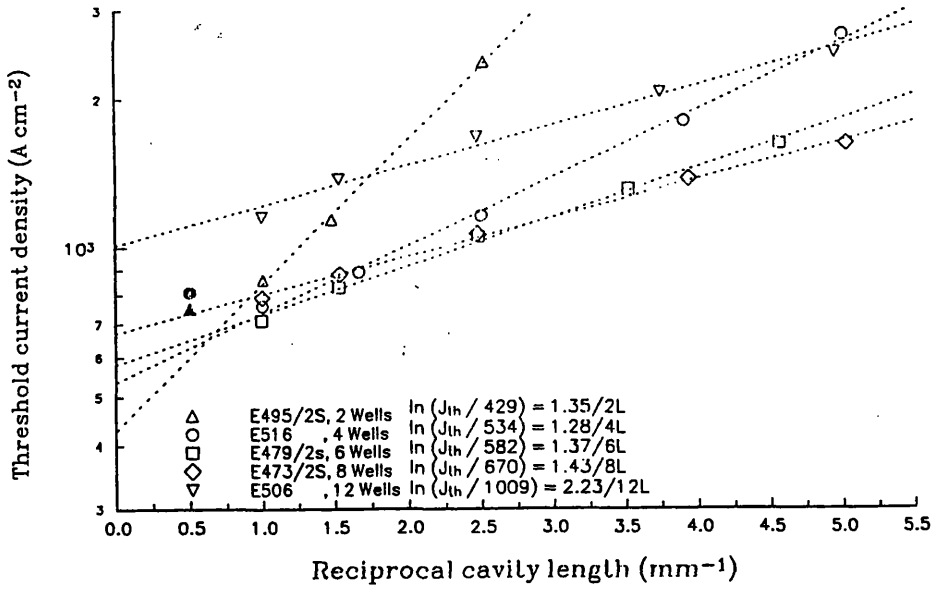

Figure 7.14 Logarithm of threshold current density versus reciprocal cavity length for 2, 4, 6, 8 and 12 well samples. Measurements were made on 50μm oxide stripes with cavity lengths between 200 μm and 2000μm.

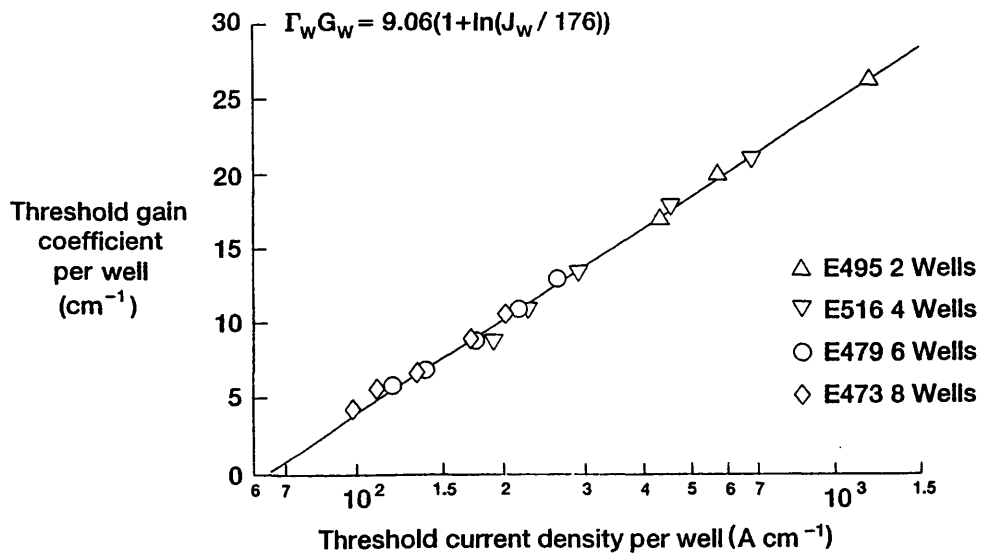

Figure 7.15 Plot of threshold gain co-efficient per well against threshold current density per well for the 2, 4, 6 and 8 well samples. In order to obtain this fit an α value of 22 cm^{-1} was assumed.

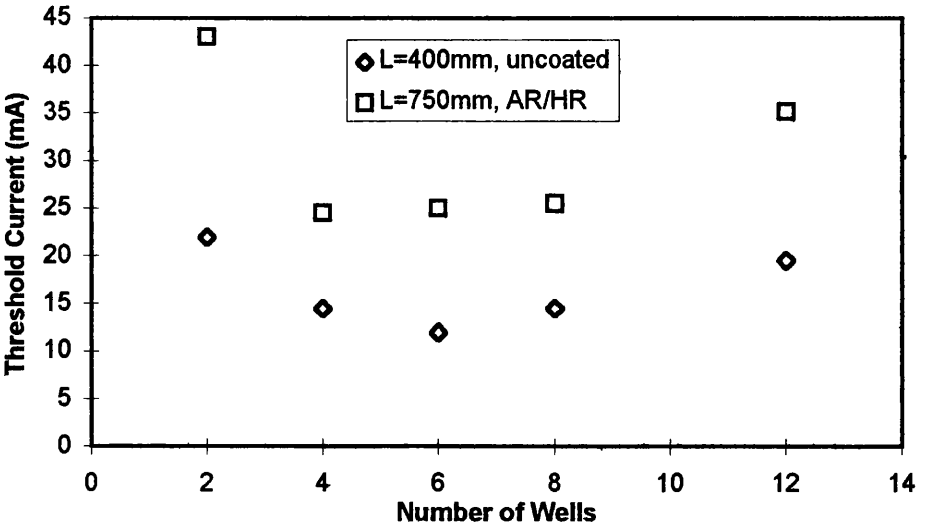

Figure 7.16 Dependence of threshold current on number of wells for two sets of 2μm ridge waveguide Fabry-Perot lasers: 400 μm long uncoated devices and 750 μm long AR/HR coated devices.

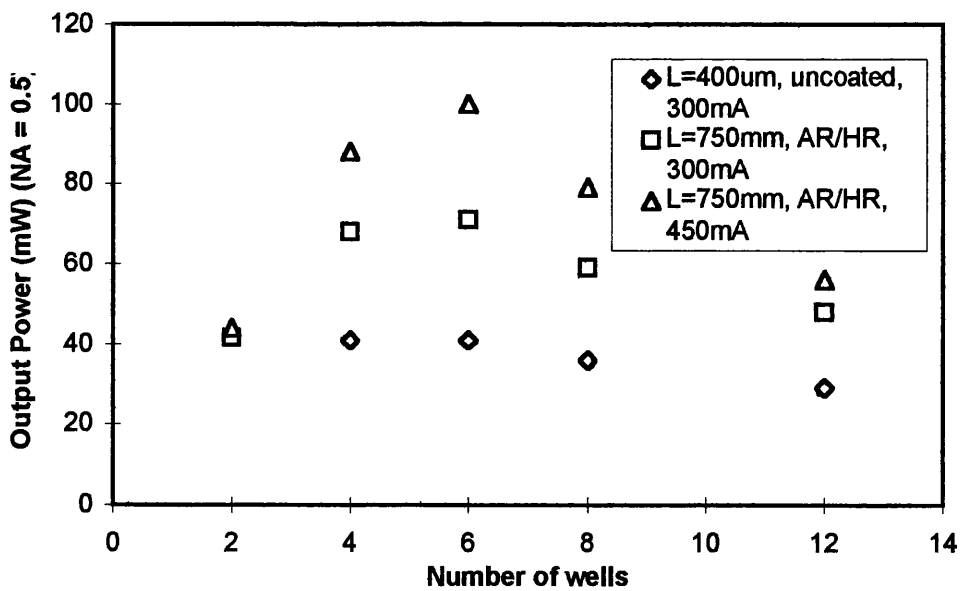

Figure 7.17 Dependence of output power on number of wells for three sets of 2μm ridge waveguide Fabry-Perot lasers: 400 μm long uncoated devices biassed at 300 mA, 750 μm long AR/HR coated devices biassed at 300 mA and 750 μm long AR/HR coated devices biassed at 450 mA.

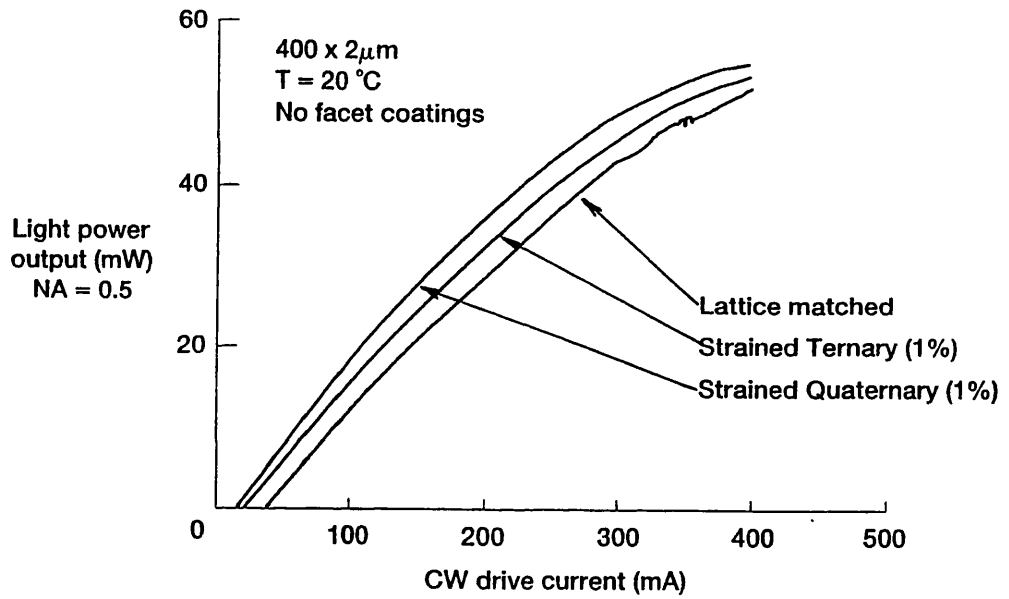

Figure 7.18 Comparison of the L-I characteristics of MQW ridge waveguide lasers with lattice matched, compressively strained ternary and compressively strained quaternary wells. The geometries of the devices were essentially identical (2μm ridge width and 400μm cavity length with no facet coatings)

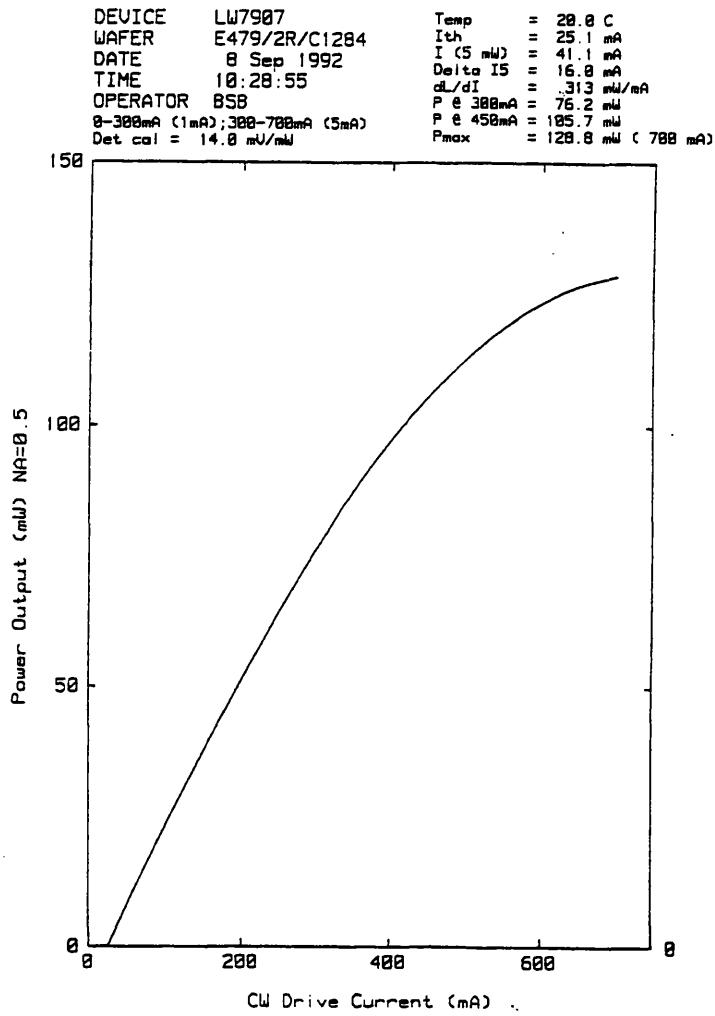

Figure 7.19 L-I characteristic of 6-well, 750μm long, 2μm wide MQW ridge laser with HR/LR coatings. This laser exhibits a maximum output power of 129 mW at 700mA bias measured with a numerical aperture of 0.5.

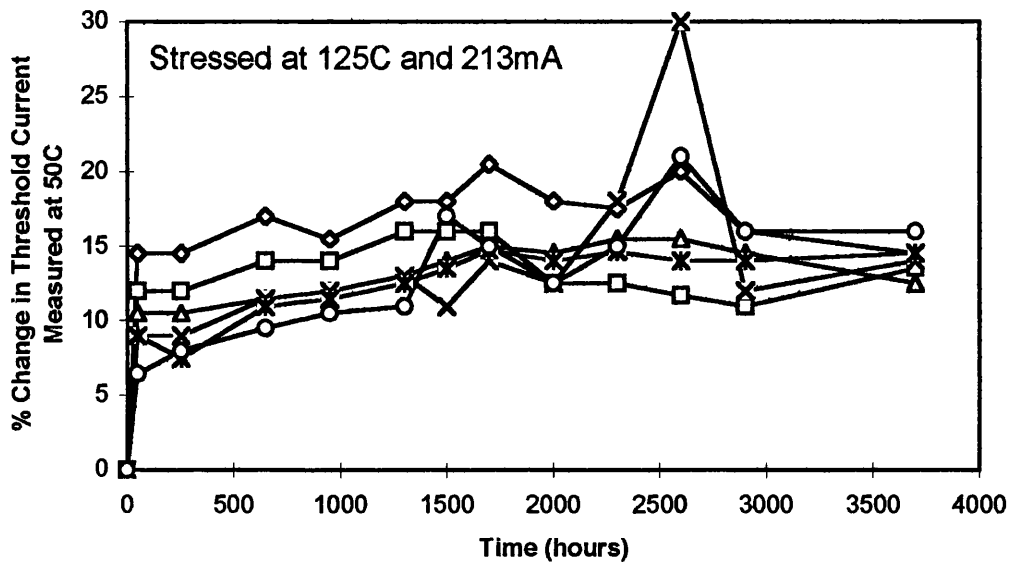

Figure 7.20 Plot of threshold current against time for a 4 well laser structure stressed at 125°C and 213 mA. It can be seen that, after burn-in, the threshold current degrades by only 3.6% over 3700 hours.

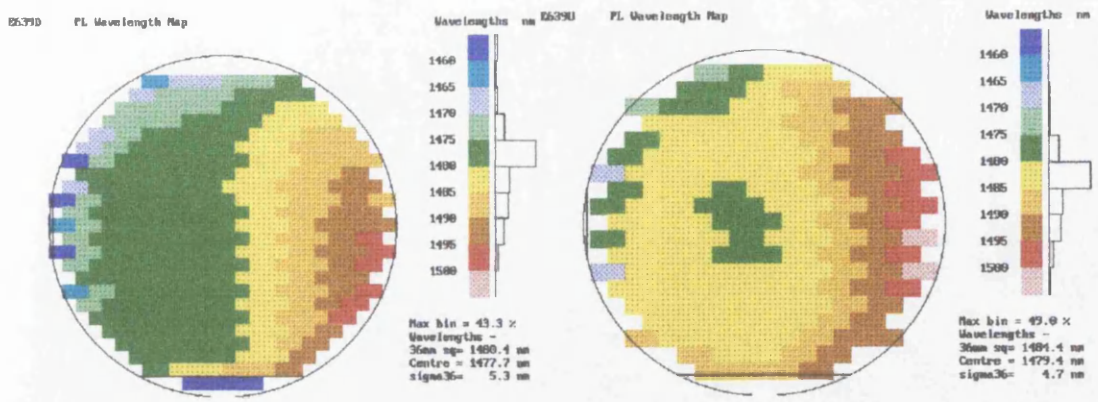

Figure 7.21 Room temperature PL wavelength map of 2x2'" wafers of third generation 1480nm pump laser structures grown simultaneously. Standard deviations in PL wavelength are 5.4 nm for the upstream wafer (shown on right) and 6.4 nm for the downstream wafer (shown on left).

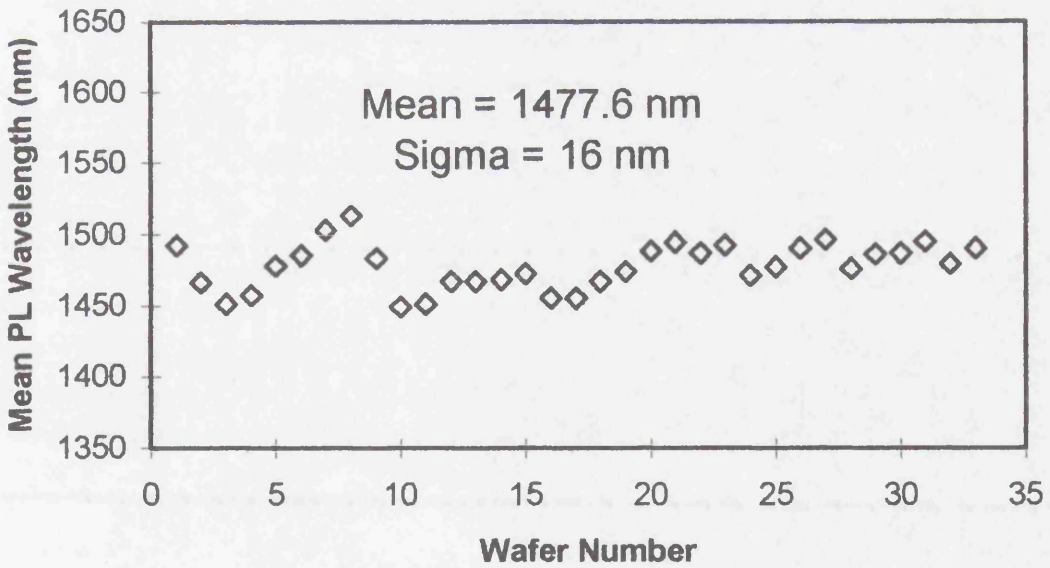

Figure 7.22 Variation in mean peak PL wavelength over 33 wafers. The standard deviation of the run to run PL mean is calculated to be 15.8 nm.

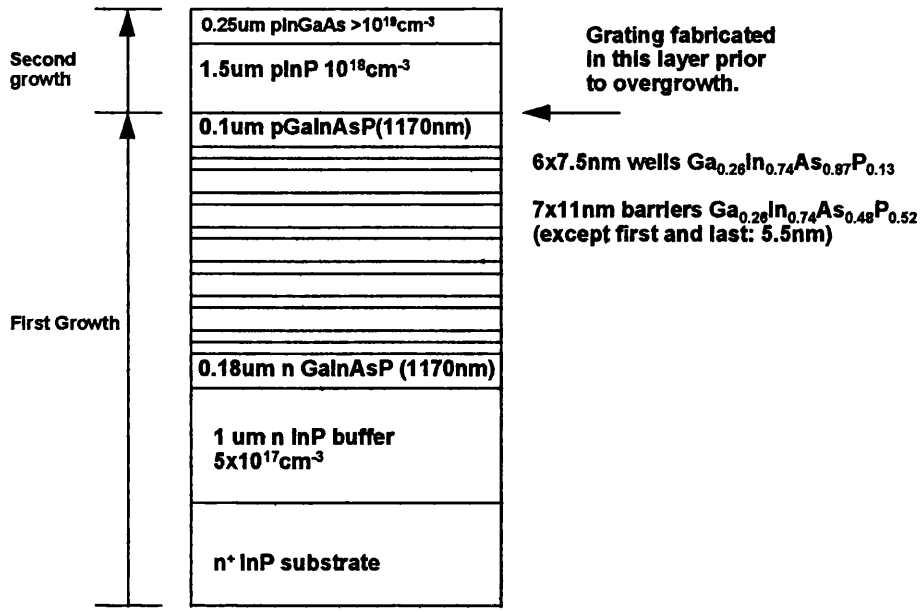

Figure 7.23 Layer structure designed for high speed laser applications. Well and barrier compositions are identical to those used in the third generation of 1480nm pump structures.

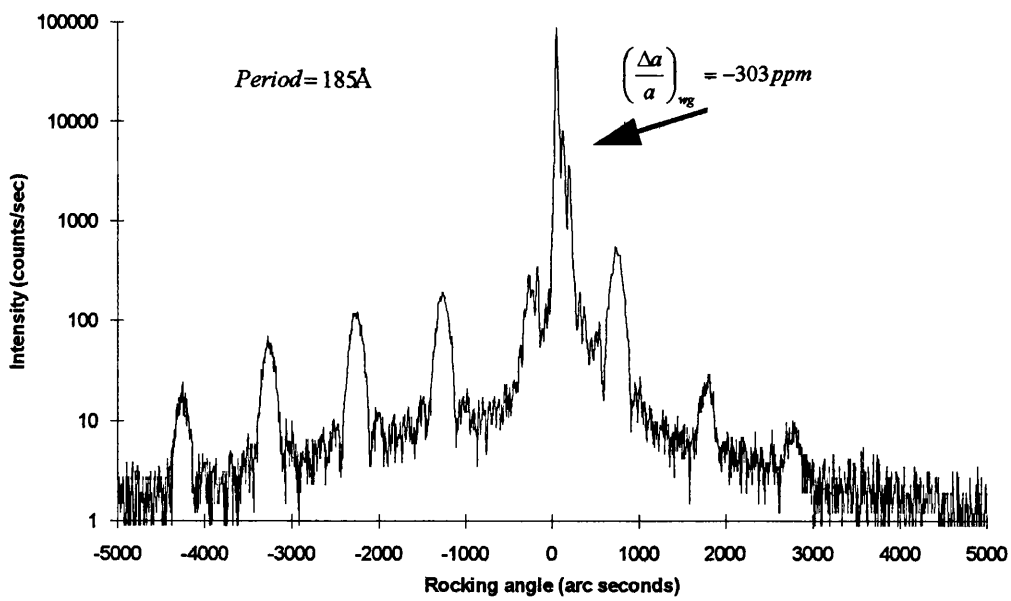

Figure 7.24 HRXRD rocking curve of high speed laser structure described in figure 7.23.

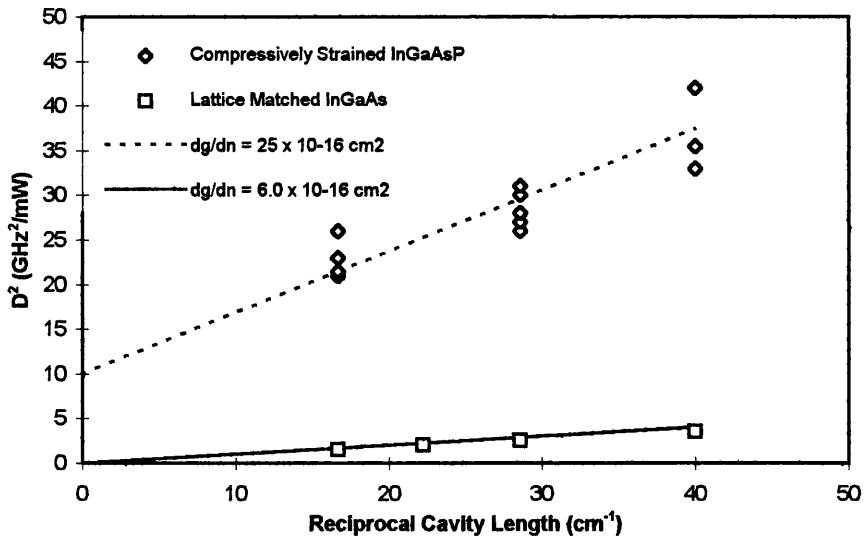

Figure 7.25 Plot of D^2 against reciprocal cavity length. D is the slope inferred from the measure dependence of laser resonant frequency against laser output power. D^2 plotted for cavity lengths of 250μm, 350μm and 600μm.

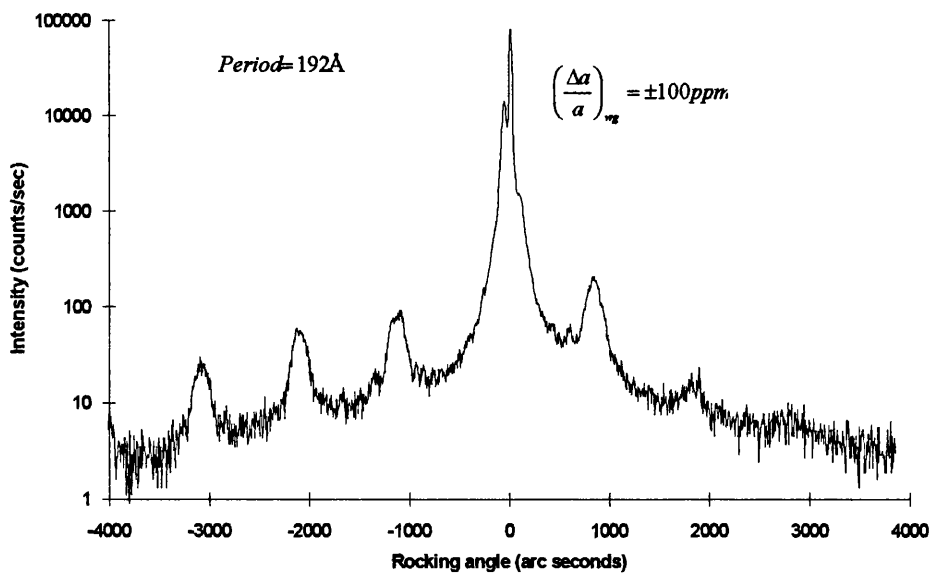

Figure 7.26 HRXRD rocking curve of high speed laser structure which has been overgrown on a grating fabricated on the n-side of the device. The structure has an identical MQW active region to that described in figure 7.23. It is therefore surprising to observe that this rocking curve is inferior to that shown in figure 7.24.

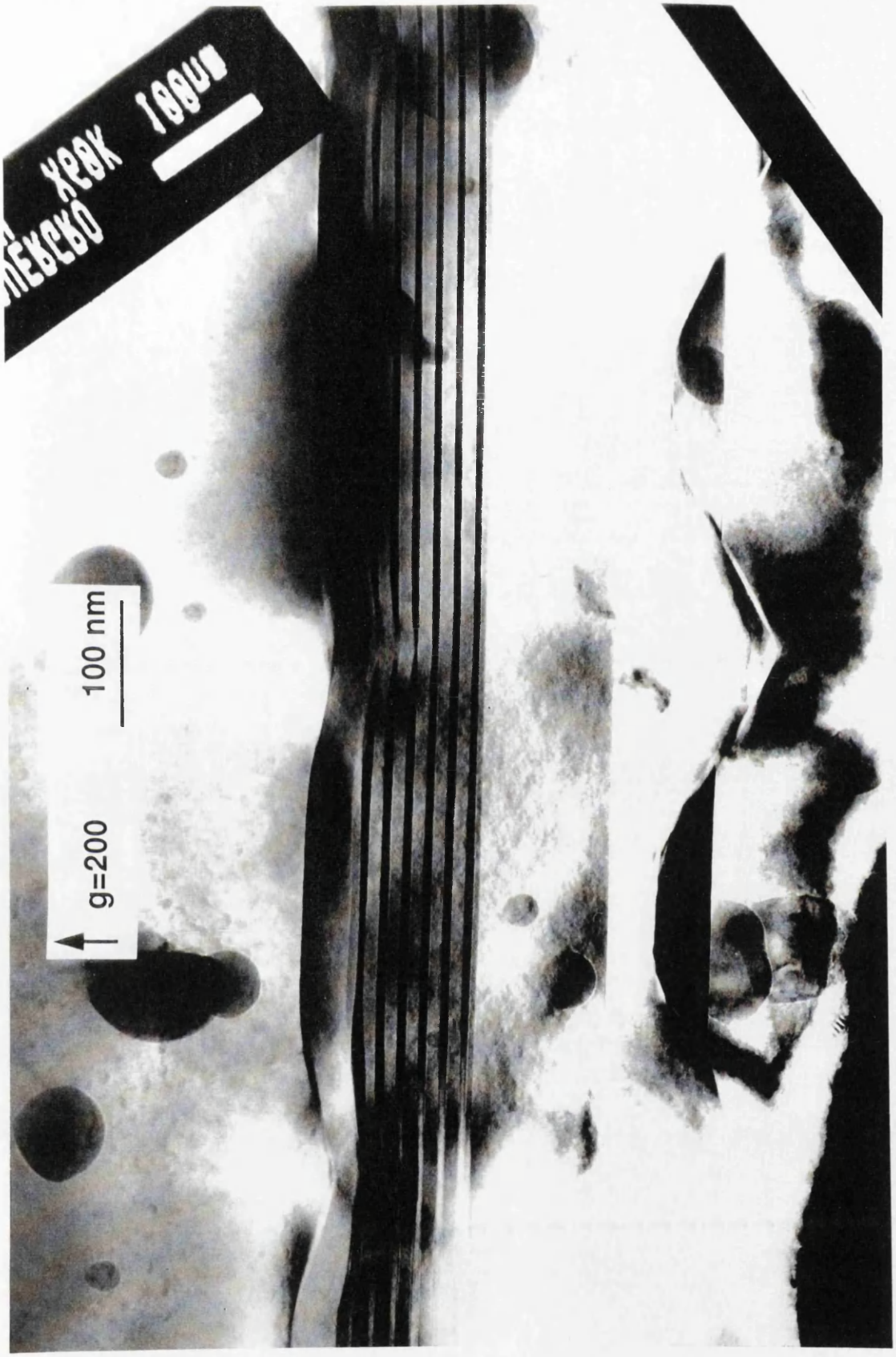

Figure 7.27 Cross sectional TEM image (g=200) of buried grating structure whose rocking curve is shown in figure 7.26. Thickness modulations are seen to occur directly above the troughs of the fabricated grating where it is known that material has 'mass-transported' from the n-GaInAsP layer. The mass transport resulted in a lateral strain variation whose period is defined by the grating.

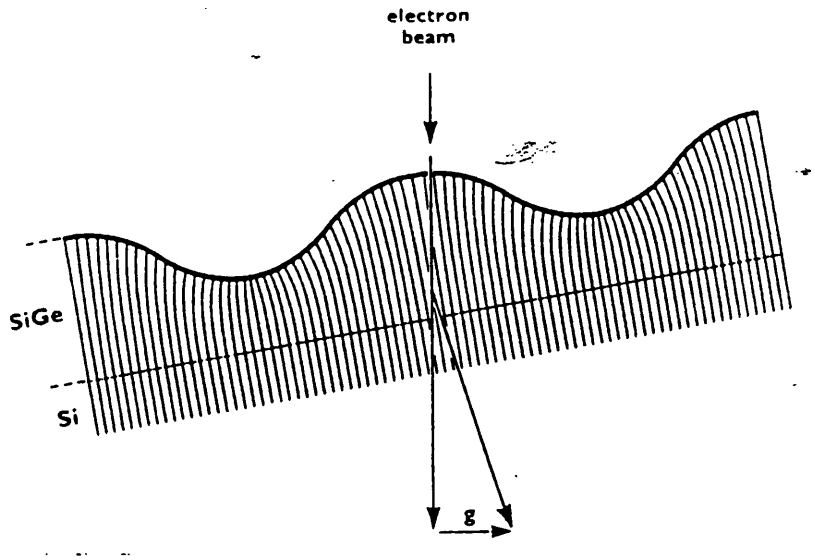

Figure 7.28 Schematic diagram which illustrates the evolution of a rippled surface in the compressively strained Si/Si_xGe_{1-x} system. As deposition progresses larger atoms, Ge, prefer to reside on peaks where the lattice constant is larger. Smaller atoms, Si, prefer to reside on troughs where the lattice constant is smaller. Such compositional clustering exacerbates the effect further.[23]

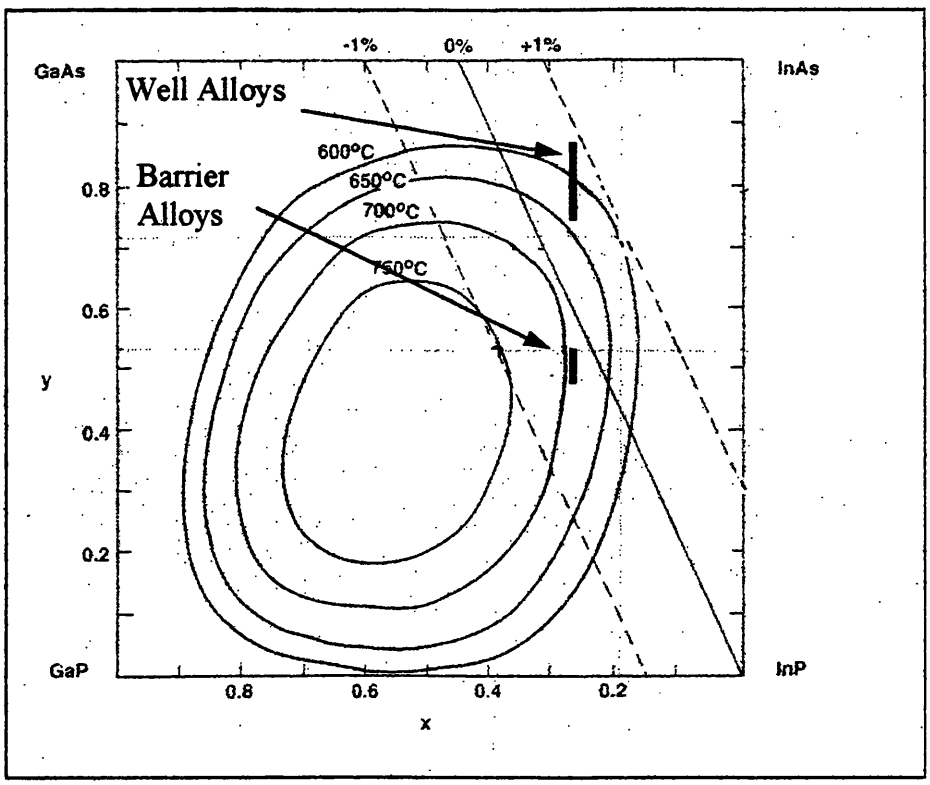

Figure 7.29 Miscibility gaps in the Ga-In-As-P parameter space for growth temperatures of 600, 650, 700 and 750°C. The composition ranges of the well and barrier alloys used so far are plotted.

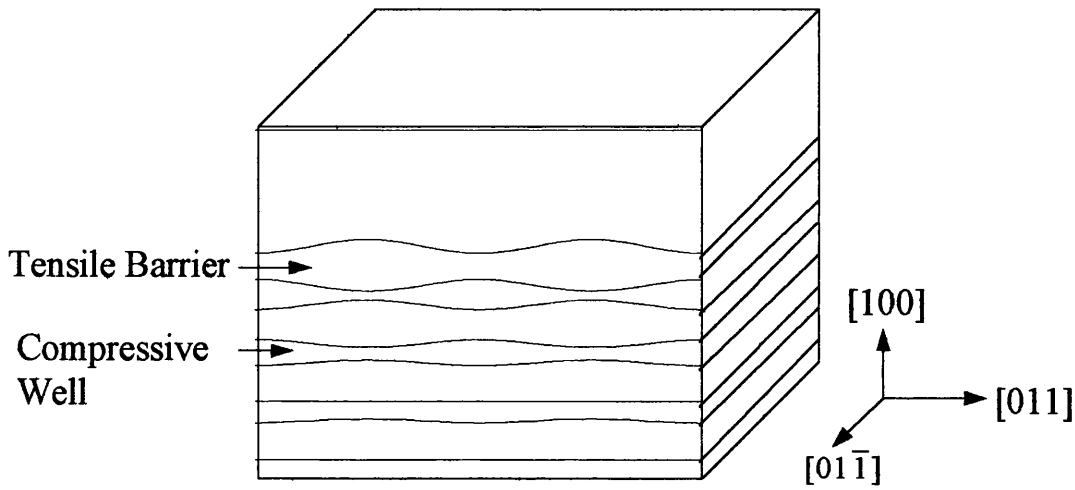

Figure 7.30 Schematic diagram depicting the anisotropy in thickness modulations of strain compensated MQW structures.[28]

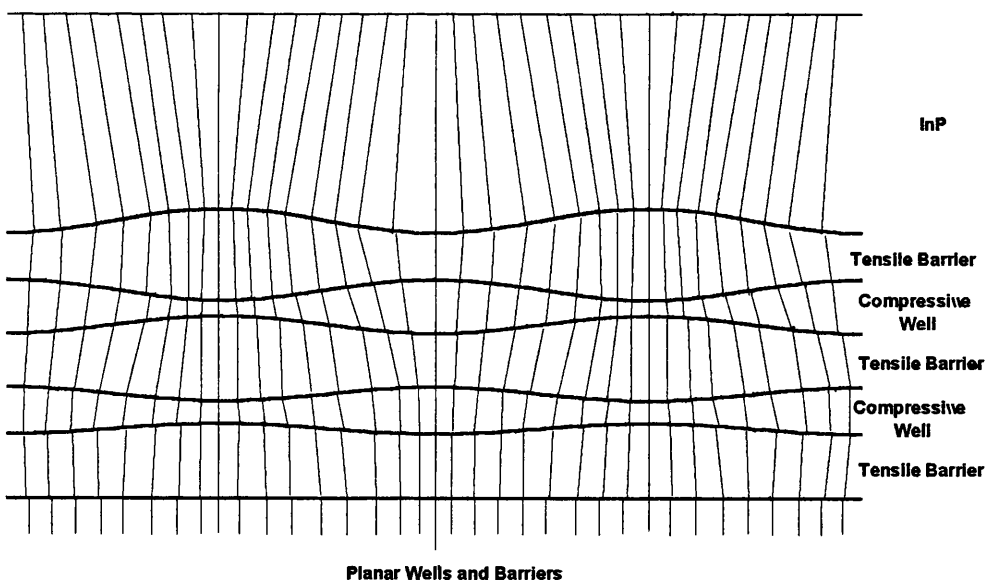

Figure 7.31 Schematic diagram describing the evolution of anti-phase thickness modulations in strain compensated MQW structures.[28]

Chapter 8

Growth and Assessment of Strain Compensated Structures with ±1% GaInAsP and ±1% GaInAs MQW Regions

8.1 Introduction: Electro-absorption Modulators

InP-based electro-absorption modulators are becomingly increasingly important for use in high speed, long haul optical communication systems. One of their key characteristics is that they suffer from less wavelength chirp at high modulation frequencies than directly modulated lasers. Wavelength chirp in a directly modulated laser arises as a result of the dependency of refractive index on the carrier density in the laser active region. When the laser is in the off state the refractive index is defined by the material alone, however at a post-threshold biasing condition the refractive index will decrease as a result of the high carrier density. The magnitude of the chirp can be related to the linewidth enhancement factor and, ultimately, the differential gain and carrier induced refractive index change[1], as defined in equations 8.1.1 and 8.1.2.

$$\Delta\nu_{chirp} \approx \sqrt{\left(1+\alpha_H^2\right)} \qquad (8.1.1)$$

$\Delta\nu_{chirp}$ - frequency chirp

α_H – linewidth enhancement factor

$$\alpha_H = \frac{-4\pi}{\lambda}\frac{dn/dN}{dg/dN} \qquad (8.1.2)$$

λ - wavelength of operation

dn/dN - carrier induced refractive index change

dg/dN - differential gain

FWHM wavelength chirp values of 2.0Å have been measured for 1.5μm strained InP-GaInAsP lasers at 10 GBits/sec[2]. Such a value of wavelength chirp is known to impair the transmission performance of lightwave systems[3]. To overcome this limitation, an alternative method of modulation can be used which relies on running the laser in a CW mode and modulating the optical signal with a separate device.

Electro-absorption (EA) modulators employing the quantum confined Stark effect (QCSE) can be designed to operate with zero chirp characteristics. An EA modulator is a device that exhibits an electric field dependent absorption co-efficient. In an MQW structure, the absorption characteristics are described by the QCSE. Figure 8.1a shows the flat band structure of a single MQW, when an electric field is applied the band structure is modified as shown in figure 8.1b. The energy difference between the conduction and valence sub-bands in the quantum wells is seen to reduce on the application of the electric field. This is caused by the transformation of the quantum well from a square potential well model to a triangular potential well model. Hence, as a result of applying an electric field the absorption edge of the quantum well structure is pushed out to longer wavelengths, attenuating the optical signal at wavelengths that were close to the flat band absorption edge. This phenomenon is described as the quantum confined Stark effect. It is therefore desirable to design the absorption band edge of the modulator to be less than the emission wavelength of the source, so that, at zero applied field, the modulator is essentially transparent.

The modulator device comprises a p-i-n structure, where the MQW EA region is located in the "intrinsic' region of the diode. An electric field is applied to the MQW by reverse biasing the p-n junction. The absorption properties at the band edge of the MQW structure are described by exciton formation. When a photon is absorbed, an electron-hole pair is generated which are Coulombically bound together in the plane of the quantum well. The generation of excitons during the absorption process produces sharp absorption peaks[4], an example of which will be presented on one of the structures grown in section 8.2.

Such modulators have been studied at BNR Europe for several years and the preferred structure comprised lattice matched wells and barriers. The devices were, however, prone to absorption saturation i.e. when the CW optical signal power at the input of the modulator was increased beyond a certain value, the photocurrent, which is generated via the absorption of the input light, would saturate. Degradation of the dynamic performance of the device was observed when the device was operated with input powers near this saturation value[5]. This effect has been observed by others[6] and attributed to the accumulation of holes trapped by the large valence band edge discontinuity between the wells and barriers present in the lattice matched quantum well structures used. Using the computer program described in section 3.4, Czajkowski[5] of BNR Europe proposed that, by careful selection of the well and barrier alloy compositions, the valence band edge discontinuity could be reduced. With compressive strain in the wells and tensile strain in the barriers, the lowest energy step for holes is between the heavy hole confined state in the wells and the light hole band in the barrier. It was hoped that this would help overcome the saturation effects. Theoretically calculated valence band offests for the previously studied lattice matched and the proposed compressive well/tensile barrier MQW structures are illustrated schematically in figures 8.2a and b respectively.

It can be seen from the lattice matched case (λ_{well}=1.58μm, $\lambda_{barrier}$=1.18μm, well width = 90Å) that the lowest potential barrier for holes in the wells is 167 meV. However, in the strain compensated case (λ_{well}=1.58μm, ε_{well}=1%, $\lambda_{barrier}$=1.25μm, $\varepsilon_{barrier}$=-1%, well width = 96Å), the behaviour of the holes in the tensile barrier becomes light-hole-like and the potential barrier for holes in the well is reduced to 63meV.

This chapter discusses the attempts made at BNR Europe to grow these structures, using wells with compressive strain of 1% and barriers with tensile strain of 1% (from now on termed ±1% MQW), and the successes and problems encountered. A series of experiments is then described to help assist our understanding of strain compensated MQW structures and their propensity to suffer from thickness modulated growth. These experiments examine both ±1% GaInAsP MQW and ±1% GaInAs MQW structures.

8.2 ±1% GaInAsP MQW Electroabsorption Modulators

8.2.1 MOVPE Growth

In chapter 7, we tended to directly calibrate strained alloys with only modest amounts of mismatch e.g. the barrier material. With the use of five crystal HRXRD, however, the determination of mismatch in layers with thickness < 200 Å, became possible. It should be stressed that this was not possible with conventional double crystal XRD, as the background noise is greater than the signal from such a thin layer. To ensure that the critical layer thickness had not been exceeded and that no relaxation had occurred, the calibration layers were examined, using PL imaging, to check for any dark line defects associated with strain relieving dislocations. Calibration layers with thicknesses between 200-300Å were grown and capped with 20Å of InP, the strained layer being thick enough to enable the PL wavelength to be interpreted as the bulk wavelength. The cap layer was deliberately thin in order that the thickness fringes generated by it in the HRXRD rocking curve would be much further apart than those of the strained layer. This allowed the strained layer thickness, and consequently the growth rate, to be determined. The growth conditions and calibration details for the alloys used in the electro-absorption modulator are given below in table 8.1:

Table 8.1 Summary of the growth conditions and calibration details for the alloys used in the electro-absorption modulator.

Growth conditions	Well V/III ratio	114
	Barrier V/III ratio	472
	Well growth rate	276 Å/min
	Barrier growth rate	380 Å/min
Assessment results	Barrier material	λ=1231.5nm, (Δa/a) = -0.95%
	Well material	λ=1579.4nm, (Δa/a) = 0.98%
Compositions	Well	$Ga_{0.19}In_{0.81}As_{0.73}P_{0.27}$
	Barrier	$Ga_{0.39}In_{0.61}As_{0.53}P_{0.47}$

The full modulator structure, comprising 6 wells, shown in figure 8.3 was grown and assessed. Note that this structure did not start and end with half the barrier thickness as used with previous structures. Therefore, exact strain symmetry would not be achieved and, instead of being fully compensated, the structure would have a small net tensile strain.

The surface morphology of the structure deteriorated from very good in the downstream area of the wafer to a rippled morphology at the upstream end. This was reminiscent of observations made on the 16 well structure described in section 7.2.2. The PL intensity, as shown in figure 8.4, and the HRXRD rocking curve, as shown in figure 8.5, both deteriorated in the rippled area of the wafer. These observations are, once again, consistent with the occurrence of the thickness modulated MQW growth effect discussed in chapter 7. As a result of these observations, the growth of the modulator structure was repeated with the number of wells reduced from six to three. This gave sufficiently good material quality across the wafer for use as electro-absorption modulators. This is demonstrated by the well defined excitonic features and the extinction of the photocurrent with increasing reverse bias highlighted in figure 8.6.

8.2.2 Characterization of Strain-Compensated EA Modulators

The modulators fabricated from this material demonstrated improved power handling characteristics, with no signs of any deterioration in absorption, with CW input powers up to 10 dBm (10mW). This compares favourably with the results from both 6 and 14 well devices using lattice matched wells (λ=1.58μm) and barriers (λ=1.18μm). These structures, whose well and barrier thicknesses were both similar to the strain compensated structure, exhibited a sub-linear relationship between the absorbed photocurrent and the CW optical input power at input power levels in excess of -2dBm (0.63mW). A comparison of the power handling characteristics of the

lattice matched and strained devices is shown graphically in figure 8.7. The fibre coupled output power of the lattice matched device saturates at input powers in excess of -2dBm, whereas the strained device is capable of handling input powers up to 8dBm. In addition to observed improvement in power handling, the strained EA devices exhibited improved 10 Gbit/sec modulation properties as a result of the suppression of hole trapping effects. Figure 8.8 shows the 10 Gbit/sec transmitted eye's for lattice matched and strained modulators with input powers of +5.3 dBm and +10dBm respectively. The input power launched into the lattice matched device is known, from figure 8.7, to be in the power saturation mode. The eye diagram is a time domain electrical measurement that is acquired by feeding the fibre couple output of the EA modulator into a high bandwidth (>10GHz) detector and then connecting the electrical ouput from the detector into a sufficiently fast oscilloscope. The EA modulator is packaged in a similar way to the high speed laser described in section 7.3.1 and modulated using a 10 Gbit/sec digital pattern generator which is also used to trigger the high speed oscilloscope. The modulator was biassed at -2.0V with a 3.6V pk-pk modulation. The eye diagrams shown in figure 8.8 are a superposition of all possible digital states or patterns (000, 001, 010, 011, etc) and give feedback as to whether there is a pattern dependence or a modulation problem with the device under test. In the case of the lattice matched device we can discern an eye closure which is not present in the strained device, the long 'turn-off' time observed in the lattice matched devices is a direct result of holes being trapped. It should also be noted that the strained device is operated at significantly higher input launch power. The combination of high launch power and an eye pattern with no closure make this device most suitable for 10Gbit/sec transmission applications.

Instead of allowing the growth of a limitless number of strained compensated quantum wells, the use of strain compensation is now seriously limiting the number of wells that can be grown, placing unwelcome constraints on device design. Several points can be listed from the observations made so far regarding the limits of strain compensation:

- it is possible to grow more wells of one composition than of another. The six well structure, grown in section 7.3, had a total thickness-mismatch product of 6x75 Åx1% = 450 Å.% and showed no signs of thickness modulated growth, whereas the 6 well sample discussed above exhibited thickness modulated growth after 4x92 Åx1% = 368 Å.%.
- the onset of thickness modulated growth may be exacerbated by using tensile alloys with higher strain. For example, the six well structure described in section 7.3 had a barrier tensile strain of between 0.25% and 0.3%, whereas the six well structure above had a barrier tensile strain of 1%.
- the value of net strain may affect the introduction of thickness modulations. The six well sample in section 7.3 had a net compressive strain whereas the structure described above

had a net tensile strain. It is not known if there is an influence of the sign of the net strain (this will be discussed in chapter 9).

- the susceptibility of a given pair of well and barrier compositions to suffer from the thickness modulated growth effect may be related to their proximity to the miscibility gap as proposed earlier.

The last point is illustrated in figure 8.9. The well and barrier compositions grown in this section are closer to (in fact the barrier is far inside) the influence of the miscibility gap at 650°C than the combination of alloys discussed in section 7.3. The area of the miscibility is known to reduce with increasing growth temperature[7]. If the occurrence of thickness modulated growth is related, or partially related, to the miscibility gap then we should observe a variation in the severity of this effect with growth temperature, on a structure with a given combination of well and barrier alloys.

8.3 The Effect of Growth Temperature on the Quality of ±1% GaInAsP MQW Structures

The object of this investigation was to assess the influence of changing the growth temperature on the severity of thickness modulated growth present in a strain compensated MQW structure, with fixed well and barrier compositions. The biggest problem in undertaking this type of investigation is that it can be very calibration intensive, i.e. the growth conditions for the well and barrier compositions need to be calibrated at each growth temperature studied. This is a result of the variation of the cracking efficiency of PH_3 with growth temperature, i.e. if the growth temperature is reduced the amount of reactants that supply Phosphorus to the growing layer is also reduced, hence the PH_3 flow has to be increased to compensate. In an attempt to reduce some of the effort involved, the following procedure was adopted:

- the well and barrier alloy compositions were chosen so that they had identical As:P ratios and consequently could use the same AsH_3 and PH_3 gas flows. Such structures have received much attention recently as they have been shown to have reduced well/barrier interdiffusion[8].
- the well and barrier growth conditions were determined at 650°C. The growth conditions for a lattice matched alloy with the same As:P ratio as the wells and barriers was also determined at 650°C.
- the use of TMGa and TMIn gas flows determined at 650°C for growths at other temperatures. The decomposition of TMGa and TMIn over the temperature range 600°C-700°C is known to be constant.

- evaluating the AsH_3 and PH_3 flows required at each temperature of interest through the growth of the lattice matched alloy with the same As:P ratio as the wells and barriers.
- using the TMGa and TMIn gas flows determined at 650°C and the AsH_3 and PH_3 flows determined from the lattice matched alloy at the new growth temperature for the growth of well and barrier material at the new growth temperature. The compositions selected are give below in table 8.2:

Table 8.2 - Chosen compositions for the study of growth temperature on strain compensated quaternary MQW growth.

	Wavelength	**Mismatch**	**Inferred Composition**
Well	λ = 1590 nm	$\Delta a/a$ = +1%	$Ga_{0.19}In_{0.81}As_{0.72}P_{0.28}$
Lattice match	λ = 1420nm	$\Delta a/a$ = 0%	$Ga_{0.34}In_{0.66}As_{0.72}P_{0.28}$
Barrier	λ = 1370 nm	$\Delta a/a$ = -1%	$Ga_{0.48}In_{0.52}As_{0.72}P_{0.28}$

These compositions are plotted on the Ga-In-As-P composition diagram shown in figure 8.10. For growth at 600°C, the barrier alloy is inside the miscibility gap and the well alloy just outside. At 650°C, the well alloy is further outside and the barrier alloy is still inside the miscibility gap. At 700 °C, the well alloy is yet further outside and barrier alloy is just inside the miscibility gap. The gas phase V/III ratios used for growing the well and barrier alloys at 600°C, 650°C and 700°C are listed below in table 8.3.

Table 8.3 - Gas phase V/III ratios used in the growth of the well and barrier alloys

	600°C	**650°C**	**700°C**
Well material	773	134	875
Barrier material	291	50	329

The PL intensity of the lattice matched alloy did not vary appreciably between these growth temperatures indicating that the steps taken to overcome the cracking of PH_3 at 600°C were successful.

A schematic diagram of the structures grown is shown in figure 8.11; note there are no lattice matched waveguide layers sandwiching the MQW region as in all previous growths. Half thickness barriers are again used at the beginning and end of the MQW region to maintain strain symmetry and achieve exact strain compensation.

Three, identical six well structures were grown at 600°C, 650°C and 700°C respectively. The sample grown at 600°C had the worst surface morphology and did not photoluminesce. The structures grown at 650°C and 700°C exhibited improved surface morphologies and PL intensities. Figure 8.12 compares the rocking curves of the three samples. It is obvious that the 600°C sample has the most inferior rocking curve, whereas those grown at 650°C and 700°C have similar features. The behaviour of the 600°C sample supports the miscibility gap argument as the barrier material is far inside, and the well material just outside the calculated miscibility gap. However, the observation that the 650°C and 700°C samples behave alike, taken alone, does not support the miscibility gap argument. To further investigate the efficacy of strain compensation at these two temperatures, two twelve well samples were grown. Both samples had similar surface morphologies, the 650°C sample did not luminesce but the 700°C sample showed similar PL intensity to the 6 well sample grown at the same temperature. Figure 8.13 compares the rocking curves of the 650°C and 700°C growths and shows that the 700°C sample is structurally superior. This adds further support to the miscibility gap argument but does not account for the observation that both the six well samples looked similar. Figure 8.14 shows the cross sectional TEM's of both the 12 well samples. In the 650 °C sample, 5 wells were grown before the commencement of thickness modulated growth, whereas in the 700°C sample, 9 wells were grown before the growth is perturbed.

Thus, a significant improvement in the crystalline quality of an identical ±1% GaInAsP MQW structure has been observed with increasing growth temperature. At 600°C the growth was generally poor, at 650°C, 400 Å.% (=5x80 Åx1%) of well material was grown and, at 700°C, 720 Å.% (=9x80 Åx1%) of well material was grown. The latter represents the largest amount of well material, as part of a strain compensated MQW, grown so far in this study. Further questions arise as a result of these observations :

- how far outside the miscibility gap do we need to operate so as not to be influenced by it?
- are the other growth conditions important, e.g. does the gas phase V/III ratio play a role?
- does the mechanism that promotes thickness modulated growth in the Si/Si_xGe_{1-x} system, i.e. one that is independent of spinodal decomposition, also occur in strain compensated GaInAsP MQW structures?

All of the above points are addressed in the next section which deals with the growth of ±1% strain compensated GaInAs structures.

8.4 The Effect of Growth Conditions on the Quality of ±1% GaInAs MQW Structures.

An MQW structure comprising alternate GaInAs tensile barriers and compressive wells, has many advantages over a similar structure using GaInAsP for the study of the effect of growth conditions on the occurrence of thickness modulated growth. These ternary alloys are far outside the miscibility gap of the growth temperatures studied so far, hence they should not be prone to spinodal decomposition. The change of growth conditions is relatively straightforward requiring no re-calibration. The V/III ratio can be changed simply by altering the AsH_3 flow and both the composition and growth rate are independent of temperature in the range studied. The cracking of AsH_3 is also thought to be constant over these temperatures, hence we should expect to see little variation in the supply of group V reactants to the growing layer. The structure used to study the effect of these growth conditions comprised 20 x 1% compressively strained ($Ga_{0.32}In_{0.68}As$) wells and 21 x 1% tensile strained ($Ga_{0.61}In_{0.39}As$) barriers, with the first and last barriers being half the standard thickness of 50Å. A schematic of this structure is shown in figure 8.15. A higher number of wells was chosen than in the GaInAsP study as it was expected that these structures would not suffer from thickness modulated growth. Similar structures have been grown previously by Quillec et al, but no comments were made regarding the occurrence of thickness modulations[9].

The expectation that a 20 well ±1% GaInAs structure would not suffer from thickness modulated growth, however, proved to be invalid. A structure grown at 650°C had the characteristic morphology, X-ray rocking curve and PL image of a structure suffering from this phenomenon. A constant AsH_3 flow was used to grow the well and barrier material. The flow could be varied so that a range of AsH_3 partial pressures between 0.063 Torr and 2.336 Torr could be achieved, the latter representing the highest AsH_3 gas flow that the reactor would permit. Figure 8.16 shows the rocking curves of two samples, both grown at 650°C, with these 2 extreme values of AsH_3 partial pressure, and it is clear that the structure grown with the higher AsH_3 flow exhibits more intense, sharper satellite peaks. The improvement in the rocking curve quality represents, as previously shown, an increased ability to grow more planar wells and barriers. The growth conditions for this 'improved' sample were then used as a benchmark, to investigate the effect of growth temperature. The temperature was varied, in 25°C steps, between 550°C and 700°C.

In contrast to the ±1% GaInAsP MQW structures, an improvement in surface morphology was observed with reduced growth temperature, the samples grown at and below 600°C all having featureless surfaces. Figure 8.17 illustrates the rocking curves of samples grown at 600°C, 650°C and 700°C. They confirm the morphology observations, indicating an improvement in structural quality at lower temperatures. Figure 8.18 illustrates the PL intensity maps for all the samples

grown between 550°C and 675°C. The 700°C sample did not luminesce. The best intensities, and intensity uniformities, were obtained at 550°C and 575°C. As these results were so contrary to the ±1% GaInAsP results, the samples grown at 600°C, 650°C and 700°C were assessed by cross sectional TEM to confirm that thickness modulated growth was occurring and not some other deleterious growth effect; these are shown in figure 8.19. No modulations were observed in the 600° C sample, merely perfectly planar wells and barriers, representing a total of 20 x 1% x 46 Å = 920 Å.% compressively strained material, the largest grown in this study so far. The samples grown at 650°C and 700°C both showed thickness modulations in the upper wells and barriers of the stack and, in the 700°C sample the modulations had become so strong that three dimensional growth and dislocation generation was observed. It should be noted that the samples grown below 550°C showed reduced PL intensity and reduced growth rates, as observed from the MQW periodicity in the HRXRD rocking curve. This reduction in growth rate below a certain temperature is known to be a characteristic of the MOVPE process[10].

Hence it appeared that by carefully selecting the growth conditions, thickness modulations could be suppressed. To confirm that these optimisations in growth conditions were not limited to this specific structure, the number of wells was increased from 20 to 50. A 50 well structure grown at 600°C had similar properties to the 20 well structure with the TEM image shown in figure 8.20, demonstrating planar well and barrier growth throughout the structure. To demonstrate the need for strain compensation in strained layer MQW's with large numbers of wells, a similar structure was grown with no compensating tension in the barriers as lattice matched InGaAs were used instead. Figure 8.21 shows the details of the assessment of this structure, with cross-hatched surface morphology (a common characteristic observed in mismatched bulk layers), very diffuse X-ray satellite peaks and dislocations present in the TEM micrograph. The dislocations observed in the TEM micrograph seemed to be generated from the base of the uncompensated MQW stack, this being consistent with observations made on uncompensated strained GaAs/InGaAs MQW structures[11].

One other possible cause for the onset of thickness modulated growth is the effect of well width. It was noted that thickness modulated growth occurred more readily for thicker wells (section 8.2, 4x92 Åx1%) than for thinner wells (section 7.3, 6x75 Åx1%). To investigate this, and to test further the above optimisation conditions, i.e. high AsH_3 flow and Tg=600°C, the well and barrier thicknesses were doubled and the number of wells kept at 50. The structure exhibited similar characteristics to the other 'optimised' structures reported above. The rocking curve shown in figure 8.22 illustrates well defined satellite peaks up to the 11th order. This represents a total thickness-mismatch product of 4650 Å.% for both the compressive and tensile material, i.e. almost 0.5μm of 1% strained material, grown as part of a strain compensated MQW structure, with no evidence of

any strain related growth defects such as thickness modulated growth or dark line defects in the PL image. It was, however, interesting to note that when this growth was repeated at 550°C the assessment results indicated that thickness modulated growth had occurred, though this was not observed in a 20 well structure with half the well and barrier thicknesses. Figure 8.23 illustrates the deterioration of the rocking curve of the 550°C sample compared to the 600°C sample.

8.5 Discussion

The incorporation of coherent strain in the wells and barriers of InP-based quantum well devices has again been shown to offer an improvement over lattice matched structures. By engineering the valence band profile, with careful selection of the well and barrier compositions, an electro-absorption modulator with improved power handling characteristics has been developed. However the thickness modulated growth, discussed in the previous chapter, occurred again and limited the number of wells that could be grown to three. This serious limitation initiated further study.

Circumstantial evidence for the effect of spinodal decomposition on the propensity of a structure to suffer from thickness modulated growth was observed. The growth of a strain compensated ±1% GaInAsP MQW stack at different temperatures, with fixed well and barrier compositions, showed an improvement in structural quality, i.e. the number of planar cycles that could be grown, with increasing growth temperature. At 700°C however, thickness modulations were still apparent in the upper wells and barriers of a twelve well structure. Direct evidence for the presence of spinodal decomposition in wells and barriers is difficult to obtain. One possible technique is the use of STEM/EDX to profile the composition of the wells or barriers. Several researchers are known to be attempting this[12] but at the time of writing there have been no successful reports.

In contrast, strain compensated MQW structures using only GaInAs alloys, improve in structural quality with reducing growth temperature. These alloys are far enough outside the miscibility gap to be regarded as insensitive to spinodal decomposition. Thickness modulated growth was observed in samples grown above 600°C. In order for this to occur, there must be a diffusion of surface reactants (namely group III species) from the thinner regions to the thicker regions of the growing layer. This diffusion can be suppressed by providing more group V species to bury the mobile group III species, i.e. they have less time to diffuse across the surface before reacting with a group V species, as demonstrated with increasing AsH_3 partial pressure. The diffusion of group III species can be most successfully suppressed by the reduction of growth temperature. Using this approach, a 50 cycle ±1% GaInAs MQW stack was grown with a total thickness of 0.93μm, with no sign of thickness modulated growth or any other crystallographic defects. The suppression of thickness modulations caused by the reduction of growth temperature was also reported for the $Si/Si_{1-x}Ge_x$ system. It is

not, however, advisable to reduce the growth temperature too far, as a repeat of the above 50 cycle structure at 550°C showed characteristic signs of thickness modulated growth. Here the miscibility gap may be large enough to influence the growth of alloys on the boundary of the Ga-In-As-P parameter space. Following the demonstration of apparently limitless growth of ±1% GaInAs MQW's, Glew of BNR Europe[13] proved that the same optimisation steps, of reduced growth temperature and higher group V partial pressure, were valid in growing 50 cycle ±1% GaInP MQW's on a GaAs substrate. Other reports of successful ternary alloy strain compensated MQW growth have also appeared. Jiang et al[14] demonstrated a similar 50 cycle $InAs_{0.66}P_{0.34}/InP/In_{0.74}Ga_{0.26}P$ (the barrier material comprised a $InP/In_{0.74}Ga_{0.26}P/InP$ sandwich) structure grown at 550°C with good rocking curves and surface morphology. The above results, together with these reports on other ternary alloy structures, suggest that growing alloys on the periphery of the Ga-In-As-P parameter space is relatively straightforward as the growth can be optimised by similar methods.

However, the optimisation of growth conditions for GaInAsP strain compensated alloys seems to be more difficult. To suppress spinodal decomposition, evidence shows that we need a high growth temperature, but this in turn promotes the diffusion of group III species that gives rise to thickness undulations, as observed in ±1% InGaAs structures grown at higher growth temperatures. This may explain why the 700°C, 12 well sample grown in section 8.3 still had thickness modulations in the upper layers. The only optimisation steps remaining were to increase the gas phase group V concentration and to choose a combination of well and barrier alloys that are less influenced by the miscibility gap. Glew, of BNR Europe[15], confirmed the former by repeating the 650°C growth of the structure described in section 8.3 but with well and barrier V/III ratios of 1080 and 580 respectively; the structure had thicker wells and barriers (100Å) than the structure described in section 8.3. He succeeded in growing 12 wells with no thickness undulations but had problems in growing 25. He also grew a series of constant y, i.e. As:P ratio, ±1% GaInAsP MQW structures with different values of y[15]. This enabled him to investigate the effect of the proximity of the alloy compositions to the 650°C miscibility gap, on the maximum number of planar wells that could be grown. His experiment is illustrated in the Ga-In-As-P composition diagram in figure 8.24. Three planar wells were grown with alloy combination C, twelve with B, 25 with D and 50 with A. The 50 well structure had a high density of surface defects and close examination of the TEM cross-section in the defect ridden regions showed that the sample was at the onset of thickness modulated growth. Glew's results give further support to the theory that spinodal decomposition is a cause of thickness modulated growth in strain compensated GaInAsP/GaInAsP MQW structures. However, choosing the optimum well and barrier compositions so that a structure is less prone to thickness modulations, may not be compatible with the optimum choice for device operation. By using higher V/III ratio's in the growth of the wells and barriers Thrush, of BNR Europe, demonstrated the successful growth

of an six well electro-absorption modulator[16] structure similar to that described in section 8.2, with the same improved power handling characteristics of the 3 well device.

One further interesting observation was that the 50 well uncompensated $Ga_{0.47}In_{0.53}As/Ga_{0.32}In_{0.68}As$ structure had no symptoms of thickness modulated growth. The relaxation mechanism was provided by the generation of misfit dislocations, this being consistent with the observations made by Gourley et al[11] for the strain relief mechanism of compressively strained InGaAs wells grown with GaAs barriers and on a GaAs substrate. Cross hatching was also observed on the surface of this sample, a further indication of misfit dislocation generation. The generation of dislocations has only been observed in strain compensated material as a secondary effect to thickness modulations, occurring when the amplitude of the undulation exceeds the individual layer thickness. The next chapter investigates these differences further by studying the growth of un-compensated InP-based MQW structures.

References

1. PJA Thijs, LK Tiemeijer, JJM Binsma and T van Dongen, IEEE J. Quantum Electronics, 30(2), pp477-498, February 1994.

2 Y Matsui, M Nakajima, H Horikawa, T Kunii, Y Ogawa and T Kamijoh, Tech. Dig. OFC Conf., San Jose CA, paper FB2, p 271, 1992.

3 F Dorgeuille and F Devaux, IEEE J Quantum Electronics, 30, pp2565-2572, 1994.

4 DS Chemla and DAB Miller, J Optical Society of America B, Vol. 2, pp1155-1173, 1985.

5. IK Czajkowski, MA Gibbon, GHB Thompson, PD Greene, AD Smith and M Silver, IEE Electron. Lett., 30(11), pp900-901, May 1994.

6. TH Wood, JZ Pastalan, BC Johnson, BI Miller, JL De Miguel, U Koren and MG Young, App. Phys. Lett, 57, pp1081-1083, 1988.

7. GB Stringfellow,, J Cryst. Growth, 58, pp194-202, 1982.

8. A Mircea, A Ouggazzeden, G Promot and C Kazmierski, J. Gryst. Growth, 124,p737, 1992.

9. M Quillec, JY Marzin, J Primot, G Le Roux, JL Benchiomi and J Burgeat, J. Appl. Phys, 59, p2447, 1986.

10. SK Ghandi and IB Bhat, MRS Bulletin, pp37-43, November 1988.

11. PL Gourley, IJ Fritz and LR Dawson, Appl. Phys. Lett, 52(5), pp377-379, 1988.

12. Private communication, U Bangert.

13. Private communication, R Glew.

14. XS Jiang and PKL Yu, Appl. Phys. Lett., 65(20), Nov 1994.

15. RW Glew, K Scarrott, ATR Briggs, AD Smith, VA Wlikinson, X Zhou and M Silver, J. Crystal Growth, 145, pp764-770, 1994.

16. EJ Thrush, RW Glew, PD Greene, MA Gibbon, CJ Armistead, AD Smith, ATR Briggs, K Scarrott, IK Czajkowski, CJ Jones and BL Patel, Proc. International Conference on InP and related materials, Santa Barbara, 1994.

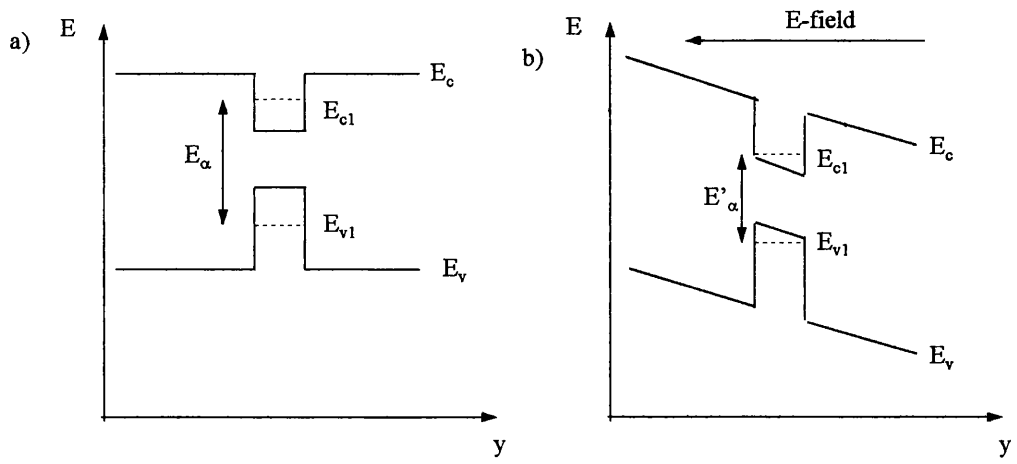

Figure 8.1 Band structure of quantum well under a) no bias (flat band), and b) applied bias. The reduction in energy difference between the conduction and valence quantum well sub-bands is shown schematically upon the application of bias.

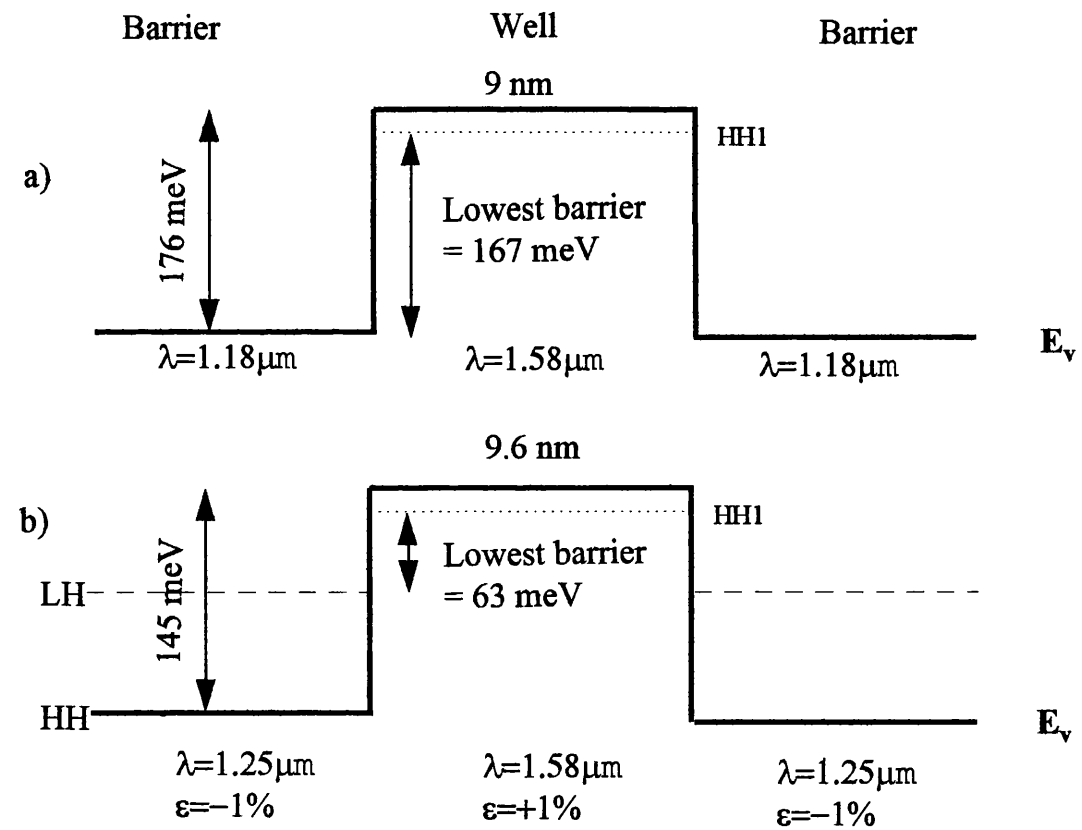

Figure 8.2 Schematic diagrams of valence band offsets and lowest potential barriers for holes in the case of a) the lattice matched structure and b) the proposed strained strauctured.

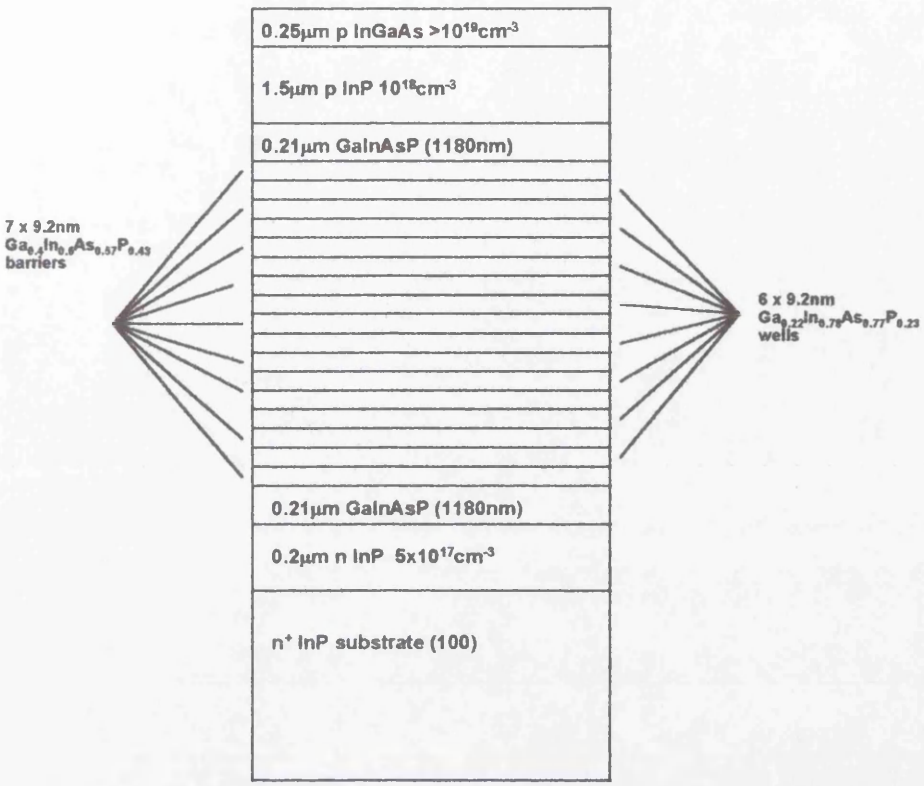

Figure 8.3 Schematic diagram of 6 well strain-compensated electro-absorption modulator structure.

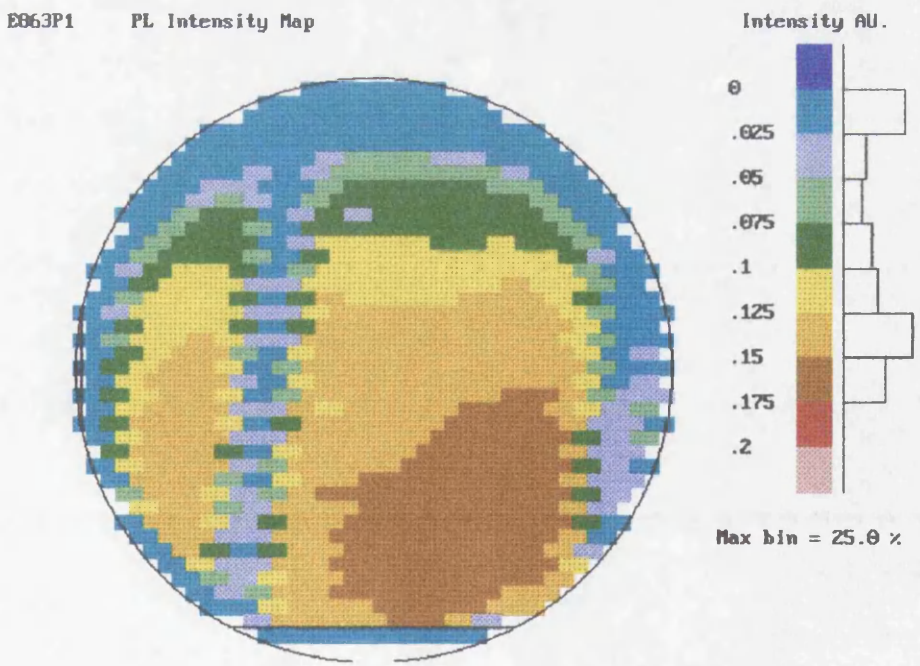

Figure 8.4 Room temperature PL intensity wafer map of structure shown in figure 8.1. A deterioration in the intensity can be observed from the downstream area of the wafer (near the major flat) to the upstream are of the wafer (opposite the major flat)

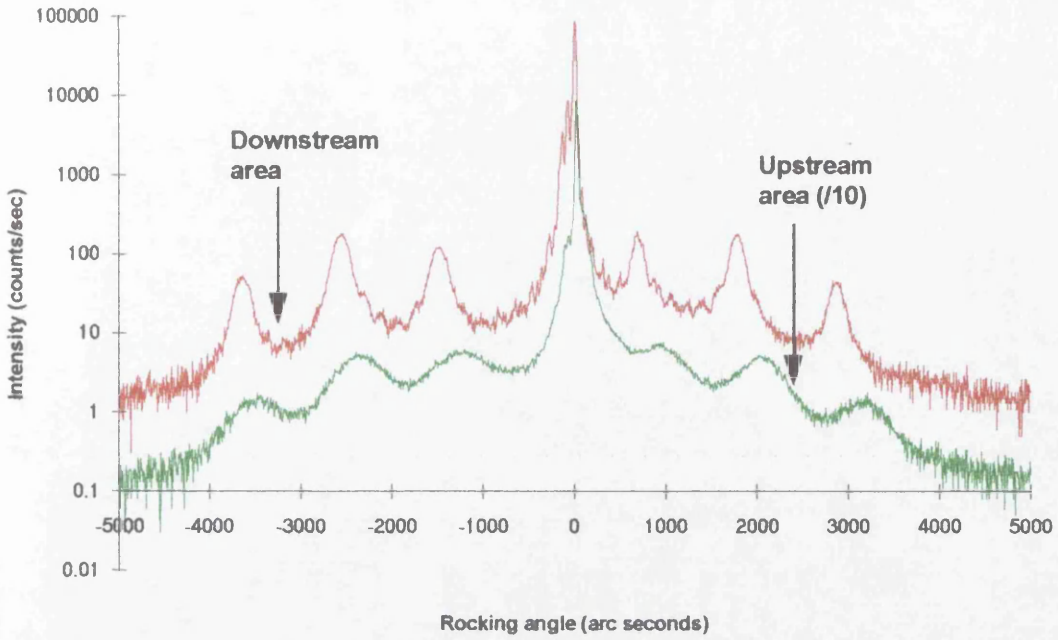

Figure 8.5 Rocking curves taken from the modulator structure shown in figure 8.1. An inferior curve is measured in the low PL intensity upstream area, whereas the (relatively) superior curve is measured in the high intensity downstream area.

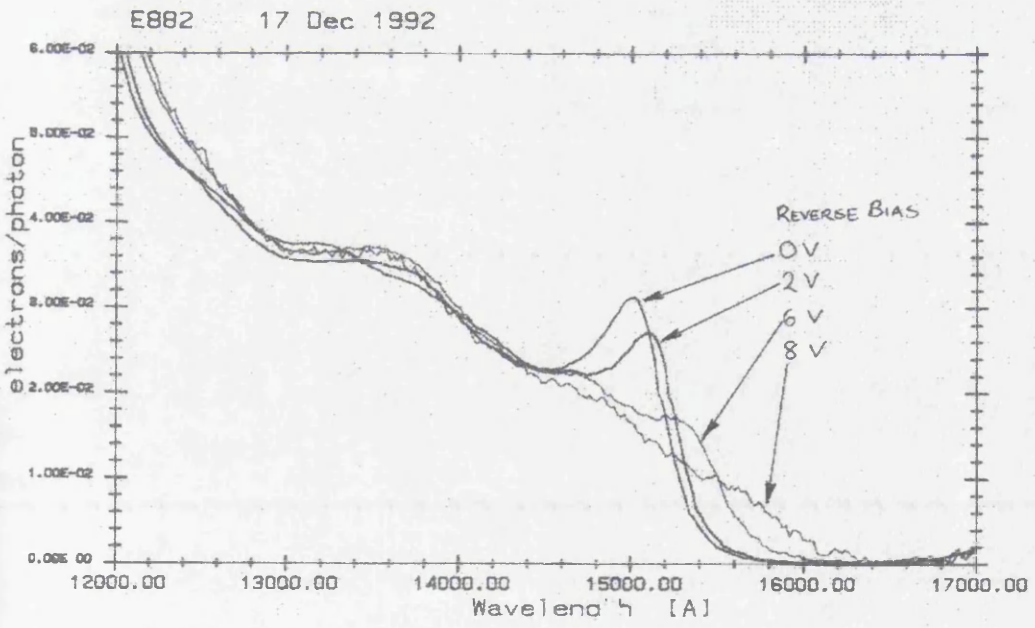

Figure 8.6 Photocurrent spectra of modulator structure grown with the number of wells reduced from six to three. The structure exhibits well defined exitonic features with an extinction of the photocurrent with increasing reverse bias.

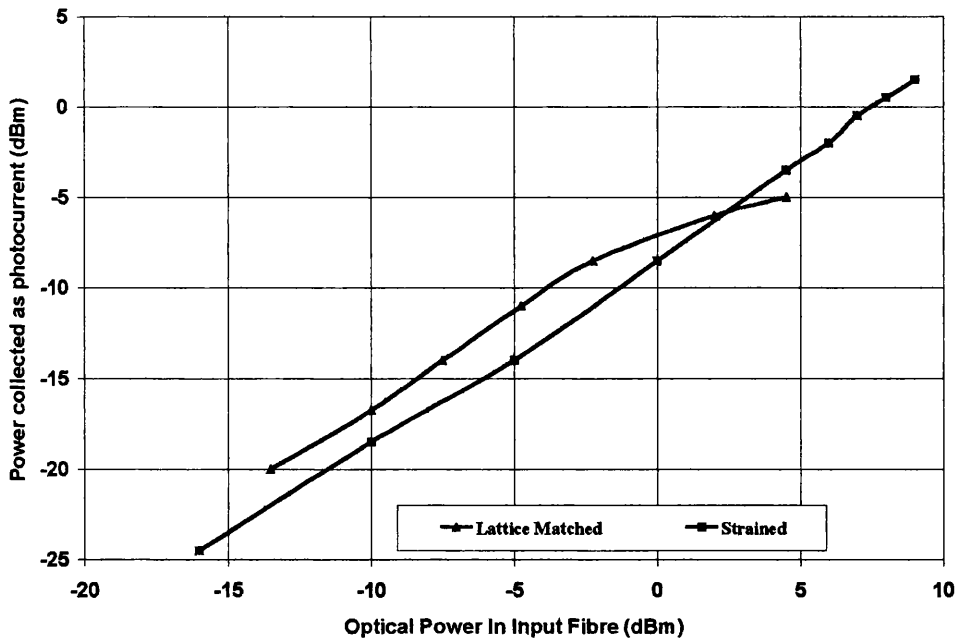

Figure 8.7 Comparison of modulator optical power handling characteristics for lattice matched and strained devices.

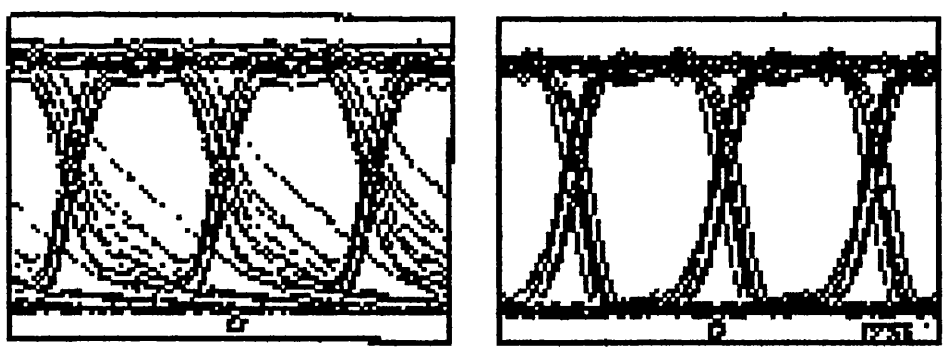

Figure 8.8 Comparison of 10 Gbit/sec transmitted eyes for the lattice matched device at an input power of +5.3 dBm (left) and a strained device with an input power of +10dBm (right).

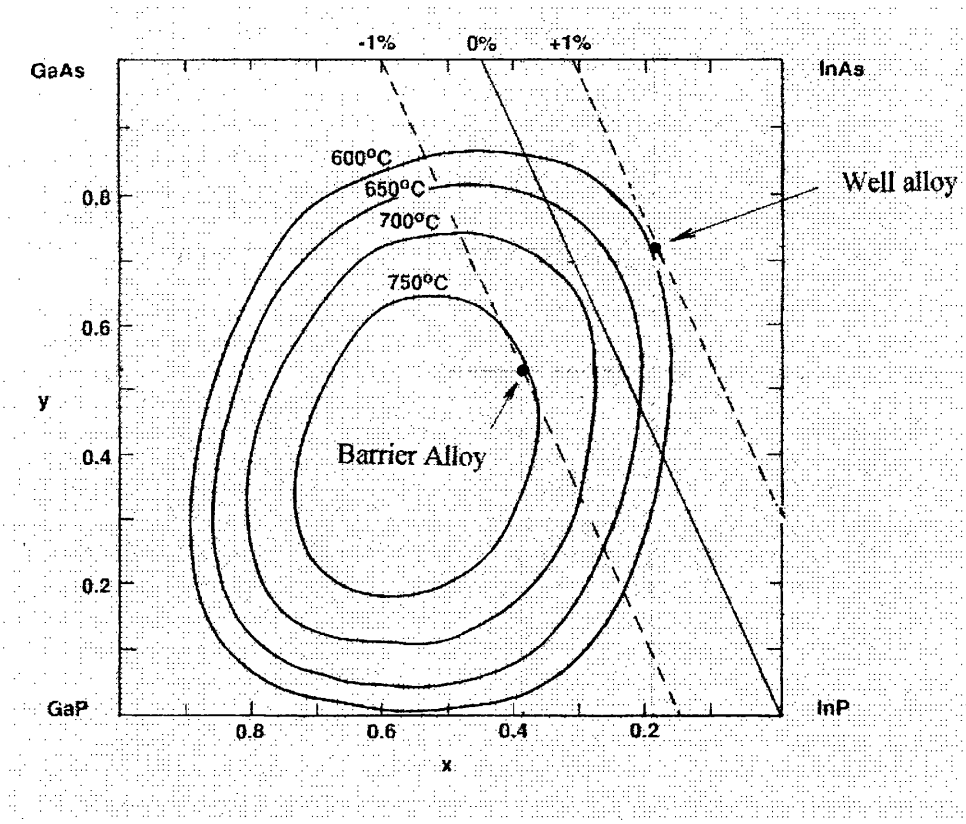

Figure 8.9 Location of the well and barrier alloys used in the modulator structures in relation to the Ga-In-As-P miscibility gaps

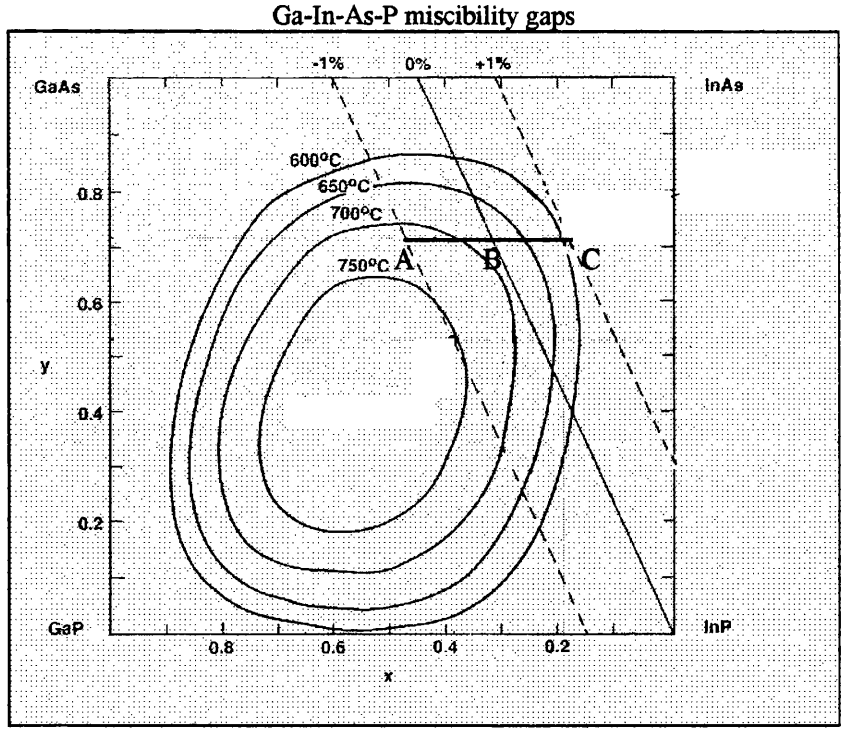

Figure 8.10 Location of the chosen 'constant-y' compositions in relation to the miscibility gaps of $Ga_xIn_{1-x}As_yP_{1-y}$ calculated at different growth temperatures.

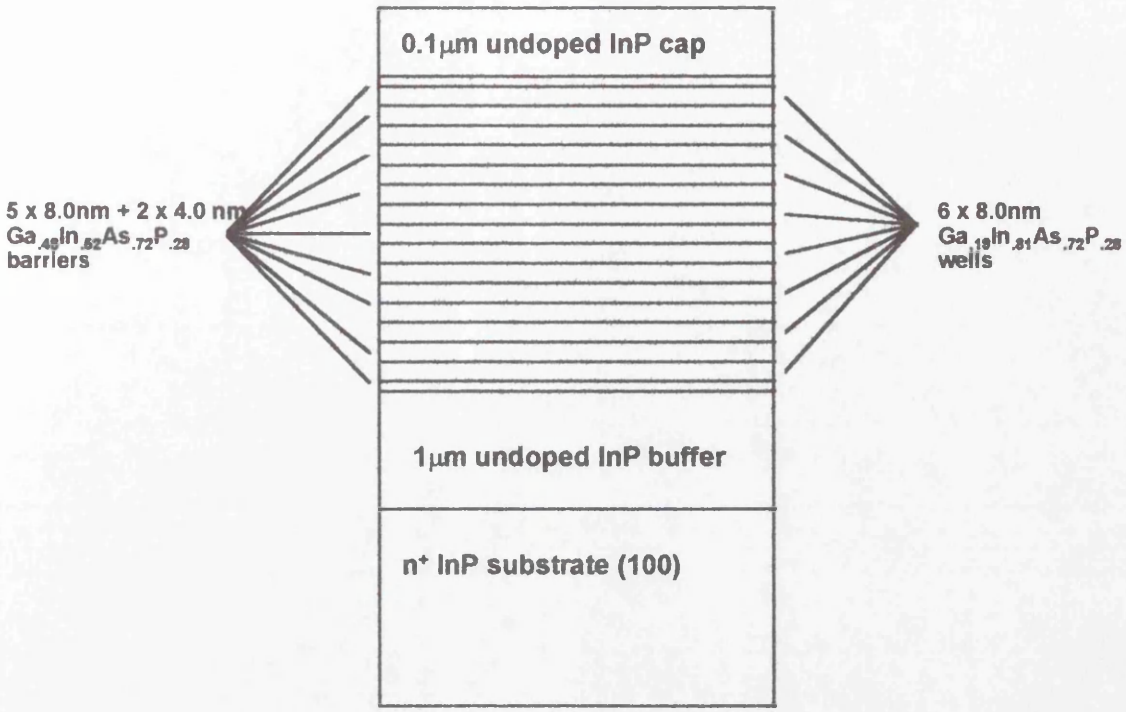

Figure 8.11 Schematic diagram of ±1% GaInAsP MQW structure used to evaluate the effect of growth temperature on structural quality.

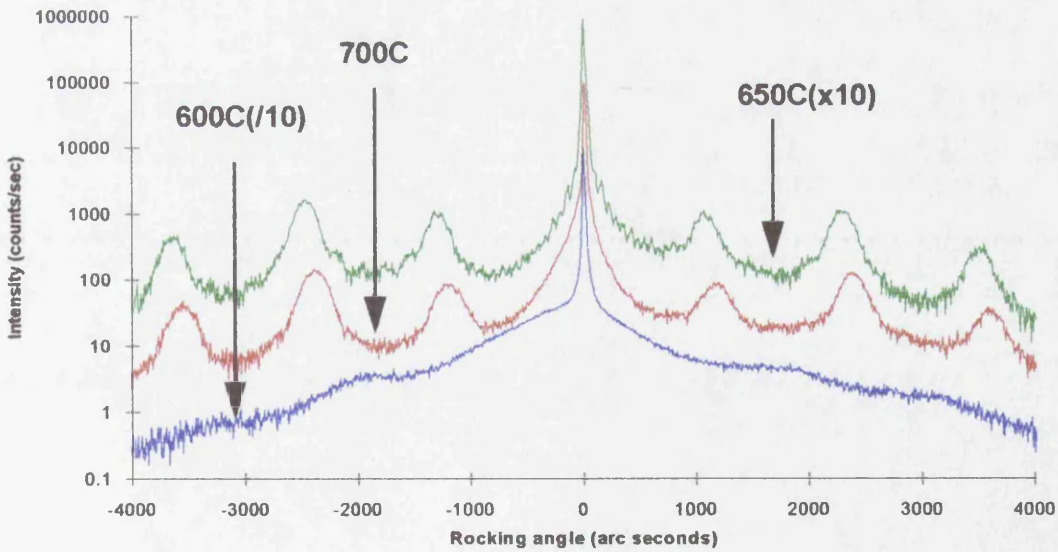

Figure 8.12 HRXRD rocking curves of 6 well ±1% GaInAsP MQW structures grown at 600, 650 and 700 ° C. The intensities of the 600 and 650 ° C rocking curves are both offset by a decade to aid viewing. A deterioration in the quality of the rocking curves can be observed with decreasing growth temperatures, although the 650 and 700 ° C curves look similar.

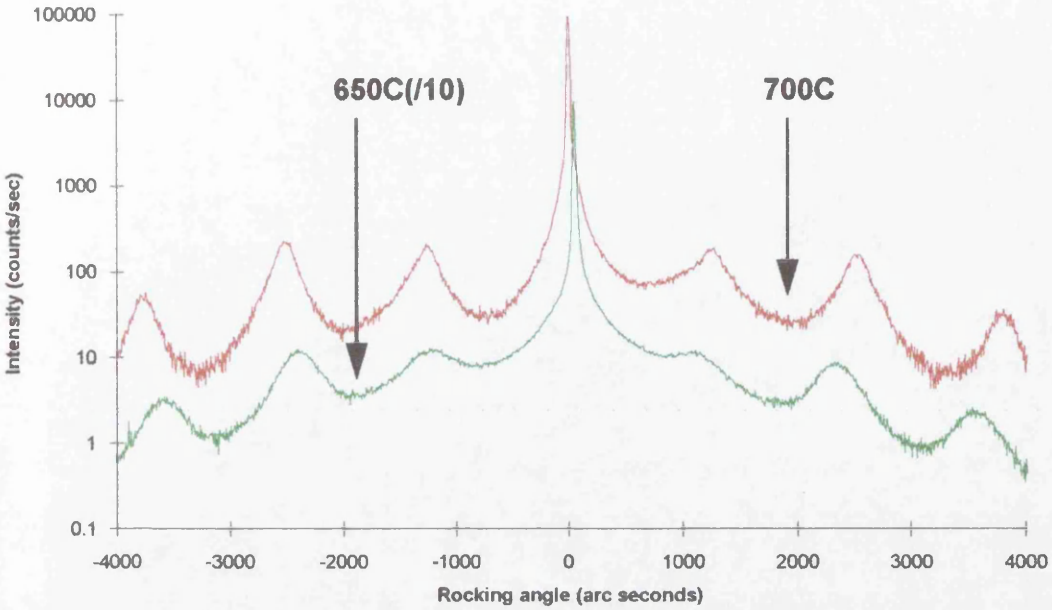

Figure 8.13 HRXRD rocking curves of 12 well ±1% GaInAsP MQW structures grown at 650 and 700 ° C. The intensity of the 650 ° C rocking curve is offset by a decade to aid viewing. It is clear the 650 ° C sample has a slightly inferior rocking curve to the 700 ° C sample.

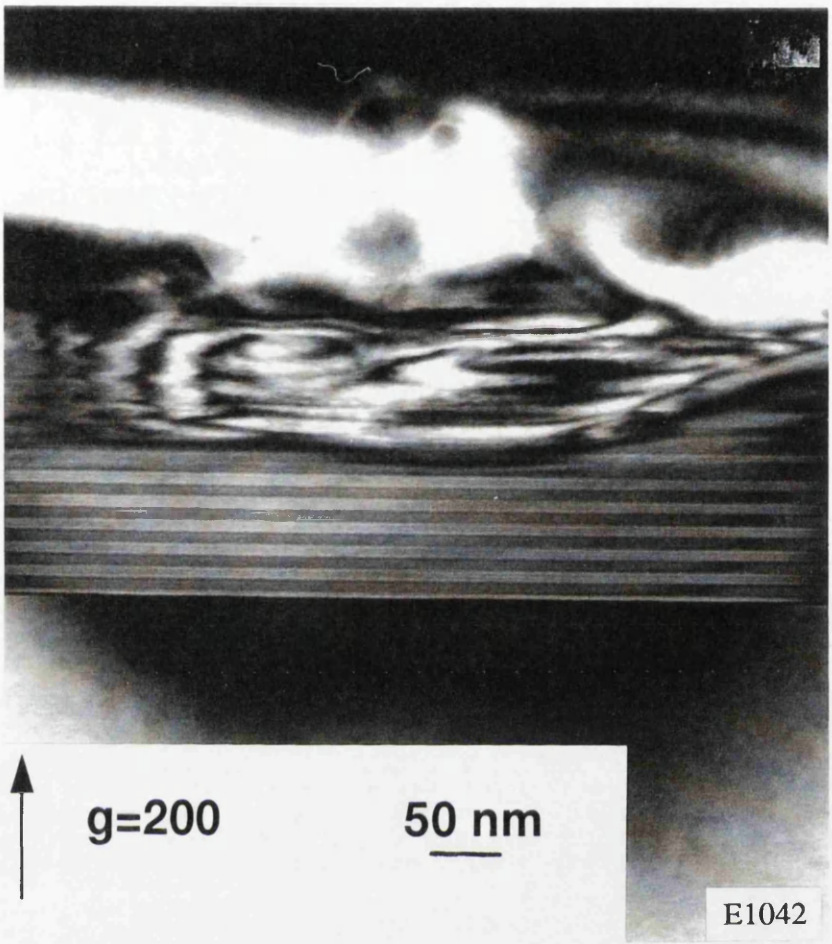

Figure 8.14a Cross-sectional TEM of 12 well ±1% structure grown at 650 ° C. Planar growth of the wells and barriers ceases after the deposition of approximately 5 wells.

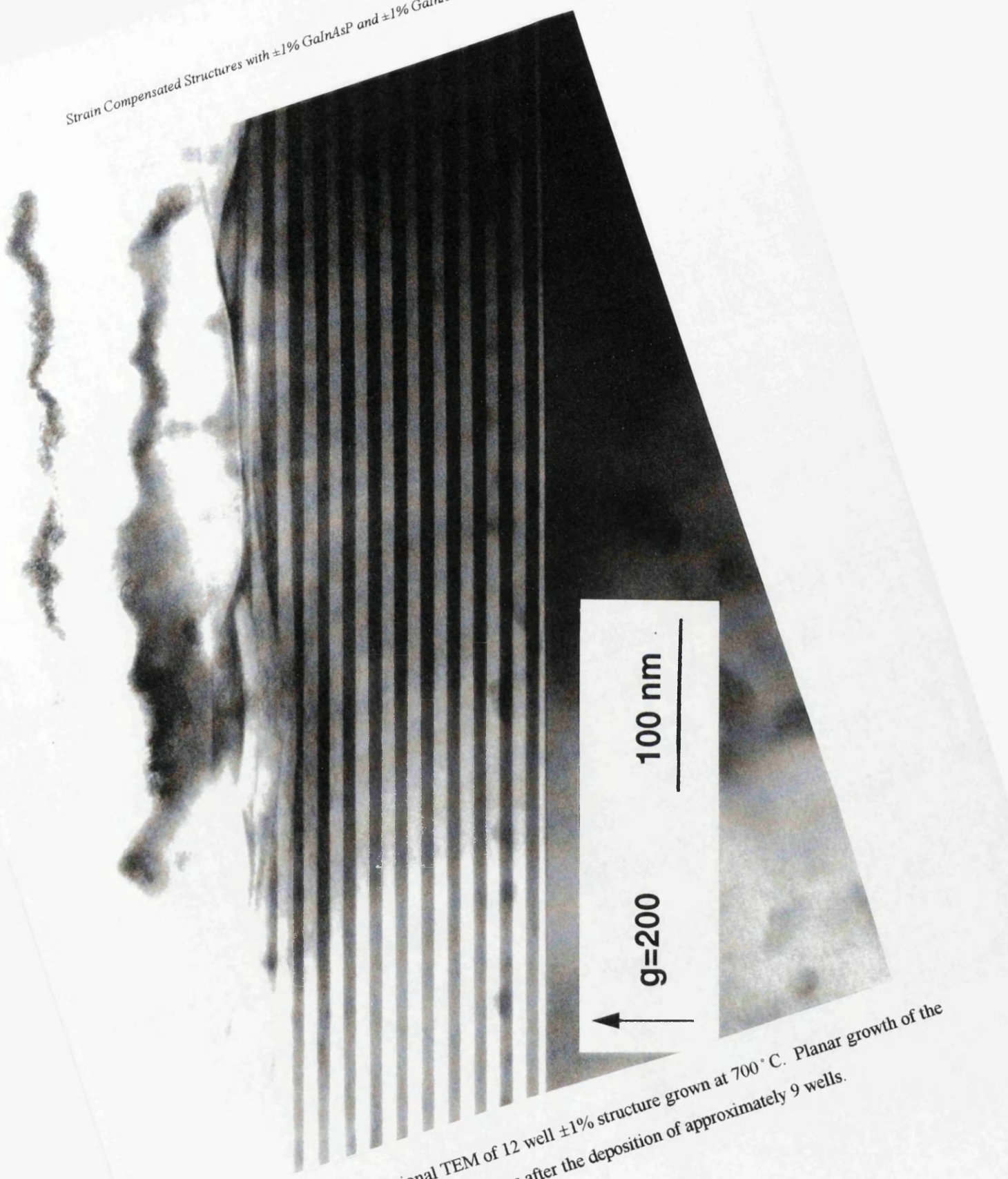

Figure 8.14b Cross-sectional TEM of 12 well ±1% structure grown at 700° C. Planar growth of the wells and barriers ceases after the deposition of approximately 9 wells.

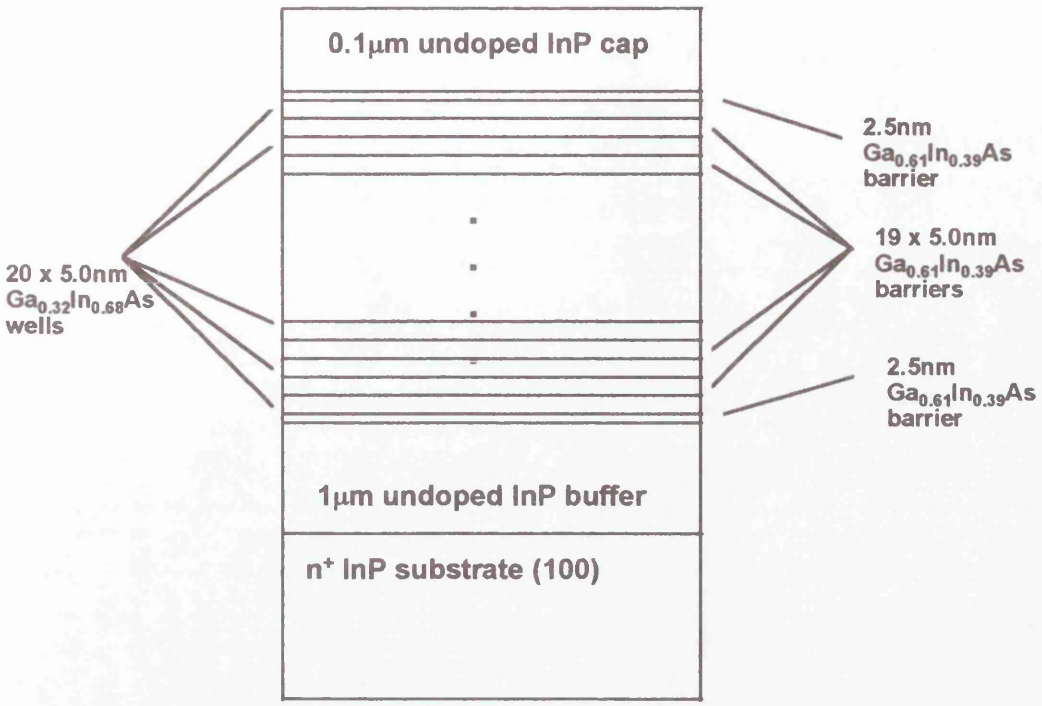

Figure 8.15 Schematic diagram of ±1% GaInAs MQW structure used to evaluate the effect of growth conditions on structural quality.

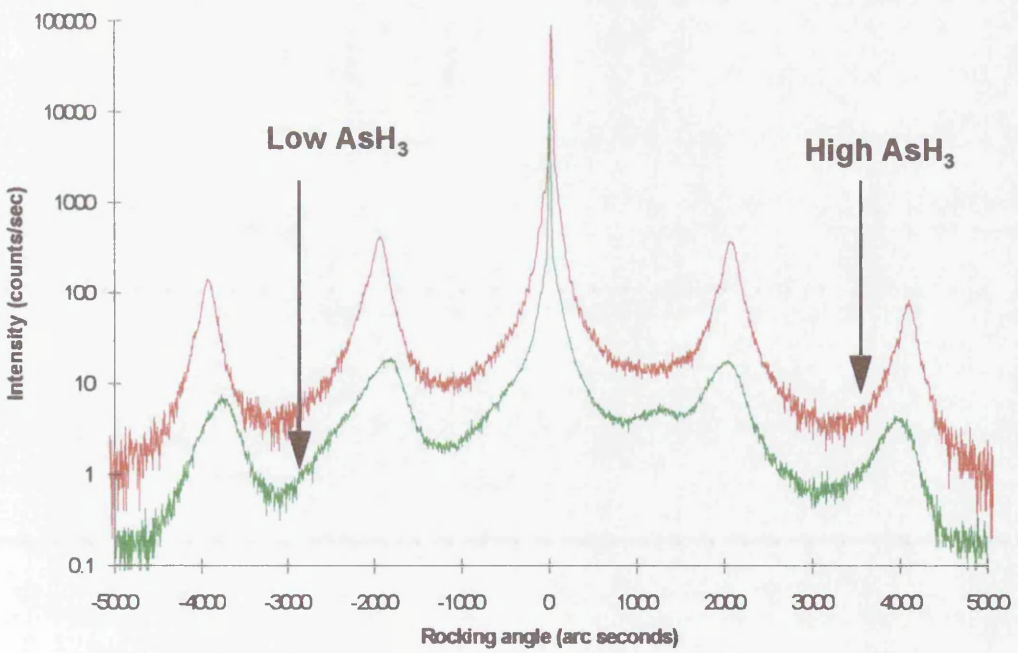

Figure 8.16 HRXRD rocking curves of 20 well ±1% GaInAs MQW structures grown at 650 °C with AsH_3 partial pressures of 0.063 Torr (low) and 2.336 Torr (high). It is clear the low AsH_3 sample has an inferior rocking curve to the high AsH_3 sample.

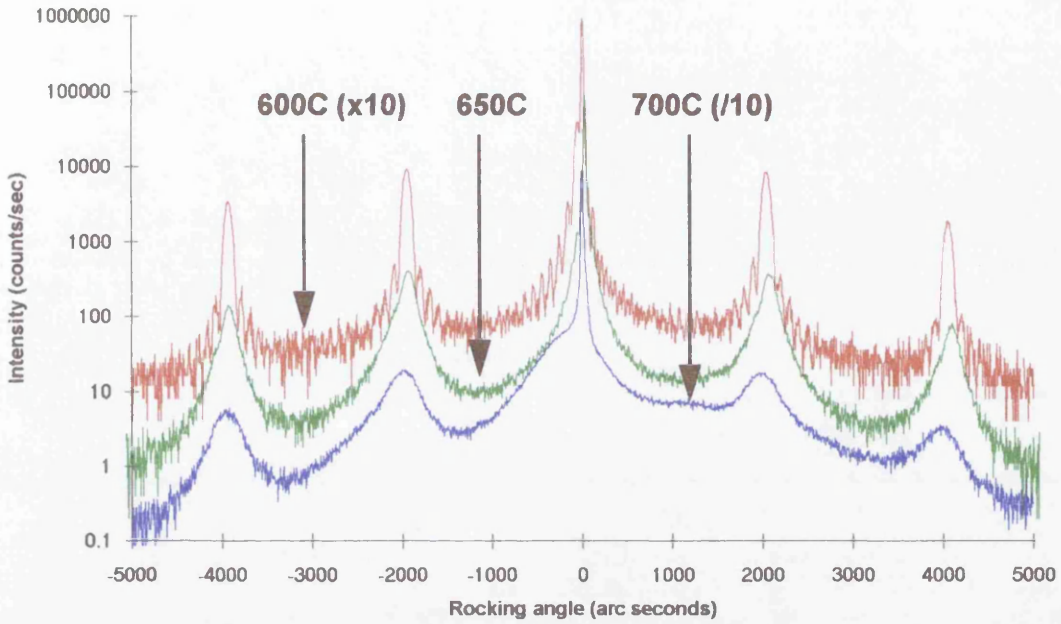

Figure 8.17 HRXRD rocking curves of 20 well ±1% GaInAs MQW structures grown at 600, 650 and 700 ° C. The intensities of the 600 and 700 ° C rocking curves are both offset by a decade to aid viewing. A deterioration in the quality of the rocking curves can be observed with increasing growth temperatures.

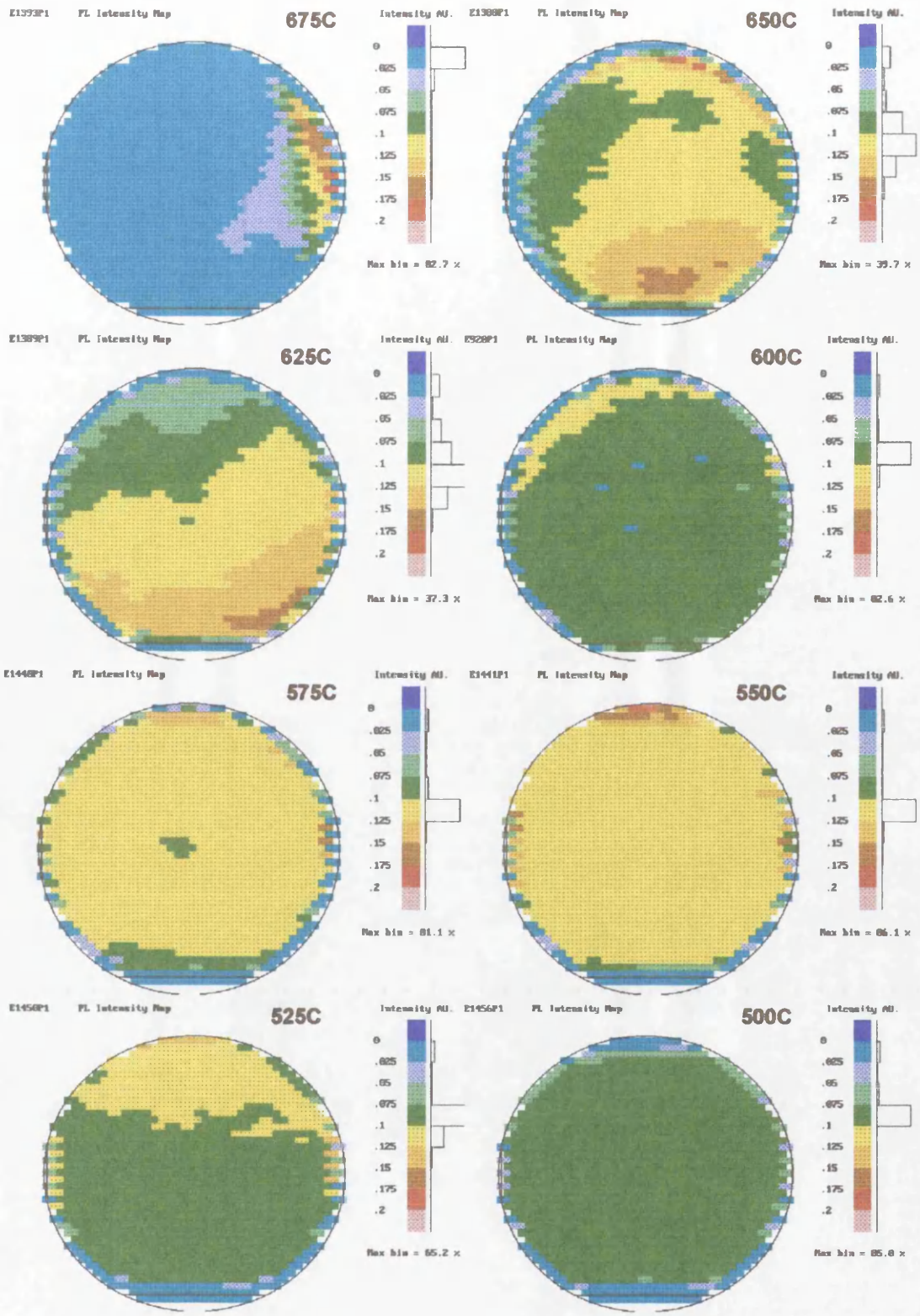

Figure 8.18 Room temperature PL intensity wafer maps of an identical 20 well ±1% GaInAs MQW structure grown at 8 temperatures between 500 ° C and 675 ° C. The most intense and most uniform structures are grown in the 550 ° C to 575 ° C temperature range.

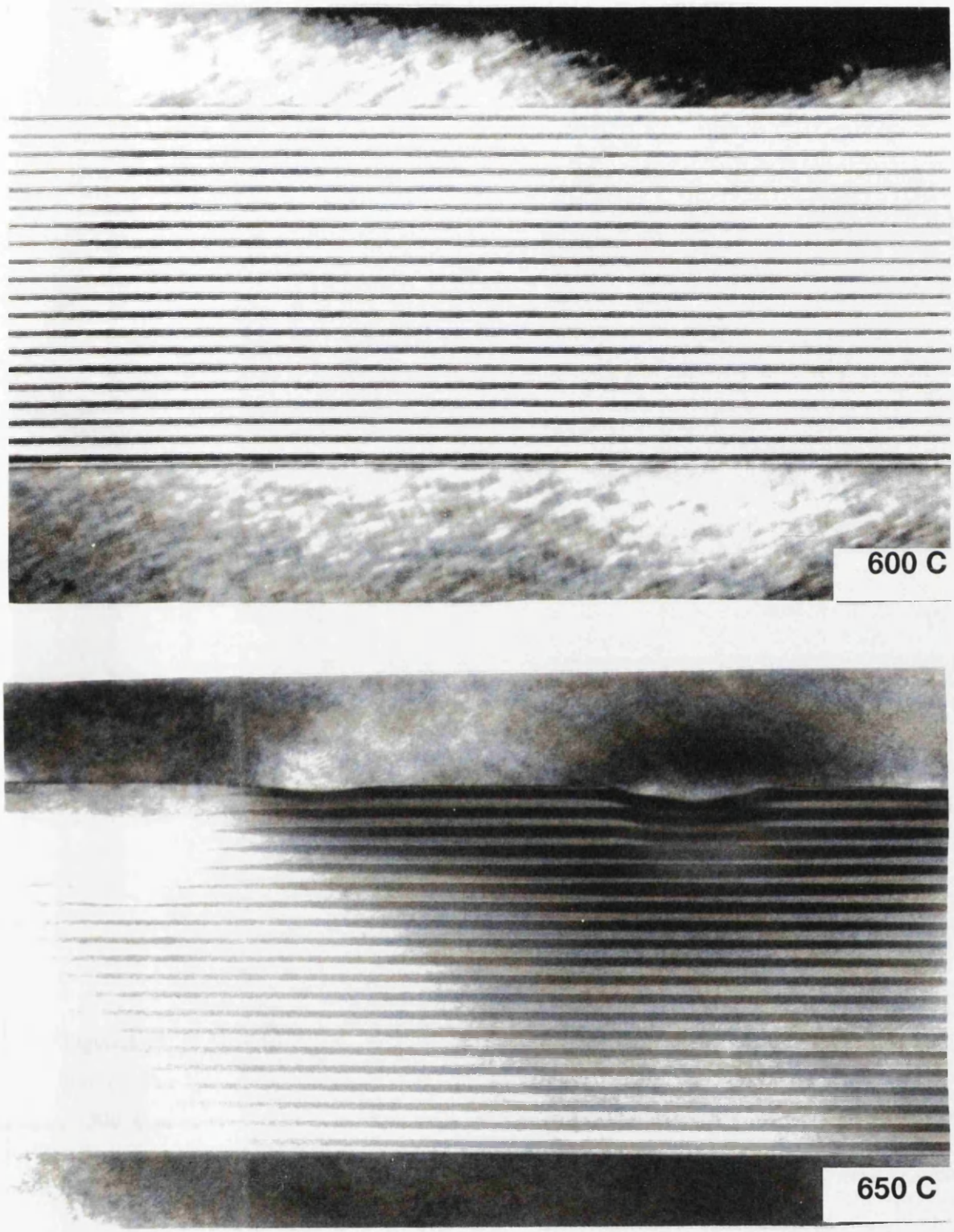

Figure 8.19 Cross-sectional TEM's of 20 well ±1% GaInAs MQW structure grown at 600, 650 and 700 ° C. The growth at 600 ° C appears perfect, whereas the 650 and 700 ° C (next page) growths show thickness modulations to an increasingly severe effect with temperature.

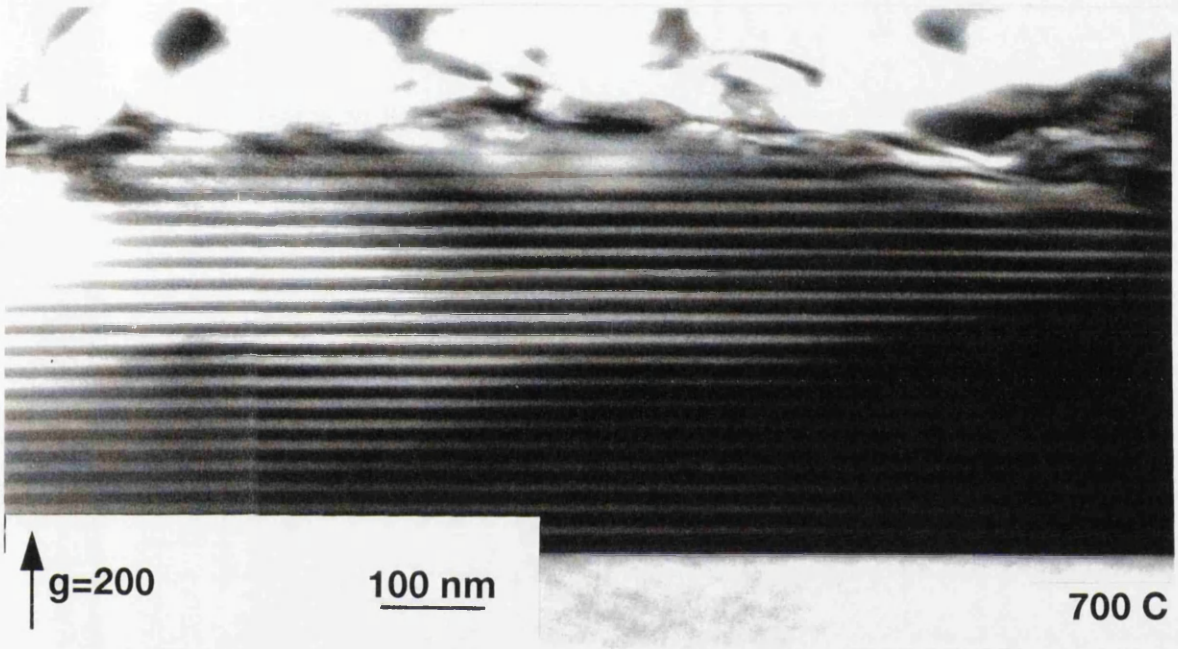

Figure 8.19 Cross-sectional TEM's of 20 well ±1% GaInAs MQW structure grown at 600, 650 and 700 ° C. The growth at 600 ° C (previous page) appears perfect, whereas the 650 (previous page) and 700 ° C growths show thickness modulations to an increasingly severe effect with temperature.

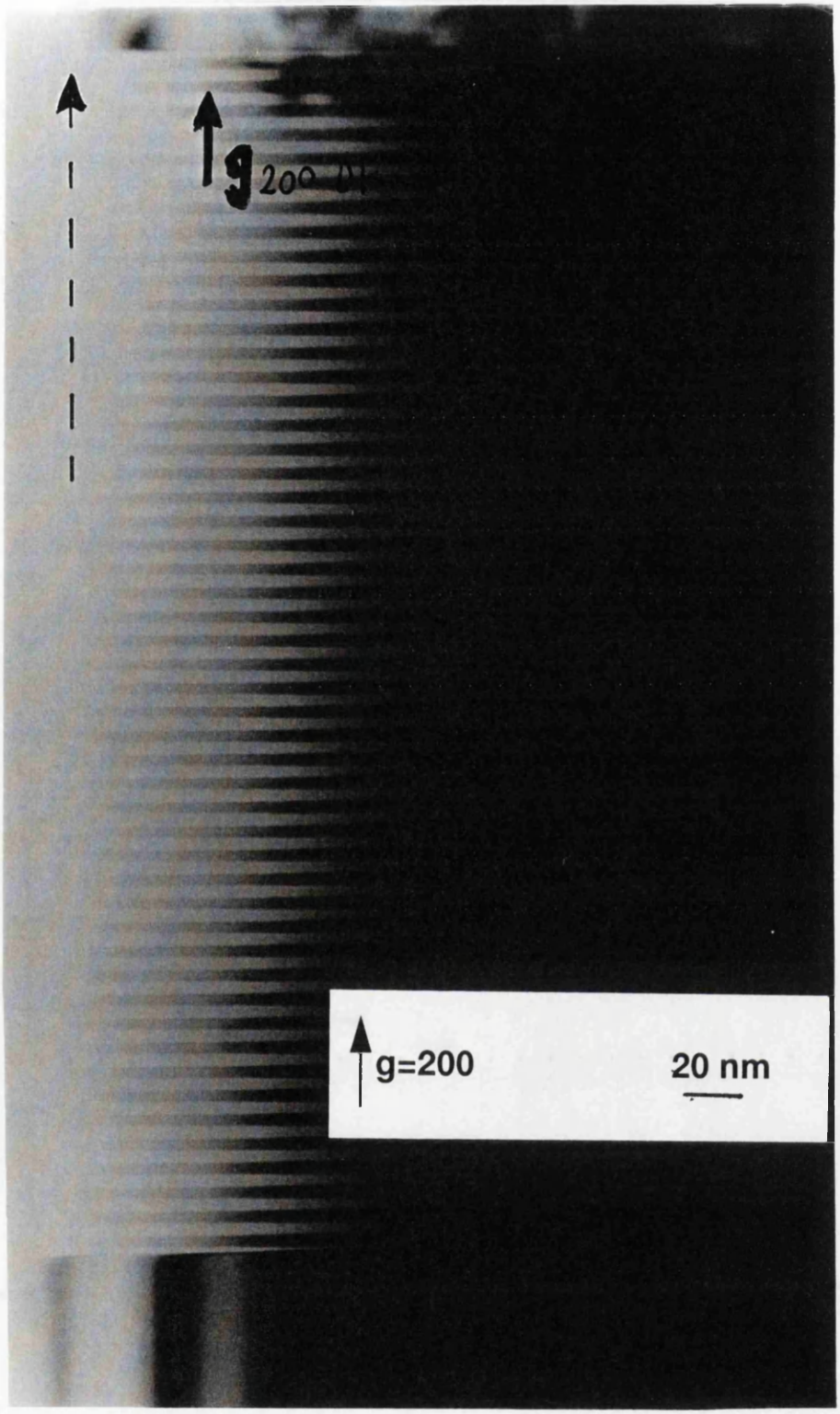

Figure 8.20 Cleaved edge TEM of 50 well ±1% GaInAs MQW structure grown at 600 °C. The growth still appears perfect, indicating that the optimised growth conditions potentially permit a limitless number of MQW cycles to be grown.

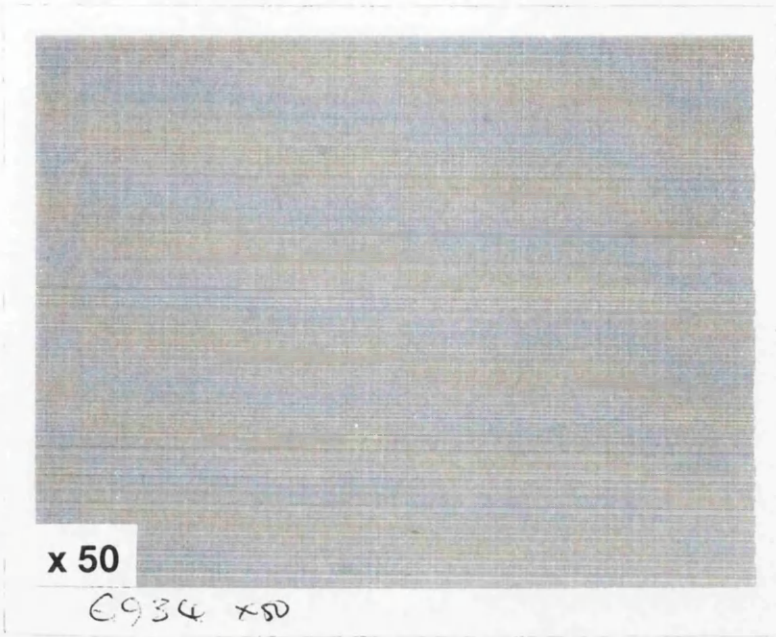

Figure 8.21a Normarski interference optical micrograph (x50) of 50 cycle +1%/lattice matched MQW structure grown at 600 ° C (i.e. no compensating tension in the barriers). A 'cross-hatched' surface is observed which is indicative of samples having far exceeded their critical layer thickness.

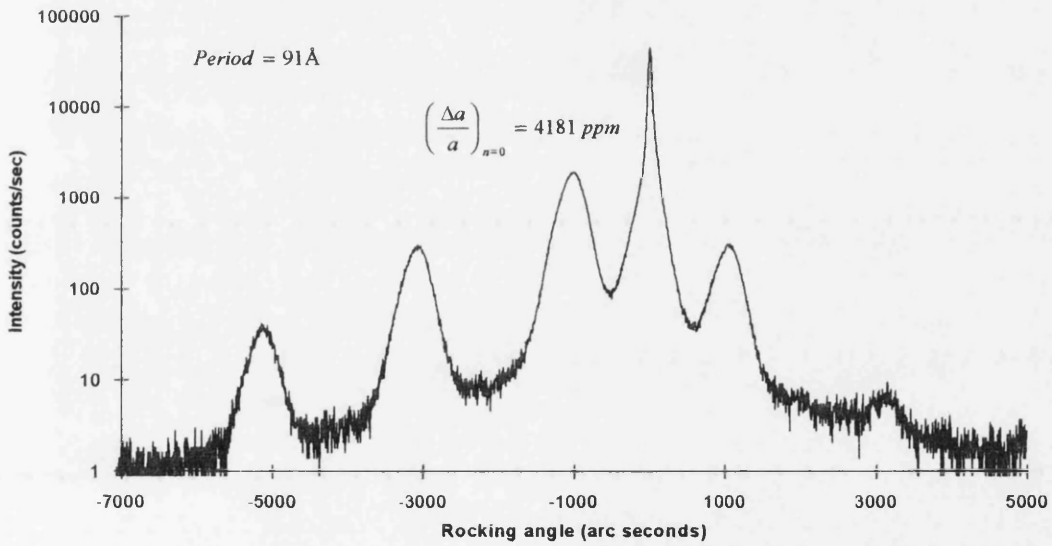

Figure 8.21b HRXRD rocking curve of 50 cycle +1%/lattice matched MQW structure. Note how diffuse the satellite peaks are in relation to the strain compensated sample grown at 600 ° C in figure 8.15.

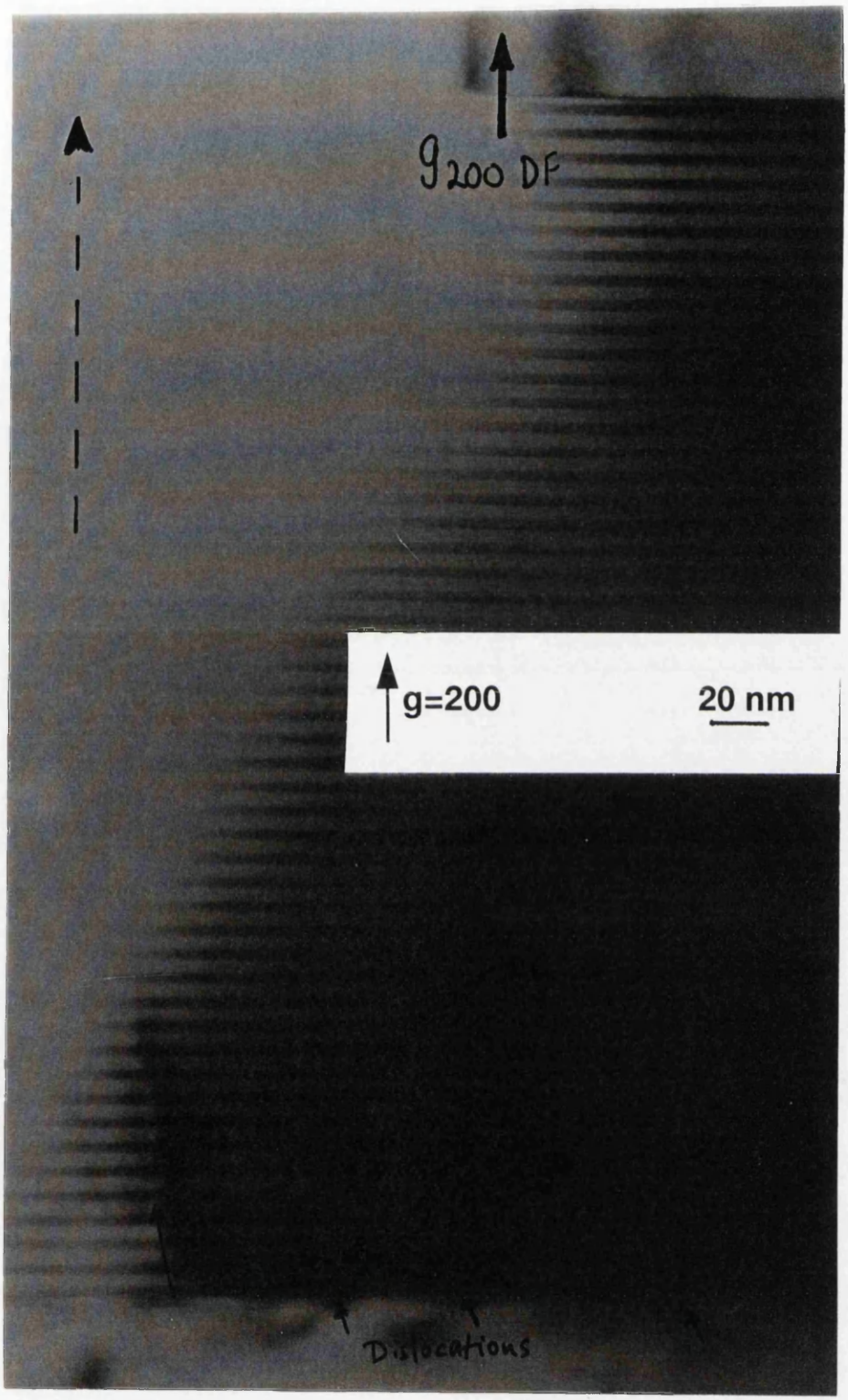

Figure 8.21c Cleaved edge TEM of 50 well +1%/lattice matched GaInAs MQW structure grown at 600 ° C. The well and barrier growth remains planar throughout the structure but dislocations are present at the interface of the MQW stack and the buffer layer.

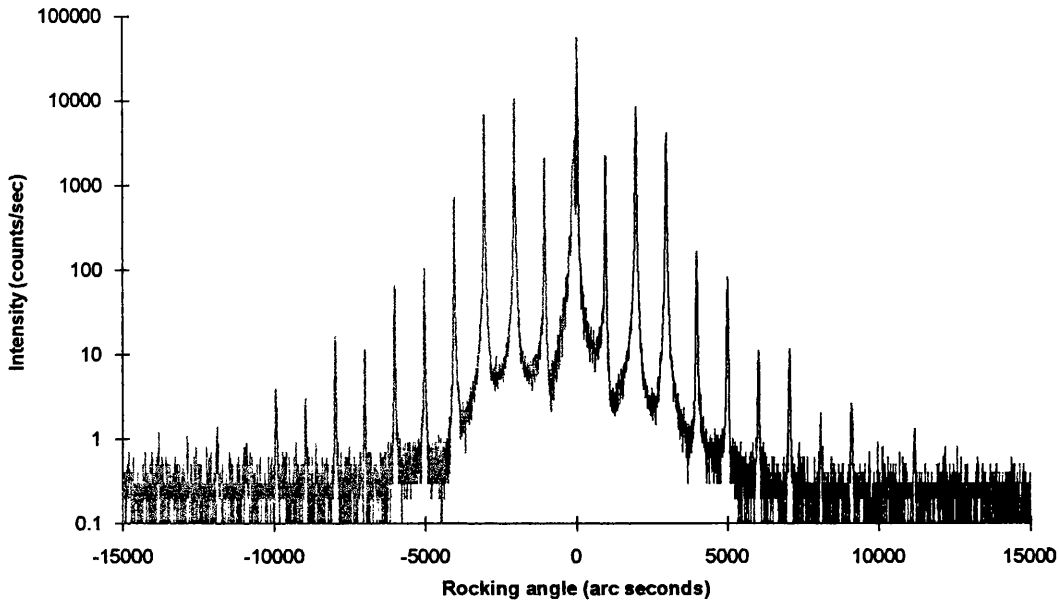

Figure 8.22 HRXRD rocking curve of 50 cycle ±1% GaInAs MQW structure grown at 600 ° C with well = barrier = 93Å,i.e. double the well and barrier thicknesses of the samples grown previously. Satellite peaks up to the 11th order are observed, a sign of excellent MQW quality. This structure represents the thickest strain compensated MQW structure grown so far in this thesis.

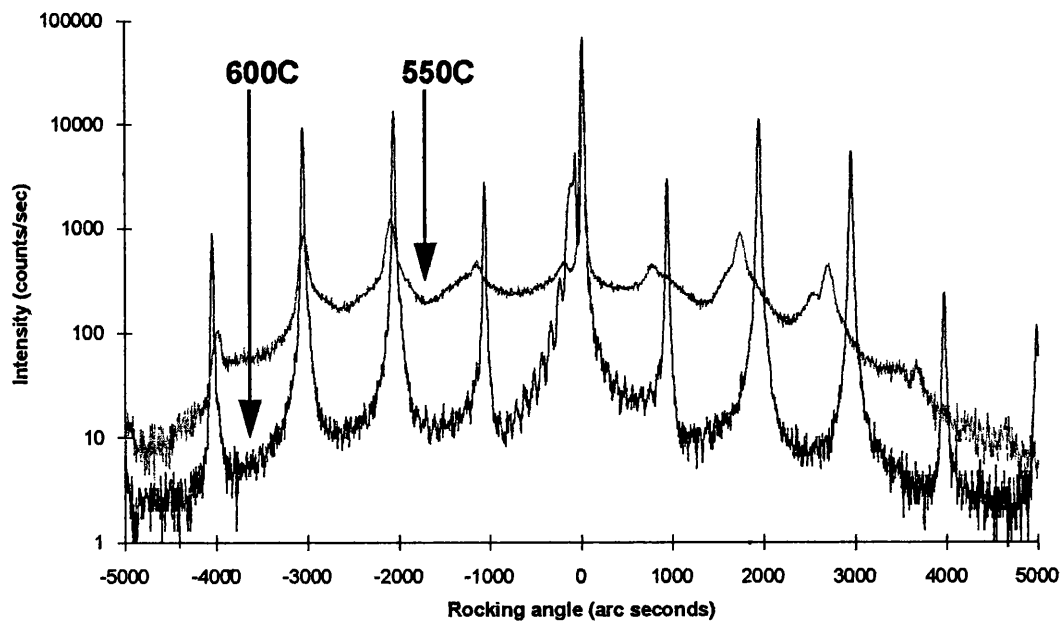

Figure 8.23 HRXRD rocking curves of 50 cycle ±1% GaInAs MQW structures grown at 600 ° C and 550 ° C with well = barrier = 93Å. A deterioration in MQW structural quality is noted with reduced growth temperature.

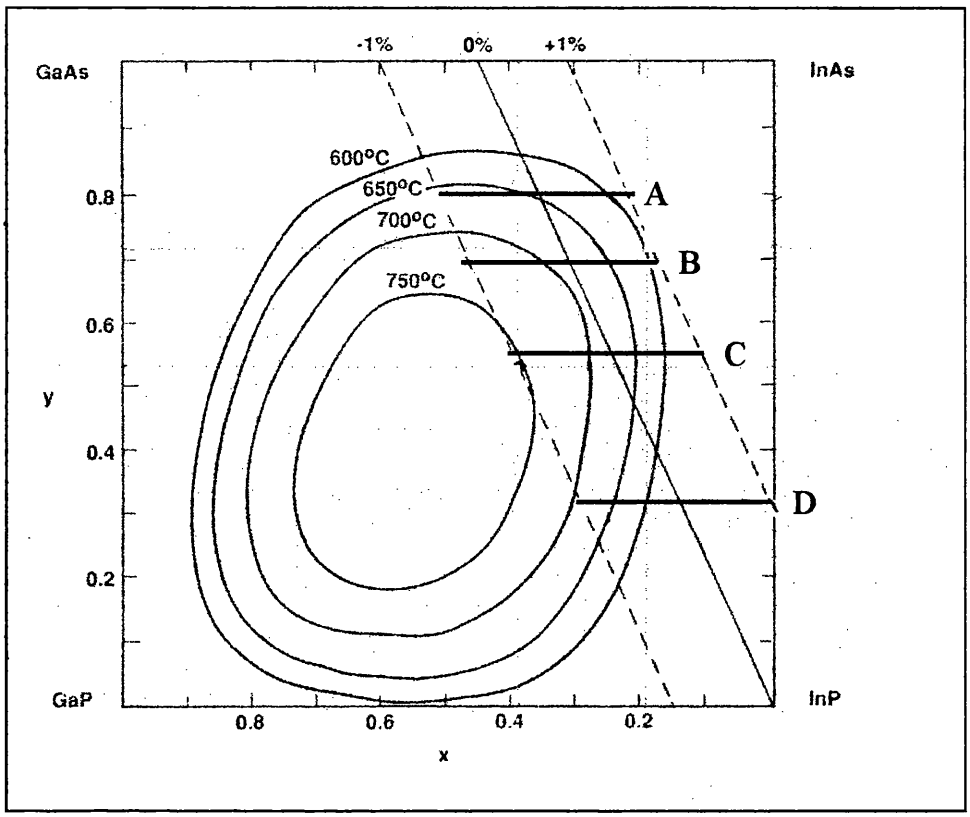

Figure 8.24 'Constant-y' structures investigated by Glew et al[10]. By choosing combinations of well and barrier compositions at the periphery of the 650 ° C spinodal isotherm they were able to grow 50 cycle ±1% GaInAsP MQW structures with planar wells and barriers.

Chapter 9

Growth and Assessment of Non-Compensated Strained InGaAs(P)/InGaAsP MQW Structures

9.1 Introduction

The majority of InP-based strained MQW device results that appear in the literature are based on structures with no compensation, i.e. a lattice matched alloy is used as the barrier material. In such non-compensated structures, the number of coherently strained wells that can be grown is limited by the critical layer thickness as discussed in section 4.3. The effects of exceeding this limit were demonstrated in the last chapter, when a 50 period $Ga_{0.47}In_{0.53}As/Ga_{0.32}In_{0.68}As$ non-compensated MQW structure was grown with well and barrier thicknesses of 50Å. The grown structure exhibited gross 'cross-hatching' of the surface morphology and the X-ray rocking curve exhibited diffuse satellite peaks. When the critical thickness limit is exceeded it is often accompanied by a degradation in the device performance, e.g. lasing threshold current as reported by Thijs et al[1] or reverse bias leakage currents as reported by Temkin et al[2]. With the exception of Temkin's paper on critical thicknesses in $InP/Ga_{1-x}In_xAs$ MQW structures[2], little attention has been paid to what exactly happens in InP based structures when the critical thickness limit is exceeded, i.e. what type of defects are introduced. Gourley et al[3] studied such structures in GaAs/InGaAs using PL imaging and showed that the critical thickness for MQW structures was greater than that for single layers.

Up until October 1992, most of the recorded InP-based strained layer MQW laser structures were based on the use of compressive strain in the wells. This concentration on compressive strain was undoubtedly fuelled by the initial theoretical predictions of Adams[4], O'Reilly[5] and Yablonivitch and Kane[6]. Once the experimental demonstration of the benefits of compressive strain had become widespread, several reports appeared showing that tensile strain in the wells also produced very low threshold current densities and high output powers when compared with lattice matched structures.

This chapter attempts to examine the behaviour of non-compensated structures when the magnitude of well strain is increased, in both the compressive and tensile sense, in a InGaAs/InGaAsP MQW stack. Most of the following results are for tensile strain in the wells, with a detailed study of both the strain relieving mechanisms and the effect of tensile strain on the threshold current density of broad area devices. Some ridge laser results are also given. A brief examination of the effect of

compressive strain on the structural properties of an non-compensated MQW structure is also included for completeness.

9.2 InGaAs/InGaAsP MQW Structures with Tensile Strained Wells

InP-based devices with tensile strain in the wells of MQW active regions have, generally, received less attention than those with compressive strain. Initial theoretical predictions suggested that the use of tensile strain was not as beneficial as compressive strain as it has the effect of restoring the degeneracy between the light-hole and heavy-hole sub-bands that the quantum confinement helps remove. Recent reports[1,7], however, show that for certain values of tensile strain, reduced threshold current densities, higher output powers and improved high temperature operation were observed when compared to lattice matched devices. Conflicting reports, however, have been made on the effect of modest (<1%) tensile strain on the behaviour of the threshold current density. The aim of this work is to investigate the effect of increasing well tensile strain on a fixed 4-well non-compensated MQW laser structure. The structural properties were investigated and, wherever possible, the observations used to explain any trends observed in the measurements of broad area and Fabry Perot ridge lasers.

9.2.1 Growth and Assessment

The laser structures that were grown as part of this investigation were identical except for the magnitude of tensile strain in the 4 GaInAs wells, which was varied from lattice match to 1.6%. The GaInAs wells were approximately 95Å thick with the barriers and waveguide being composed of lattice matched GaInAsP (λ = 1.17μm). All the layers were kept a constant thickness throughout: the structure is shown in figure 9.1. The TMGa and TMIn flows required to grow tensile strained GaInAs were estimated by assuming a linear relationship between the gas phase TMGa:TMIn ratio and the solid phase Ga:In ratio, as found in the growth of lattice matched GaInAsP alloys[8]. The TMIn and AsH_3 flows for the well material were kept constant and the TMGa flow increased to provide increased tensile strain. The growth rate of the GaInAs alloy will increase as a result and, in order to keep the well width constant, the growth time of the well was reduced. This was determined by calculating the ratio of growth rates of the tensile strained alloy of interest to the lattice matched case, whose growth rate was well known. The derivation of this relationship is given below:

Vegard's law for $Ga_xIn_{1-x}As$ was described in section 3.4.1 and is given by:

$$a_{Ga_xIn_{1-x}As} = x.a_{GaAs} + (1-x).a_{InAs} \qquad (9.2.1)$$

as mentioned above,

$$\frac{x}{1-x} = \frac{[TMGa]}{[TMIn]} \qquad [....] \text{ indicates gas phase concentration} \qquad (9.2.2)$$

$$G_r \propto [\text{TMIn}].a_{InAs}.+[\text{TMGa}].a_{GaAs}$$

$$G_r \propto [\text{TMIn}].a_{InAs} + \frac{\text{x}}{1\text{-x}}[\text{TMIn}].a_{GaAs}$$

$$G_r \propto \frac{[\text{TMIn}]}{1\text{-x}}.\left(x.a_{GaAs} + (1-x).a_{InAs}\right)$$

$$G_r \propto \frac{[\text{TMIn}]}{1\text{-x}}.\ a_{Ga_xIn_{1-x}As} \qquad (9.2.3)$$

Under lattice match conditions $1\text{-x} = 0.532$ and $a_{Ga_xIn_{1-x}As} = a_{InP}$ then

$$G_{r@LM} \propto \frac{[\text{TMIn}]}{0.532}.a_{InP} \qquad (9.2.4)$$

but the TMIn is kept constant hence

$$\frac{G_r}{G_{r@LM}} = \frac{a_{Ga_xIn_{1-x}As}}{a_{InP}}.\frac{0.532}{1-x}$$

$$\left(\text{but } \frac{a_{Ga_xIn_{1-x}As}}{a_{InP}} = 1 + \frac{\Delta a}{a}\right)$$

$$\text{hence } \frac{G_r}{G_{r@LM}} = \left(1 + \frac{\Delta a}{a}\right).\frac{0.532}{1-x} \qquad (9.2.5)$$

x - Ga content of non-lattice matched alloy a - lattice constant

G_r - growth rate of tensile alloy $G_{r@LM}$ - growth rate of lattice matched alloy

HRXRD was again used to determine the actual well strain and the periodicity of the MQW active region. The former was possible as the HRXRD rocking curve could resolve the nominally lattice matched peak from the waveguide layers. As these layers are of the same composition as the barrier material, it can be confirmed that the barriers have a negligible contribution to the overall net strain. Hence the formula:

$$L_w\varepsilon_w + L_b\varepsilon_b = \Lambda\left(\frac{\Delta \text{a}}{\text{a}}\right)_{n=0} \qquad (9.2.6)$$

L_b , L_w - barrier and well thicknesses Λ - well + barrier thickness i.e. MQW periodicity

ε_w, ε_b - well and barrier strain $\left(\frac{\Delta a}{a}\right)_{n=0}$ - mismatch of zeroeth order peak

reduces to

$$L_w\varepsilon_w = \Lambda\left(\frac{\Delta a}{a}\right)_{n=0} \qquad (9.2.7)$$

The value of the parameters on the RHS of equation 9.2.7 can be determined from the rocking curve measurements and the well width is assumed constant (this was proved later by TEM to be a reasonable assumption), hence the well strain can be estimated. Figure 9.2 shows the rocking curve of a sample grown with an intended well tensile strain of 1%. Applying the above formula to the measurements:

$\left(\frac{\Delta a}{a}\right)_{n=0}$ = -4003 ppm, Λ = 237Å, and assuming L_w = 95Å

then $\varepsilon_w = (237/95).(-4003) = -9986$ ppm $\approx$ -1%.

Note how the satellite peaks are to the RHS of the substrate peak, indicating that the structure has a net tensile strain. Table 9.1 below, lists the inferred well strain, composition and MQW periodicity for each of the tensile MQW structures grown.

Table 9.1 - Inferred well strain, composition and MQW periodicity for each of the tensile MQW structures grown

Inferred Strain(%)	Well composition	Λ(Å)
0	$Ga_{0.47}In_{0.53}As$	236
-0.28	$Ga_{0.51}In_{0.49}As$	240
-0.52	$Ga_{0.54}In_{0.46}As$	236
-0.79	$Ga_{0.58}In_{0.42}As$	234
-0.97	$Ga_{0.61}In_{0.39}As$	237
-1.12	$Ga_{0.63}In_{0.37}As$	229
-1.29	$Ga_{0.66}In_{0.34}As$	236
-1.6	$Ga_{0.71}In_{0.29}As$	235

The maximum deviation of the MQW periodicity was only 6Å from the mean value, indicating the success of maintaining a constant quantum well thickness using the technique described above.

The structures were also assessed by room temperature PL. Each PL spectrum showed a single, but increasingly broad, peak from lattice match to 0.5%. At 0.8% well strain and above, a doublet was

observed with the long wavelength peak being attributed to the E1-LH1 light hole transition and the short wavelength peak to the E1-HH1 heavy hole transition. Luminescence from the E1-HH1 transition decreased in intensity with increasing well strain. It is known that quantum confinement lifts the degeneracy of the light and heavy holes and, in the case of lattice matched quantum well structures, the E1-HH1 transition becomes energetically more favourable[5,6,9]. As the tensile strain in the well is increased, the heavy and light hole levels are pushed together and, as observed at 0.8% and above, the effect of the tensile strain is so great that the light hole transition becomes the most energetically favourable. Figure 9.3 illustrates the effect of well strain on the PL wavelength: the light hole-heavy hole cross-over point would appear to be at 0.5%. Note that this is not to be interpreted as a universal value of light hole-heavy hole cross-over, because the value depends on the level of quantum confinement present. The cross-over strain value will increase with reduced well thickness and vice-versa. It is also interesting to note that the E1-LH1 transition is relatively insensitive to increasing strain .

The samples were examined further using spatially resolved PL imaging. At tensile strains >1%, dark lines, many millimetres long, and running almost exclusively in the $[01\bar{1}]$ direction, appeared in the PL image. These dark lines are believed to be due to non-radiative recombination at dislocations and are similar to defects observed in single layers of GaInAsP alloys that have been grown in excess of some critical layer thickness, as discussed in section 4.2. Figures 9.4a and 9.4b show the PL images of the 1% and 1.12% structures. From these it is evident that the dislocations are introduced to the structure at some value of well strain between these two limits. It is noted in figure 9.4b that some of the dark lines are broader than others, a feature which is explained in figure 9.4c via a plan view TEM image of one of the dark lines. The image reveals a network of orthogonal dislocations running predominantly in the $[01\bar{1}]$ direction. Other micrographs show that these dislocation networks vary in thickness in the [011] direction. Taken together, these observations would suggest that the critical thickness-mismatch product of such an MQW structure lies in the range 380-425 Å.%. At 1.3% tensile strain, dark spots, as well as dark lines, were observed in the PL image, as illustrated in figure 9.4d, with the density of line defects being reduced over the 1.12% case. At 1.6% tensile strain, spots were the dominant defect type as illustrated in figure 9.4e. Room temperature PL mapping of this series of structures showed that the luminescence intensity was significantly reduced in the upstream areas of the samples with 1.12% well strain and above, these maps being shown in figure 9.5. It was known that the mismatch uniformity was poorer in this area and the alloys grown were more negatively mismatched than the rest of the wafer. The density of dark spots was highest in these low intensity areas. The combination of dark spots and reduced PL intensity was reminiscent of the effects of thickness modulations in the quantum well region on the electro-absorption modulator structures reported in section 8.2. Indeed, it was

observed from the rocking curves of samples with 1.12%, 1.3% and 1.6% well strain, that the satellite peaks became more diffuse with increasing strain. These curves are shown in figure 9.6.

Cross-sectional TEM of these three samples proved that thickness modulations were indeed occurring. Figure 9.7 shows the micrographs taken under the g=002 diffraction condition in the direction shown. Thickness modulations are just discernible in the 1.12% case and are pronounced in the 1.3% and 1.6% cases. It is interesting to note that the period of undulation decreases with increasing well strain, confirming the observations made by HRXRD. The 1.6% sample was examined further under the g=$\bar{2}02$ condition, which delineates variations in strain, the micrograph being shown in figure 9.8. A periodic contrast variation is observed which is associated with a variation in the strain, this variation having a similar periodicity to the thickness undulations shown in figure 9.7. The micrograph also shows several defects propagating from the MQW stack, these were identified as threading dislocations and stacking faults. It is quite probable that it is this type of defect that gives rise to the dark spots that are observed in the PL image. These defects only seem to occur as an adjunct to thickness modulated growth.

As with previous thickness modulated MQW structures, improvements in the planarity of the 1.3% and 1.6% samples were observed when the group V partial pressure, used to grow the strained material, was increased. Figure 9.9 demonstrates the improvement in these two structures when the AsH_3 partial pressure was increased from 0.063 Torr to 2.336 Torr. It should be noted that, although the increased AsH_3 partial pressure suppresses the thickness modulations, it did not prevent the generation of dislocations, as they were still observed in the PL image.

A fraction of the 2" wafer of each of these structures was then overgrown with 1.7μm of p-InP and 0.2μm of lattice matched p-GaInAs to make lasers. All the samples were overgrown in the same single MOVPE growth. This was to minimise the influence of different p doping concentrations on the measured threshold current densities, as described previously in chapter 7.

9.2.2 Device Results

9.2.2.1 Broad Area Stripe Lasers

In order to minimise the possible effect of any dislocations on the device performance, the lasers were processed so that the stripes were in the $[01\bar{1}]$ direction, parallel to the dislocations. The stripes are normally defined in the orthogonal direction. The rationale was to define the stripes in the area between the dislocations, and this is easier if the stripes are running parallel to the dislocations. The polarisation of the lasing mode was determined by measuring the output power after the beam had been passed through a TE or TM polariser. If the device is lasing in the TE mode, then a higher output power will be measured at the output of a TE polariser than a TM polariser, the opposite being true if the device is lasing in the TM mode. The lasing wavelength and polarisation mode are plotted as a function of well strain in figure 9.10. A strong correlation exists between the lasing wavelength and the dominant PL wavelength in figure 9.3. The devices lase in the TE mode up to 0.5% well strain and beyond in the TM mode. This is consistent with the observation that the light hole to heavy hole cross-over point in these structures, is in the region of 0.5% well strain.

Laser chips were cleaved to lengths between 200 μm and 1000 μm. Threshold current densities were measured at 20°C on broad (50 μm) stripes without facet coatings. For each combination of cavity length and well strain, at least six lasers were measured to determine the mean threshold current. Devices with radically different values from their neighbours were discarded from the analysis. Figure 9.11 shows the relationship between the logarithm of the threshold current density and the reciprocal cavity length for the structures with well strains up to 1.6%. These data show a good fit to the logarithmic relationship described by:

$$\ln\left(\frac{J_{th}}{J_{\infty}}\right) = \frac{k}{NL} \qquad (9.2.8)$$

for each of the well strains. In section 5.3 it was shown that:

$$k = \frac{1}{2\Gamma_w G_0}.\ln\left(\frac{1}{R_1 R_2}\right) \qquad (9.2.9)$$

For these broad area devices, the facets are cleaved and not coated, thus their reflectivities, R_1 and R_2, will be similar for all structures, although there is a weak dependence on the polarisation of the lasing mode[10]. The term $\Gamma_W G_0$ is an indication of the gain per well. The optical confinement factor, Γ_W, is primarily dependent on the well thickness, which is kept constant. Hence, by

evaluating 1/k for each of the grown laser structures, we can comment on the influence of well strain on the gain per well. Figure 9.12 shows a plot of J_∞, the infinite cavity length threshold current density, and 1/k versus well strain. J_∞ increases with well strain between lattice match and 0.5% well strain, decreases between 0.5% and 1.3% well strain and then increases again beyond 1.3% well strain. The first increase can be explained by a rise in the effective density of states as the E1-HH1 and E1-LH1 levels move closer. At the cross-over point, the light and heavy hole levels become co-incident. Hence, the threshold current density peaks since more states have to be populated in the valence band before lasing action commences. Beyond 0.5% well strain, the E1-LH1 transition begins to dominate and the resulting reduction in threshold current density most probably reflects the reduced density of states caused by the reduced curvature of the light hole sub-band. At 1.6% well strain, the threshold current density begins to increase, most probably due to the high density of defects, be they lines or spots, that give rise to non radiative recombination. These observations differ, in some regions of well strain, from previous reports. Thijs et al[1] report no lasing at 0.9% and implied very high threshold current densities between lattice match and 1% tensile strain. Zah et al[7] reported a continuous decrease in the threshold current density with well strain. Thijs et al also observe a 5-6 times improvement in the threshold current density of their best tensile strained device over their lattice matched device, whereas here the improvement is only a factor of 1.3. Thijs's best tensile strained device has a proportionally similar infinite cavity length threshold current density (he used one and two wells as opposed to the four wells here) but his lattice matched device is proportionally much worse. Figure 9.11 also shows a reduction in k (an increase in gain per well), between 0.5% and 1.6%, suggesting that tensile strain in this region gives improved performance over structures grown with lattice matched or modest tensile strained wells.

The threshold current densities of two of these structures, lattice match and 1.12% well strain, were evaluated as a function of chip temperature between 10°C and 50°C. The characteristic temperature, T_0, was estimated to be 55K and 68K respectively. This is in agreement with other observations that tensile strained devices offer improved high temperature operation. The value of 68K is similar to a value measured by Thijs[11] on a 1.6% well strain device over the same temperature range.

9.2.2.2 Ridge Laser Structures

Fabry Perot ridge devices were also fabricated in order to further evaluate the effect of the observed improvement in threshold current density and gain per well of broad area device structures. Three of the structures, 0%, 1% and 1.12% well strain, were processed into 400μm long, 2μm wide Fabry Perot ridge waveguide lasers. Low and high reflectivity facet coatings were evaporated on to either facet. Again the devices were processed with the ridges along the $[01\bar{1}]$ direction to minimise the

influence of line defects. In order to avoid the strong under cutting effects of wet chemical etchants in this crystallographic direction, the ridges were defined using methane(CH_4):hydrogen(H_2) reactive ion etching (a very light wet etch was used to remove the damage after RIE etching). Figure 9.13 shows the light-current characteristics of each of these structures, the output power being measured with a broad area detector with a numerical aperture of 0.5. The effect of tensile strain is obvious, giving higher output powers and lower threshold current densities than lattice matched devices, confirming the results from the broad area structures.

9.3 InGaAs/InGaAsP MQW Structures with Compressive Strain in the Wells

The series of structures grown within section 9.2 was very informative in describing the strain relieving process that occurs in non-compensated tensile strained InGaAs/InGaAsP MQW structures. In an attempt to complete this picture, a similar series of samples was grown with increasing compressive strain in the InGaAs wells.

9.3.1 Growth and Assessment

Nine structures were grown, which were identical except for variations in the magnitude of compressive strain in the 4 GaInAs wells from lattice match to beyond 1.6%. The structures were of the same dimensions as those grown for the tensile strain study and the growth procedure was also identical. The magnitude of compressive strain was varied by increasing the InAs mole fraction which was achieved by changing the TMIn flow. Attempts were again made to keep the well width constant by reducing the well growth time in proportion to the well strain. The well growth rates at the desired strain were calculated using a similar analysis to section 9.2.2., but this time for constant TMGa flows, giving:

$$\frac{G_r}{G_{r@LM}} = \left(1 + \frac{\Delta a}{a}\right).\frac{0.468}{x} \qquad (9.3.1)$$

x - Ga content of non lattice matched alloy.
G_r - growth rate of tensile alloy
$G_{r@LM}$ - growth rate of lattice matched alloy
a - lattice constant

The well strain was inferred from the HRXRD rocking curve in the same manner as the tensile strained structures. Table 9.2 below lists the inferred well strain, well compositions, MQW periodicity and the peak PL wavelength.

Table 9.2 - Inferred well strain, well compositions, MQW periodicity and the peak PL wavelength for each of the compressive MQW structures grown

Inferred Strain(%)	Well composition	Λ(Å)	λ(μm)
0	$Ga_{0.47}In_{0.53}As$	232	1.57
0.2	$Ga_{0.44}In_{0.56}As$	232	1.625
0.48	$Ga_{0.4}In_{0.6}As$	219	1.661
0.7	$Ga_{0.37}In_{0.63}As$	227	1.78
0.95	$Ga_{0.33}In_{0.67}As$	231	1.78
1.18	$Ga_{0.3}In_{0.7}As$	220	1.838
1.4	$Ga_{0.27}In_{0.73}As$	228	1.889
1.6	$Ga_{0.24}In_{0.76}As$	227	1.95

The HRXRD rocking curves for all of the above strained samples showed well resolved satellite peaks with none of the broadening associated with the thickness modulated growth effect. The success in controlling the MQW periodicity, Λ in table 9.2, can be seen as the maximum deviation from the mean was only 8Å. Figure 9.14 shows the rocking curves of the samples grown with 1.4% and 1.6% compressive strain in the wells; note how the well defined satellite peaks are grouped to the left hand side of the substrate peak, indicating that the structure has a net compressive strain. Figure 9.14 also illustrates the rocking curve of a further structure grown with an estimated compressive strain of between 1.8 and 1.9%. This sample showed no sign of any satellite peaks, only a very diffuse signal could be seen where the satellite peaks would be expected to lie. This is in contrast to the tensile structures, where a gradual, rather than a sudden, degradation in structural quality was observed with increasing well strain.

Room temperature PL of these samples showed a single peak at increasingly longer wavelengths as the well strain was increased. The rate of change of wavelength with well strain is consistent with the observations made on the effect of increasing tensile strain on the E1-HH1 transition. Figure 9.15 shows the effect of both compressive and tensile strain on the PL wavelength. The PL intensity of the compressively strained samples was similar from lattice match up to 1.4%. At 1.6%, the intensity reduced by a factor of 3 and the sample grown with higher strain did not luminesce. Surprisingly, no dark lines were observed in the PL image of any of these structures. Figure 9.16 shows typical PL images of samples with 0.2%,1.4% and 1.6% compressive strain in the wells. The

'mottled' appearance of these images is known to arise from the un-polished back surface of the wafer and appears as a background to all PL images, although it does not appear on wafers that have both sides polished. The 0.2% and 1.4% structures have identical images, the 1.6% case is similar but with reduced intensity.

The PL imaging observations were supported by the optical microscopy of the samples surface. Featureless surfaces were obtained at up to, and including, 1.4%. At 1.6%, point defects were observed on the sample surface as shown in figure 9.17a, though the material between these defects had good morphology. The situation degraded further above 1.6% as the micrograph shows in figure 9.17b. Here the sample had a generally much worse surface morphology.

These samples were grown towards the end of the research period and TEM analysis was no longer available. This was unfortunate as it would have been enlightening to study the type of defects that were occurring in the 1.6% and >1.6% samples and compare them with those observed in the tensile structures.

9.4 Discussion

It has been demonstrated that, by increasing the magnitude of tensile strain in the InGaAs wells of InGaAs/InGaAsP MQW structures, the most favourable transition can be altered from E1-HH1 to E1-LH1. This was shown experimentally by the evolution of the E1-LH1 associated peak in room temperature PL and also by determining the mode of polarisation in the laser devices made from these structures. The "light hole-heavy hole" cross over point for a 95Å well width occurred at a tensile strain of approximately 0.5%. Magneto optic measurements on these samples by Martin et al[12] also confirmed that the HH1-LH1 splitting energy was near zero at this value.

When the tensile strain was increased beyond 1%, a degradation in the structural quality was observed. Dark line defects, as observed by PL imaging, were introduced at tensile strains of 1.12% and above. This was different from the strain compensated structures discussed in the previous two chapters where the dislocations were only formed as an adjunct to thickness modulated growth. However, at tensile strains of 1.3% and above, thickness modulated growth was observed, with the severity of the modulation worsening as the strain was increased further. At 1.6% tensile strain, defects arise as a result of the severity of the thickness modulated growth, as seen previously with the strain compensated samples. By comparing TEM observations with the effect of increasing tensile strain on the PL image, we can deduce

- dark lines in the PL image correspond to networks of dislocations in the growth plane;
- dark spots in the PL image correspond to threading dislocations or stacking faults, i.e. vertically propagating defects, caused by the thickness modulated growth.

It was also observed from the cross-sectional TEM micrograph of the 1.6% tensile sample in figure 9.7, that the lattice matched barrier material tends to have a planarising effect on the growth, i.e. the lower interfaces of the third and fourth wells are planar whereas the upper interfaces are not. This is different from the strain compensated case where the wells and barriers exhibited thickness modulations in anti-phase. This observation adds some credence to the proposed reason for anti-phase modulations occurring in strain compensated structures discussed in chapter 7. The lattice matched layer will find it energetically more favourable to grow on the trough of a tensile layer as the material is thought to be relaxed in this region with a lattice constant closer to that of InP. However it could be argued that the overall process is going to be less extreme, as the difference in lattice constants of the well and barrier alloys is less in a non-compensated than in a compensated structure, hence the difference in growth rates between material growing on a peak and on a trough should also be less.

The presence of dislocations in the tensile strained MQW structures suggests that the critical thickness-mismatch product was encountered at some point between the growth of 4x95 Åx1% wells and 4x95 Åx1.12% wells. These two points are plotted in figure 9.18a alongside the Matthews and Blakeslee[13] curve for tensile strained GaInAs/InP. It appears that the 'defect free' and 'dark line defect' thickness-mismatch combinations straddle the critical layer thickness curve for uncapped layers. This is surprising, as the growth is essentially capped by the deposition of the subsequent barrier. The role of the MQW stack net mismatch and total stack thickness must also be considered. Figure 9.18b plots the 6 stacks grown with well strain between -0.28% and -1.29% well tensile strain, the stack thickness was calculated as 4 times the MQW periodicity as measured from the HRXRD rocking curve. The plotted stack mismatch is the net mismatch measured from the HRXRD rocking curve. It appears from this plot that the introduction of deleterious growth effects in the stacks can be related to the proximity of the stack thickness-mismatch to the critical layer thickness for a capped structure. It should be highlighted that the -0.97% sample, in which no defects were found, conflicts with the Matthews-Blakeslee prediction. Occasional experimental 'violations' of the Matthews Blakeslee model were also observed by Temkin[2].

In summary we have observed the following behaviour in strained MQW structures:

- structures with tensile GaInAs wells and lattice matched GaInAsP barriers are prone to dark line defect introduction as the un-capped Matthews-Blakeslee limit for the individual well is approached. Subsequent increases in well tensile strain introduce thickness modulated growth effects;
- structures with compressive GaInAs wells and GaInAsP barriers, did not seem susceptible to dark line defect introduction nor thickness modulated growth. Insufficient characterisation data is available to quantify these observations further;
- structures with compressive GaInAs wells and latticed matched GaInAs barriers, where the well thickness-mismatch is less than the predicted Matthews-Blakeslee limit, are prone to dislocation introduction when the stack thickness exceeds its critical value.
- structures with compressive GaInAsP wells and tensile GaInAsP barriers are prone to thickness modulated growth effects. Any dislocation introduction is as an adjunct to the thickness modulated growth effect.

It therefore appears that the type of 'strain relieving' mechanism which occurs is strongly dependent on the combination of the well/barrier composition. This conclusion was given further support by experimental observations made on two 0.5% compressively strained GaInAsP structures. The two structures were identical except for the type of 'barrier' material which, in one case was InP and in the other lattice matched GaInAsP. Schematic diagrams of the structures are shown in figure 9.19. They are not quantum well structures but a series of relatively thick layers (500-1500 Å) of 'well' material separated by 2000Å of 'barrier' material. The $Ga_{0.335}In_{0.665}As_{0.71}P_{0.29}/Ga_{0.34}As_{0.66}As_{0.9}P_{0.1}$ structure exhibited poor surface morphology of the type indicative of thickness modulated growth. Figure 9.20 shows plan view and cross sectional TEM's of this sample. Figure 9.20a is an image of the cross section ($g=2\bar{2}0$), which shows only the lower 'wells' which are light field. It is clear from these micrographs that the surface has a rippled appearance and thickness modulations have indeed occurred. No misfit dislocations were observed and the line defect that appears in the plan view is thought to be a threading dislocation. The $InP/Ga_{0.34}As_{0.66}As_{0.9}P_{0.1}$ structure, however, had very different characteristics. The surface morphology was cross hatched in a similar way to the 50 cycle $Ga_{0.47}In_{0.53}As/Ga_{0.32}In_{0.68}As$ structure. Figure 9.21 shows cross sectional (a) and plan view (b) TEM micrographs of this sample, the cross-section shows all 6 'wells'. Here, all the well/barrier interfaces are abrupt and the strain relief mechanism is supplied solely through the generation of dislocations. Other TEM analyses on this sample indicated that dislocations occurred when the 'well' thickness exceeded 900Å.

It is clear from all of the above evidence that the type of barrier material, be it InP, GaInAs or GaInAsP, is important in governing the strain relief mechanism of non-compensated InP-based MQW structures. The presence of thickness modulations in these structures makes the comparison with InP/GaInAs[2] and GaAs/GaInAs[14] results and the Matthews and Blakeslee model[13] difficult. The occurrence of thickness modulations is not accounted for in the Matthews and Blakeslee model. The observed effect of the barrier material gives further credence to the results of Bangert[15], who suggested that the barrier composition may have an effect on the severity of thickness modulated growth.

The detailed study of the effect of tensile strain on the behaviour of the threshold current density has yielded results whose trends are consistent with PL spectra measurements, the mode of lasing and magneto-optic measurements. This study, which assessed 8 values of strain, gives a more detailed account than either of the studies referenced, Thijs measured 5 points and Zah measured 4 points. In spite of the crystallographic defects that were introduced into the tensile strained structures at, and above, 1.12% a reduction in the threshold current densities over the lattice matched case were observed when the E1-LH1 transition became the most favourable. A decrease in the parameter k, which has been shown to be related inversely to the gain per well, has also been observed in these structures at similar values of strain. In fact, the value of k measured is lower than any of the strained or lattice matched MQW lasers discussed hitherto in this thesis. A fuller comparison of these devices will be presented in the thesis conclusions.

References

1. PJA Thijs, JJM Binsma, LF Tiemeijer, PI Kuindersma and T. van Dongen, Microelectronic Engineering, 18(1992), pp57-74.

2. H Temkin, DG Gershoni, SNG Chu, JM Vandenberg, RA Hamm and MB Panish, Appl. Phys. Letts., 55(16), Oct. 1989, pp1668-1670.

3. PL Gourley, IJ Fritz and LR Dawson, Appl. Phys. Letts., 52(5), Feb 1988, pp377-379.

4. AR Adams, IEE Elect. Letts., 22(5), Feb 1986, pp249-250.

5. EP O'Reilly, Semicond. Sci. Technol. , 4(1989), pp121-137.

6. E Yablonovitch and EO Kane, IEEE J. Lightwave. Tech., 6(8), August 1988, pp1292-1299.

7. CE Zah, R Bhat, B Pathak, C Caneau, FJ Favire, NC Andreadakis, DM Hwang, MA Koza, CY Chan and TP Lee, IEE electron Lett, 27(16), 1991, pp1414-1416.

8. S Sogou, A Kameyama, Y Miyamoto, K Furuya, Y Suematsu, Jap. J. Appl. Phys., 23(9), Sept. 1984, pp1182-1189.

9. MPCM Krijn, GW 't Hooft, MJB Boermans, PJA Thijs, T van Dongen, JJM Binsma, LF Tiemeijer and CJ van der Poel, Appl. Phys. Letts., 61(15), Oct 1992, pp1772-1774.

10. GHB Thompson, 'Physics of semiconductor laser devices', Chapter 4 - Optical Waveguides, 1980, John Wiley & sons Ltd.

11. PJA Thijs, JJM Binsma, EWA Young and WME van Gils, IEE Electron. Letts., 1991, 27(10), pp791-793.

12. RW Martin, SL Wong, RJ Warburton, RJ Nicholas, AD Smith, MA Gibbon and EJ Thrush, Phys. Rev. B, 50(11), Sept. 1994, pp7660-7667.

13. JW Matthews and AE Blakeslee, J. Cryst. Growth., 27, 1974, pp118-125.

14. IJ Fritz, ST Picraux, LR Dawson, TJ Drummond, WD Laidig and NG Anderson, Pppl. Phys. Letts., 46(10), May 1985, pp967-969.

15. U Bangert, AJ Harvey, VA Wilkinson, C Dieker, JM Jowett, AD Smith, SD Perrin and CJ Gibbings, J Cryst Growth, 132, 1993, pp231-240.

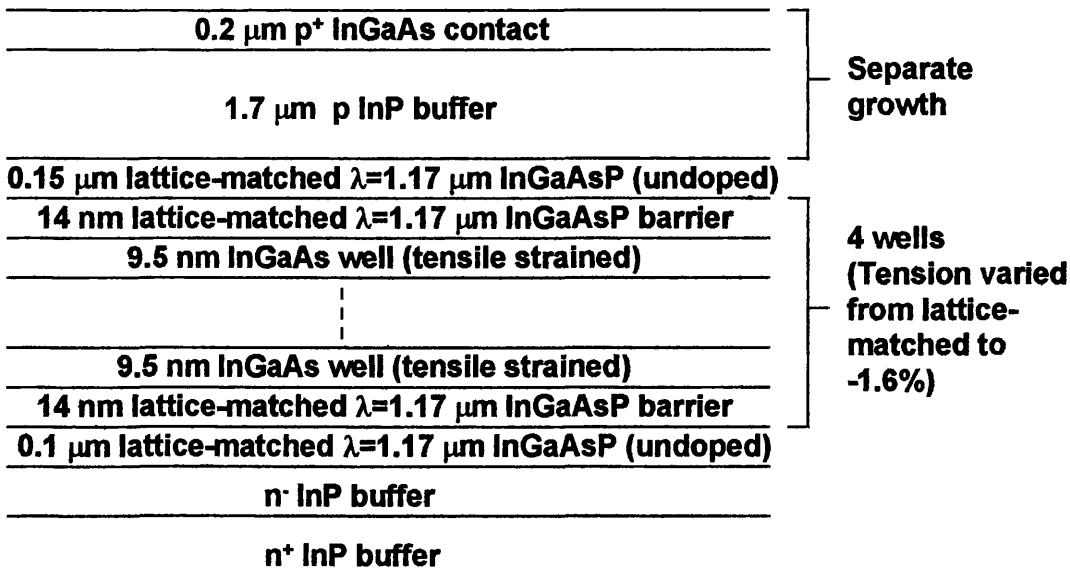

Figure 9.1 Layer structure used to investigate the effect of increasing tensile well strain on the structural properties and the behaviour of subsequently fabricated devices.

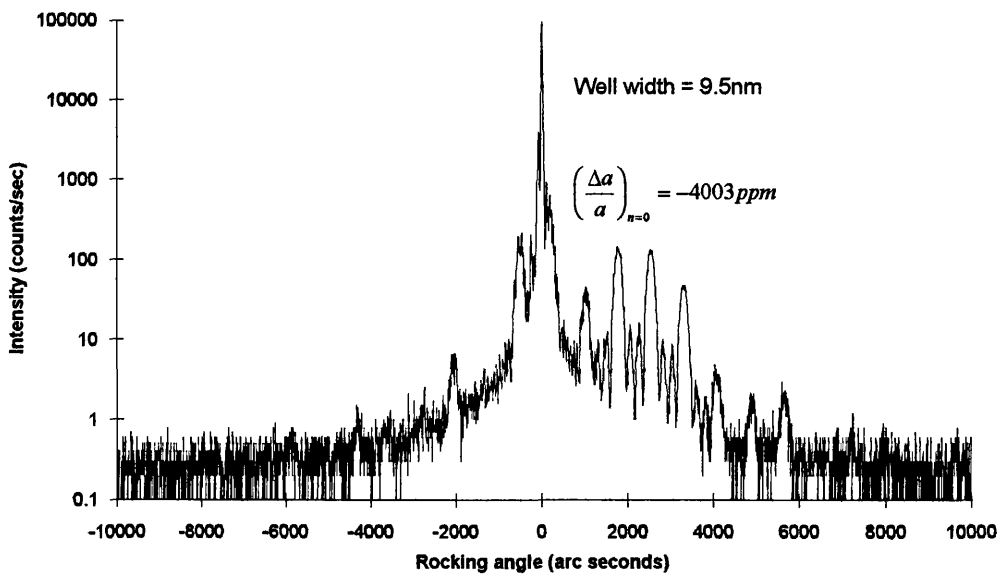

Figure 9.2 HRXRD rocking curve of structure with an intended 1% tensile strain in the wells. Well defined, intense satellite peaks are evident in this 4-well structure.

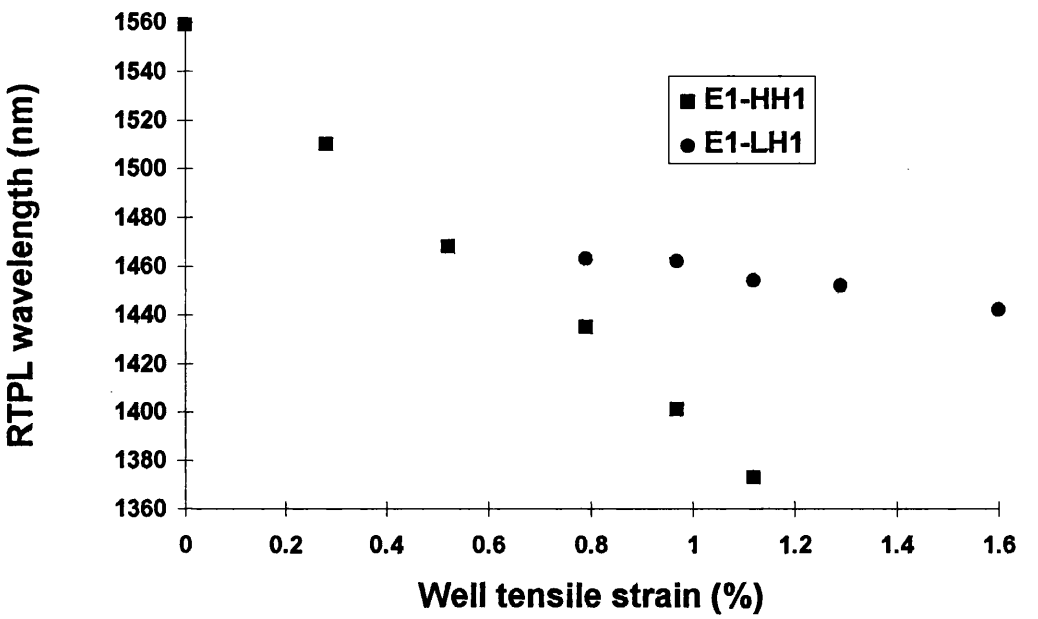

Figure 9.3 The effect of increasing well tensile strain on room temperature PL wavelength. It would appear that, by extrapolation, the LH-HH cross-over point is achieved at approximately 0.5%.

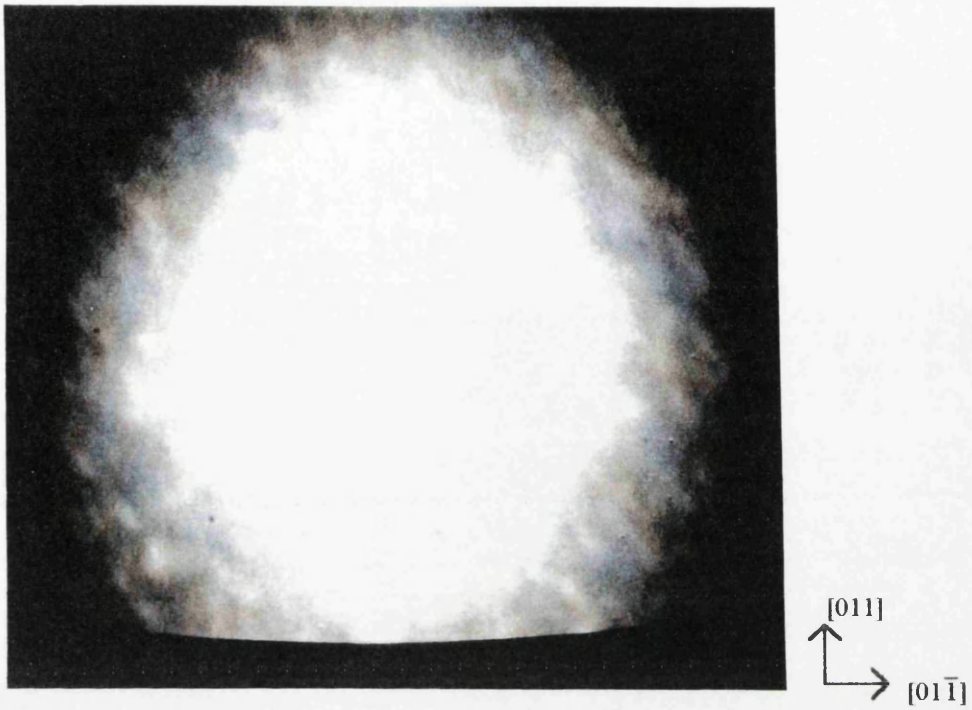

Figure 9.4a PL image of structure with 1% tensile strain in the wells.

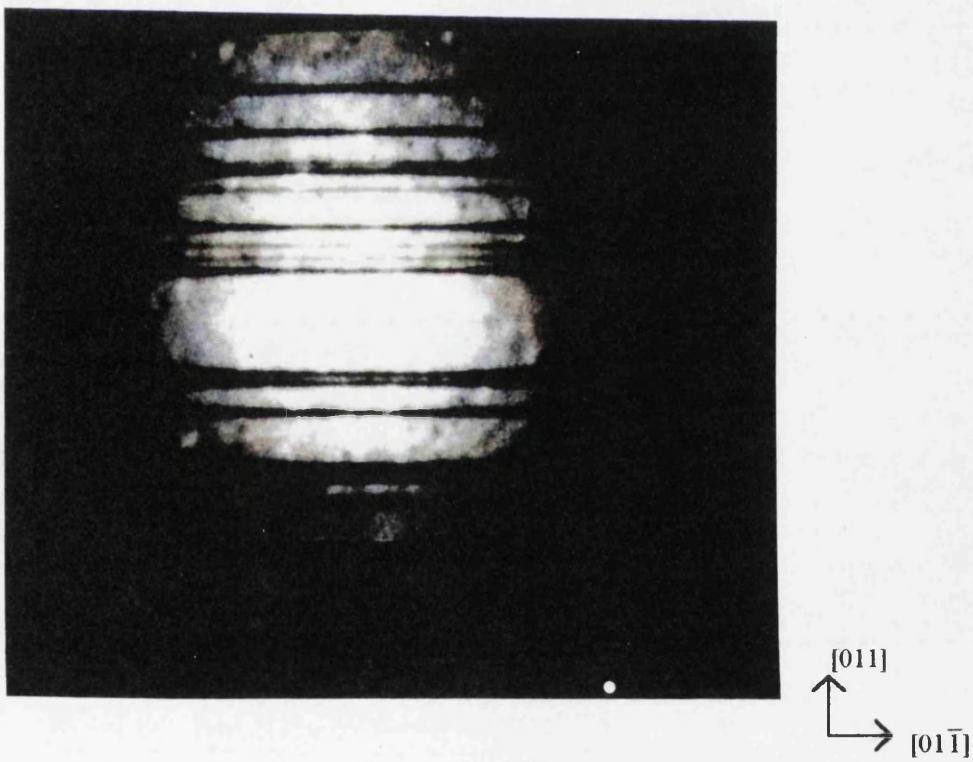

Figure 9.4b PL image of structure with 1.12% tensile strain in the wells. Dark lines can be seen running in the [01$\bar{1}$] direction.

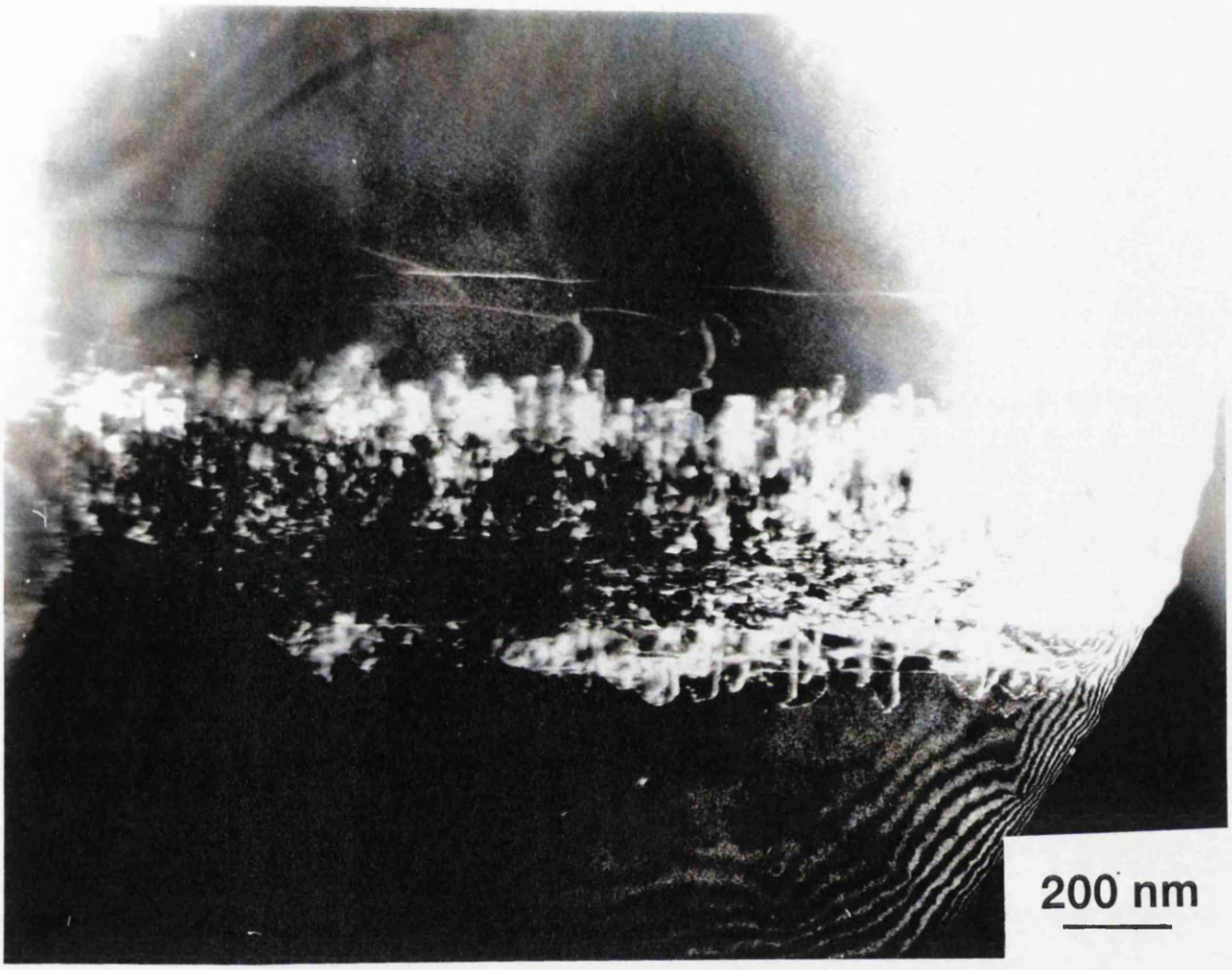

Figure 9.4c Plan view TEM of 'one' dark line shown in figure 9.4b. The dark line seems to comprise a network of orthogonal dislocations running predominantly in the $[01\bar{1}]$ direction.

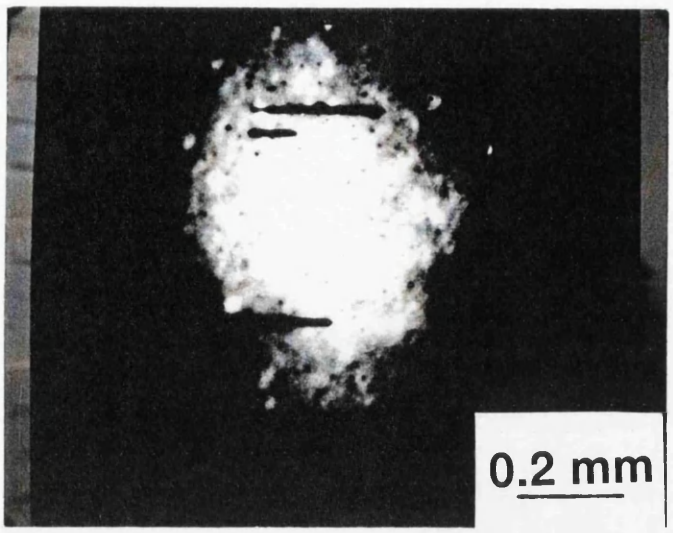

Figure 9.4d PL image of structure with 1.3% tensile strain in the wells. The image consists of a combination of short 'dark line' and 'dark spot' features.

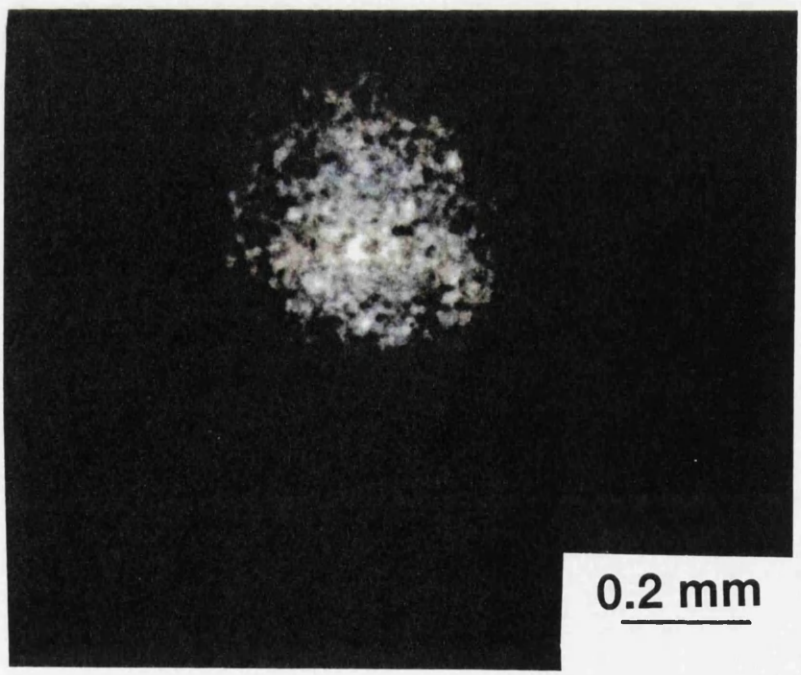

Figure 9.4e PL image of structure with 1.6% tensile strain in the wells. The poor image consists predominantly of 'dark spot' features.

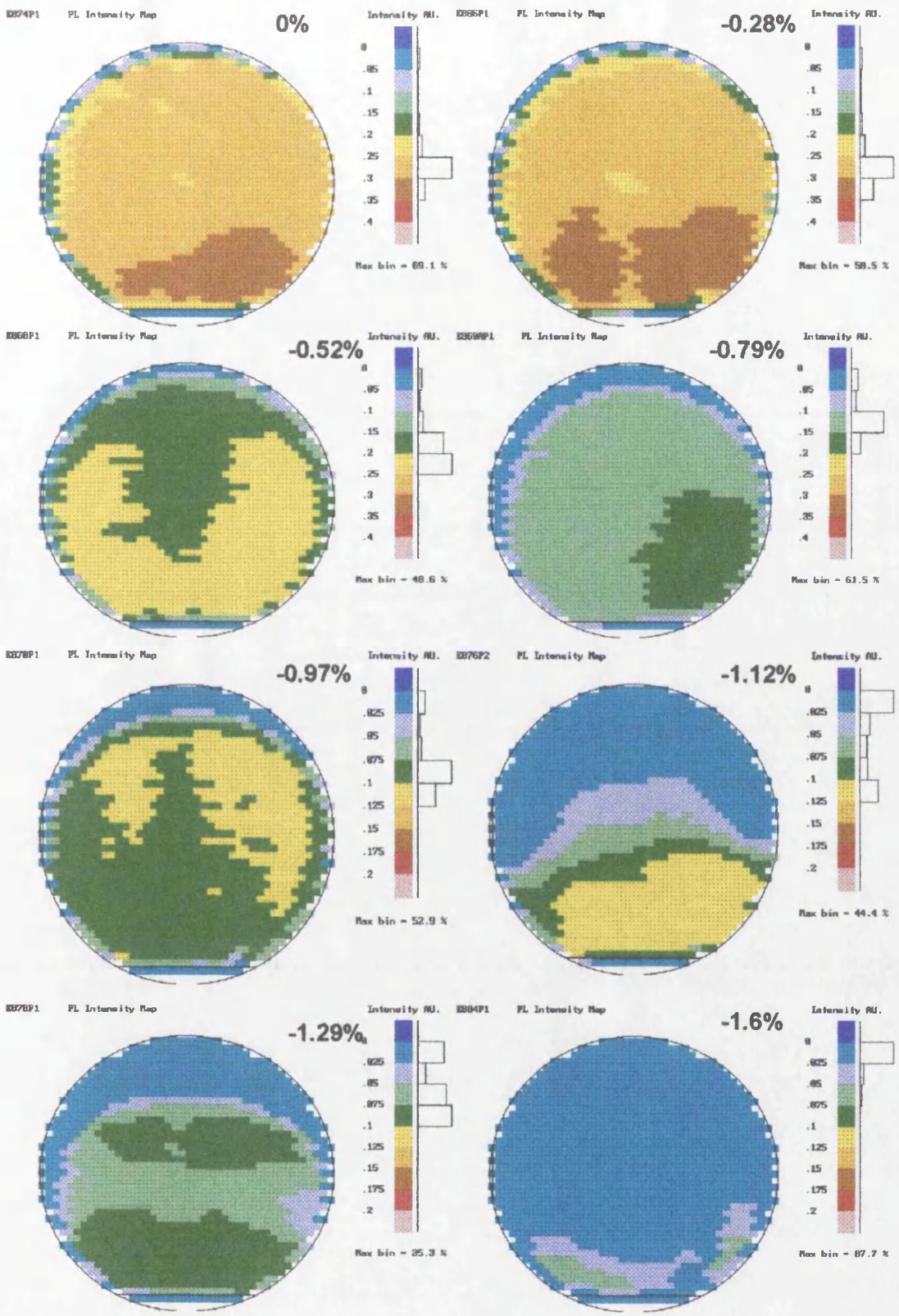

Figure 9.5 Full wafer room temperature PL intensity maps of the 8 structures with well strains ranging from lattice matched to 1.6%. Note how the intensity starts to diminish in the upstream (known high mismatch) areas of the wafer first.

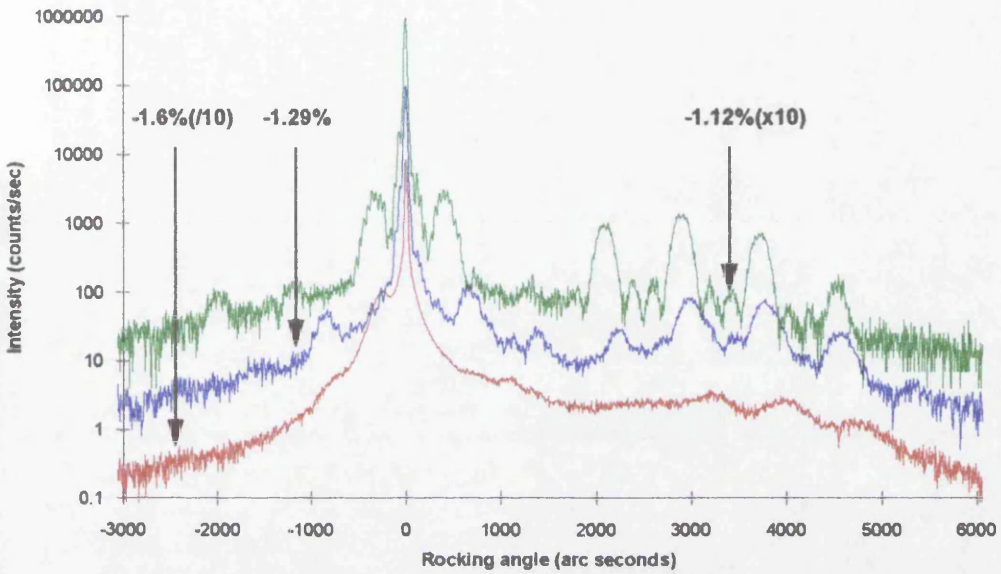

Figure 9.6 HRXRD rocking curves of structures grown with 1.12, 1.29 and 1.6% well tensile strain. The three curves have been offset in intensity each by one decade. A deterioration in the quality of the satellite peaks is observed when we increase well tensile strain above 1.12%.

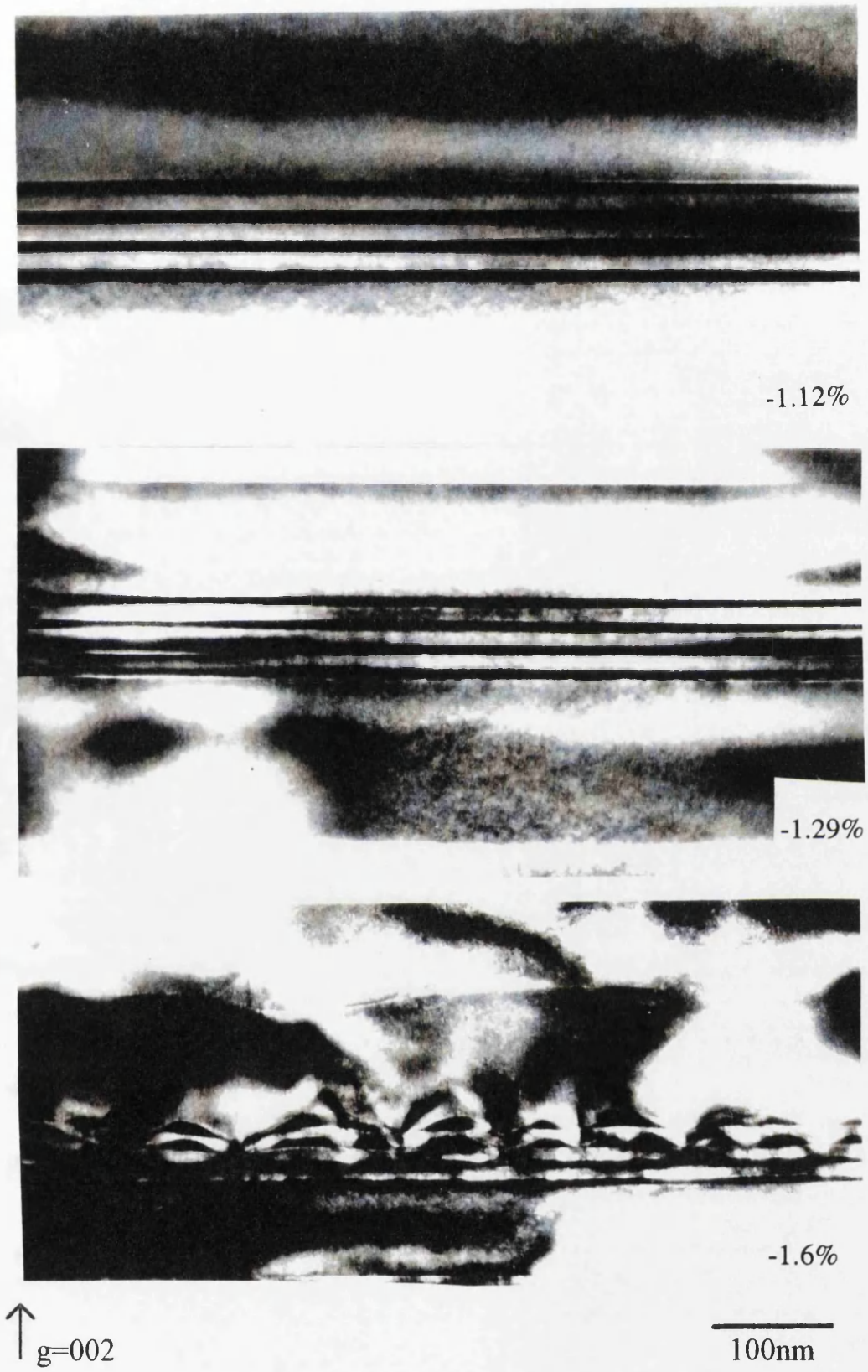

Figure 9.7 Cross-sectional TEM images (g=002) of the three structures whose rocking curves are shown in figure 9.6. It is evident that at well tensile strains greater than 1.12%, thickness modulated growth occurs. The 1.6% sample best exemplifying this phenomenon.

Figure 9.8 Cross-sectional TEM (g=$\bar{2}$02) image of structure with 1.6% tensile strain in the wells. The periodic contrast which is observed is an indication of the variation on strain. Thickness modulated growth is so bad in this sample that threading dislocations and stacking faults have been generated in the upper part of the structure.

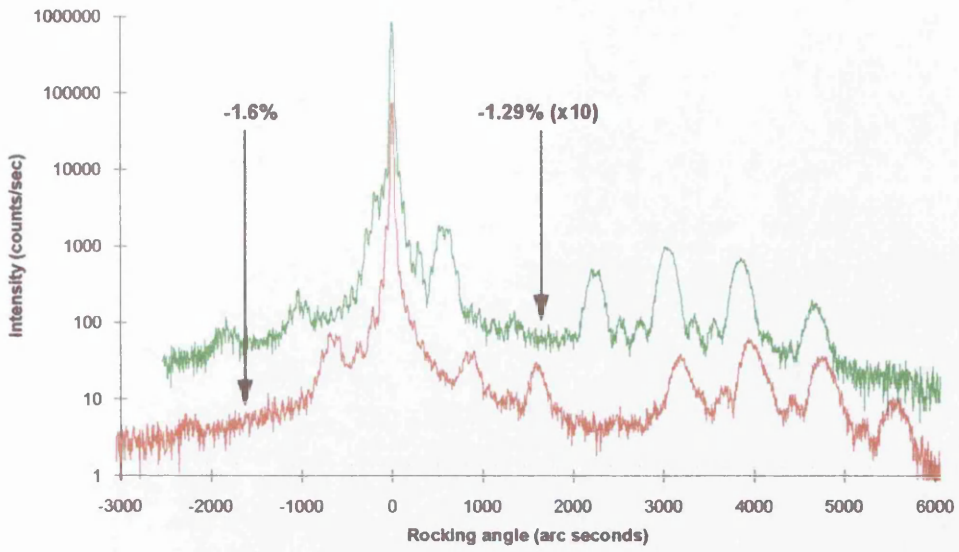

Figure 9.9 HRXRD Rocking curve of structures with 1.29% and 1.6% tensile strain in the wells. These structures were grown with a 37 times increase in the AsH_3 gas flow during the well growth.

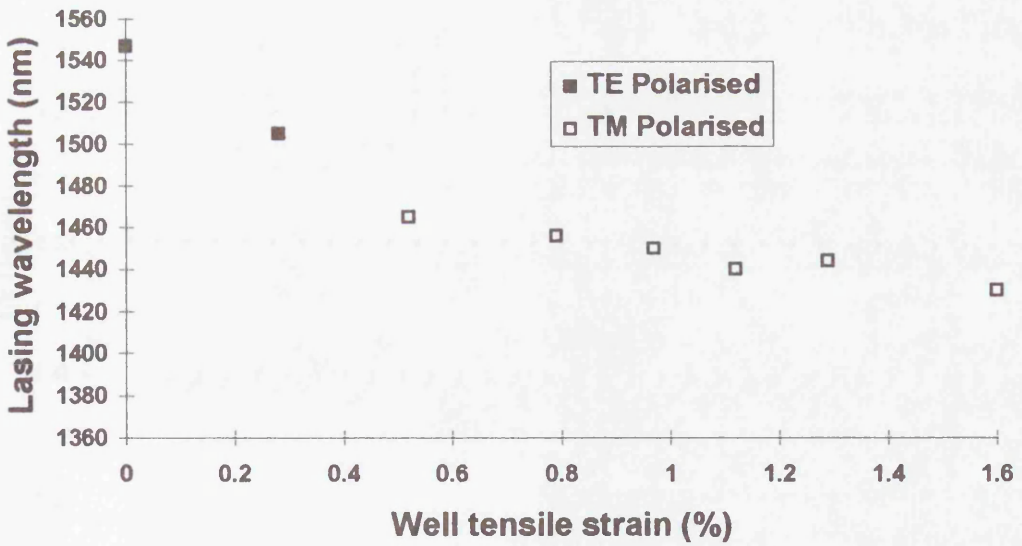

Figure 9.10 Lasing wavelength and polarisation state as a function of well tensile strain. The TE/TM crossover point is co-incident with the change from HH to LH behaviour as seen in figure 9.3.

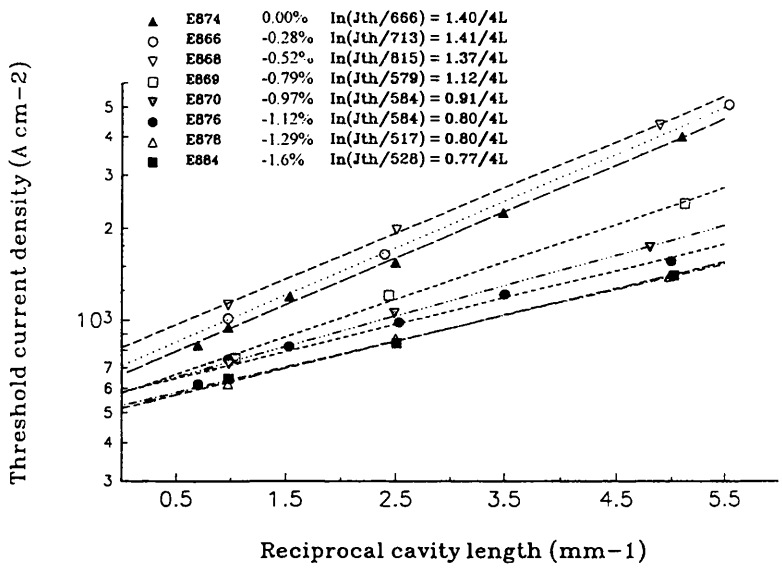

Figure 9.11 Plot of threshold current density versus reciprocal cavity length for each of the eight structures with well tensile strains ranging from lattice matched to 1.6%.

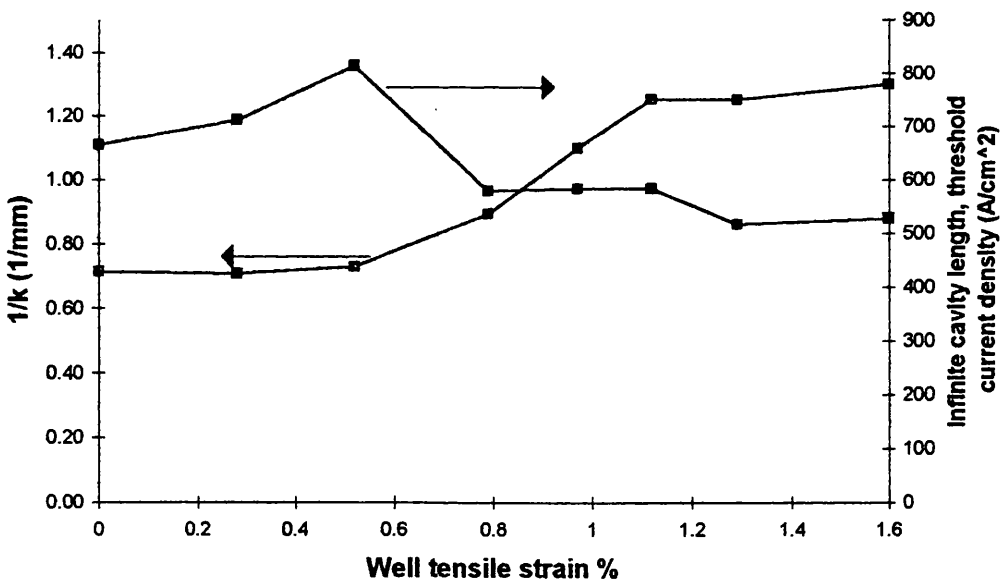

Figure 9.12 Plot of the infinite cavity length threshold current density and the k parameter versus well tensile strain. The former is derived from the y-axis intercept and the latter the inverse of the slope of the curves shown in figure 9.11.

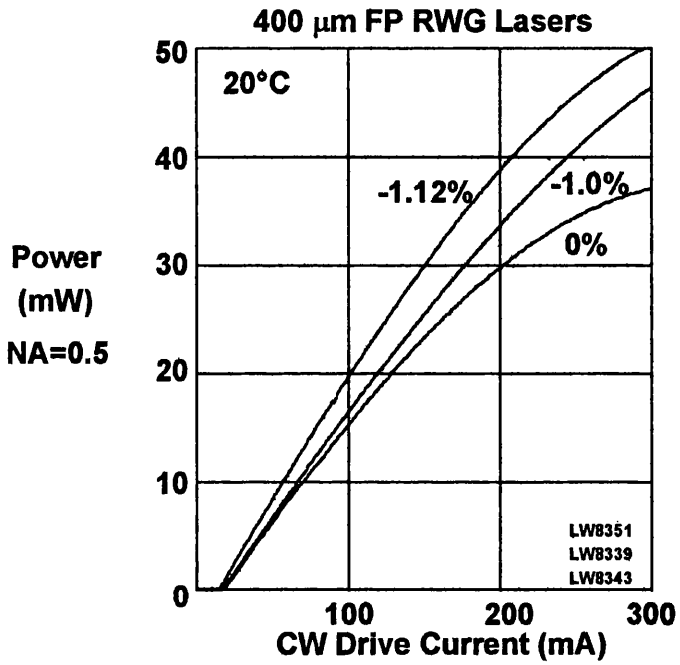

Figure 9.13 20°C L-I characteristics of 400μm long, 2μm wide, Fabry-Perot devices. The ridges were fabricated using CH_4:H_2 RIE.

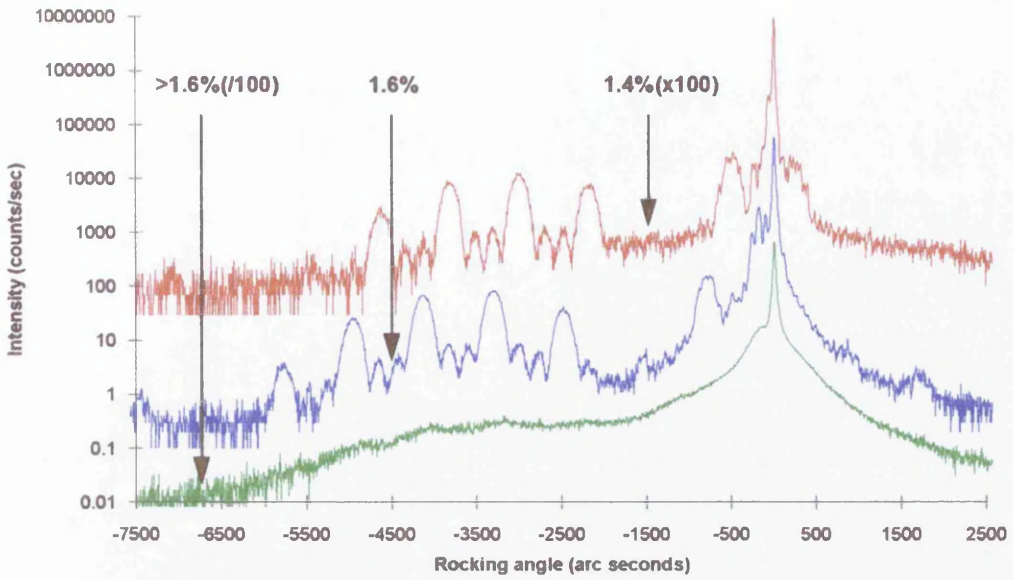

Figure 9.14 HRXRD Rocking curves of three structures with well compressive strains of 1.4%, 1.6% and >1.6%. A sudden deterioration is observed in quality of the structure grown in excess of 1.6% well strain. The rocking curves are all offset by one decade to assist viewing.

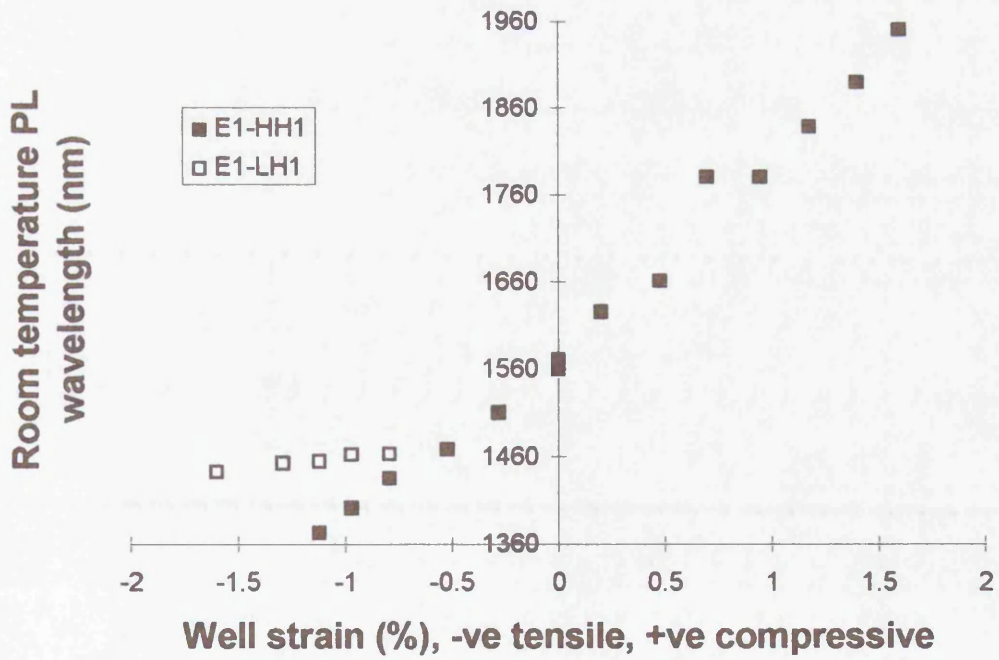

Figure 9.15 Plot of room temperature PL wavelength versus well strain for both tensile and compressively strained quantum well devices. The E1-HH1 transition appears to depend linearly on well strain, whereas the E1-LH1 transition is relatively insensitive to well strain.

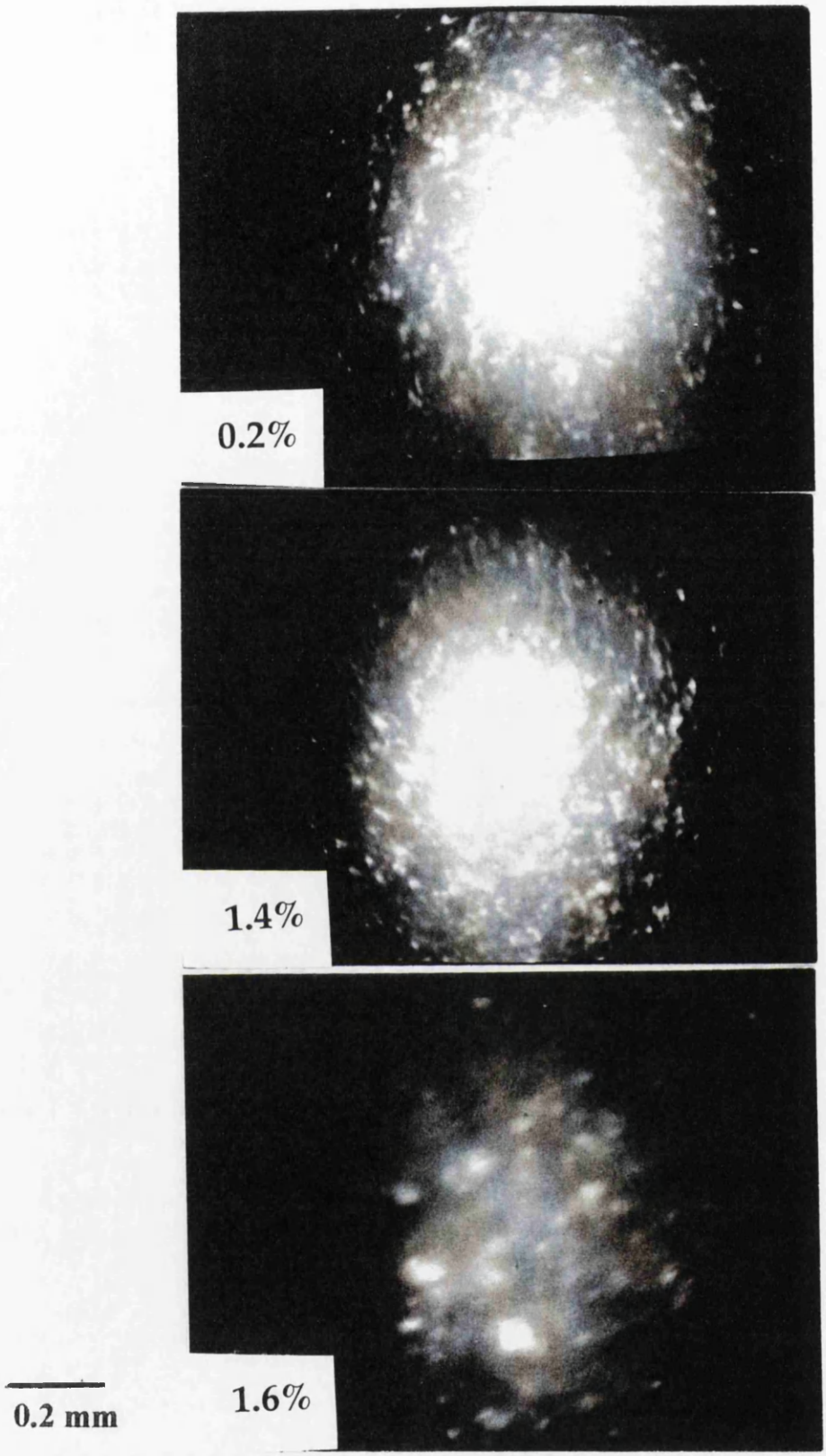

Figure 9.16 Room temperature PL images taken from structures with 0.2%, 1.4% and 1.6% compressive strain in the wells. The images are similar for all samples with the 1.6% sample having reduced intensity.

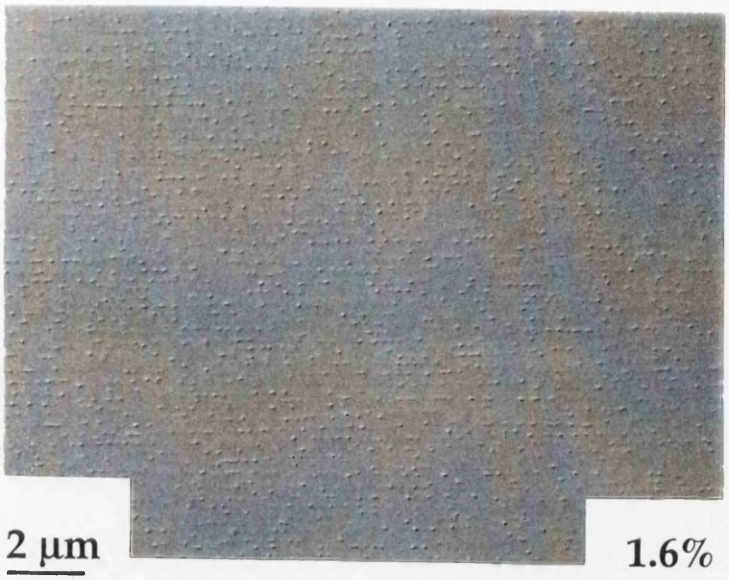

Figure 9.17a Normarski interference micrograph illustrating the surface morphology of the structure with 1.6% compressive strain in the wells. Surface defects are evident.

Figure 9.17b Normarski interference micrograph illustrating the surface morphology of the structure with >1.6% compressive strain in the wells. A further deterioration in the surface is observed when compared to the 1.6% sample.

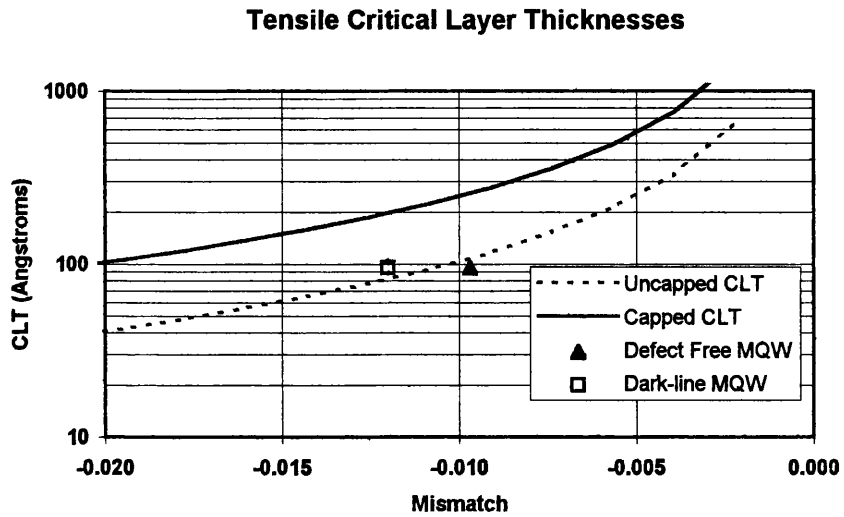

Figure 9.18a Plot of well thickness versus mismatch for the -0.97% and -1.29% tensile strained wells compared to the Matthews-Blakeslee plot for capped and uncapped tensile strained GaInAs.

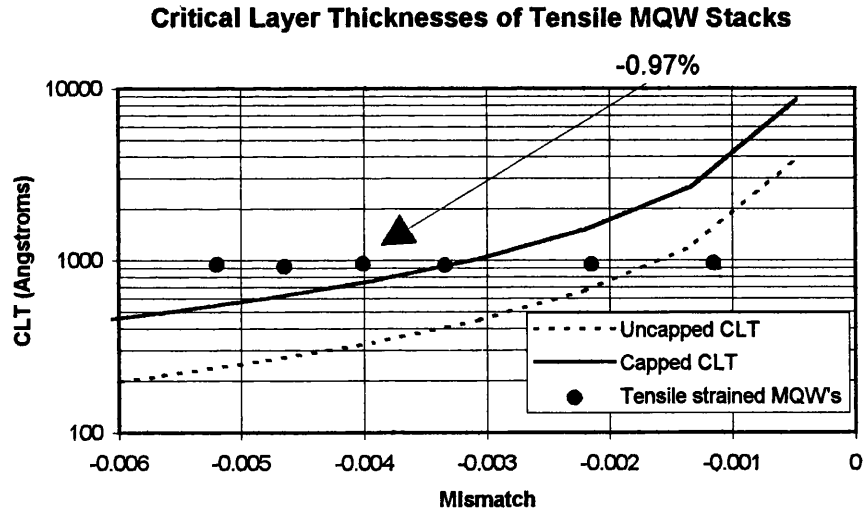

Figure 9.18b Plot of MQW stack thickness versus mismatch for the -0.28% to -1.29% tensile strained MQW structures compared to the Matthews-Blakeslee plot for capped and uncapped tensile strained GaInAs.

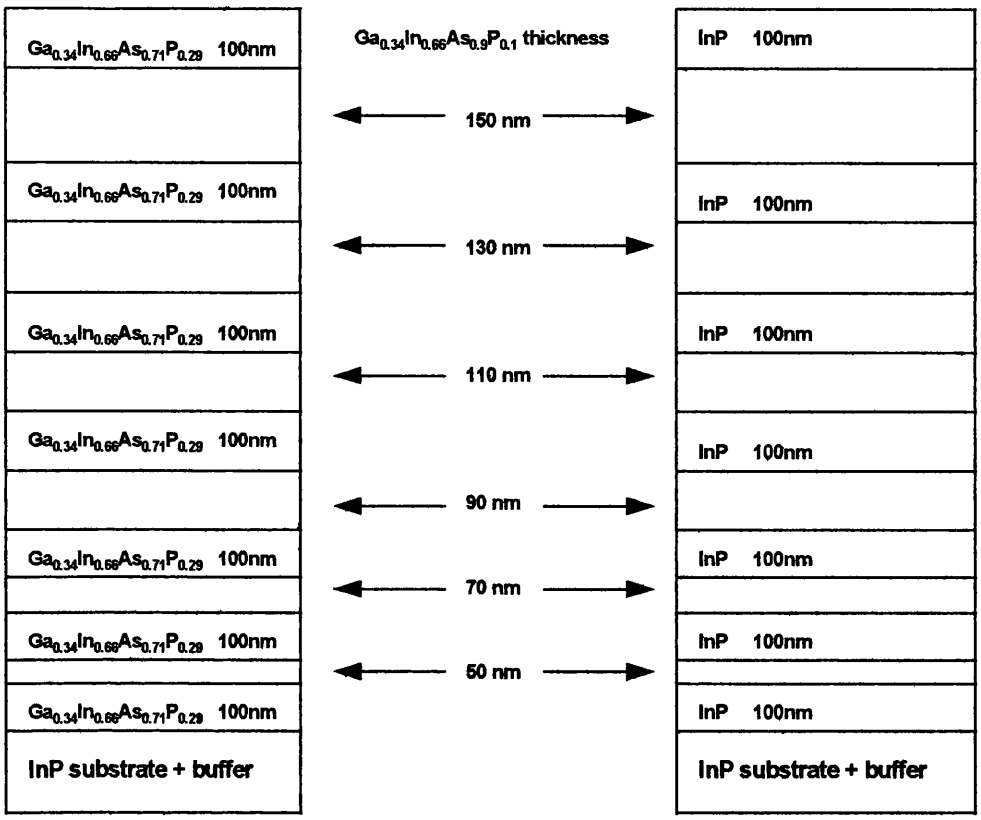

Figure 9.19 Layer structures of two similar structures grown with varying thicknesses of 0.5% comparatively strained material. Different 'barrier' material is used in each structure: the first uses lattice matched $Ga_{.34}In_{.66}As_{.71}P_{.29}$ (same Ga:In ratio as the strained material) and the second uses InP.

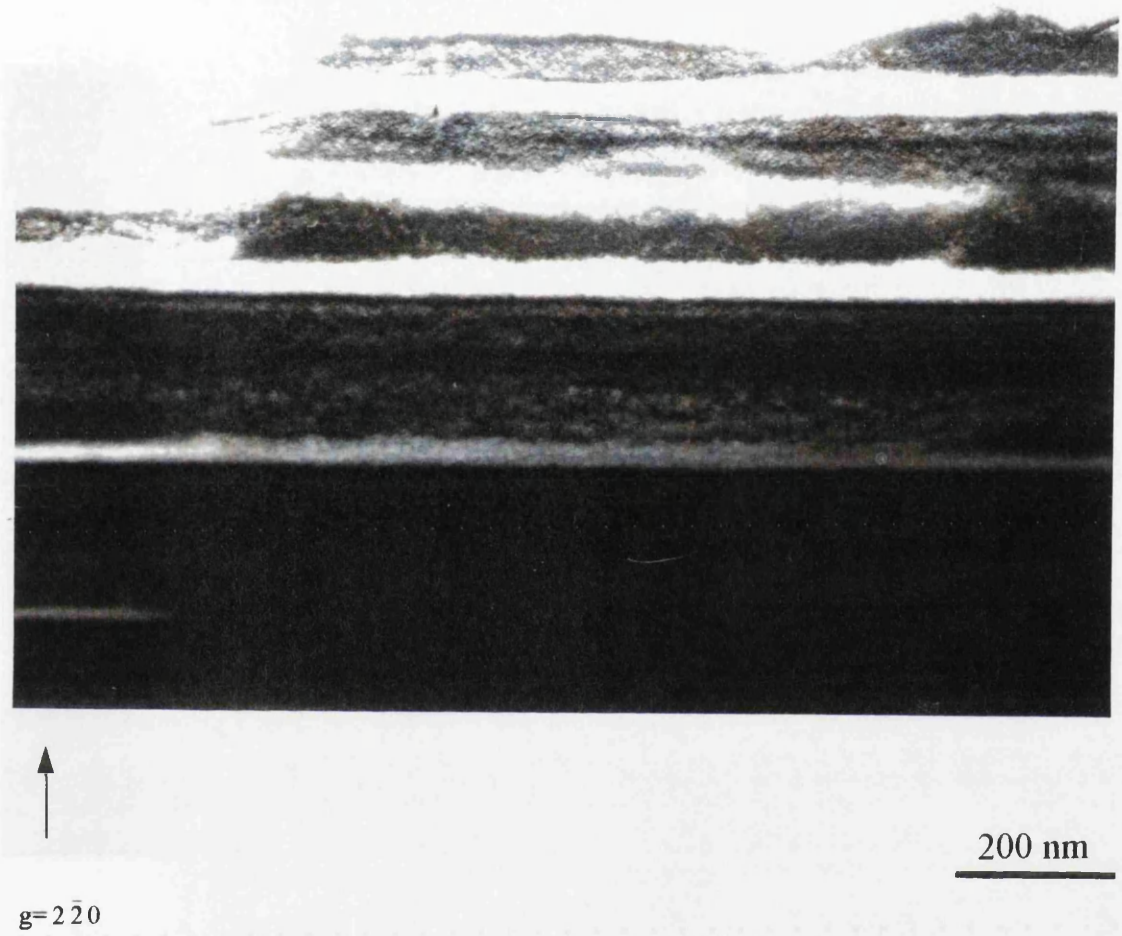

Figure 9.20a Cross section TEM ($g=2\,\bar{2}\,0$) of GaInAsP/GaInAsP structure shown on the left of figure 9.19. The lower part of the structure is shown here, it is clear that thickness modulated growth has occurred.

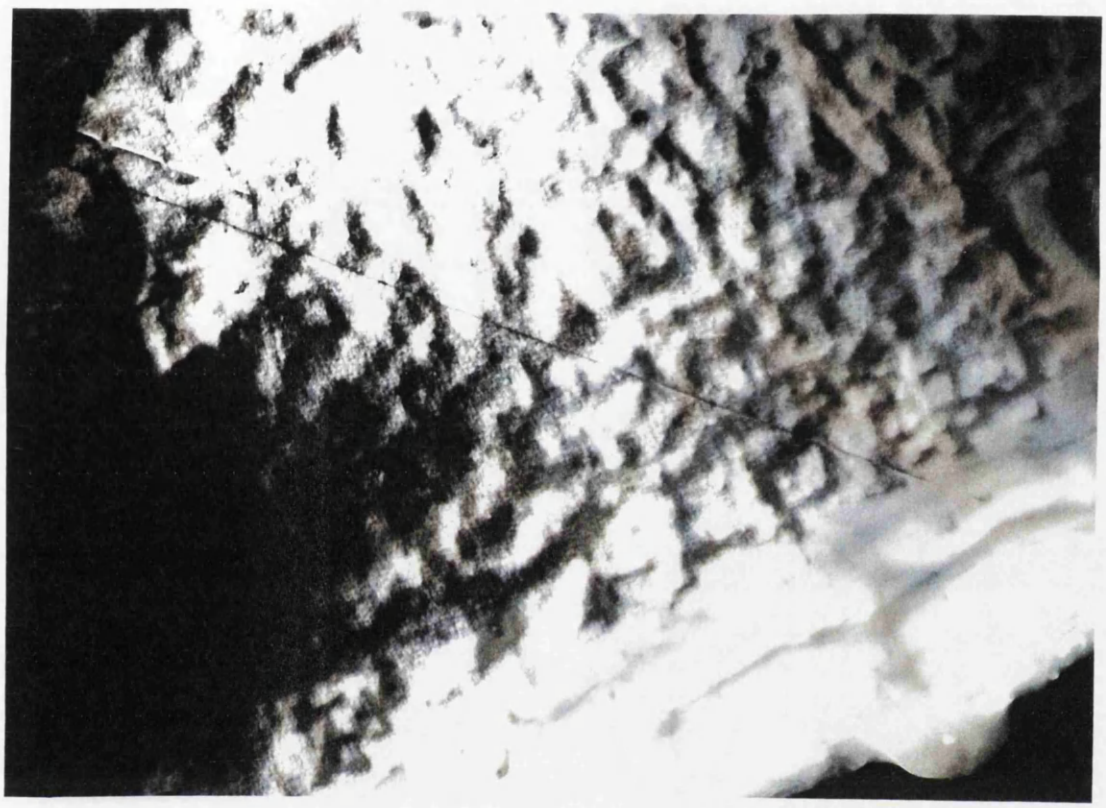

200 nm

g=2$\bar{2}$0

Figure 9.20b Plan view TEM (g=2$\bar{2}$0) of GaInAsP/GaInAsP structure shown on the left of figure 9.19. The rippled surface morphology is also confirmation of thickness modulated growth.

Figure 9.21a Cross section (g=040) of GaInAsP/InP structure shown on the right of figure 9.19. The entire structure is shown here, it is clear that there is no evidence of thickness modulated growth and all the interfaces are planar

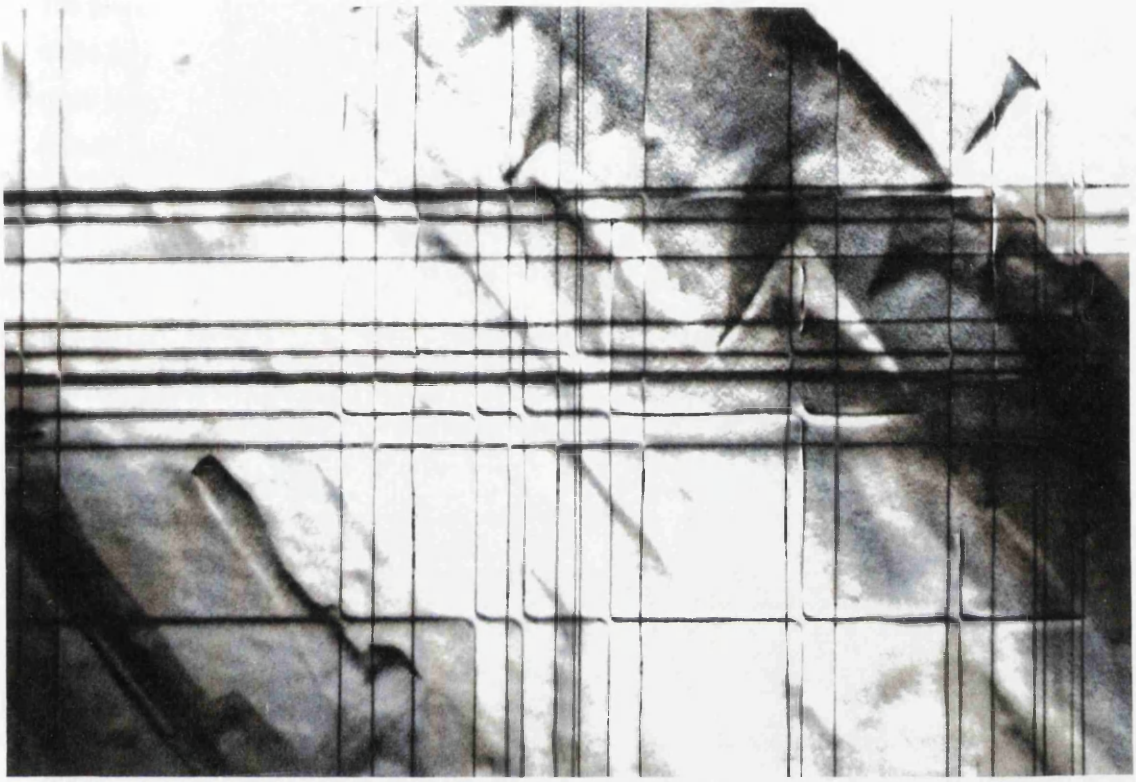

Figure 9.21b Plan view TEM (g=040) of GaInAsP/InP structure shown on the right of figure 9.19. The orthogonal misfit dislocation network indicates that the GaInAsP/InP structure has a different strain relief mechanism to the GaInAsP/GaInAsP structure.

Chapter 10

Thesis Conclusions

The primary aims of the research described in this thesis were, to evaluate the effects of introducing strain in the wells and barriers of $Ga_xIn_{1-x}As_yP_{1-y}$ based MQW structures, to fabricate devices from these structures and to assess device performance in such a way that the dependence on material properties, intentionally varied by the strain, could be elucidated. An extensive growth study has been presented that examined different combinations of well and barrier alloys incorporating varying amounts of well and barrier strains. In addition, device results have been presented on strain-compensated compressive well structures and non-compensated tensile well structures, which include detailed analyses on the dependence of parameters such as cavity length, well strain and number of wells. Discussions of the results and conclusions were presented at the end of each chapter. The purpose of this final chapter is to present the broader conclusions of this work. This is best achieved in two parts: firstly through an analysis of the material growth conclusions, and secondly by a discussion of the trends observed in the device results.

10.1 The Growth of $Ga_xIn_{1-x}As_yP_{1-y}$ Strained Layer Multiple Quantum Wells

Initial attempts to grow strain compensated $Ga_xIn_{1-x}As_yP_{1-y}/Ga_xIn_{1-x}As_yP_{1-y}$ MQW lasers were successful, when the number of wells did not exceed 8. When thicker structures were grown, the wells and barriers began to suffer from modulations in the growth rate. In order for these lateral variations in thickness to develop, it is believed that either, or both, of the following must occur:

- compositional clustering (also known as spinodal decomposition). This gives rise to localised variations in the alloy composition and, consequently, strain. Subsequently deposited material will exacerbate the effects of clustering, as highly strained material will grow on the strain enhanced areas and less strained material will grow on the strain reduced regions. The susceptibility of a given alloy to this effect can be predicted by its proximity to the Ga-In-As-P miscibility gap. It is therefore assumed that this effect would be minimised by growing at higher temperatures.
- strain relaxation via the expansion and contraction of lattice planes. This behaviour is well documented in the Si/Si_xGe_{1-x} strained layer system[1]. In the case of a compressive layer, the strain is reduced in the regions of expansion and increased in the regions of contraction. In the Si/Si_xGe_{1-x} system ,strain is relieved as the volume of the strain

reduced regions is greater than the volume of strain increased regions. Lateral compositional variations arise as a result of the lattice plane expansion/contraction. Reports from the Si/Si_xGe_{1-x} system showed that this effect could be reduced by lowering the growth temperature.

The proposal that thickness modulated growth was an important strain relief mechanism in $Ga_xIn_{1-x}As_yP_{1-y}/Ga_xIn_{1-x}As_yP_{1-y}$ MQW structures, was given further credence by the unintentional introduction of a laterally defined strain variation, caused by mass transport of $Ga_xIn_{1-x}As_yP_{1-y}$ into grooves etched in InP. Strain compensated MQW growth above lattice matched areas exhibited planar growth, whereas growth above the strained area exhibited thickness modulated growth.

An improvement in the structural quality of ±1% $Ga_xIn_{1-x}As_yP_{1-y}$ MQW structures was observed when the growth temperature was increased to 700°C, but it was not the panacea for this cumulative thickness limiting effect. To simplify the problem, the effects of compositional clustering were inhibited by operating as far outside the miscibility gap as possible with the growth of ±1% $Ga_xIn_{1-x}As$ MQW structures. At a growth temperature of 650°C, however, thickness modulations were also observed in the ±1% $Ga_xIn_{1-x}As$ structures. It was observed that the thickness modulations were suppressed, but not eliminated, by increasing the group V partial pressure. More importantly, and in contradiction to the observations made with the quaternary structures, it was found that the structural quality improved with the reduction of growth temperature. The parameter space for the growth of strain compensated ±1% $Ga_xIn_{1-x}As$ MQW structures was optimised so that essentially limitless numbers of wells and barriers could be grown. In fact a 50 cycle ±1% $Ga_xIn_{1-x}As$ MQW with a total strained thickness of 0.93μm was demonstrated[2].

The above observations would suggest that there are two temperature dependent effects in the growth of strained $Ga_xIn_{1-x}As_yP_{1-y}$ alloys. The likelihood of compositional clustering decreases with increasing growth temperature, however the likelihood of strain relief via lattice expansion/contraction increases with increasing growth temperature. It was further demonstrated that the quality of strain compensated $Ga_xIn_{1-x}As_yP_{1-y}/Ga_xIn_{1-x}As_yP_{1-y}$ MQW structures improved when the alloys used were selected outside the effects of the miscibility gap[3]. The limitation of alloy selection to those outside the miscibility gap, placed unwelcome constraints on the choice of alloys available to a device designer. The observation that the group V partial pressure improved the quality of ±1% $Ga_xIn_{1-x}As$ MQW structures, was also applied to increase the number of wells that could be grown in a ±1% $Ga_xIn_{1-x}As_yP_{1-y}$ structure. By increasing the AsH_3 and PH_3 flows used, high quality device structures could be grown with the desired number of wells[4]. It should be emphasised that this solution was insufficient for the growth of higher numbers (>12) of wells.

The role of group V partial pressure was also validated by observations reported in the open literature and discussions with colleagues in other laboratories. The reports on Gas Source MBE grown structures showed thickness modulations occurring much earlier in an MQW stack, after only the second barrier layer had been deposited[5]. Similar structures grown by atmospheric MOVPE seemed less prone to the thickness limitations observed with low-pressure MOVPE.

Non-compensated $Ga_xIn_{1-x}As_yP_{1-y}$ MQW structures were also shown to experience growth limitations. The classical limitation of dislocation generation in a strained stack was observed in tensile strained $Ga_xIn_{1-x}As_yP_{1-y}/Ga_xIn_{1-x}As$ MQW structures, compressively strained $Ga_{0.47}In_{0.53}As/Ga_{0.32}In_{0.68}As$ structures and compressively strained $InP/Ga_{0.34}As_{0.66}As_{0.9}P_{0.1}$ structures. Thickness modulations were also observed as a second strain relief mechanism in the tensile strained $Ga_xIn_{1-x}As_yP_{1-y}/Ga_xIn_{1-x}As$ MQW structures. The type of the lattice matched barrier material used, was also shown to control the type of strain relief mechanism that occurred. In the case of a compressively strained $Ga_xIn_{1-x}As_yP_{1-y}$, planar growth was maintained and strain relief was introduced via dislocation generation when InP was used as the barrier material. However, thickness modulated growth was observed in an identical structure, when lattice matched $Ga_xIn_{1-x}As_yP_{1-y}$ material (whose composition was inside the miscibility gap) was used as the barrier material.

The thickness modulated growth effect could also be suppressed in the non-compensated samples by using a higher group V partial pressure but, like the compensated structures, the effect could not be completely eliminated. The introduction of strain relieving dislocations was not affected by changes in group V partial pressure. The occurrence of strain relieving dislocations in tensile strained $Ga_xIn_{1-x}As_yP_{1-y}/Ga_xIn_{1-x}As$ MQW structures was shown to be governed by the behaviour of the individual well complying to the Matthews-Blakeslee condition for an un-capped layer, agreeing with previous reports in the literature[6].

In spite of some of the growth limitations imposed, the samples grown in this work afforded a detailed study into the effects of strain incorporation on device performance.

10.2 The Performance of $Ga_xIn_{1-x}As_yP_{1-y}$ Strained Layer Multiple Quantum Well Based Devices

Broad-area 50μm stripe lasers were used extensively throughout this thesis, to relate device performance with variations in material parameters. Table 10.1 below represents a summary of data acquired and compares the results with others presented in the open literature.

Table 10.1 k-parameter and J_{∞} comparison of laser structures discussed in this thesis with others presented in the literature.

Worker	Well Type	Well Thickness(Å)	k (mm)	J_{∞} (Acm^{-2})
Greene et al[7]	Lattice matched $Ga_xIn_{1-x}As$	85	1.74	494*
Briggs et al[8]	1% Compressive $Ga_xIn_{1-x}As$	21	1.5	406*
This Work	0.83% compressive $Ga_xIn_{1-x}As_yP_{1-y}$	40	1.28	534**
Osinski et al[9]	1.1% compressive $Ga_xIn_{1-x}As$	50	1.24	412**
This Work	1.29% tensile $Ga_xIn_{1-x}As$	95	0.8	517**
Tsang et al[10]	980nm 2-well GaAs-$Ga_xIn_{1-x}As$		0.4	-

* 3-well device

** 4 well device

It can be seen from the above table that the incorporation of coherent strain increases the effective gain per well (1/k). A significant improvement (factor of two) is observed in the use of tensile strained wells. The light-hole like nature and the influence of the larger well width on the optical confinement both serve to increase the available gain per well. It is evident, however, that the gain of the best InP-based device is still a factor of 2 below the value measured in a GaAs/$Ga_xIn_{1-x}As$ 980nm device. This observation would suggest that non-radiative recombination via Auger processes and inter-valence band absorption are still limiting the performance of InP-based MQW lasers, when compared to GaAs-based devices. The larger band-gap energy of GaAs has the effect of reducing the probability of either Auger recombination or IVBA occurring.

The beneficial effects of the incorporation of coherent strain were best exemplified by the improvements observed in the gain per well, when sufficient tensile strain was introduced in the quantum well to make E1-LH1 the most energetically favourable transition. Reductions in threshold current, and increases in output power, were observed for ridge waveguide devices incorporating compressively strained quaternary and tensile strained ternary wells. These improvements were evident when compared to either strained ternary or lattice matched devices.

Direct evidence of the expected improvements in differential gain, due to the introduction of compressive strain in quantum wells, was presented. A fourfold improvement in the differential gain was observed in a compressively strained $Ga_xIn_{1-x}As_yP_{1-y}$ MQW structure when compared to a lattice matched $Ga_xIn_{1-x}As$ MQW structure. The observed improvements in differential gain, together with other optimisation steps, resulted in a DFB laser with a 3dB frequency response bandwidth of 22GHz, at a drive current of 125mA[11].

The ability to improve the performance of a device by utilising 'valence band engineering' was also demonstrated. The deleterious effects on the performance of a 10 Gbits/sec electro-absorption modulator, due to the large valence band discontinuity present in a lattice matched $Ga_xIn_{1-x}As_yP_{1-y}$ MQW structure, were discussed. By introducing certain compressively strained compositions in the wells, and tensile strained compositions in the barrier, the effective potential barrier seen by holes in the well was reduced, alleviating hole trapping effects and improving carrier transport. The resultant improvements in the CW power handling characteristics and the 10Gbits/sec performance[12], enabled such a device to be used in 10Gbits/sec optical transmission evaluation systems.

10.3 Prospects for Future Research

As with any body of research, as many questions can be raised as answers and hindsight can often make the researcher query his original experimental designs. In terms of the work described in this thesis, there are several areas that would merit further research to more fully describe the influence of coherent strain on device performance. The unintentionally large amount of p-dopant used in the overgrowth of the compressively strained samples described in section 7.2.2 obviously resulted in greater material loss, α, than in previous lattice matched and strained ternary devices grown. A repeat of the experiment with a lower Zn profile would undoubtedly yield lower threshold and higher output power devices. Notwithstanding, the samples grown were capable of describing the effects of coherent strain on parameters such as gain per well. In addition, an implementation of the growth optimisation steps (detailed in chapter 8) in the form of a higher gas phase V/III ratio could be used to suppress the onset of thickness modulations in laser structures with more than 8 wells.

The rectification of another unintentional experimental error would be to repeat of the growth of the high speed, buried grating structure described in section 7.3.2. This would require the process optimisation of the overgrowth of the described strain compensated MQW structure over a grating which had *not* been overetched into the substrate. Such a structure will hopefully demonstrate an even higher 3dB bandwidth than the structure described in section 7.3.2, for the reasons described

therein. An evaluation of the high speed performance of tensile strained devices, particularly a determination of the differential gain, would have provided further insight into the relative merits of compressive and tensile strain. From the superior gain per well performance demonstrated in tensile devices reported in chapter 9, one would expect the 3dB bandwidth to be greater than the compressively strained case, as a result of the improved gain. In fact, theoretical predictions by Seki et al[13] have indicated that tensile strained MQW devices should have significantly reduced gain saturation when compared to compressively strained ones. However, Wu et al[14] have suggested that higher gain compression exists in tensile strained MQW devices. The thickness-mismatch product limitations observed in the reported tensile strained MQW samples could be overcome by using compensating compressive strain in the barriers.

A detailed study of the dependence of threshold current on the magnitude of compressive strain in the wells of the GaInAsP/GaInAs, non-compensated structures grown in section 9.3 would have provided an insightful contrast to the analysis that was performed on tensile strained structures described in section 9.2. Even though a similar study was performed by Thijs et al[15], the style in which the samples described in this thesis were grown, with constant well width and consequently constant confinement factor, would have afforded an elegant study of the evolution of gain per well as a function of compressive strain.

Moving on from device performance to further growth studies, the most obvious area for future evaluation is a more detailed material assessment of the non-compensated compressively strained samples reported in section 9.3. Transmission electron microscopy evaluation (both plan view and cross-section) of these samples may have both provided insight into the predominant strain relief mechanisms, and an explanation for the sudden loss in structural quality observed when the compressive strain was increased beyond 1.6%.

The observation of the role of the barrier material in defining the strain relief mechanism of compressively strained GaInAsP, which was reported in chapter 9, also merits further investigation. Structures with InP barriers relaxed via dislocation introduction, whereas lattice matched GaInAsP barriers resulted in thickness modulated growth. Although the role of the miscibility gap has already been investigated and discussed in chapter 8, a more detailed evaluation of the transition from dislocation generation to thickness modulations would be ultimately useful in mapping out barrier compositions of $Ga_xIn_{1-x}As_yP_{1-y}$ that are least likely to induce thickness modulations. The respective positions of the wells and barriers to the miscibility gap also merits evaluation. It was further demonstrated in chapter 9 that tensile strained $Ga_xIn_{1-x}As/Ga_xIn_{1-x}As_yP_{1-y}$ MQW's suffered from thickness modulations, but it appeared (from XRD measurements only) that compressively strained $Ga_xIn_{1-x}As/Ga_xIn_{1-x}As_yP_{1-y}$ MQW's did not. This observation that tensile

strained, non-compensated devices are more susceptible to thickness modulations than compressively strained ones needs to be understood.

10.4 Progress since 1994

The experimental work described in this thesis terminated in the summer of 1994. Since then, coherently strained $Ga_xIn_{1-x}As_yP_{1-y}/Ga_xIn_{1-x}As_yP_{1-y}$ MQW lasers and modulators have evolved from laboratory demonstrations to generally available products from numerous optoelectronic component suppliers such as Nortel, Alcatel, Uniphase (formerly Philips Optoelectronics), Lucent, Lasertron, Fujitsu and NEC (to name a few!). In the area of high speed, directly modulated lasers, Morton et al[16] achieved a small improvement in modulation bandwidth of a DFB version of the FP structure referred to in chapter 7, reference 18. Their DFB achieved a -3dB bandwidth of 26 GHz. More recently, Matsui et al.[17] fabricated a strain compensated MQW laser with 0.89% compressively strained GaInAsP wells and 0.83% tensile strained GaInAlAs barriers. In a 20 well structure, with a 120 μm cavity length, a -3dB modulation bandwidth of 30 GHz was reported. However the reported differential gain of $15x10^{-16}cm^2$ was less than the $25x10^{-16}cm^2$ measured in chapter 7 on a 300μm cavity length device. It is assumed that the higher modulation bandwidth (compared to 22 GHz measured in chapter 7) was achieved through the use of a shorter cavity length device. As the authors did not present the ex-facet power emitted by the 30GHz bandwidth device it makes further comparisons difficult.

Another area in which the use of coherently strained materials has developed is in the fabrication of polarisation insensitive devices. As described in chapter 9, tensile strain-based MQW structures can be grown to allow the tensile strain to overcome the quantum confinement and restore the valence band degeneracy which quantum confinement has lifted. It can be shown[18] that the absorption co-efficients in the TE and TM modes can be made equal if the valence band is degenerate. Devaux et al[18], have fabricated tensile strained GaInAs well devices with InAlAs barriers and GaInAsP well devices with GaInAsP barriers into polarisation insensitive modulators. A modulation bandwidth of 42 GHz was measured for the InGaAs/InAlAs structure (75μm cavity length) and a bandwidth of 30 GHz was inferred for the GaInAsP/GaInAsP structure (90μm cavity length). The main limitation of the InGaAs/InAlAs structure was optical power saturation evident at input powers as low as a few μ W. In a subsequent publication, Devaux et al.[19] fabricated a GaInAsP/GaInAsP structure with a modulation bandwidth of 25 GHz for a cavity length of 125 μm and power saturation levels in excess of 100mW input power.

A further area of development is in the optoelectronic integration of lasers, modulators and other active and passive optoelectronic components. Thrush et al[4] developed the electroabsorption

modulator described in chapter 8 into an integrated laser modulator; the laser and modulator MQW active regions being deposited in a single step MOVPE process. The different quantum well layer thicknesses required by both the laser and modulator were achieved using selective area epitaxy and growing the laser structure between two oxide stripes where the growth rate is enhanced. Integration is also fueling the next generation of components for wavelength division multiplexing optical transmission systems. Fang et al[20] fabricated a 4-wavelength DFB array, coupled via 4x1 star coupler and s-bends, into a semiconductor optical amplifier and an EA modulator. All this was achieved monolithically and the four channels could be collectively modulated at 2.5 Gbit/sec.

The improvements in the temperature sensitivity of laser threshold current offered by coherent strain have made the un-cooled laser a practical option. Historically, semiconductors lasers have always been temperature controlled by a thermo-electric cooler, to prevent environmental temperature changes altering the device characteristics. The higher T_0 values observed for coherently strained MQW devices have made them candidates for such applications where cost is the main driving force rather than high performance, e.g. intra-office optical communication. The status of strained layer MQW lasers for un-cooled applications was recently reviewed by Ring[21].

Since 1994 additional reports on the growth of InP-based strain compensated ternary MQW structures have been made. Tu et al[22] reported on the gas-source MBE growth of a 30 period $InAs_{0.4}P_{0.6}/Ga_{0.17}In_{0.83}P$ structure which corresponds to 1.3% compressive strain in the wells and 0.93% tensile strain in the barriers. The growth temperature used was approximately 500°C. Although they did not present TEM data, the HRXRD rocking curve would suggest that planar interfaces were maintained during the growth of the stack. This observation, that strain-compensated ternary MQW structures are being grown with planar interfaces at lower growth temperatures, further validates the experimental observations made in chapter 8 on ±1% GaInAs MQW's grown on InP and ±1% GaInP MQW's grown in GaAs.

The InAsP/GaInP strain compensated MQW structure has also been studied in MOVPE by Patriarche et al[23], where growth temperatures of 610°C were used. At this growth temperature, thickness modulations were observed in their six period $InAs_{0.5}P_{0.5}/Ga_{0.2}In_{0.8}P$ stack. The well and barrier strains were 1.7% compressive and 1.5% tensile respectively, but no comment was made on group V partial pressure used to grow the wells and barriers. To overcome the thickness modulations that evolved in this structure, Patriarche et al[23] grew a second structure which was identical to the first but had 15Å InP layers surrounding the each well. The addition of these layers did not prevent thickness modulations occurring in the individual compressively strained wells or tensile strained barriers but they did succeed in temporarily planarising the growth interface, inhibiting the magnification of the thickness modulations as the stack is grown. These observations

support those made in chapter 9 which showed that InP barriers resulted in planar interfaces being observed in a non-compensated stack.

Further reports have also been made on the growth of strain compensated GaInAs(P)/GaInAsP MQW structures since 1994. Shimose et al[24] grew a 10 period, +1%/-0.5% strain compensated GaInAsP/GaInAsP structure at growth rates varying between 0.2 nm/s to over 0.5 nm/s by MOVPE. They observed that the lateral periodicity of the thickness modulations reduced with increasing growth rate. They also demonstrated empirically that the magnitude of thickness modulation could be reduced by implementing a growth sequence that did not pause the growth between the deposition of the well and the barrier material. Patriarche et al[23] demonstrated that the use of thin InP material, sandwiching the well material in a strain compensated InAsP/GaInAsP MQW, was also successful in suppressing the magnification of thickness modulations in structures with GaInAsP barriers. They also demonstrated that the use of lattice matched GaInAsP material to sandwich the InAsP well material was unsuccessful in suppressing the magnification of thickness modulations in the stack, adding further support to the observations made in chapter 9.

Progress has also been made on direct measurements of the characteristics of thickness modulated layers. Ponchet et al[25] have performed high resolution TEM on +1.5%/-0.5% GaInAsP structures. They have shown that, although the nominal mismatch between the well and barrier is 2%, variations of (110) lattice spacing can be as high as 3.5%. Ponchet at al[25] propose that the driving force for thickness modulations in these structures is the expansion and contraction of lattice planes leading to elastic relaxation of the layer by modulations of the thickness and strain. Chen et al[26], on the other hand, suggest that compositional clustering is the driving force for thickness modulation. They have used atomic force microscopy and scanning tunneling microscopy to evaluate strain compensated InGaP/InGaAsP structures that suppress magnification of the modulations by using InP in a similar way to Patriarche at al[23]. In an individual tensile strained GaInAsP layer they have presented evidence of a cation (Ga and In) variation of ±3% and an anion (As and P) variation of ± 6%.

References

1. A.G. Cullis, D.J. Robbins, A.J. Pidduck and P.W. Smith, J Cryst Growth, 123, pp333-343, 1992.

2. A.D. Smith, A.T.R. Briggs, K. Scarrott, X. Zhou, U. Bangert, Applied Physics Letters, 65(18), 1994, p2311-2313.

3. R.W. Glew, K. Scarrott, A.T.R. Briggs, A.D. Smith, V.A. Wilkinson, X. Zhou and M. Silver, Journal of Crystal Growth, 145(1994), p764-770.

4. EJ Thrush, RW Glew, PD Greene, MA Gibbon, CJ Armistead, AD Smith, ATR Briggs, K Scarrott, IK Czajkowski, CJ Jones and BL Patel, Proc. International Conference on InP and related materials, Santa Barbara, 1994.

5. A. Ponchet, A. Rocher, JY. Emery, C. Starck and L. Goldstein, J Appl Phys, 74(6), Sept 1993, pp3778-3782.

6. H Temkin, DG Gershoni, SNG Chu, JM Vandenberg, RA Hamm and MB Panish, Appl. Phys. Letts., 55(16), Oct. 1989, pp1668-1670.

7. P.D. Greene, J.E.A. Whiteaway, G.D. Henshall, R.W. Glew, C.M. Lowney, B. Bhumbra and D.J. Moule, Proc. 17th international Symposium on GaAs and related compounds, Inst Phys Conf Series vol 112, pp555-560, 1990.

8. A.T.R. Briggs, P.D. Greene and J.M. Jowett, , IEEE Phot. Tech. Lett., 4(5), May 1992.

9. J.S. Osinski, P. Grodinski, Y. Zou and P.D. Dapkus, IEE Elect. Letts., 27(5), 1991, pp469-470.

10. W.T. Tsang, R. Kapre, M.C. Wu and Y.K. Chen, Applied Physics Letters, 61, 1992, pp755-757.

11. A.P. Wright, A.T.R. Briggs, A.D. Smith, R.S. Baulcomb and K.J. Warbrick, IEE Electronics Letters, 29(21), October 1993, p1848-1849.

12. I.K. Czajkowski, M.A. Gibbon, G.H.B. Thompson, P.D. Greene, A.D. Smith and M. Silver, IEE Electronics Letters, 30(11), May 1994, p900-901.

13. S. Seki, T. Yamanaka, K. Yokoyama, P. Sotirelis and K. Hess, J App Phys, 74, pp2971-2973, 1993.

14. T.C. Wu, S.C. Kan, D.C. Vassilovski, K.Y. Lau, C.E. Zah, B. Pathak and T.P. Lee, App. Phys. Lett., 60, pp1794-1796, 1992.

15. P.J.A. Thijs, J.J.M. Binsma, L.F. Tiemeijer, P.I. Kuindersma and T. van Dongen, Microelectronic Engineering, 18(1992), pp57-74.

16. PA Morton, T Tanbun-Ek, RA Logan, DA Ackerman, G Sctengel, N Chand, JE Johnson, RD Yadvish, M Sergent and PF Sciortino, Conf. Dig. OFC 1996, San Jose CA, Paper TuH6, pp39-40.

17. Y. Matsui, H. Murai, A. Suzuki and Y. Ogawa, Conf. Dig. ECOC 1998, Madrid, Spain, pp633-634.

18. F. Devaux, S. Chelles, A. Ougazzaden, A. Mircea and J.C. Harmand, Semiconductor Science Technology, 10(1995), pp887-901.

19. F. Devaux, A. Ougazzaden, M. Carre and F. Huet, Conf. Dig. OFC 1997, Dallas TX, Paper WG4, pp139-140.

20. W. Fang, T. Tanbun-Ek, C.G. Bethea, P. Wisk, P.J. Sciortino, A.M. Sergent, S.N.G. Chu, R. Pawelek, R. People, G. Nykolak, Y.K. Chen and W.T. Tsang, Conf. Dig. CLEO 1997, Baltimore MD, 1997 OSA Technical Digest Series Number 11, Paper CMG4, pp28-29.

21. W.S. Ring, Conf. Dig. OFC 1997, Dallas TX, Paper ThR4(Invited), pp329-330.

22. C.W. Tu, X.B. Mei, C.H. Yan and W.G. Bi, Materials Science and Engineering, B35 (1995), pp166-170.

23. G. Patriarche, A. Ougazzaden and F.Glas, App. Phys. Lett., 69(15), 7 October 1996, pp2279-2281.

24. Y. Shimose, T. Kikugawa and H. Nagai, Proc. International Conference on InP and related materials, 1995, paper WP35, pp210-212.

25. A. Ponchet, A. Rocher, J-Y. Emery, C. Starck and L. Goldstein, J. Appl. Phys., 77(5), 1 March 1995, pp1977-1984.

26. H. Chen, R.M. Feenstra, R.S. Goldman, C. Silfvenius and G. Landgren, App. Phys. Lett, 72, 1998.